TESIS DE LA UNIVERSIDAD DE ZARAGOZA

2019

18

Mohd Zamidi Ahmad

Synthesis and characterization of polyimide-based mixed matrix membranes for CO2/CH4 separation

Departamento

Ingeniería Química y Tecnologías del Medio Ambiente

Director/es

TELLEZ ARISO, CARLOS
FILA, VLASTIMIL
BENES, NIECK

ISSN 2254-7606

Prensas de la Universidad Universidad Zaragoza

ISSN 2254-7606

Universidad Zaragoza
1542

Tesis Doctoral

SYNTHESIS AND CHARACTERIZATION OF POLYIMIDE-BASED MIXED MATRIX MEMBRANES FOR CO2/CH4 SEPARATION

Autor

Mohd Zamidi Ahmad

Director/es

TELLEZ ARISO, CARLOS
FILA, VLASTIMIL
BENES, NIECK

UNIVERSIDAD DE ZARAGOZA

Ingeniería Química y Tecnologías del Medio Ambiente

2018

UNIVERSITY OF
CHEMISTRY AND TECHNOLOGY
PRAGUE

UNIVERSITY OF TWENTE.

Universidad
Zaragoza

Synthesis and characterization of polyimide-based mixed matrix membranes for CO_2/CH_4 separation

DISSERTATION

AUTHOR	**Mohd Zamidi Ahmad**
SUPERVISOR	**Dr. Ing. Vlastimil Fíla** **prof. Dr. Ir. Nieck E. Benes** **prof. Dr. Carlos Téllez Ariso**
STUDY PROGRAMME	Chemistry and Chemical Technologies
FIELD OF STUDY	Inorganic Technology
YEAR	**2018**

VYSOKÁ ŠKOLA
CHEMICKO-TECHNOLOGICKÁ
V PRAZE

UNIVERSITY OF TWENTE.

Universidad
Zaragoza
1542

Syntéza a charakterizace membrán se smíšenou matricí na bázi polyimidů pro separaci CO_2 /CH_4

DISERTAČNÍ PRÁCE

AUTOR | **Mohd Zamidi Ahmad**

ŠKOLITEL | **Dr. Ing. Vlastimil Fíla**
prof. Dr. Ir. Nieck E. Benes
prof. Dr. Carlos Téllez Ariso

STUDIJNÍ PROGRAM | Chemie a chemické technologie

STUDIJNÍ OBOR | Anorganická technologie

ROK | **2018**

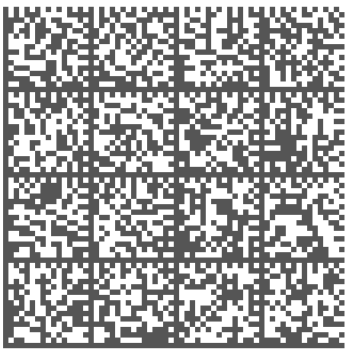

I would like to acknowledge Assoc. Prof. Dr. Vlastimil Fila, doctorate thesis supervisor of the hosting university, University of Chemistry and Technology Prague (UCTP), CZECH REPUBLIC. My utmost appreciation to Prof. Dr. Joaquín Coronas-Ceresuela and Prof. Dr. Carlos Téllez-Ariso from University of Zaragoza (UNIZAR), SPAIN for the continuous guidance and assistance. Not forgetting Prof. Dr. Ir. Nieck E. Benes and Assoc. Prof. Wiebe M. de Vos of University of Twente (UTwente), NETHERLANDS for your kindest support and assistance.

The research was performed under the ERASMUS MUNDUS Joint Doctorate Program in Membrane Engineering, FPA n. 2011-0014, SGA n. 2012-1719, under the financial support of EACEA/European Commission. Acknowledgement also to the financial assistance of Operational Programme Prague – Competitiveness (CZ.2.16/3.1.00/24501) and "National Program of Sustainability" (NPU I LO1613) MSMT-43760/2015.

TO THE MOST GRACIOUS WOMAN IN MY LIFE,
IBUNDA BIDAH M. SALLEH.

You are the pillar of my strength.
No words can describe my gratitude for your being, your sacrifice and your smile. No words can thank you enough.
I love you.

"All that I am, or hope to be, I owe to my angel mother" – Abraham Lincoln.

To my siblings, my nephews and nieces.

I wish my journey inspires you.
Remember that those at the top of the mountain didn't fall there.
Take the challenge of your life and reach out to your goals.
There is no limit to what you can achieve.

"We know what we are, but not what we may be" – Hamlet.

SUMMARY

The acid gasses content in raw natural gas resources is ever increasing, making the need for higher efficiency separation technologies more crucial. Many significant advancements to the existing gas separation membrane technology are required to produce a membrane system with higher thermal stability, tolerance to contaminants and resistance to CO_2-induced plasticization, and to compete with other well-established technologies. One of the most feasible approaches is by making mixed matrix membrane (MMM), combining the organic (polymer) with inorganic particles with the aim to exploit the synergistic advantages from each phase: commonly the excellent permeability of the dispersed fillers, high selectivity and easy processability of the polymers. The research focuses on the development of MMMs for natural gas separation applications. The investigation involved aromatic-constituted moieties and highly rigid-backbone 6FDA-based co-polyimides (novel 6FDA-bisP, 6FDA-ODA, and 6FDA-DAM) with zeolite-based and zirconium-based metal-organic framework nanoparticles (ZIF-8 and CO_2-philic UiO-66, Zr-BDC), into several types of mixed matrix membrane systems. In this thesis, a detailed nano-sized MOFs synthesis and post-synthesis modification methodology, MMM fabrication methods as well as the strategies to have an optimized interface interaction are given. A thorough and systematic characterization to understand the membrane morphologies and its formations were presented to apprehend their effects on the gas separation. The gas separation performances were evaluated with a mixed gas which mainly constituted of CO_2 and CH_4, at various molar concentrations, feed pressures, and temperatures. The stability of MMM systems in high-pressure separation, with various testing parameter variants including in the presence of natural gas impurities (i.e., H_2S), mimicking an actual membrane separation process was also investigated. Overall, the study affirms that with an appropriate MMM fabrication method, inorganic filler selection to the intended membrane improvements, the investigated co-polyimides have a tremendous potential for CO_2/CH_4 gas separation applications.

SOUHRN

Se zvyšujícím se obsahem kyselých plynů ve zdrojích surového zemního plynu stále roste zájem o vývoj nových separačních technologií s vyšší účinností a nižší energetickou náročností. Pro vývoj konkurenceschopných membránových technologií je zapotřebí se zaměřit zejména na vytvoření membránového systému s vyšší tepelnou stabilitou, tolerancí vůči kontaminujícím látkám a odolností proti plastifikaci indukované oxidem uhličitým. Jedním z nejpravděpodobněji realizovatelných přístupů je použití smíšené matricové membrány (MMM), která kombinuje organický (polymer) s anorganickými částicemi za účelem využití synergických výhod z každé fáze: vysoké selektivity a snadné zpracovatelnosti polymerů a vysoké propustnosti dispergovaného plniva. Tato práce se zaměřuje na vývoj MMM pro aplikaci při čistění zemního plynu a bioplynu. Bylo studováno několik typů MMM vycházejících s kopolyimidů s vysoce stabilním páteřním řetězcem na bázi 6FDA (6FDA-bisP, 6FDA-ODA a 6FDA-DAM) a nanočástic mikroporézních molekulových sít tvořených organickými linkery spojujícími kationty kovů nebo klastry kovových oxidů, tzv. MOF (metal organic frameworks), na bázi zinku a zirkonu (ZIF-8 a CO_2-philic UiO-66, Zr-BDC).

V této práci je podrobně řešena problematika syntézy a post-syntetické úpravy nanočástic MOF, metodika přípravy MMM a způsoby optimalizace fázového rozhraní polymer-částice.

Pro pochopení morfologie membrány, jejího formování a zachycení jejich účinků na výslednou separaci plynů byla provedena důkladná charakterizace připravených membrán v jednotlivých krocích jejich přípravy.

Separační účinnost připravených membrán byla testována pomocí separací binárních směsí CO_2 a CH_4, při různých molárních koncentracích, tlacích a teplotách. Stabilita připravených MMM byla také testována za různých podmínek i při vysokotlakové separaci simulující reálný proces čistění zemního plynu s přítomností nečistot (H_2S). Výsledky této studie potvrzují, že zkoumané kopolyimidy mají obrovský potenciál pro použití při separaci plynů CO_2/CH_4 a při použití vhodného postupu přípravy MMM a vhodné volbě plniva lze dosáhnout značného zlepšení parametrů připravených membrán.

RESUMEN

El contenido de componentes ácidos en el gas natural crudo es cada vez mayor por lo que es crucial la necesidad del uso de tecnologías de separación con mayor eficiencia. Se requieren avances significativos en las tecnologías existentes de separación de gases por membrana para tener un proceso con mayor estabilidad térmica, resistencia a los contaminantes y evitar la plastificación inducida por el CO_2 con ello se podrá competir con otras tecnologías. Uno de los enfoques más factibles es hacer una membrana de matriz mixta (MMM), que combina materiales orgánicos (polímero) con partículas inorgánicas con el objetivo de explotar las ventajas sinérgicas de cada material: alta permeabilidad y alta selectividad de los rellenos dispersos, y fácil procesabilidad de los polímeros. Esta tesis doctoral se enfoca en el desarrollo de MMMs para aplicaciones de separación de gas natural. En la investigación se usaron copolímeros constituidos por aromáticos y de estructura altamente rígida como el 6FDA (6FDA-bisP, 6FDA-ODA y 6FDA-DAM) con nanopartículas que poseen estructuras metal-orgánicas como las zeolíticas de imidazol ((ZIF-8) o carboxilatos de zirconio (UiO-66 y materiales relacionados). En este trabajo se desarrolla una síntesis detallada de MOFs nanométricos, así como un procedimiento de modificación posterior a la síntesis, métodos de fabricación de MMMs, y finalmente estrategias para tener una interacción optimizada de la interfase polímero-relleno. Se presenta una caracterización exhaustiva y sistemática de las membranas para entender la separación de gases. Además, se evaluaron los rendimientos de separación de gases utilizando mezclas de gases constituidas principalmente por CO_2 y CH_4 en varias concentraciones molares, a diferentes presiones de alimentación y temperatura. También se investigó la estabilidad de las MMMs en separaciones a alta presión incluyendo la presencia de impurezas en el gas natural (por ejemplo, H_2S) con el objetivo de imitar un proceso real de separación de membrana. En general, el estudio confirma que con un método apropiado de fabricación de MMMs así como la selección apropiada del relleno inorgánico se obtienen las mejoras deseadas en la membrana, en este aspecto las copolíimidas investigadas tienen un enorme potencial para aplicaciones de separación de gases CO_2/CH_4.

OVERZICHT

De hoeveelheid zure gassen in aardgasbronnen groeit, met als gevolg een cruciale nood aan meer effectieve scheidingstechnologieën. Een beduidende vooruitgang op de bestaande membraantechnologie voor gasscheiding is nodig, om zo een membraansysteem te produceren met een hogere thermische stabiliteit, tolerantie voor verontreinigers en weerstand tegen plastificering door CO_2, en ook om te concurreren met andere technologieën. Een van de meest realiseerbare aanpakken ligt bij mixed matrix membranen (MMMs), welke organische (polymeer) met anorganisch partikels combineren, met het doel de synergetische voordelen van elke fase te gebruiken: hoge permeabiliteit van de vuldeeltjes, hoge selectiviteit en makkelijke verwerking van de polymeren. De studie concentreert zich op de ontwikkeling van MMMs toegepast op aardgasscheiding. Het onderzoek betrekt aromatische groepen en zeer rigid-backbone 6FDA-gebaseerde co-polyimiden (nieuwe 6FDA-bisP, 6FDA-ODA en 6FDA-DAM) met zeoliet- en zirkonium-gebaseerde metaal-organische rooster nanodeeltjes (ZIF-8 en CO_2-fiel UiO-66, Zr-BDC) in verschillende types MMM-systemen. In deze thesis wordt een gedetailleerde -op nanoschaal- MOF-synthese en post-synthese modificatiemethodologie, MMM-fabricatiemethodes, alsook strategieën voor een geoptimaliseerde interface-interactie, aangegeven. Een grondige systematische kenschets, welke moleculaire modellering bevat, om de membraanmorfologie en vorming ervan te begrijpen, wordt gepresenteerd teneinde de effecten op gasscheiding te vatten. De scheidingsprestaties worden geëvalueerd aan de hand van een gemixt gas, vnl. bestaande uit CO_2 en CH_4, bij variërende molaire concentraties, voedingsdruk en temperaturen. De stabiliteit van MMM-systemen bij hogedrukscheiding, via verscheidene testparameters, inclusief de aanwezigheid van aardgasonzuiverheden (d.i., H_2S) in nabootsing van een reëel membraanscheidingsproces, worden eveneens onderzocht. Zo bevestigt deze studie dat met een gepaste MMM-fabricatiemethode, anorganische vulmiddelselectie voor de bedoelde verbetering van membranen, de onderzochte co-polyimiden een groot potentieel bevatten voor de toepassing op gasscheiding van CO_2/CH_4.

TABLE OF CONTENTS

CHAPTER 1: INTRODUCTION

1.1. BACKGROUNDS

The content of acid gasses (carbon dioxide, CO_2; hydrogen sulfide, H_2S) in raw natural gas varies with its locations and hydrocarbon origins [1–3], commonly in the range of 25 – 55 mol.% for CO_2 and below 2 mol.% for H_2S [4]. The acid gas removal is conventionally achieved by solvent-based absorption or adsorption processes. CO_2, is one of the most undesirable diluents aside from H_2S and it is essential to be discarded from the gas stream as it corrodes the transmission pipeline in the presence of water [4–6]. Additionally, CO_2 lowers the natural gas calorific value and causes atmospheric pollution [3–6]. Therefore, the impurities concentration must be reduced to meet the industrial processing and distribution requirements. The advances in gas separation membrane throughout the last decades have shown that the technology has accomplished a new level of maturity, comprises of over 400 hundred million US dollars per year or 24% of the total membrane market [7,8] (see Table 1-1), and has now arose to be the most viable alternative to substitute the conservative energy driven processes [9] (see Fig. 1-1).

In comparison to the conventional gas separation techniques (absorption, cryogenic distillation or pressure swing adsorption), the cutting-edge membrane separation technology offers [10–12]:

1. lower capital cost and investment,
2. a more straightforward operation; a process with no phase-change and minimal number moving/rotating parts, thus there is no need for intense monitoring or supervision,
3. a compact and modular system; using membrane modules with high membrane area density minimizes the space requirement and consequently lowers the capital cost,

4. ease of transportation and installation procedure especially for remote locations (i.e., offshore facilities) and limited spaces in the existing infrastructures,
5. environmental friendly unit operation.

Table 1-1: Main industrial applications of membrane gas separation, involving natural gas [8], and several examples of the use polymer types and their producers/suppliers [9,13].

Separation	Process
H_2/hydrocarbons	Hydrogen recovery in refineries, e.g., i. Silicone rubber coated with PS by Monsanto/Air Products ii. Polyaramid by Dupont iii. Polyimide (PI) by Ube, Air Liquide, and Praxair
CO_2/hydrocarbons	Natural gas sweetening, e.g., i. Cellulose acetate (CA) by Dow Generon, Membrane Systems, and AIR Products
H_2O/hydrocarbons	Natural gas dehydration
H_2S/hydrocarbons	Sour gas treating
He/hydrocarbons	Helium separation, e.g., ii. Polyetherimide (PEI) by Asashi Glass
Hydrocarbons/air	Hydrocarbons recovery

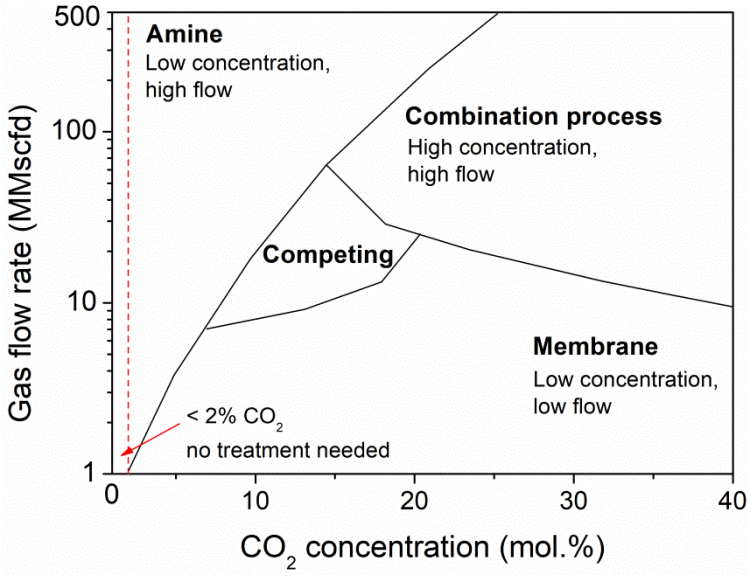

Fig. 1-1: Selection of suitable CO_2 removal technology based on the relationship between the flow rate and CO_2 concentration in the gas stream, adapted from Baker and Lokhandwala [9].

The theory of gas mixture separation by membrane technology means has been globally acknowledged, and processing of low-quality gas reservoirs with a high content of acid gas

using membrane will become more common [9,14]. Being the key performance, membranes permeability (inversely proportional to the membrane thickness) and selectivity remains as the most significant challenge to ensure higher separation efficiency [15], among other required characteristics such as excellent thermal stability, high tolerance to contaminants and plasticizing agents (CO_2, H_2S, water vapor), highly available and good reducibility [15]. Polymeric membrane, being one to three order magnitude cheaper than the inorganic-based membranes [16], needs to be further enhanced to compete with the chemically and thermally stable inorganic membrane (commonly produced from metals, ceramics or pyrolyzed carbon [17–19]) with five to ten times higher perm-selectivity [16]. Nonetheless, the inorganic membranes are prohibitively expensive and delicate to fashion into continuous and defect-free membranes [17,19]. An approach of exploiting both polymeric and inorganic membranes advantages, in the form of a mixed matrix membrane (MMM) is getting its deserving attention in the last decade. Most MMMs are comprised of more rigid glassy polymers due to their acceptable selectivity (e.g., commercialized cellulose acetate, CA and polysulfone, PSF possess CO_2/CH_4 selectivity of 15 – 20 [12]) and mechanical strength compared to the rubbery polymers which show higher permeability but high vulnerability to swelling and plasticization. The CO_2/CH_4 separation performance comparison of the three types of membranes are presented in Fig. 1-2, with the permeability-selectivity trade-off limit, introduced by Lloyd Robeson [20,21].

The number of an engineered inorganic materials: metal-organic frameworks (MOFs) investigations on has grown rapidly for natural gas sweetening and CO_2 capture due to their remarkable inherent, such as high CO_2 uptakes (e.g. HKUST-1 of 7.32 [22] and 10.71 $mmol \cdot g^{-1}$ [23], MIL-53 of 10.02 $mmol \cdot g^{-1}$ [23], MIL-100 of 9.98 $mmol \cdot g^{-1}$ [24], MIL-101 of 7.20 $mmol \cdot g^{-1}$ [25]), open porous framework structures with large accessible pore volumes, tuneable pore affinity and most importantly their relatively high chemical and thermal stabilities. MOFs can be classified by their three-dimensional crystalline frameworks with permanent porosity, formed with metal-based clusters linked by organic ligands [26]. Several intensive reviews on MOFs for CO_2 separation [10,27–29] and their incorporation in MMMs has been reported using both low flux (e.g. PSF [30], PVAc [31] and PBI [32]) and high flux (e.g. rubbery PDMS [33] and glassy 6FDA-DAM [34,35]) polymers. With the increasing numbers of MOFs discovery, syntheses and characterizations (more than 4000 per year since 2010), as reported in the Cambridge Structural Database (CSD) [10], the possibility of fabricating MMMs with MOFs increases simultaneously. Several MOFs exhibited very high CO_2 permeability (P_{CO2}) and CO_2/CH_4 selectivity ($\alpha_{CO2/CH4}$) when tested

with 50:50 vol.% CO_2 and CH_4 mixture, i.e., bioMOF-14; P_{CO2} = 41600 Barrer, $\alpha_{CO2/CH4}$ = 3.5 [36], $Co_3(HCOO)_6$; P_{CO2} = 19700 Barrer, $\alpha_{CO2/CH4}$ = 12.6 [37], ZIF-69; P_{CO2} = 1023 Barrer, $\alpha_{CO2/CH4}$ = 4.6 [38], ZIF-8; P_{CO2} = 260 Barrer, $\alpha_{CO2/CH4}$ = 13.4 [39]. The cast selection provides a limitless possibility of MOFs incorporation into polymeric phase as MMMs.

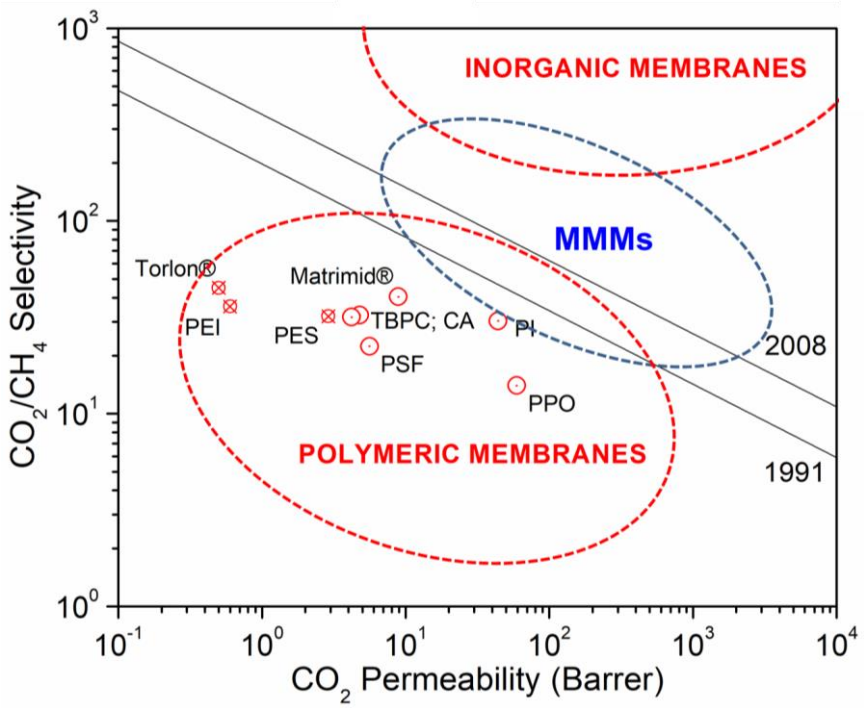

Fig. 1-2: Performance regions of polymeric, inorganic and mixed matrix membranes [40]. Highlighted are the industrially relevant polymeric membranes (tetra-bromo-polycarbonate, TBPC; cellulose acetate, CA; polysulfone, PSF; Matrimid®; polyimide, PI; poly(2,6-dimethyl-1,4-phenylene oxide, PPO) [41] and several of easily accessible and most intensively studied polymers (Torlon® polyamide-imide, PAI; polyetherimide, PEI; polyethersulfone, PES) in the last decade, in comparison to the Robeson permeability-selectivity 1991 and 2008 upper bounds [20,21].

1.2. SCOPE AND RESEARCH CONTRIBUTION

The previous section established the importance of investigating new membrane for gas separation, and the MMM provides the means for enhanced gas separation performances and to broaden membrane future applications. MMMs based on the 6FDA-copolyimide and MOF filler has been identified as one of the material groups with high potential in membrane gas separations. Based on this knowledge the research aims of this thesis were defined as follow:

1. To synthesize a novel 6FDA-copolyimide for CO_2/CH_4 separation, and investigate the fabrication of mixed matrix membranes based on the 6FDA-copolyimides with nano-sized metal-organic frameworks,
2. To investigate other the readily available 6FDA-copolyimides for CO_2/CH_4 separation, and its application into mixed matrix membrane with the nano-sized metal-organic frameworks,
3. To develop a guided methodology for MOFs-6FDA co-polyimide mixed matrix membranes fabrication with selected MOFs, in this case, a zeolitic imidazolate framework MOF, ZIF-8 and zirconium-based MOF, UiO-66 were chosen,
4. To investigate the strategies for an optimized MMM interface interaction, the formation mechanisms and systematically improve their gas separation performances,
5. To demonstrate the stability of prepared MMM systems in high-pressure CO_2/CH_4 separation, with various parameter variants including in the presence of natural gas impurities (i.e., H_2S).

The overall research is collaboration between Department of Inorganic Technology, University of Chemistry and Technology Prague (Czech Republic), Chemical and Environmental Engineering Department and Instituto de Nanociencia de Aragón (INA), University of Zaragoza (Spain) and Membrane Science and Technology, Faculty of Science and Technology, MESA+ Institute for Nanotechnology, University of Twente (The Netherlands), under ERASMUS MUNDUS framework of Joint Doctorate in Membrane Engineering (EUDIME).

1.3. THESIS STRUCTURE

The thesis is separated into seven chapters, and their overviews are as the following:

1. **CHAPTER 1: Introduction**.

   This chapter introduces the research background, scopes and its key contribution to the field of research.

2. **CHAPTER 2: Literature review**.

   This chapter presents an overview of the polymeric membrane research and technology for gas separation purposes, focusing on polyimide and hexafluoro substituted co-polyimide. The introduction of MOFs and its incorporation in mixed matrix membrane are also presented.

3. **CHAPTER 3: Investigation of a new co-polyimide, 6FDA-bisP and its ZIF-8 mixed matrix membranes for CO_2/CH_4 separation**.

   In this chapter, synthesis and CO_2/CH_4 separation performance of a novel 6FDA-based co-polyimide, namely 6FDA-bisP are presented. *bis*-aniline P consisting of multiple aromatic rings is selected as the diamine moiety in the new co-polyimide, with the aim to produce a polyimide with high free volume and thus higher gas permeability than the commercialized polyimide [41]. An imidazolate-based MOF (zeolitic imidazolate framework, ZIF-8), synthesized with the particle size of less than 100 nm, is incorporated into this polymer to form mixed matrix membranes. The characterization of the neat 6FDA-bisP, ZIF-8 and MMMs are performed and discussed accordingly. The separation performance of the derived MMMs, measured with a 50:50 vol% CO_2 and CH_4 at a constant pressure of 5 bar, at 25 °C. All the work in this chapter is conducted in Department of Inorganic Technology, University of Chemistry and Technology Prague (UCTP).

4. **CHAPTER 4: Enhanced CO_2/CH_4 separation performances of 6FDA-based co-polyimides mixed matrix membranes embedded with UiO-66 nanoparticles**.

   The focus in this chapter is shifted to the synthesis of a relatively new high surface area zirconium-based MOF (University of Oslo, UiO-66) with a particle size of less than 50 nm and incorporated into three types of 6FDA-copolyimides, namely

6FDA-bisP, 6FDA-ODA, both low permeable co-polyimides and 6FDA-DAM, a high permeable co-polyimide. The UiO-66 and MMMs are characterized accordingly. Gas separation performance is evaluated using a feed composition of 50:50 vol.% CO_2: CH_4 binary mixture at 35 °C and a pressure difference of 2 bar. The performances are also compared to MMMs with bigger UiO-66 nanoparticles (particle size of ca. 100 and 200 nm). The study confirmed the UiO-66 incorporation into these co-polyimides has brought positive improvements of the dense membranes, without jeopardizing their positive attributes. The work in this chapter is conducted within EUDIME framework's first mobility in the Department of Chemical and Environmental Engineering and Instituto de Nanociencia de Aragón (INA), University of Zaragoza (UNIZAR), with a full collaboration from the home university, UCTP.

5. **CHAPTER 5: Further enhancement of CO_2/CH_4 separation of 6FDA-DAM based mixed matrix membrane with UiO-66 and its functionalized derivatives.**

Gas selectivity improvement of a highly permeable polymer membrane is known to be difficult to achieve, and this chapter presents gas separation performance of 6FDA-DAM MMMs with UiO-66 nanoparticles (<50 nm) and its functionalized derivatives, namely UiO-66-NH_2 and UiO-66-NH-$COCH_3$. UiO-66-NH-$COCH_3$ was obtained through a post-synthesis modification (PSM) of UiO-66-NH_2 [42]. Functionalization of UiO-66 is known to increase its CO_2 uptakes [43–45] while improving filler-polymer interface interaction and thus the CO_2 permeability and CO_2/CH_4 selectivity. Gas separation performance was evaluated using a feed composition of 50:50 vol.% CO_2 and CH_4 binary mixture for a standard measurement at 35 °C and a pressure difference of 2 bar. Additional measurements are conducted with 10 – 90 vol.% of the CO_2 binary mixture with CH_4, both at low (2 bar pressure difference) and high pressure (up to 40 bar), at 35 °C. The work is performed in both UNIZAR and the second hosting university within the EUDIME framework, University of Twente (UTwente) in the Membrane Science and Technology Group, Faculty of Science and Technology.

6. **CHAPTER 6: Understanding high-pressure CO_2/CH_4 separation of Zr-MOFs based MMMs to various separation parameter variances and in the presence of hydrogen sulfide, H_2S.**

In this chapter, an extended investigation of the membranes is reported, where the focus on separation performance of best performing 6FDA-DAM MMMs with various Zr-MOFs, tested with mixed CO_2/CH_4 mixture (10 – 50 CO_2 vol.%) up to 20 bar, at 35 °C in a membrane separation pilot infrastructure in SINTEF Energy Research, Norway. The performances are further evaluated systematically to simulate the actual natural gas separation with; (1) pressure variation, conducted between 5 – 20 bar, (2) CO_2 feed content variation, between 10 – 50 vol.% at elevated pressure, (c) temperature investigation at high pressure, between 35 – 55 °C, and finally (d) the performance effect in the presence of H_2S up to 5 vol.%. The collaboration is achieved under the framework of European Carbon Dioxide Capture and Storage Laboratory Infrastructure (ECCSEL), involving SINTEF and UTwente. The scope is conducted within the supervision of UNIZAR and UCTP.

7. **CHAPTER 7: Conclusions and recommendations**.

This chapter concludes the overall research findings and its conclusions. Future work recommendations are also presented.

CHAPTER 2: LITERATURE REVIEW

2.1. POLYIMIDE

Besides the gas separation performance, a polymeric membrane needs to have excellent thermal stability, high tolerance to contaminants and plasticizing agents and good reducibility, as previously mentioned [15]. Among the glassy polymers, aromatic polyimides have emerged over the last two decades as promising materials as they exhibit a number of those appealing features, e.g., thermal and mechanical stability, and high chemical resistance [46]. However, they have poor processability including limited solubility in organic solvents, caused by its rigid polymer backbone and strong inter-chain interaction. Structure modifications have been made extensively with the incorporation of both aliphatic [47] and aromatic moieties [48,49], to enhance its solubility and low optical properties (caused by intermolecular charge-transfer, CTC) [50].

In general, the performance of a membrane appears to be limited by a trade-off between permeability and selectivity, where every highly permeable membrane tends to present low gas selectivity, and the trade-off relationship of a specific gas pair (i.e., CO_2/CH_4, CO_2/N_2, H_2/N_2, etc.) had been presented by Lloyd Robeson. [20,21]. Other limiting factors are (1) physical aging of the glassy polyimide; where the polymer segmental movement is kinetically restrained below its glass transition temperature (T_g), however, the movement will gradually increase over time (increase the polymer density and therefore reduces the free volumes), towards the thermodynamic equilibrium state [41,51,52], and (2) plasticization; occurs when the concentration of a gas increases inside a polymer particularly at high pressure, the polymer chain swells and increases the chain motion and free motion over time [53,54]. Both phenomenon often results in higher gas flux and lower gas selectivity.

2.1.1. 6FDA dianhydride constituted co-polyimides

Polyimide structure modification and optimization have led the first researchers to synthesis co-polyimides over two decades ago; co-polyimide is a coupling of two different polyimides with different permeability and selectivity properties for optimized separation properties. The introduction of high-performing aromatic co-polyimides, constituted with 6FDA dianhydride for instance in the later years, which display CO_2 permeability of more than 500 Barrer [55–57], clearly indicates the sensitivity of the performance to the constituent groups. Particularly the number of methyl side groups attached to the diamine benzene ring, will lead to order-of-magnitude difference in permeability [46,58], added advantage to the 6FDA's hexafluoro substituted carbon (e.g., $–C(CF_3)_2–$ bulky groups) (see Fig. 2-1), which contributes to 6FDA-copolyimide reduced chain packing and stiffness, thus the increase permeability and appear to be more gas selective.

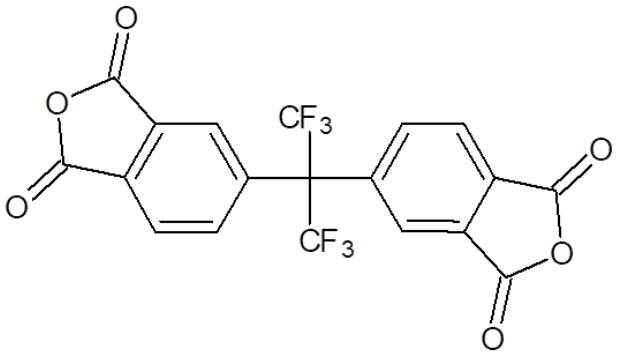

Fig. 2-1: Chemical structure of 4,4'-(hexafluoroisopropylidene)diphthalic anhydride (molecular formula: $C_{19}H_6F_6O_6$; molecular weight: 444.24 $g \cdot mol^{-1}$).

6FDA co-polyimides have been extensively studied with various aromatic diamine moieties, single- or multiple-ring [55,58–66]. Traditionally, these co-polyimides were synthesized using a two-step poly-condensation reaction [67,68], where a dianhydride and a diamine were reacted in a polar aprotic solvent under N_2 atmosphere to produce poly(amic) acid solution (PAA). The intermediate PAA formation is due to nucleophilic attack by the diamine amino group onto the anhydride carbonyl carbon [69], and the cyclodehydration of amide group can be obtained by either chemical imidization or thermal imidization in the solid or soluble state. The huge potential of these co-polyimides in gas separation is again contributed by (1) $–CF_3$ groups, causing limited chain packing, thus the higher free volumes, and (2) aromatic rings, which increases the chain rigidity and mobility and consequently affecting the gas selectivity [63,70]. The abundance of functional groups in the co-polyimide

will also enhance the solubility of polar CO_2 and CO_2/light gas solubility selectivity [21,71,72], and inorganic filler distribution when it is made into a mixed matrix membrane. Table 2-1 and Table 2-2 summarize several 6FDA-copolyimides, synthesized from single- (Fig. 2-2) or multiple-ring (Fig. 2-3) aromatic diamines.

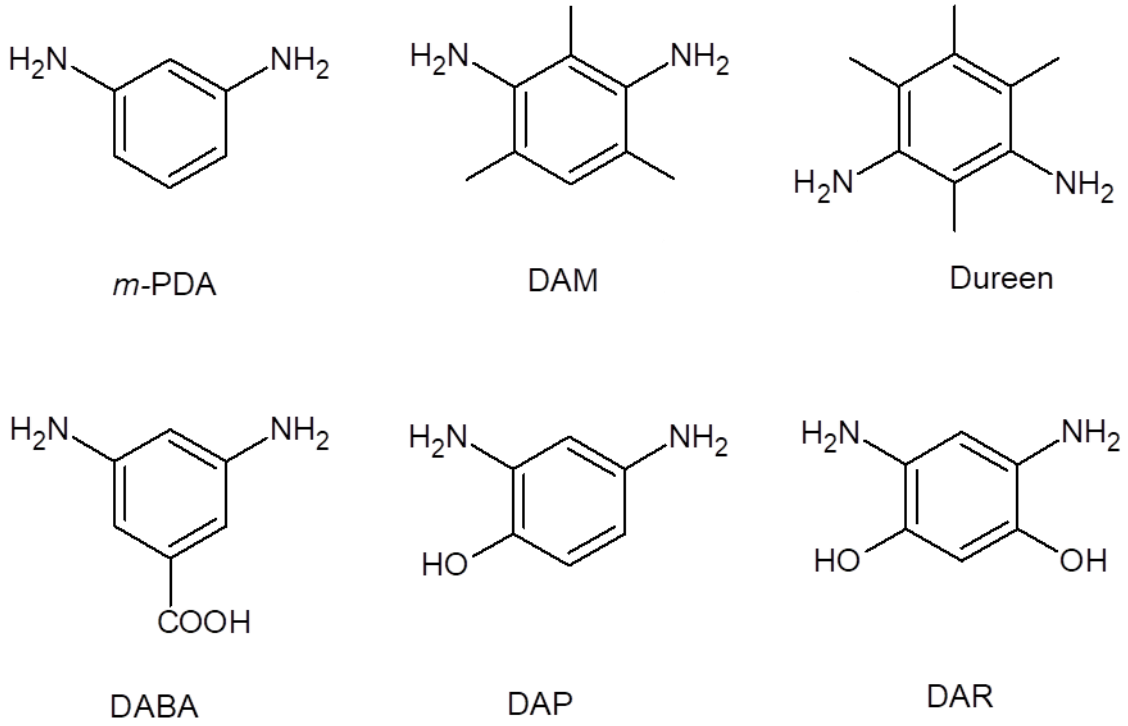

Fig. 2-2: Chemical structures of single-ring diamine monomers, *m*-PDA: 3,3′-diamino-4,4′-dihydroxybiphenyl; DAM: diaminomesitylene; Durene: 2,3,5,6-tetramethyl-1,4-phenylenediamine, DABA: 3,5-diaminobenzoic acid; DAP: 2,4-diaminophenol-dihydroxyl; and DAR: 4,6-diamino resorcinol di hydroxyl; among others.

Table 2-1: CO_2 and CH_4 single gas permeability, and the ideal selectivity of 6FDA-copolyimides, obtained from 6FDA dianhydride syntheses with single-ring aromatic diamine monomers.

Membrane	Measurement parameters		Gas permeability		Ideal selectivity, $\alpha_{CO2/CH4}$	Ref
	Temperature (°C)	Pressure (bar)	P_{CO2} (Barrer)	P_{CH4} (Barrer)		
6FDA-*m*PDA	35	6.9	20.3	0.4	57.7	[59]
	35	2.0	14.0	0.2	70.0	[60]
6FDA-DAM	35	6.9	842.4	46.8	18.0	[59]
	35	2.0	997.5	34.3	29.2	[55]
6FDA-Dureen	30	3.5	468.0	66.6	7.0	[61]
	25	2.0	1468	65.0	22.6	[62]
6FDA-DABA	35	6.9	12.8	0.2	62.2	[59]
	25	-	26.3	0.6	47.0	[58]
6FDA-DAP	25	-	38.6	0.5	78.8	[58]
	35	2.0	11.0	0.1	92.0	[60]
6FDA-DAR	35	2	8.0	0.09	94.0	[60]

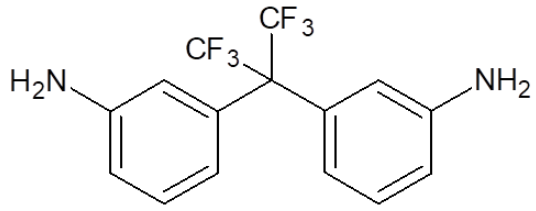

6FmDA

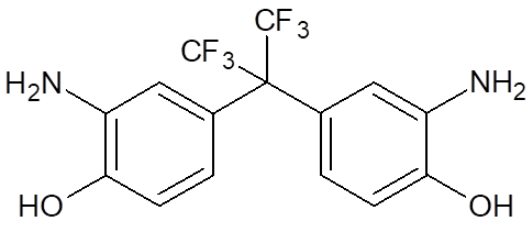

BAPAF

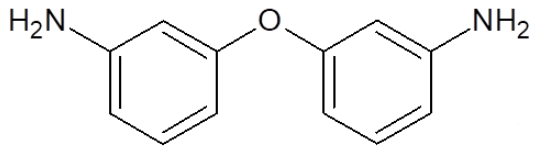

ODA

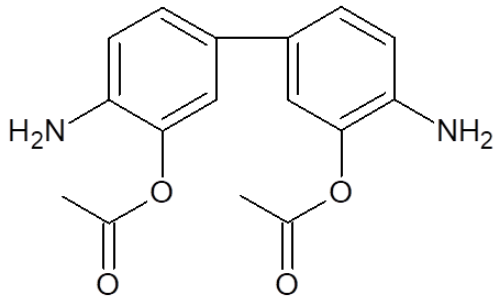

HAB

Fig. 2-3: Chemical structures of multiple-ring diamine monomers, 6FmDA: 2,2′-(hexaflouro-isopropylidene)-dianiline; BAPAF: 2,2-bis(3-amino-4-hydroxyphenyl)hexafluoropropane; ODA: 3,3′-oxydianiline, and HAB: 3,3′-diamino-4,4′-dihydroxy-biphenyl; among others.

Table 2-2: CO_2 and CH_4 single gas permeability, and the ideal selectivity of 6FDA-copolyimides, obtained from multiple-ring aromatic diamine monomers.

Membrane	Measurement parameters		Gas permeability		Ideal selectivity, $\alpha_{CO2/CH4}$	Ref
	Temperature (°C)	Pressure (bar)	P_{CO2} (Barrer)	P_{CH4} (Barrer)		
6FDA-6FmDA	35	10	5.6	-	65.9	[63]
6FDA-BAPAF	25	-	24.6	1.1	22.8	[58]
6FDA-ODA	35	2.0	25.9	1.3	20.6	[55]
	35	10.3	16.5	0.3	53.2	[64]
6FDA-HAB	35	10.0	14.5	0.4	41.0	[65]
	35	10.0	12.0	0.3	38	[66]

2.2. METAL ORGANIC FRAMEWORKS (MOFs)

Various materials, generally porous, such as carbon molecular sieves, (CMS) [73,74], zeolites and silicas [74,75], metal oxides [76], carbon nanotubes (CNTs) [77], metal organic frameworks (MOFs) [78–80], graphene [81,82], etc. have been embedded in a continuous polymer matrix to form MMMs, and leading to improved separation performances.

MOFs, classified by their three-dimensional crystalline frameworks with permanent porosity, formed with metal-based clusters linked by organic ligands [26], are ones of the emerging alternative fillers [83]. They are gaining substantial attention due to their high CO_2 uptake (i.e., HKUST-1 of 7.32 $mmol \cdot g^{-1}$ [22], MOF-74 of 4.9 $mmol \cdot g^{-1}$ [23], at 1 bar, 273 – 298 K), large surface areas up to 7000 $m^2 \cdot g^{-1}$ [84], well-defined selective pores due their crystallinity and superior thermal and chemical stability [10], among other features. Compared with other sorption or porous materials like active carbon or zeolites, the MOFs sorption properties can be designed and fine-tuned through the organic ligands including their post-synthetic modification (PSM) [42,85]. These tunable pore geometries and flexible framework properties [10,27], give rise to various gas separation purposes. Indeed, MOF-containing membranes have been reported to perform better than the current Robeson upper bounds [21] for several gas pairs of great interest, CO_2/CH_4 (e.g. UiO-66 with 6FDA-DAM [55], ZIF-90 with 6FDA-DAM [86], ZIF-8 with PIM-1 [87]), CO_2/N_2 (e.g. ZIF-7 in Pebax® 1657 [88], ZIF-8 in Pebax® 2533 [89]), and H_2/CO_2 (e.g. NH_2-CAU-1 in PMMA [90], ZIF-8 in PBI [91]).

While most of the MOFs were synthesized based on their distinctive static frameworks (i.e., HKUST-1, a rigid pore of 10.8 Å [92]; UiO-66 with rigid 11 Å octahedral and 8 Å tetrahedral pores [93]), as to maintain their robustness for adsorption application, a second generation of 'breathing MOFs' (i.e., MIL-53(Al), with interchangeable pores of 7.7 – 19.7 Å and 13.0 – 16.8 Å pores with and without H_2O molecules, respectively; di-MTZ, expandable based on the aryl moieties in the center linker of between 11.0 – 15.5 Å [94,95]) and 'flexible MOFs' (i.e., ZIF-8, with 3.4 Å pore apertures but expandable to a certain degree and allows larger kinetic diameter molecules to pass [96]) has been introduced and stable in the multiple states.

All the three-dimensional representations of the MOFs hereafter were drawn with Diamond 3.2, using CIF files from The Cambridge Crystallographic Data Centre (CCDC) open database and referred accordingly.

2.2.1. Cu-based MOFs

The first MOF incorporation into a polymer for MMM fabrication may have been by Yehia *et al.* in 2004 [97]: where copper (II) biphenyl-dicarboxylate-triethylenediamine, [Cu_2BPDC-TED], which adsorbs methane preferentially was added into a rubbery poly(3-(2-acetoxyethyl)thiophene), PAET for methane facilitated transport [97]. The study showed an improvement of between 50 – 175% CH_4 permeability with 20 – 30 wt.% particle loadings. The MMM system was later tested for CO_2/CH_4, O_2/N_2 and CH_4/N_2 separations in both PAET and Matrimid® 5218 [98]. Following the first success of Yehia *et al.* [97] with the Cu-MOF MMM with PAET, Car *et al.* [99] and Perez *et al.* [100] incorporated [$Cu(BTC)_2$], [$Mn(HCOO)_2$] and MOF-5 into PSF, PDMS and Matrimid® 5218 and showed significant improvements to their respectively gas separation testing. The reports later influenced others to prepare defect-free MMMs using other MOFs for various gas separation purposes, started by the addition of [$Cu(\mu\text{-}SiF_6)(4,4'\text{-}BIPY)_2$] (4,4′BIPY = 4,4′-bipyridine) into Matrimid® 5218 [101] and Cu-TPA into PVAc [102]. The reports led other researchers to explore many more polymer-MOF MMMs and also continued in this work.

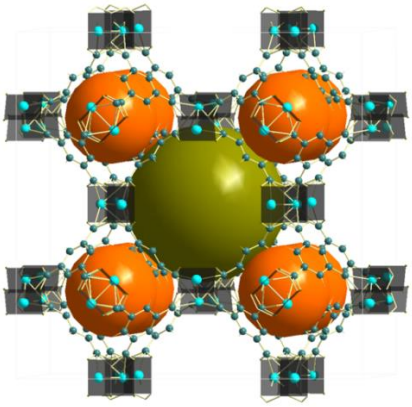

Fig. 2-4: Three-dimensional presentation of $[Cu_3(BTC)_2]$, HKUST-1 [92], with intersectional pores consisting of permanent 10.8 x 10.8 Å square cage (green sphere) with an opening window size of 6.9 Å, and an addition of eight 5.3 Å pores (orange sphere), surrounding the central cage. The additional pores present in the result of terminal water molecules removal during activation.

Currently, one of the most investigated Cu-MOFs is copper benzene-1,3,5-tricarboxylate, $[Cu_3(BTC)_2(H_2O)_3]$, better known as $[Cu_3(BTC)_2]$ or HKUST-1 (Hong Kong University of Science and Technology) [103], and commercialized under the name of Basolite® C-300 by BASF (Fig. 2-4). HKUST-1 crystallizes with the formation of a highly porous cubic structure, large square channels of 10.8 x 10.8 Å square, with a surface area of between 1500 – 2095 $m^2 \cdot g^{-1}$ [83,92], and is thermally stable up to 240 °C [103]. HKUST-1 MMMs have been reported with several polymers over the years including the commercially available PSF Ultrason S [104] and PSF Udel® P-350 [105].

In polyimide, Shahid and Nijmeijer [106] reported more than 2 folds selectivity improvement of Matrimid® 5218 MMM with 30 wt.% of HKUST-1 when tested with 50:50 vol.% of CO_2/CH_4 mixture at 5 bar, 35 °C. The improvement was due to higher CO_2 adsorption (thus permeability) in the MMM, owing to CO_2 stronger interaction with unsaturated Cu sites. CH_4 permeability on the other hand reduced and it has concluded to be the effect of HKUST-1 dominant molecular sieving. The MMMs also presented to suppress the CO_2-induced plasticization effect of the pristine polymer (at ca. 10 bar) to 15 bar (equimolar CO_2/CH_4 mixture, up to 40 bar at 35 °C). Basu *et al.* [104] revealed a 71% CO_2-permeability improvements of Matrimid® 9725/PSF Ultrason S (3:1 blend) MMMs with an optimum loading of 30 wt.% HKUST-1, tested with 35:65 vol.% CO_2/CH_4 at 10 bar, 35 °C. D-spacing increments in the MMM supported the permeability enhancement, which facilitated the gas diffusion. The CO_2/CH_4 selectivity however decreased, but rather independently to the filler loading.

2.2.2. Zn-based MOFs

Amongst the best known prototypical zinc-based IRMOF-*n* series MOFs, IRMOF-1 or MOF-5 [$Zn_4O(BDC)_3$] (BDC = benzene-1,4-dicarboxylate, terephthalate) is mostly used in MMMs for gas separation purposes (see Fig. 2-5(a)). Fully activated MOF-5 gives a high surface area, up to 3000 $m^2 \cdot g^{-1}$, is highly stable up to 400 °C [107] and possess high CO_2 uptake (up to 2 mmol g^{-1} at 25 °C and 1 bar [108]). MOF-5 incorporation into both low and high permeable polymers had shown excellent improvements in CO_2/CH_4 separation. Arjmandi and Pakizeh [109] reported a 220% CO_2 permeability improvement of low permeable PEI with 25 wt.% MOF-5 loading, with single gas separation measurement at 6 bar, 25 °C. This remarkable improvement was paired by a 25% ideal selectivity improvement.

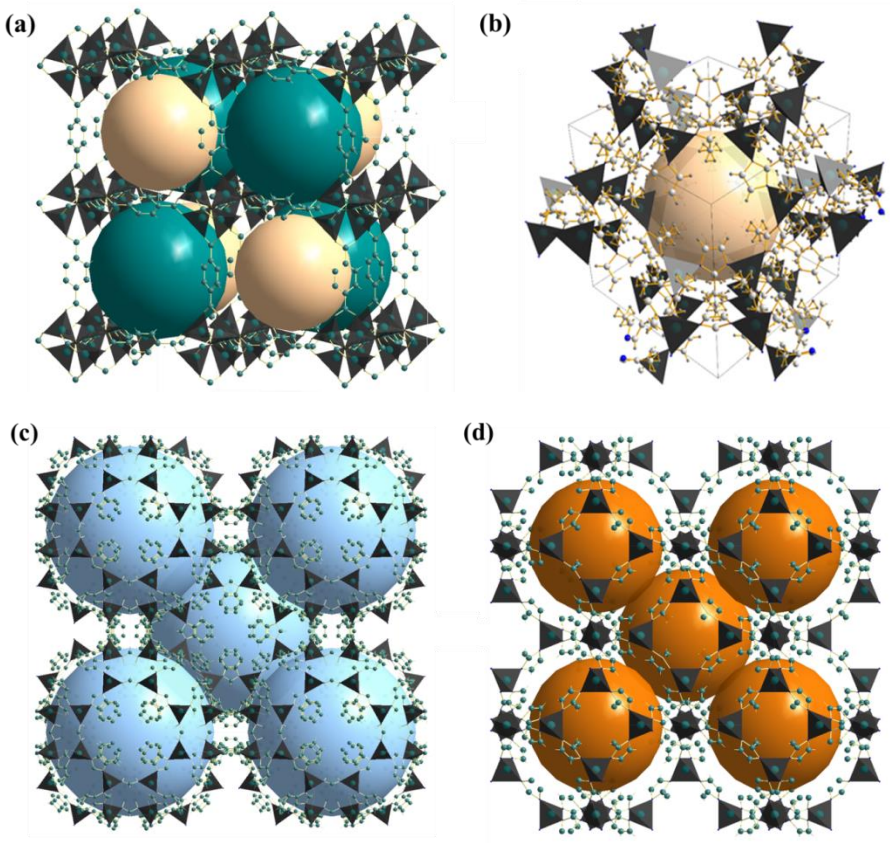

Fig. 2-5: 3D representatives of (a) MOF-5 [110], showing its tetrahedral Zn-O-C polyhedral clusters with a main permanent pore network of 15.0 Å (green spheres) and a secondary pore of 7.8 Å (yellow spheres) [107]; (b) ZIF-8 [111], indicating its zeolitic tetrahedral SOD topology, with 11.6 Å pore (yellow spheres) with a small 6-membered ring pore openings of 3.4 Å ;(c) ZIF-11 [112], viewed through one of the connecting eight-membered rings with permanent cavities of 14.6 Å (blue spheres), connected with 3.0 Å pore apertures, and (d) ZIF-90 [113], presenting its Zn-N-N-Zn SOD cage, with 6 Å pore (orange spheres) and 3.4 Å hexagonal window apertures.

Zeolitic imidazolate framework, a MOF subclass, is based on imidazolate (im) anionic organic ligands, tetrahedrally coordinated transition metals and possess zeolite sodalite topology (SOD) [114,115] (Fig. 2-5(b)). The M-im-M bridges at 145° give rise to its tetrahedral topological networks. The ZIF-8, the best known ZIFs comprises of $[Zn(mim)_2]\cdot nG$ (Hmim = 2-methylimidazole, G = guest) crystallites, have shown promising properties in CO_2 capture and separation due to its high CO_2 adsorption capacity (up to 0.8 $mmol\cdot g^{-1}$ at 1 bar, 25 °C [116]), owing to inherent large pore size of 11.6 Å with a small 6-membered ring pore apertures of 3.4 Å [117] and high surface area (up to ca. 1700 $m^2\cdot g^{-1}$) [118]. Additionally, ZIF-8 adsorbs preferentially in the order of $CO_2 > CH_4 > N_2$ [117] and reported having excellent permeability and selectivity for the following gas pairs, e.g., H_2/C_2H_8 [119], and propylene/propane [120,121], among others. Several researchers had demonstrated excellent improvements in a few glassy polymer MMMs incorporated with ZIF-8 nanoparticles (NPs) of less than 100 nm. Jusoh *et al.* [61] presented a 48% CO_2 permeability and 135% CO_2/CH_4 selectivity improvements by adding only 5 wt.% of ca. 50 nm ZIF-8 into 6FDA-dureen, and suppressed the CO_2-induced plasticization pressure by 5 bar. Chi *et al.* [122] on the other hand reported polystyrene-*block*-poly(ethylene-*ran*-butylene)-*block*-polystyrene (SEBS) MMM with 30 wt.% of ca. 88 nm ZIF-8 to have an enhanced P_{CO2} of 158% and $\alpha_{CO2/CH4}$ of 21%, while Eiras *et al.* [123] improved Ultem® 1000 P_{CO2} up to 600% while maintaining its $\alpha_{CO2/CH4}$ with the same ZIF-8 loading.

ZIF-11 [Zn(2-benzimidazolate)$_2$], in particularly has exceptional thermal and chemical properties among other ZIFs, usually synthesized using the solvothermal process at a lower surface area (240 – 460 $m^2\cdot g^{-1}$ [124,125]). The framework presented a rhombic dodecahedron (RHO) type zeolite structure with large permanent cavities of 14.6 Å, connected with 3.0 Å pore apertures (Fig. 2-5(c)). Due to its higher H_2 adsorption capacity (compared to ZIF-8), ZIF-11 presented an excellent opportunity in H_2/CO_2 separation, as reported in polybenzimidazole (PBI) MMM with an optimum loading of 16.1 wt.% and exhibited an H_2/CO_2 selectivity of 5.6 [126]. However H_2/CO_2 separation properties of ZIF-11 in high permeable 6FDA-DAM did not produce any selectivity improvement [124].

ZIF-90, [Zn(2-carboxyaldehyde imidazolate)$_2$], conventionally synthesized a micro scale (ca. 100 μm), has the similar zeolitic SOD topology as ZIF-8, by replacing the 2-methylimidazolate with 2-carboxyaldehyde imidazolate ligand (see Fig. 2-5(d)). Its incorporation into MMMs have been reported using triptycene-containing polyimide [127], PEI Ultem® [86], Matrimid® [86] and most significant report was with the high permeable 6FDA-DAM, surpassing 1991 [20] and closing to 2008 Robeson upper bound [21], when

tested with equimolar CO_2: CH_4 mixture at 2 bar, 25 °C [86]. They reported a 85% CO_2 permeability and 54% CO_2/CH_4 selectivity improvement with a smaller size ZIF-90 (named ZIF-90A, micron-sized) and 51% CO_2 permeability and 42% CO_2/CH_4 selectivity with its bigger counterpart (named ZIF-90B, sub-micron sized), at similar 15 wt.% particle loading [86].

2.2.3. Al-based MOFs

MIL-53 MOF, $[Al(OH)(bdc)]_2$, (bdc = 1,4-benzenedicarboxylate), one of the excellent examples of a 'breathing' MOF, formed by doubly interpenetrated and rod-packing MOFs, with a 1D straight channel of 7.7 x 7.7 Å [92,128](see Fig. 2-6(a)). The $Al_4(OH)_2$ octahedral infinite chain frameworks give the MOF breathing character in the presence of CO_2 and make it an ideal CO_2 adsorbent for CO_2 storage [104,129]. Its high affinity towards CO_2 is attributed to the strong interaction between CO_2 quadrupole moment and the framework hydroxyl group, thus the higher CO_2 adsorption [104]. The interaction also decreases the framework pore sizes, allowing MIL-53 to separate CO_2 from other bigger kinetic diameter molecules better than some MOFs. The incorporation of MIL-53 into continuous polymer phases were demonstrated to exhibit good interfacial adhesion and presented improved gas separation performances. Recently, Dorosti *et al.* [129] showed a 94% CO_2 permeability and 84% CO_2/CH_4 ideal selectivity increments of Matrimid® 5218 with 20 wt.% MIL-53, tested at a constant feed pressure of 3 bar, higher than MOF-5 [130] and Cu-BHY-HFS [101] MMMs of the same polymer. Additionally, Hsieh *et al.* [131] exhibited ideal selectivity increments of H_2/O_2 by 69%, CO_2/CH_4 by 129% H_2/CH_4 by 20% and H_2/N_2 by 50%, when incorporated 37.5 wt.% of as-synthesized MIL-53 (50 – 100 nm particle size) into Matrimid® 5218, tested at 2 bar, 35 °C.

Many MOFs have been reported over the years and possessing the required characteristics for both CO_2 capture and storage. An example, a new highly stable (up to 300 °C) polymorphous Al-MOF was recently reported in 2017 consisting of Al^{3+}/4,4′-benzophenone dicarboxylic acid (H_2BPDC) and denoted as CAU-21-BPDC [132]. The $[Al_8O_8]$ inorganic building units (IBUs) were formed by cis corner-sharing of AlO_6 polyhedral, consequently produced accessible 1D modulated pores between 3.6 – 6.5 Å, in additional to its permanent tetrahedral (17.3 Å) and octahedral (23.9 Å) pores (see Fig. 2-6(b)). Even though CAU-21-BPDC CO_2 uptakes, was lower than the as-synthesized MOF-5, MIL-53(Al), and HKUST-1 and only comparable to ZIF-8, MIL-101(Cr), the MOF shows a great potential in

CO_2 capture, separation and storage due to its complex rigid build-up and large accessible pore volumes.

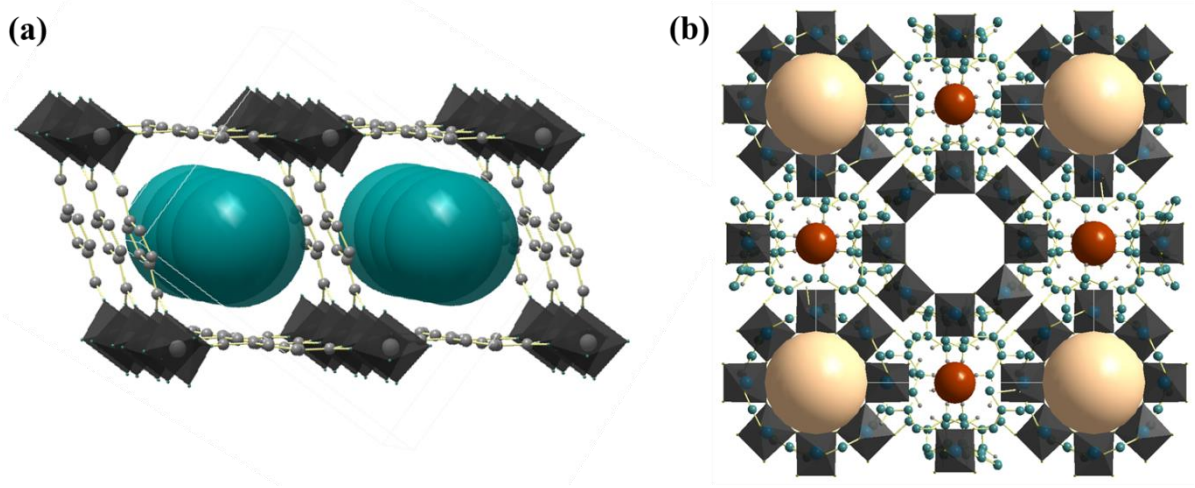

Fig. 2-6: 3D representatives of Al-based MOFs, (a) MIL-53 (Al) [128], formed in an orthorhombic rod-packing arrangement with a 1D straight channel of 7.7 x 7.7 Å (green spheres), and (b) CAU-21-BPDC [132], indicating its IBU structure, formed by eight cis corner-sharing AlO_6 polyhedral forming very large tetrahedral (17.3 Å) and octahedral (23.9 Å, yellow spheres) pores, with accessible 1D modulated channel pores between 3.6 – 6.5 Å (indicated by red spheres, is its 3.6 Å channel openings).

2.2.4. Zr-based MOFs

MMM studies on a relatively new class of highly crystalline zirconium-based MOFs, especially UiO-66 (UiO: University of Oslo) grows rapidly. UiO-66 is based on a $Zr_6O_4(OH)_4$ octahedron, forming 12-fold lattices connected by the organic linker, 1,4-benzene-dicarboxylate (BDC) (Fig. 2-7) [93]. This zirconium terephthalate has high surface area, of experimental values 850 – 1300 $m^2 \cdot g^{-1}$ [30,67,133,134], and the theoretically accessible surface of 1021 $m^2 \cdot g^{-1}$ [135]. The microporous framework composes of centric octahedral cages (ca. 11 Å) each connects with eight corner tetrahedral cages (ca. 8 Å) using trigonal windows (ca. 6 Å). The crystal face-centered-cubic contributes to its high stability towards heat (reported between 430 and 540 ºC [136,137]), pressure [138], water [138,139], common solvents [138], even strong acid (HCl) and base (NaOH) [137].

The incorporation of UiO-66 has been reported to produce outstanding gas separation performances recently, i.e., by Castarlenas *et al.* [30] exhibited H_2/CH_4 and CO_2/CH_4 separation with UiO-66 MMMs, where the H_2/CH_4 selectivity improved by 6.5% in polysulfone Udel® 3500-P and 7.7% in polyimide Matrimid® with 32 wt.% loading. Remarkable H_2 permeability improvements of 475% and 148% were recorded for the stated

MMMs, respectively. They also reported a 3-fold CO_2 permeability enhancement in the CO_2/CH_4 mixed gas separation, while the selectivity increased by 21% and 31%, respectively for Udel® 3500-P (32 wt.% UiO-66) and Matrimid® (16 wt.% UiO-66). Ahmad *et al.* [55] on the other hand reported CO_2/CH_4 mixed gas separation at 2 bar, 35 °C for three 6FDA-based co-polyimides, namely 6FDA-bisP, 6FDA-ODA, and 6FDA-DAM. At the optimum loading of between 14 – 17 wt.% UiO-66 (ca. 50 nm), 6FDA-DAM MMMs presented an excellent performance of well-above the 2008 Robeson upper bound [21] while 6FDA-bisP and 6FDA-ODA MMM felt short under, yet above 1991 upper bound [20].

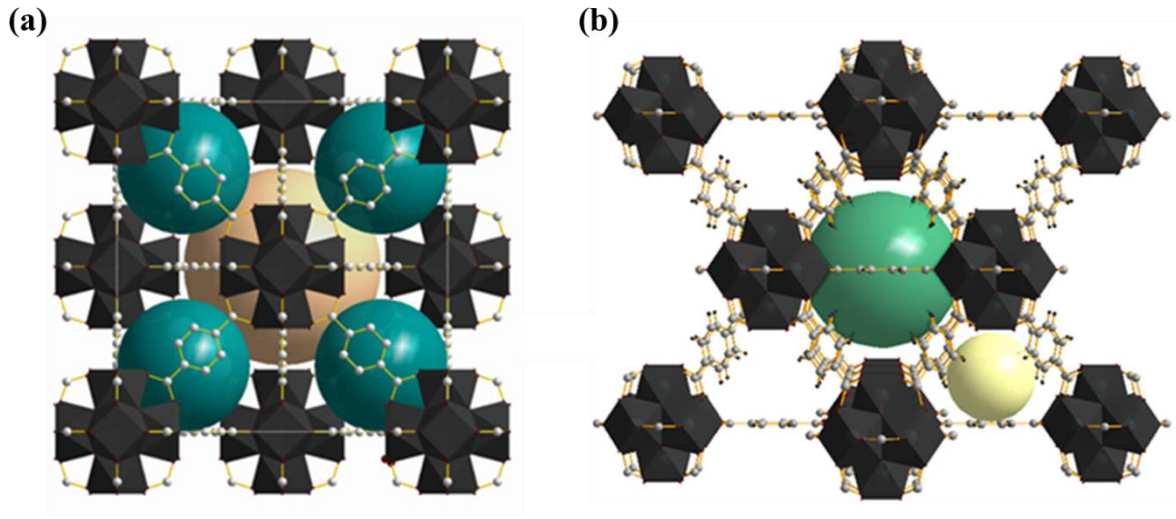

Fig. 2-7: Representation of iso-reticular UiO-66 framework [93], with its Zr_6O_6 cuboctahedron polyhedral (dark grey) with octahedron (green ball) and tetrahedron (yellow ball) permanent pores.

2.2.5. Ligand functionalization of MOFs

Further functionalization of the MOFs can be achieved by post-synthetic modification (PSM) reactions of the amino functionality, through nucleophilic substitution, acid-base reactions and condensation reaction [42]. For instance, UiO-66-NH_2 was synthesized by a direct synthesis using amino-functionalized organic linker (UiO-66-NH_2 = $Zr_6(\mu_3\text{-}O)_4(\mu_3\text{-}OH)_4$ $(O_2C{-}C_6H_3(NH_2){-}CO_2)_{12}$) and the amino group is chemically inert in most solvents and does not participate in the coordination chemistry of the metal ions [85], an additional reaction with anhydride-based molecules in chloroform at elevated temperature will produce an acetamide-functionalized UiO-66s [133,140]. This can simultaneously change the MOF properties such as pore accessibility and pore sorption behavior, depending on the orientation of the modified linkers [85].

The incorporation of functionalized-MOFs has been reported to produce a better performing MMM of the same MOFs. Tien-Binh *et al.* [141] improved the CO_2 permeability of polyimide 6FDA-DAM-HABby adding 10 wt.% MIL-53(Al) and obtained a more impressive CO_2/CH_4 selectivity improvement with 10 wt.% of NH_2-MIL(Al)-53. Anjum *et al.* [134] incorporated 30 wt.% of UiO-66 and UiO-66-NH_2 into polyimide Matrimid® 9725 and improved the CO_2 permeability by 160 - 200%. Xin *et al.* [142] enhanced both CO_2 permeability of SPEEK polymer by around 100%, using 40 wt.% of MIL-101(Cr) and HSO_3-MIL-101(Cr).

2.3. MIXED MATRIX MEMBRANE

Mixed matrix membranes (MMMs) is defined as composite materials comprise of solid or rigid phases, dispersed in a continuous polymer phase [27,143]. The combination of the organic (polymer) with inorganic particles aims to exploit the synergistic advantages from each phase: high permeability and/or selectivity of the dispersed fillers, high selectivity and easy processability of the polymers. Also, MMMs may offer enhanced physical, thermal and mechanical properties for the aggressive and adverse environments in actual gas separation systems [16].

2.3.1. Morphologies of the MMMs

In principle, fabrication of an MMM is more straightforward than a pure inorganic membrane, owing to the polymer continuous matrix's flexibility, the brittleness of an inorganic membrane could be avoided [17,144–147]. MMM research, on the other hand, has been concentrated on dense flat sheet membrane (symmetric) due to its easier fabrication compared to the asymmetric flat sheet and hollow fiber. However, the dense membrane presents a lower gas permeability than asymmetric membranes of the same polymer [104,145]. A comparative study presented by Basu *et al.* [104] exhibited higher fluxes in Matrimid®-$Cu_3(BTC)_2$ asymmetric MMM, due to a less resistance for the specific gas to permeate across its thinner selective layer (Table 2-3). Khayet [148] and Hasbullah *et al.* [149] also reported similar findings in polyvinylidene fluoride (PVDF) and in-house synthesis polyaniline-based membranes, respectively. Additionally, for the actual industrial application, dense flat sheet membrane will require a specific porous support or module system due to its lower mechanical strength compared to the asymmetric membranes [16,148].

Table 2-3: Comparison between dense neat Matrimid® 9725 and its asymmetric MMM with $Cu_3(BTC)_2$ as inorganic filler [104].

Membrane	[1]Permeability (GPU)	Selectivity
Dense, neat	0.65	32.0
Asymmetric MMM	17.5	24.0

[1]Tested with CO_2/CH_4 binary gas mixture (35/65 vol.%) at 35°C and 5 bar

Regardless of this known fact, fundamental investigation of a new MMM system in the form of flat sheet dense membrane is more suitable due to its easier processability and higher reproducibility. This thesis will provide proof of concept and the valuable separation insights (diffusivity and solubility behavior of gas species through the new MMM). Fig. 2-8 shows the schematic presentation of the MMM morphologies.

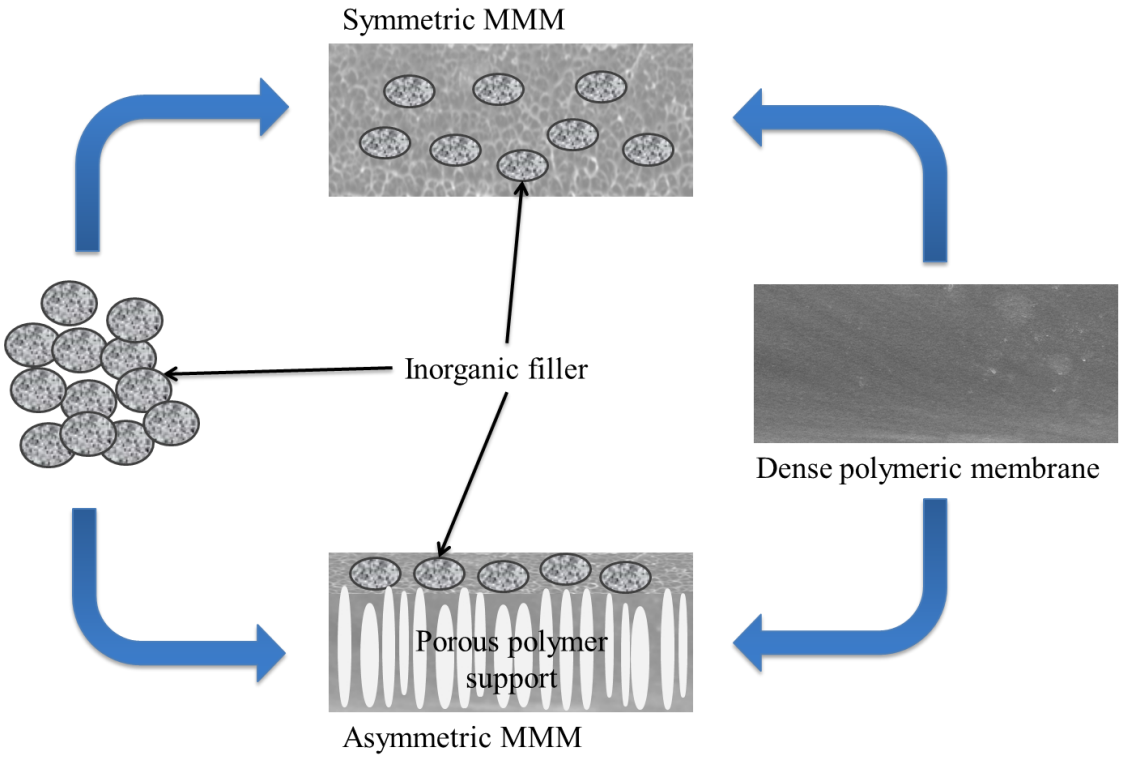

Fig. 2-8: Schematic representation of symmetric MMM and asymmetric MMM with porous polymer support.

Three methodologies have been reported to produce MMMs: (1) filler dispersion in a solvent, followed by polymer addition, (2) dissolving polymer into a solvent, before the addition of dry filler particles into the polymeric solution, (3) dissolving polymer and particle dispersion separately in solvent, and both solutions are mixed. The methods (1) and (3) were reported to produce MMMs with better filler dispersions [17,21,143]. The mixed solution

was casted on a flat surface for solvent evaporation and thermally heated (with or without vacuum) to remove the remaining solvent. Final heat treatment is depending on the polymer glass transition temperature, T_g.

2.3.2. Gas transport theory in membranes

Gas molecules transport through a membrane is a combination of several mechanisms, fundamentally depending on the membrane structure. Transport of gases through porous membranes will obey the Knudsen diffusion, surface diffusion, or molecular sieving depending on the gas molecule characteristic and surface characteristics or chemistry of the membranes (i.e., pore size, mean free path of the molecule, pore surface interaction with adsorbed gas, and pore length) [150,151]. On the other hand, the separation in a non-porous dense membrane is governed by solution-diffusion principle; a mechanism which depends significantly on the gas penetrant solubility and diffusivity in the membrane. It is, however, an important mechanism in membrane separation field, where gas molecules with similar kinetic diameters can be separated provided their solubility in the membrane differs significantly. The transport mechanisms are illustrated in Fig. 2-9.

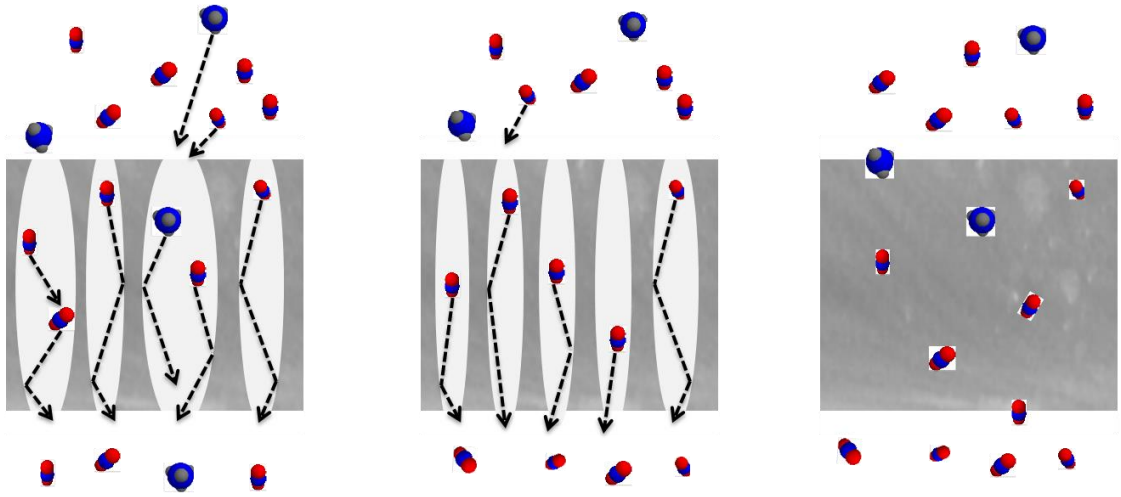

Fig. 2-9: Schematic representations of possible gas transport mechanisms, (a) Knudsen diffusion, (b) molecular sieving and (c) solution diffusion, through polymeric membranes. The dominating mechanism is significantly depending on the membrane structure porosity.

Diffusion, the basis of the solution-diffusion mechanism, is a process by which a chemical species is transported from one part of a system to another by a concentration gradient [117,143,150]. Penetrating molecules are first being adsorbed or absorbed on the

upstream membrane boundary, subsequently diffused through the membrane matrix through diffusion transverse to the other side of the membrane, then emerged or desorbed out to the downstream of the membrane (Fig. 2-10).

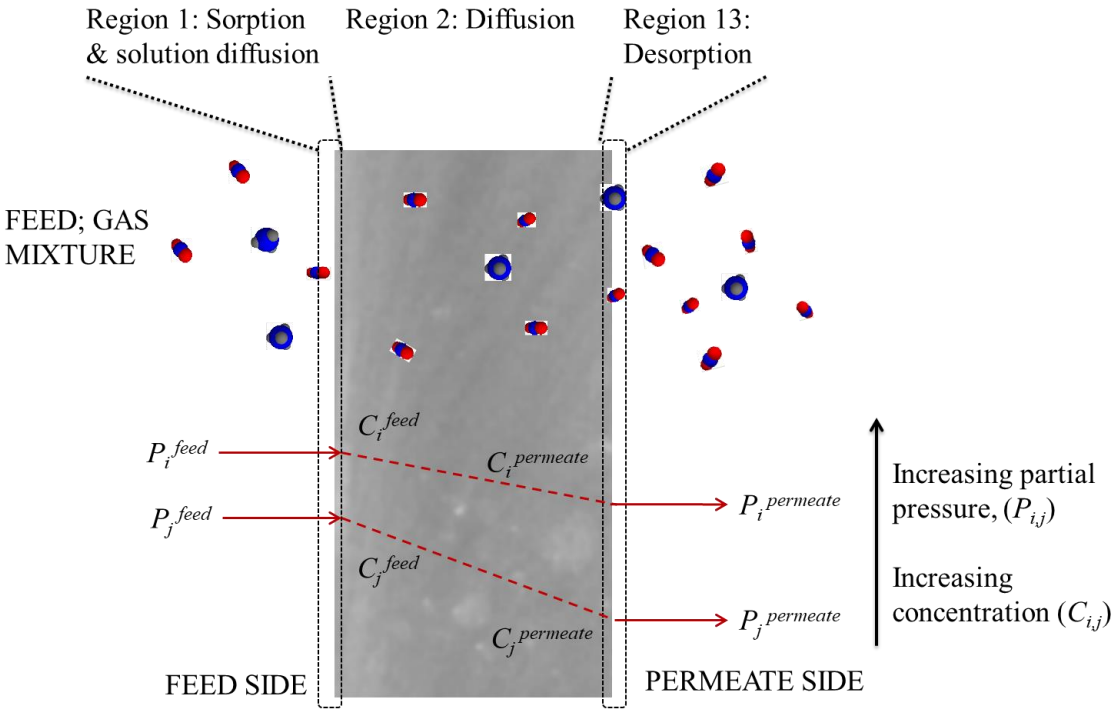

Fig. 2-10: Solution-diffusion mechanism of two gasses (gas *i* and *j*) through a dense membrane. Adapted from Weng *et al.* [152].

The quality of a membrane separation system is determined by its permeability and selectivity, where the permeability is a measure of the process productivity and selectivity is its efficiency. In other words, the permeability is the ease of which a particular molecular species pass through the membrane, and can be defined as a product of both solubility and diffusion coefficients and described by Eq. 2.1.

$$P = D.S \qquad \text{Eq. 2.1}$$

Where;

P Permeability coefficient; a measure of membrane flux and derived from the solubility and diffusion coefficients

D Diffusivity coefficient

S Solubility coefficient

This expression signifies that permeability coefficient dependency on both diffusivity and solubility coefficients and the solution-diffusion models supported this fact [16,150]. The

studies on the permeability coefficient dependency also include the separation mechanism determination in MMMs and the effects of inorganic filler agglomeration, using the existing solution-diffusion models, i.e., Maxwell and Bruggeman models [17]. The selectivity (separation efficiency) is the permeation rate ratio of a more permeable to a least permeable penetrant through a membrane. The ideal selectivity for gas A over gas B is defined as the ratio of their pure gas permeability (Eq. 2.2) while the gas selectivity/separation factor is permeability ratio of gas A over gas B in a mixture (Eq. 2.3).

$$\alpha_{A/B;ideal} = \frac{P_A}{P_B} = \left(\frac{D_A}{D_B}\right) \times \left(\frac{S_A}{S_B}\right) \quad \text{Eq. 2.2}$$

Where;

D_A/D_B Diffusivity selectivity, gas A, and gas B diffusion coefficients ratio

S_A/S_B Solubility selectivity, gas A and gas B solubility coefficients ratio

$$\alpha_{A/B} = \frac{Y_A/Y_B}{X_A/X_B} \quad \text{Eq. 2.3}$$

Where;

Y_A, Y_B Mole fractions of gas A and B in the permeate

X_A, X_B Mole fractions of gas A and B in the retentate

In principle, both permeability and selectivity are the keys determining membrane process feasibility. A highly permeable membrane requires a lesser membrane area for a given separation, thus lowers the system size and expenditures, and a high selectivity membrane separates contaminant-product mixture effectively with a minimal loss of the valuable products. For instance, in a natural gas processing, higher selectivity means a lesser hydrocarbon loss during CO_2 removal. Therefore higher purity gas products are recovered.

2.3.3. Factor affecting the MMMs structure and separation performances

Many have concluded that the permeation and separation behavior in an MMM is not merely an adding approach of the inorganic and organic phases' intrinsic properties [17,29,143]. The morphology of the MMM strongly affects its gas transport properties [153]. Therefore fabrication of an ideal MMM with no filler-polymer interfacial defects and particle agglomeration is very crucial. Several main challenges were encountered by the researchers in MMM preparation particularly related to the inorganic filler such as to 'control and maintain' its chemical structure upon addition into continuous polymer matrix and to

understand their surface chemistry, which would potentially affect the membrane performance [145]. The following section will discuss the several known factors influencing the MMM structure and its gas separation performances. A few method utilized in the recent years to overcome the problems is presented accordingly.

2.3.3.1. Particle agglomeration

The filler particles, by nature, tend to aggregate and cause poor particle distribution within the polymer matrix, particularly when introduced at high loadings. Both filler and polymer chemical properties (i.e., group functionality and stability in organic solvents) and their compatibility will determine the filler aggregation degree and tendency in an MMM. In the case of an asymmetric membrane, the increase in extends of particle agglomeration sometimes may exceed the selective thin layer thickness and tear the membrane surfaces.

This will severely reduce the membrane separation performance since the agglomerates provide pathways for slow gasses to diffuse faster through the voids and the membrane will be rendered as less selective [29,154]. Zornoza *et al.* [29] presented, in the presence of large agglomerate of big nanoparticles (ca. 500 nm), the polymer matrix is unable to fully-surround the agglomerates and causes interfacial voids. In addition to the non-selective by-pass channels formed in the agglomerates, the interfacial voids will increase gas permeability and reduce its selectivity. A similar observation was also reported by Ahmad *et al.* [55] where the agglomeration was more prominent in their bigger UiO-66 (ca. 100nm and 200 nm) MMMs and presented poorer separation performance than the MMM with smaller nanoparticles (ca. 50 nm). Thus, an adequate filler loading or an optimum loading needs to be determined for each specific MMM system, as well as a suitable suspension methodology to ensure a higher degree of filler dispersion throughout the membrane.

2.3.3.2. Interfacial defects

The void formation between the polymer-inorganic interface generally results from weak polymer–particle adhesion [146,153]. The void will allow the separating gas molecules to pass through quickly instead of passing through the particle pores and the presence of inorganic materials become useless. It is worth mentioning that the glassy polymers possess much attractive gas separation properties compared to the rubbery polymers [150] due to their more rigid structure and adequate free volume. Nevertheless, its poor polymer chain mobility during the membrane fabrication may result in a weak interaction with the filler particles, which may lead to the formation of unselective voids throughout the membrane

[29]. MMMs with such voids may have little or no improvements in gas selectivity over the original polymer because of the separating gasses will only by-pass around the particles. Repulsive force between the continuous and the dispersed phase, their different thermal expansion coefficients and the elongation stress effects, especially in fiber spinning, are the other causes for interface void formation [146,153,155].

A defect-free MMM (Case 0) where the MMM presents improved both the permeability and selectivity is illustrated in Fig. 2-11. The dotted lines denote the slower gas permeability in the polymer matrix and the straight lines denote the faster gas permeability in the filler phase. Case 0 represents the ideal MMM morphology and its gas separation fits into the Maxwell model perfectly [51,83]. The other MMM morphologies (Case 1 – V) is shown in Fig. 2-12, in relationt to their gas transport properties, as first presented by Moore and Koros [153] and later studied by Hashemifard *et al.* [155].

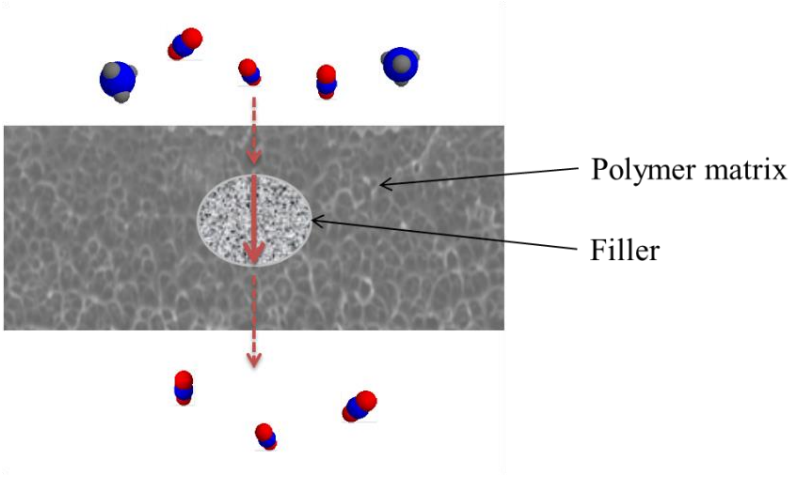

Fig. 2-11: Schematic diagram of an ideal morphology and gas transport through an MMM. The lower permeability of the polymer matrix (dotted line) and the higher permeability in filler phase (straight line) are presented.

Case I is known as ‘rigidified polymer layer’ and occurs when the polymer-particle interfacial adhesion is strong and its uniform stresses that arise during the membrane formation causes a reduction in free volume (lower chain mobility than in the bulk polymer) [55,146]. This ‘rigidified layer’ region produces a lower permeability than the bulk polymer and an improved diffusive selectivity. For a given polymer and a dispersed phase, the interface stress during membrane preparation is believed to determine whether a rigidified or a void region (could be Case II or Case III) will be formed and to which extent. The stress depends primarily on the solvent amount left to be removed when the nascent polymer matrix solidifies [153].

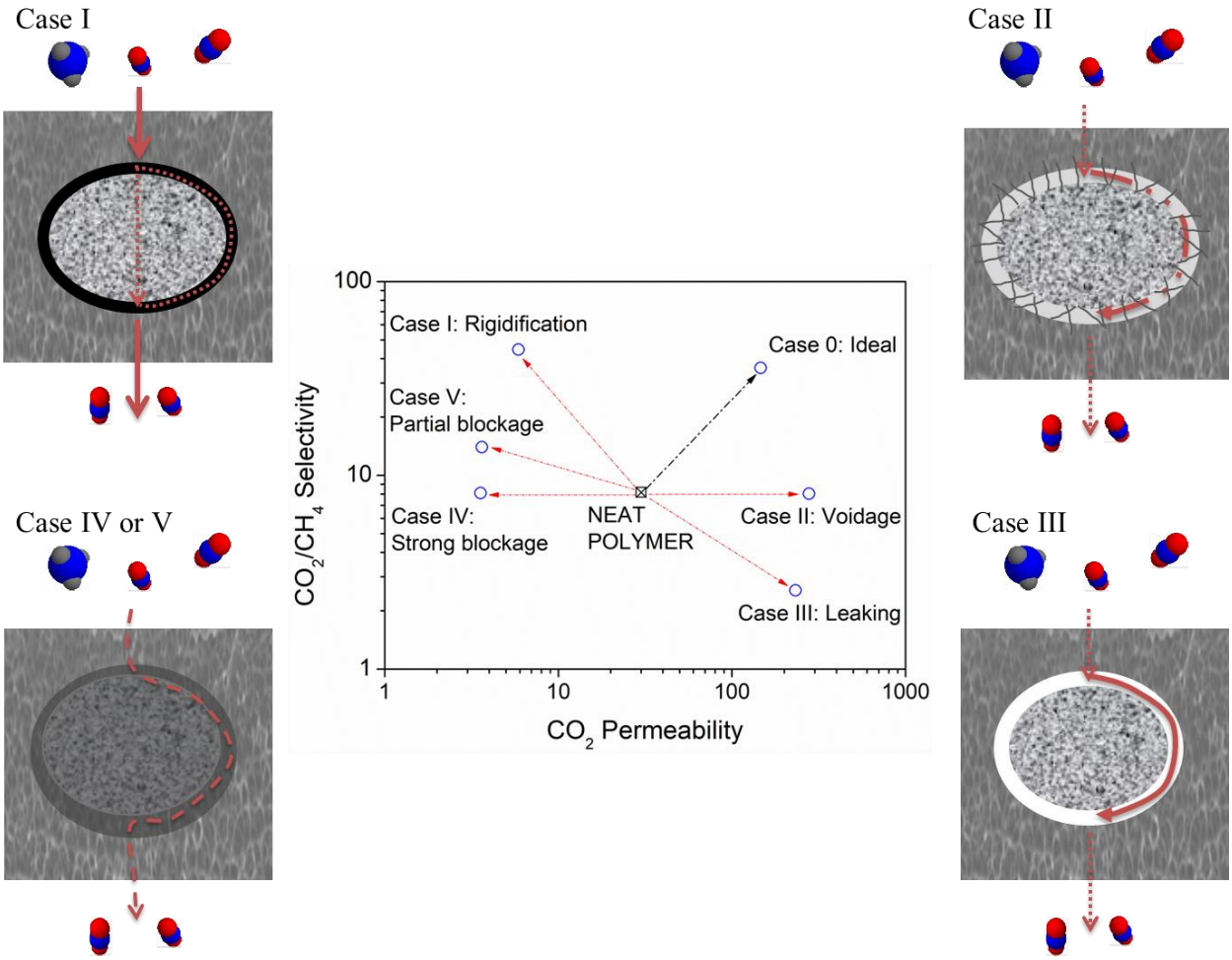

Fig. 2-12: The relationship between MMM morphologies and gas transport properties, as adapted from Moore and Koros [153]. The lower permeability (dotted line) and the higher permeability (straight line) are indicated.

Case II is known as voidage or 'sieve-in-cage' formation, formed due to poor polymer-filler interfacial adhesion and giving rise to permeability. The increase of permeability is due to a lesser resistance in the void regions, and the gas passes through this region instead of the filler. Meanwhile the selectivity can be equal or slightly higher/lower than the neat polymer, depending on the size of the voids. When the size of the void is more significant than two separating gas kinetic diameters, for example, both fluxes increase significantly, however, the region is not selective. This phenomenon is presented as Case III, leaking phenomena.

In some cases, pore blockage can occur and the phenomenon is unique to porous fillers [153,155]. Particle pores can be clogged by a sorbent, solvent, contaminant or minor component in a feed gas or polymer chains, and can occur before, during or after membrane fabrications. Depending on the degree of the blockage, the phenomenon can be classified as Case IV (strong blockage) or Case V (partial blockage). In case IV, the wholly blocked filler

will restrict gas transport through the pore windows and become the impermeable domain in an MMM, resulting in diminished permeability. Whereas in Case V, depending on the separating gas molecule dimension and blockage degree, the gas enters or passes through the pores more slowly than usual, causing a gas permeability decrease. While its effect on selectivity depends on the inorganic filler used. The gas permeability of MMM morphologies can be concluded in the following order: Case II & III > Case 0 > neat polymer > Case I > Case IV & V, whereas their selectivity are in the order of Case 0 & I > Case V > Case II & IV > Case III.

2.3.3.3. Effect of MOF pore sizes, particle size, and shape

Recently, MMM developments with MOFs have received in-depth attention in many membrane research groups [28,40,55,56,102,104]. The dispersion of MOFs having pore windows approaching to targeted gas molecule size (e.g., CO_2, 3.4 Å) will facilitate its diffusion through the MMM, while molecules with larger kinetic diameters (e.g., N_2, 3.6 Å; CH_4, 3.8 Å; C_2H_4, 3.9 Å; C_3H_6, 4.5 Å) will be discriminated from transporting through the inorganic phase. Ideally, the incorporation of MOFs in the polymer matrix aims to increase both permeability and selectivity by increasing the diffusion coefficient of one gas from the others [156]. However, in some cases where MOFs with larger pore windows, i.e., UiO-66 (ca. 6 Å [55,133,135]) and HKUST-1 (ca. 6.9 Å [22,92]), are utilized, the permeability enhancement can be observed while their perm-selectivities were maintained or presented a slight reduction. Fig. 2-13 illustrates the gas diffusion pathways through polymer-MOFs MMM, as proposed by Kim *et al.* [157] for MMMs with porous materials. The pathways will greatly determine the permeability and perm-selectivity improvement in an MMM.

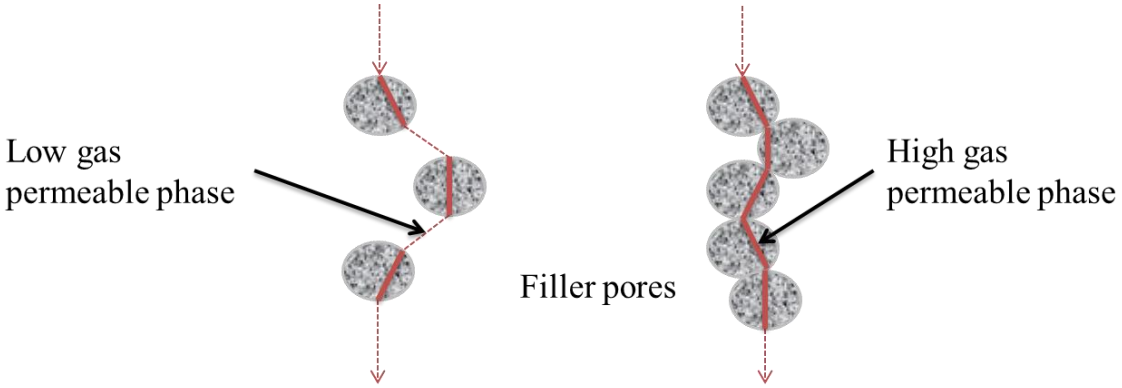

Fig. 2-13: The diffusion pathways through the MOFs phases in the polymer matrix, where a discontinuous (left) or a continuous (right) one is formed, depending on the particle distribution in an MMM [157].

Other than aiding or restricting a specific gas transport in the inorganic phase, the inclusion of MOFs also disrupts the polymeric structure and increases the polymer free volume consequently its gas permeability [57,106,158]. This phenomenon is mainly observed in the MMMs with non-porous inorganic fillers where the addition does not change the separation mechanism (solution – diffusion) but instead alters the polymer free volume distribution [158,159]. In other words, the presence of nonporous particles in between polymer chains decreases the polymer intra-chain interaction thus lower activation energy is needed for a diffusing gas. Therefore, permeability enhancement is mainly attributed to its diffusivity increment.

Another deciding aspect is the MOF geometrical properties, e.g., particle size and shape. Johnson and Koros [160] stated that micron-sized cubic particles would limit the particle packing, especially within the asymmetric membrane skin layer (thickness range of 0.1 to 0.5 μm). The particles may also protrude and as a consequence, produce highly defective surfaces. The smaller particles in nano-size (translated to the higher surface area) on the other hand, can provide a more excellent interfacial contact with the polymer matrix, hence more appropriate for MMM preparation. However, in most cases, the degree of particle dispersion is reduced with the increase of nano-filler loadings [30,83,160]. This is possibly due to the nanoparticles nature where they are difficult to be broken into smaller domains after the nanocrystal formation/synthesis or they tend to reassemble to form bulky aggregates. The effects of the filler agglomeration on gas separation performance are as given in the previous section.

2.3.3.4. Effect of filler and penetrant interaction

The metal-derived MOFs possess specific interaction with polar gasses (CO_2, H_2S, SO_2) and enhance the gas permeability by its solubility co-efficient enhancement. The inclusions of many as-synthesized [30,56,151,161–164] and functionalized MOFs [64,90,165,166] have been investigated and their interactions with CO_2 have been presented in term of solubility and CO_2 adsorption increments. The observations were due to moment-quadrupole CO_2 is selectively attracted towards the unsaturated metal atoms in the MOFs (i.e., Cu atoms in the structure of $[Cu_3(BTC)_2]$[104] and Zr atoms in UiO-66 [55]) and further influenced by the MOFs synthesis and activation methods. In the case of different synthesis methods, the use of reaction modulator (i.e., acetic acid, hydrochloric acid) usually produces substituted MOFs in their organic linker positions by stronger anions, simultaneously affecting the MOFs interaction to polar gasses (translated to gas adsorptions) [44,45,167]. The activation method

on the other hand influences the amount of functional groups in the MOFs, especially hydroxyl group as it is easily affected by thermal activation and produces less adsorptive de-hydroxylated MOFs [55,168]. All these differences are translated in the CO_2 solubility and adsorption in MMMs.

In addition, MMM with modified or treated inorganic particle with transition metal ion also presented higher affinity towards CO_2, such as silver (Ag^+) ion-exchanged onto sodium Y zeolite (NaY) powder and incorporated into Matrimid® 5218 [169], silver (Ag^+) ion-exchanged onto halloysite nanotubes in PEI [170], silver (Ag^+) ion-exchanged onto sodium A zeolite (NaA) in PES [171] and as-prepared MMM dipping-treatment into zinc ion (Zn^{2+}) solution [172].

2.3.3.5. Methods to hinder interfacial defects

Introduction of foreign materials into continuous polymer phase is not straightforward since both materials are not readily compatible [145]. Lack of interaction between these phases will result in poor adhesion and voids formation consequently diminishing the MMM separation performance. Several methods have been reported to promote particle dispersion while minimizing the defective morphologies, such as:

1. "Priming method," or also known as "sizing procedure." It is a simple technique which is carried out during the dope solution preparation where a small amount of polymer is added to the dispersed filler solution before further addition of the bulk polymer [104,145,155]. A lower concentration polymer will promote filler-polymer adhesion and formed stable filler suspension in the solvent before the polymer concentration is increased to the intended percentage. The polymer used for priming may be from the same or different than the primary polymer matrix [28,173]. For the case of the primary polymer matrix has a poor interaction with the filler surface, another polymer with a suitable surface interaction with filler, as well as good miscibility with the primary polymer matrix can be incorporated as the priming agent.
2. Controlling the MOFs particle size. Many have reported the two mostly practiced methodologies, (1) pre-dried filler dispersion in a solvent before priming step, assisted by ultrasonic [28,173], and (2) keeping the MOFs as a suspended solution before use [102,174]. The methodologies help to maintain

the particle in the as-synthesized sizes and as well as to minimize filler agglomeration.

3. Addition of low molecular weight additives (LMWAs), also regarded as filler compatibility agent [175]. It must be noted that the improvement of the interfacial properties only occurs if the nanoparticles are exfoliated, or at least intercalated, within the polymer matrix. Several LMWAs have been utilized in MMM preparation and presented improved interfacial interaction and separation performances, e.g., 2-hydroxy-5-methyl aniline (HMA) in binary and ternary MMM systems (SAPO-34/PES and PES/SAPO-34/HMA) [176,177], and 2,4,6-triaminopyrimidine (TAP) in both SPEEK-Cloisite 15A® [178] and Matrimid®-zeolites (4A, 5A, 13X and NaY) [179] MMMs. This technique aims to improve the contact between polymer and the filler, thus eliminates the needs of chemical modification.
4. Utilization of copolymer(s). An additional copolymer, usually with a higher functional group degree is added to improve the polymer-filler interfacial adhesion to achieve a defect-free MMM, i.e., zeolite dispersion in Matrimid®-POSS [169,172].

CHAPTER 3: INVESTIGATION OF A NEW CO-POLYIMIDE, 6FDA-bisP AND ITS ZIF-8 MIXED MATRIX MEMBRANES

3.1. CHAPTER OVERVIEW

As mentioned in section 2.1.1, the choice of diamine monomer used in producing 6FDA-copolyimide determines the membrane's gas separation properties. In this chapter, we investigated a novel 6FDA-copolyimide using 4,4′-(1,4-phenylenediisopropylidene) bisaniline (bis-P) diamine monomer, with the aim to reach higher gas separation performance than the commercialized polyimide [41]. Being able to achieve this goal through two different 6FDA-bisP preparation and fabrication protocols, the study was continued to produce MMMs with an imidazolate-based MOF, ZIF-8 to further improve its separation performance. The zeolitic imidazolate framework (ZIF), ZIF-8 is known to enhance gas separation properties of a mixed matrix membrane (MMM) due to its inherent molecular sieving properties. Additionally, filler dispersion in the polymer matrix is one of the important factors that affect the MMM performance. With increasing particle loading, the filler aggregation is more likely to occur and crucial especially for nano-size particles. The study includes the synthesis and membrane fabrication of the novel 6FDA-bisP and synthesis of different sizes of nano ZIF-8 for improved filler dispersion in the polymer continous phase. The gas separation performance was conducted for CO_2 and CH_4 50:50 vol. % binary mixture. The presence of multiple aromatic rings in the diamine moieties were expected to improve the filler dispersion by forming inter-molecular interactions, and consequently the CO_2/CH_4 gas separation performance.

3.2. CHAPTER CONTRIBUTIONS

In this chapter, we prepared ZIF-8 nanoparticles (NPs) in several particle sizes, characterized and incorporated (only the NPs with <100 nm) into the 6FDA-copolyimide, 6FDA-bisP between 5 – 20 wt.% loadings for CO_2/CH_4 separation (as illustrated in Fig. 3-1). The 6FDA-bisP co-polyimide membrane was obtained from a classtic two-step condensation polymerization and two fabrication protocols (protocol M1 and M2), after the synthesis of its 10 wt.% polymer concentration poly(amic) acid (PAA). Protocol M1 is a direct synthesis; whereas M2 is with an additional precipitation step. The ZIF-8 NPs and MMMs were characterized accordingly. Gas separation performance was evaluated by feeding an equimolar mixture of CO_2 and CH_4 at a constant pressure of 5 bar, at 25 °C. The 6FDA-bisP obtained from protocol M2 presented CO_2 permeability (P_{CO2}) of 35.3 Barrer and CO_2/CH_4 selectivity ($\alpha_{CO2/CH4}$) of 25.6, comparable to several commercial polymer membranes. Its ZIF-8 MMMs showed not only significant free fractional volume (FFV) increment, but also 130% and 37% improvements for P_{CO2} and $\alpha_{CO2/CH4}$, respectively, with the optimum loading of 15 wt.%. The study revealed the new 6FDA-copolyimide has the potential for CO_2/CH_4 separation, and its ZIF-8 incorporation further enhanced its gas separation performances.

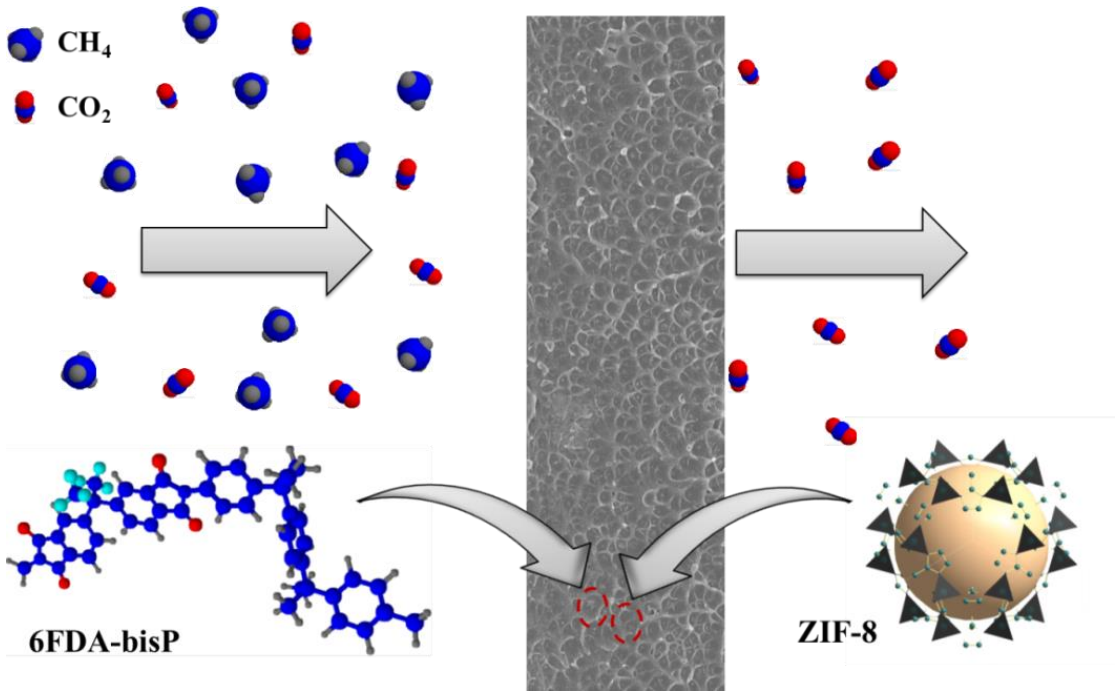

Fig. 3-1: Illustration of CO_2 and CH_4 separation by a mixed matrix membrane, consisting of 6FDA-bisP co-polyimide and imidazolate-MOF, ZIF-8.

3.3. INTRODUCTION

The incorporation of zeolitic imidazolate frameworks (ZIFs) in mixed matrix membrane (MMM) for gas separation application, especially in natural gas has increased significantly in the recent years, due to their robust porosity, high thermal and chemical stability [114]. Besides that, their excellent selectivity towards several gas pairs (H_2/CO_2 [180,181], H_2/CH_4 [138,182], CO_2/CH_4 [183,184], CO_2/N_2 [61,120]) makes them a material of choice to overcome the gas separation limitations in polymeric membranes [143]. Furthermore, ZIFs addition has been demonstrated to suppress polymer chain swelling in glassy polymers and the irreversible compaction of the rubbery polymer [143,185], allowing the MMMs to be operational at higher pressure and CO_2 content [186].

ZIFs, a subclass of metal-organic frameworks (MOFs), is based on imidazolate (im) anionic organic ligands, tetrahedrally coordinated transition metals (M = Fe, Co, Cu, Zn) and possess zeolite sodalite topology (SOD) [114,115], as previously discussed in Section 2.2.2. Due to the known fact that ZIF-8 adsorbs preferentially in the order of $CO_2 > CH_4 > N_2$ [117], making it ideal for separating CO_2 molecules (ca. 3.3 Å) from other larger kinetic diameter molecules, i.e., N_2, CH_4, O_2, C_2H_6 [187]. ZIF-8 also reported having excellent permeability and selectivity for the following gas pair, e.g., H_2/C_2H_8 [119], and propylene/propane [120,121], among other gasses.

The incorporation of smaller size inorganic filler has been proved to be a more suitable approach in gas separation MMMs. ZIF-8 nanoparticles (NPs) can be prepared through several synthesis routes [118,188,189] and controlled synthesis conditions to achieve high purity and excellent structural properties. The methodologies include the conventional solvothermal process in DMF or MeOH [190], rapid synthesis at room temperature in different solvents as well as water [191–193], microwave-assisted and sonochemical synthesis [190]. Besides that, ZIF-8's functional groups will significantly influence the polymer-filler interfacial properties in MMMs, through hydrogen bonding formation and auxiliary aromatic $\pi - \pi$ stacking interactions with the polymer's functional groups (Fig. 3-2) [186,194,195].

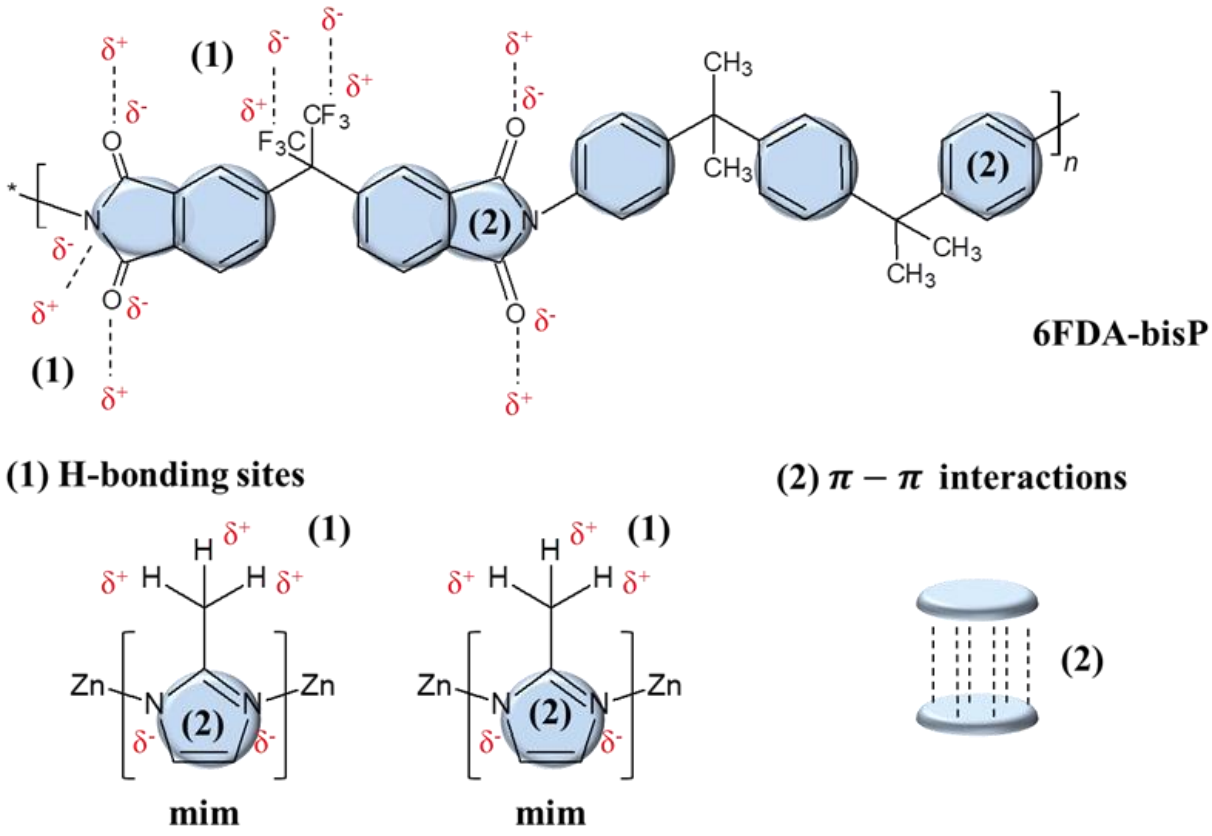

Fig. 3-2: Schematic illustration of the molecular interaction of ZIF-8 to 6FDA-copolyimide, e.g., 6FDA-bisP in MMM. (1) hydrogen bonding between ZIF-8's methyl group and 6FDA-bisP's carbonyl, hydroxyl and fluoride groups, and (2) auxiliary π – π stacking interaction due to delocalized electrons of adjacent aromatic rings [186,195].

In industrial scale membrane processes, higher fluxes membranes with acceptable gas pair separation efficiency are required to achieve its feasibility. Higher fluxes membranes reduce the membrane area requirement, thus the capital cost. Additionally, the major advantage of using ZIF-8 MMMs in the natural gas industry is that ZIF-8 has no significant impact on water adsorption (translated into a poorer separation), owing to its hydrophobic methyl groups [196].

Our focus was to improve the separation properties of low permeable perfluorinated 6FDA-copolyimide, as the polyimide generally offers superior advantages compared to several well-known polymers such as high rigidity, high thermo-oxidative and solvent resistance [197], high mechanical strength and tunable transport properties [198,199], versatility for diamine co-monomer choices and the resultant chemical structures [60,65,198]. Interestingly, the choice of diamine moieties plays a significant role in influencing gas transport properties [58]. Various 6FDA diamine co-monomers have been reported such as

diallyl phthalate (DAP) [60], 3,3′-diamino diphenyl sulfone (DDS) [198], 1,5-naphthalene diamine (NDA) [200], oxydianiline (ODA) [67,68], *m*-phenylenediamine (*m*-PDA) [60,201], 3,3'-hydroxy-4,4'- diamino biphenyl (HAB) [65], however, they presented low CO_2 permeability of less than 25 Barrer. Besides optimizing the polymer structures in the conventional forms, incorporating suitable inorganic fillers towards a more advanced material is important to overcome the latest Robeson's upper bound [21].

3.4. EXPERIMENTAL

3.4.1. Materials

Commercial aromatic dianhydride, 4,4'-(hexafluoroisopropylidene)diphthalic anhydride (6FDA, 99%, Sigma Aldrich) was dried before the synthesis in a vacuum drying at <160 °C for 6 – 7 h to discard any moisture. The aromatic diamine monomer, 4,4′-(1,4-phenylenediisopropylidene) bisaniline (bisP, ≥99%, Mitsui Japan) and synthesis grade 1-methyl-2-pyrrolidone (NMP, ≥99%, Merck) were used as received. For ZIF-8 syntheses: zinc nitrate hexahydrate ($Zn(NO_3)_2 \cdot 6H_2O$, ≥99.0%, Sigma Aldrich), 2-methylimidazole (Hmim, 99%, Sigma Aldrich), high purity CHROMASOLV® methanol (MeOH, ≥99.9%, Sigma Aldrich), anhydrous *n,n*-dimethylformamide (DMF, 99.8%, Sigma Aldrich), ACS grade pyridine (Py, ≥99.0%, Sigma Aldrich) and absolute methanol (MeOH, >99.8%, Penta Czech Republic) were used as received.

3.4.2. 6FDA-bisP co-polyimide synthesis

A classic two-step polymerization method was utilized, as presented by other researchers [67,68] to synthesis several other 6FDA-copolyimides. Firstly, the dianhydride and the diamine were reacted in a polar aprotic solvent under N_2 atmosphere to produce poly(amic) acid solution (PAA). The intermediate PAA formation is due to nucleophilic attack by the diamine amino group onto the anhydride carbonyl carbon [69]. The second step was to imidize the PAA through thermal annealing at 70 – 250 ºC, and the overall reaction scheme is presented in Fig. 3-3.

Typically, 10 mmol (4.5 g) of 6FDA was first dissolved in 72 g of NMP, followed by the addition of 10 mmol (3.5 g) bisP, making a PAA solution of 10 wt.% polymer concentration. In protocol M1, the obtained PAA was casted on a casting glass (6 x 16 cm) and thermally annealed to get a flat sheet membrane. The first annealing step was conducted at 70 ºC

overnight, followed by a gradual temperature increment (50 ºC/h) before maintaining at 250 ºC for 2 h followed by gradual cooling (30 ºC/30 min). In protocol M2, the PAA solution was precipitated into distilled water at 25 °C, collected by filtration and subjected to the said thermal annealing procedure to obtain 6FDA-bisP polyimide granules. The polyimide granules were utilized in the membrane preparation.

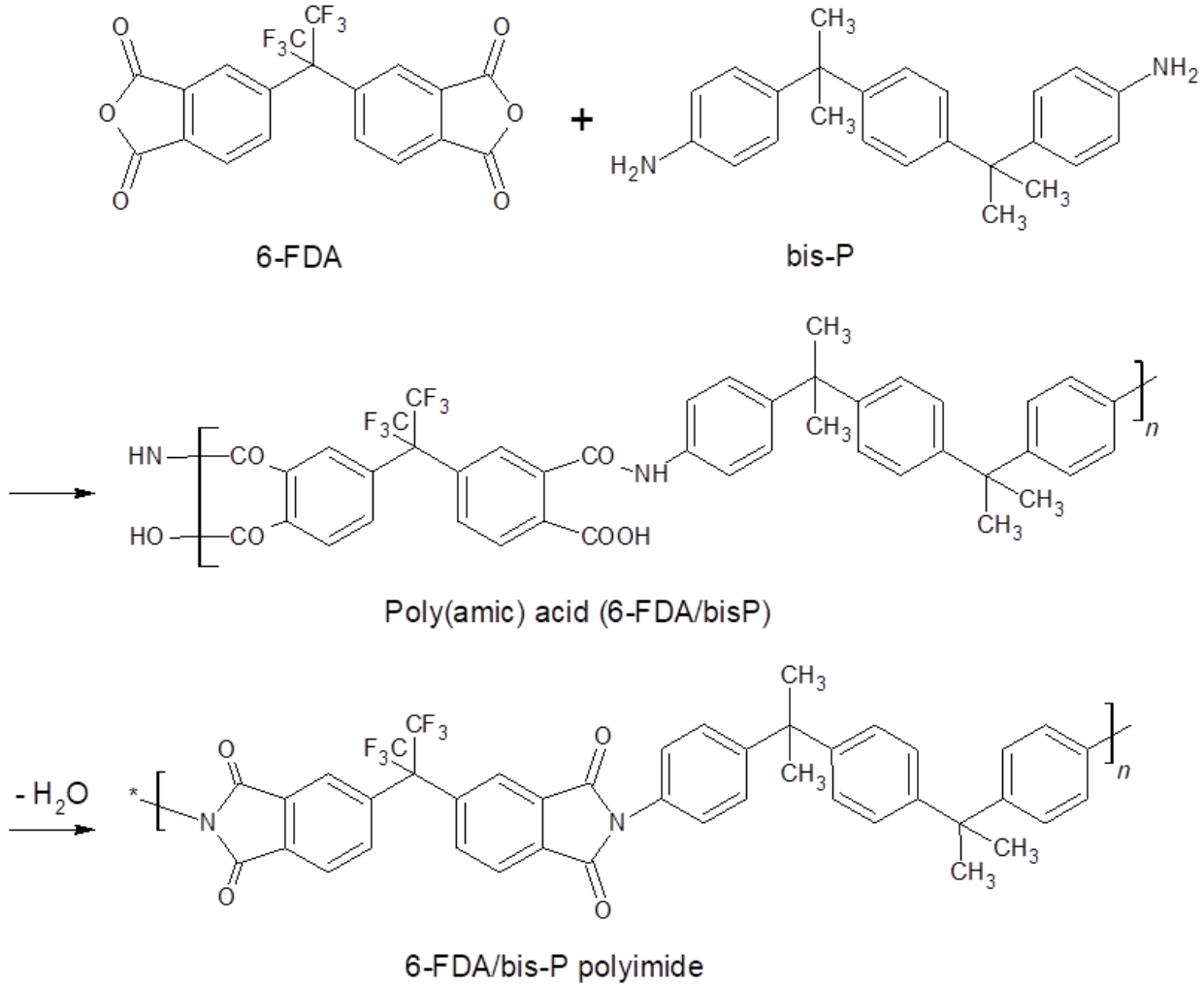

Fig. 3-3: The chemical structures of 4,4'-(hexafluoroisopropylidene)diphthalic anhydride (6FDA) and 4,4′-(1,4-phenylenediisopropylidene) bisaniline (bisP) monomers, and the proposed schematic reaction to produce 6FDA-bisP polyimide.

3.4.3. ZIF-8 syntheses

Cravillon *et al.* [191,192] reported successful synthesis of < 50 nm ZIF-8 NPs at room temperature without any stabilizing agents or conventional activation methods. Based on their methodology, we further investigated the different $Zn(NO_3)_2 \cdot 6H_2O$: Hmin: MeOH molar ratios and precursor addition to synthesize ZIF-8 (<100 nm) for 6FDA-bisP MMM.

Table 3-1 summarizes the synthesis variations conducted in this study. The reaction scheme is presented in Fig. 3-4.

Typically, in ZIF-8 synthesis at 1:8:1000 molar ratio, for example, 0.84 mmol (0.25 g) $Zn(NO_3)_2 \cdot 6H_2O$ and 6.72 mmol (0.55 g) Hmim were each dissolved in 34.24 mL MeOH. The Hmim-MeOH solution was added into $Zn(NO_3)_2$-MeOH solution under magnetic stirring of 250 rpm for 60 mins before the colloidal solution was centrifuged at 20,000 rpm at 25 °C. The NPs were then rinsed with 3 x 20 mL of fresh MeOH and sonicated between 60 – 90 mins (or until no visible agglomerates observed) for each rinsing cycle. The sonication was to separate the agglomerated particles which might have occurred in the previous stage.

Table 3-1: The variation of different $Zn(NO_3)_2 \cdot 6H_2O$: Hmin: MeOH ratios and the selected solvents used in the preparation of ZIF-8 NPs.

Naming	Solvent	Zn^{2+}: Hmim: solvent molar ratios	Ultrasonic treatment
Z8-D [1]	DMF	1:8:600	NO
Z8-DP [2]	DMF + Pyridine	1:8(1)*:600	NO
Z8-J	MeOH	1:6:400	NO
Z8-JN	MeOH	1:8:1000	YES
Z8-JZ	MeOH	1:6:350	YES

*Ratio of 1-mole pyridine to 8-mole diamine monomer
[1]synthesis at 110 °C
[2]synthesis at 80 °C

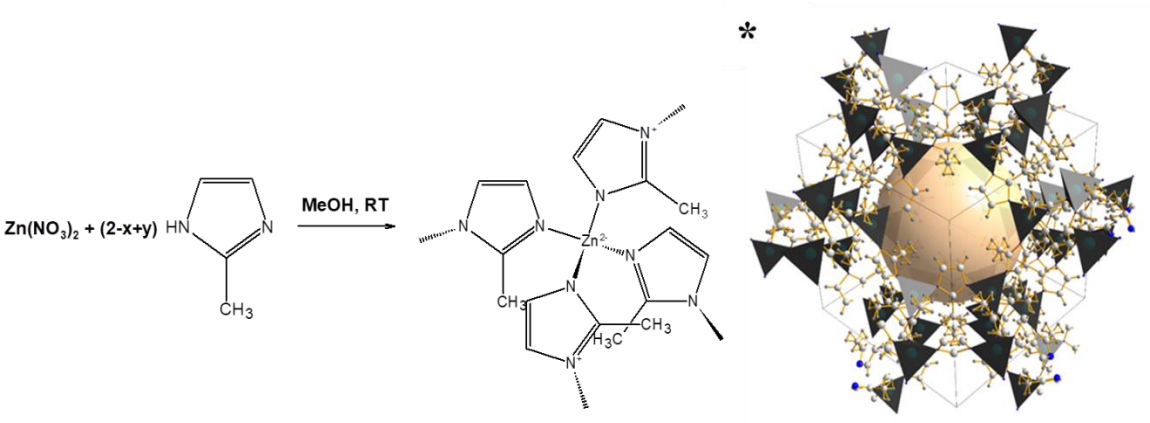

Fig. 3-4: Synthesis of ZIF-8 using Zn(NO3)2·6H2O and Hmim in the presence of excess methanol. The asterisk (*) represents ZIF-8 building block, with the ZnN4 tetrahedral polyhedral (olive green) and its free volume (dark yellow ball). This structure was drawn using Diamond 3.2 with CIF obtained from CDCC open database [111].

3.4.4. Membrane fabrication

In M1 protocol, the flat sheet pristine membrane was directly obtained after the PAA thermal annealing. Whereas in M2 protocol, usually 0.80 g 6FDA-bisP granules were dissolved in 10 mL $CHCl_3$ (making an 8 wt.% polymer concentration solution), casted on a glass plate and dried in a covered container under $CHCl_3$-atmosphere for controlled evaporation, overnight. The membrane was later dried at 110 °C before characterization and separation measurement.

Referring to M1 MMM, an additional of 2.4 mL NMP containing a known amount of re-dispersed ZIF-8 was added into 10.0 g of PAA under magnetic stirring and stirred for another 2 h. The solution was casted and thermally imidized. For M2 MMM, a known amount of ZIF-8 was sonicated in 10 mL $CHCl_3$ for 2 h, before the addition of 0.80 g 6FDA-bisP granules. The mixing was conducted for another 4 – 5 h under magnetic stirring and the similar M2 pristine membrane drying procedure was applied. Both MMMs consisted of 8 wt.% polymer concentration, and the particle loading was calculated as in Eq. 3.1.

$$Particle\ loading, wt.\% = \frac{Mass\ of\ ZIF{-}8\ (g)}{Mass\ of\ ZIF{-}8\ (g) + Mass\ of\ polymer\ (g)} \times 100 \qquad \text{Eq. 3.1}$$

3.4.5. Characterizations

The ZIF-8 crystallinity was determined by x-ray diffraction (XRD). The powder pattern was collected at room temperature with a X'Pert PRO θ-θ diffractometer, equipped with para-focusing Bragg-Brentano geometry, using Cu·K_α radiation (λ = 1.54 Å, U = 40 kV, I = 30 mA). Data were scanned with an ultrafast detector X'Celerator over the angular 2θ range of 5 – 60° (step size of 0.017° at 20.32 s·step^{-1}) and evaluated with High Score Plus 3.0e. Relative crystallinity was calculated based on the integrated peak area, with the peak at 2θ = 7.3° (110) of a highly crystalline sample was used as a reference (Eq. 3.2) [202].

$$Relative\ crystallinity = \frac{Peak\ intensities\ of\ the\ sample\ at\ (110)\ plane}{Peak\ intensity\ of\ the\ reference\ at\ (110) plane} \times 100 \qquad \text{Eq. 3.2}$$

N_2 sorption isotherms were determined using an ASAP 2050 (Micromeritics) at -196 ºC and the specific surface area was calculated using Brunauer–Emmett–Teller (BET) method at P/P_0 between 0.06 – 0.20. A ca. 100 mg sample was degassed at 100 ºC for 8 h before the measurement. Membrane morphology was characterized by scanning electron microscopy (SEM), Hitachi 4700 with a JEOL JSM – 35C, operated at 15 kV. Membrane cross-section was prepared by a cryogenic fracture in liquid N_2 and coated with gold-palladium coating

mixture. A simultaneous thermogravimetric analysis (TGA) and differential scanning calorimetry (DSC) was carried out using a Linseis STA 700LT where an 8 – 15 mg sample was placed into an alumina crucible and heated at 10 °C·min^{-1} up to 700 °C under 20 mL·min^{-1} N_2 flow. The final combustion was conducted in 20 mL·min^{-1} of air at the highest temperature for 40 mins. Glass transition temperature (T_g) was determined by an inflection point of the specific heat curve obtained.

A Zetasizer Nano ZS90 (Malvern) equipped with He-Ne as a light source was used to measure average particle size at a scattering angle of 90°. A ca. 5 mg ZIF-8 was re-dispersed in ethanol and sonicated for 2 h, at 30 °C before the measurement. The hydrodynamic diameter, d_{hy}, was calculated by the Stokes-Einstein equation (Eq. 3.3):

$$d_{hy} = \frac{kT}{3\pi\eta D} \qquad \text{Eq. 3.3}$$

Where;

k Boltzmann's constant,

T temperature in Kelvin,

η solvent viscosity

D diffusion coefficient (D =.76 × 10^{-15} m^2·s^{-1} [118]).

The fractional free volume of the membranes was calculated from Eq. 3.4 and Eq. 3.5, using solid density values. The density measurement was conducted using a pycnometer (Picnomatic Thermo) at 20 ± 0.01 °C where a ca. 100 mg sample was placed in the analysis cell and degassed using a series of pressurization He cycles at 2 – 20 bar.

$$FFV = \frac{V - V_0}{V} = 1 - \rho V_0 \qquad \text{Eq. 3.4}$$

$$V_0 = 1.288 \times V_{vdw} \qquad \text{Eq. 3.5}$$

Where;

$V = 1/\rho$ polymer specific volume at -273 °C

V_0 polymer specific and occupied volumes at -273 °C

V_{vdw} Van der Waals volume, estimated at 1.288 as recently published by Norman Horn [203].

3.4.6. Gas separation evaluation

The membranes were tested using a steady-state apparatus as previously published [204], using Wicke-Kallenbach method with an online Focus gas chromatography, equipped with a flame ionization detector (FID) with methanizer. An equimolar mixture of methane (>99.7%, 20 mL·min^{-1}, Linde) and carbon dioxide (>99.9%, 20 mL·min^{-1}, SIAD) was used as feed gas at 5 bar and 25°C, with helium (99.999%, 5 mL·min^{-1}, SIAD) as a sweep gas.

The permeability of the two gasses, reported in Barrer (1 Barrer = 10^{-10} cm^3(STP)cm·cm^{-2}·s^{-1}·cmHg^{-1}) was determined by Eq. 3.6.

$$P_i = \frac{y_i F^S l}{A(x_i p^R - y_i p^P)} \qquad \text{Eq. 3.6}$$

Where;

y_i mole fraction of component *i* in the permeate

x_i mole fraction of component *i* in the feed gas.

F^s calibrated sweep gas flow in cm^3(STP)·s^{-1}

l membrane thickness in cm

p total pressure in cmHg, where upper index P indicates permeate side and R retentate side respectively

A effective membrane area in cm^2.

Selectivity values were determined using Eq. 3.7.

$$\alpha_{CO2/CH4} = \frac{y_{CO_2}/y_{CH_4}}{x_{CO_2}/x_{CH_4}} \qquad \text{Eq. 3.7}$$

Where;

x_i molar fractions in the feed

y_i molar fractions in permeate stream.

3.5. RESULTS AND DISCUSSION

3.5.1. 6FDA-bisP characterizations

Both protocols (M1 and M2) successfully produced self-standing and stable pristine 6FDA-bisP co-polyimide membranes. The FTIR spectra in Fig. 3-5 show a complete PAA conversion into polyimide, indicated by the disappearance of the broad primary amine peak, –NH between 3500 – 3200 cm^{-1} and the carboxylic –OH at 2933 cm^{-1}, due to PAA cyclo-dehydration and formation of an imide ring. Other main imide peaks are defined as symmetric C=N stretching at 1380 cm^{-1} and both asymmetric C=O stretching at 1719 cm^{-1} and 1785 cm^{-1} [49,205]. All the membranes are in the thickness range of 50 – 70 μm (see Fig. 3-6).

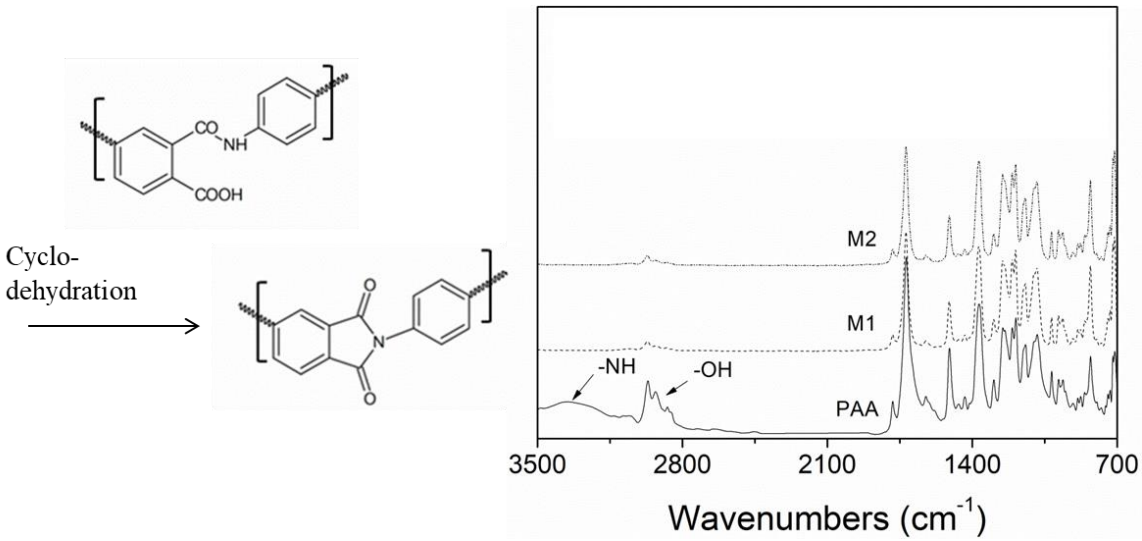

Fig. 3-5: FTIR spectra of poly(amic) acid (PAA) and the obtained 6FDA-bisP polyimides, through protocol M1 and M2.

Fig. 3-7 displays the membranes' TGA weight loss curves and its first derivatives. The first weight loss between 200 – 300 °C in both samples is related to the evaporation of the trapped solvent (NMP, b.p. 202 °C). The temperature increase during heating promotes polymer chain mobility and consequently upsurges the trapped NMP desorption from the polymer matrix [51,185]. The second prominent weight loss indicates the membrane decomposition temperature (T_d). As indicated in Table 3-2, M2 membrane shows lower T_d than M1. The difference is due to M2 membrane's lower polymer chain packing arrangement as a result of the additional step of dissolving in $CHCl_3$.

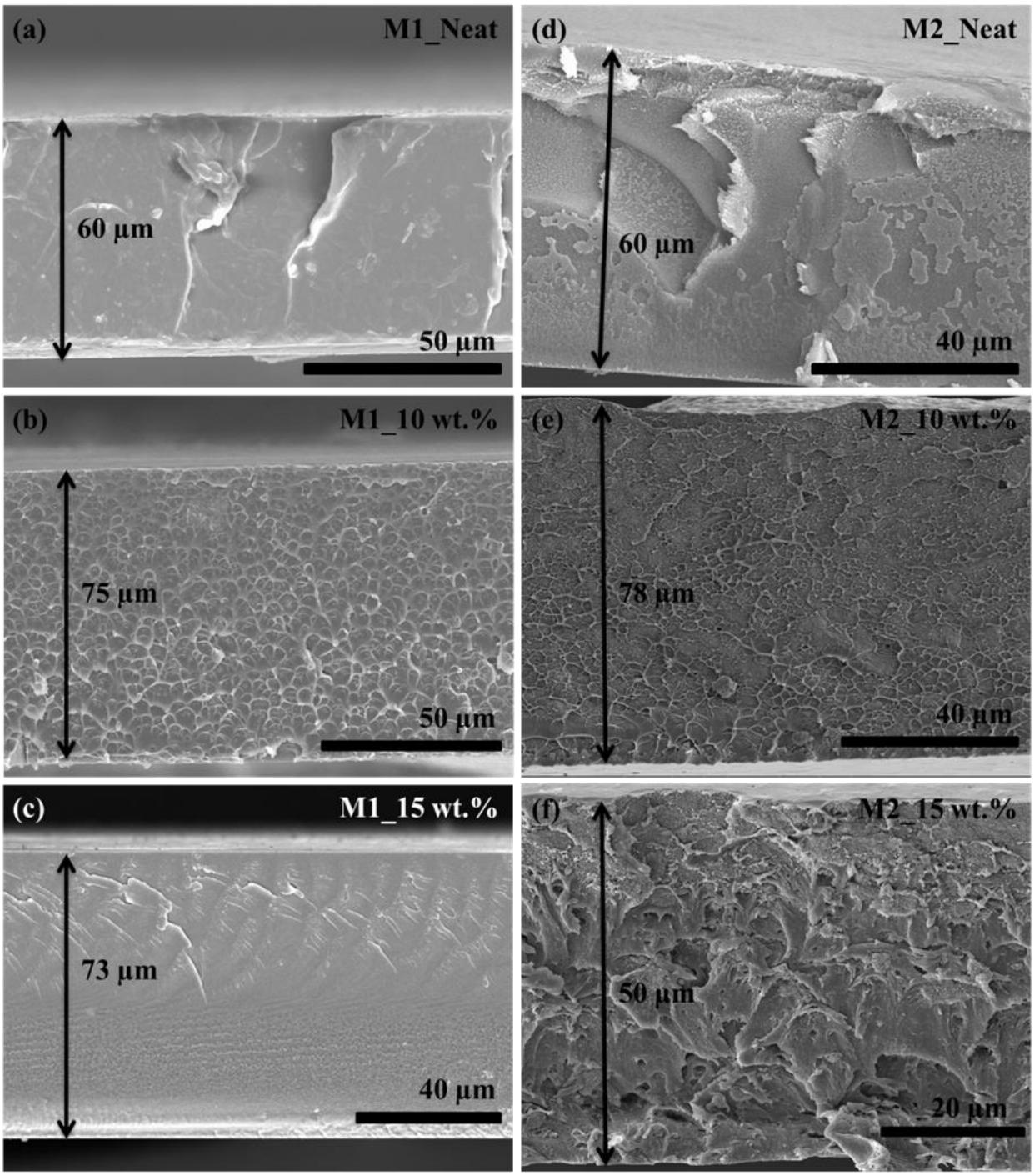

Fig. 3-6: Cross-section images of neat 6FDA-bisP and its MMMs with Z8-JZ7, 10 wt.% and 15 wt.% loading, prepared through (a-c) protocol M1 and (d-f) protocol M2. The membranes are in the thickness range of 50–70 µm.

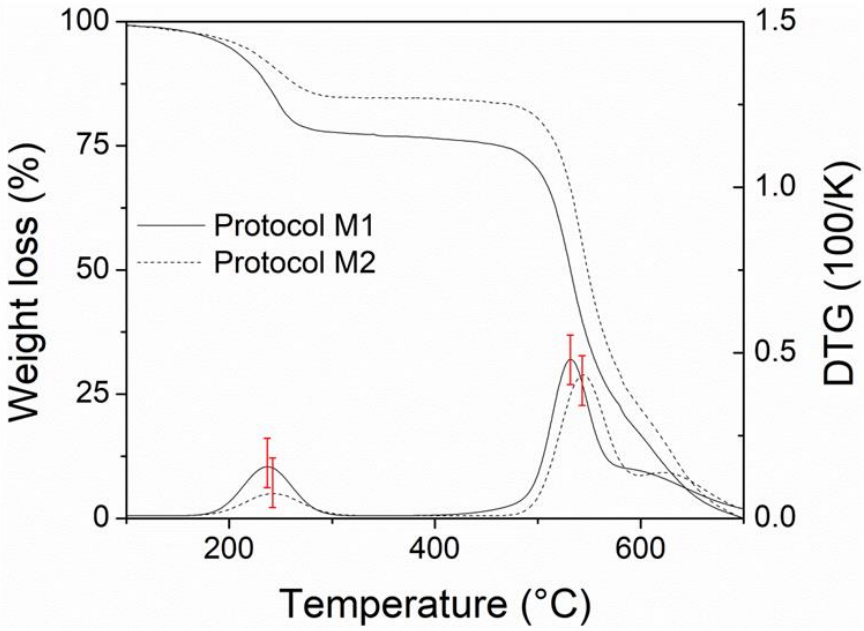

Fig. 3-7: TGA curves for the membranes the obtained 6FDA-bisP polyimides, through protocol M1 and M2 and their respective first derivatives.

Table 3-2 also displays the membranes' physical properties, obtained from DSC and density measurements. The FFVs were calculated from solid densities, measured at 20 °C with pressurized He cycles between 2 – 20 bar. 6FDA-bisP has considerably a high free volume with respect to several known 6FDA-polyimides with multiple $–CH_3$ group in their diamine moieties: 6FDA-DAM = 0.271 [206], 6FDA-TrMPD = 0.206 [58] and 6FDA-6FpDA = 0.190 [207], where the $–CH_3$ substituents in isopropylidene groups give rise to the polymer free volume by restricting an efficient packing due to its steric hindrance [206]. A higher free volume was achieved in the M2 membrane, again contributed by the re-dissolving step during fabrication.

Table 3-2: Physical properties of M1 and M2 6FDA-bisP neat membranes. FFV was calculated from solid densities, measured at 20 °C with pressurized He cycles between 2 – 20 bar.

6FDA-bisP	T_d (°C)	T_g (°C)	Density ($g \cdot cm^{-3}$)	FFV*
M1	543	390	1.353	0.196
M2	531	384	1.323	0.214

*$\sigma \leq 0.5\%$, calculated from several independent measurements

3.5.2. ZIF-8 characterization

Fig. 3-8 shows the XRD patterns for all ZIF-8s, obtained at 25 °C and well-consistent to ZIF-8 simulated pattern. 2 theta values of 7.3°, 10.4°, 12.8°, 16.5° and 18.1° corresponded to the crystal lattice directions of (110), (200), (211), (310), and (222), respectively. ZIF-8 face orientation is indicated by the primary peak at (110), and its high intensity was attributed to the stable rhombic dodecahedron shape ZIF-8 formation, which resembled the final stage of ZIF-8 structure growth [115].

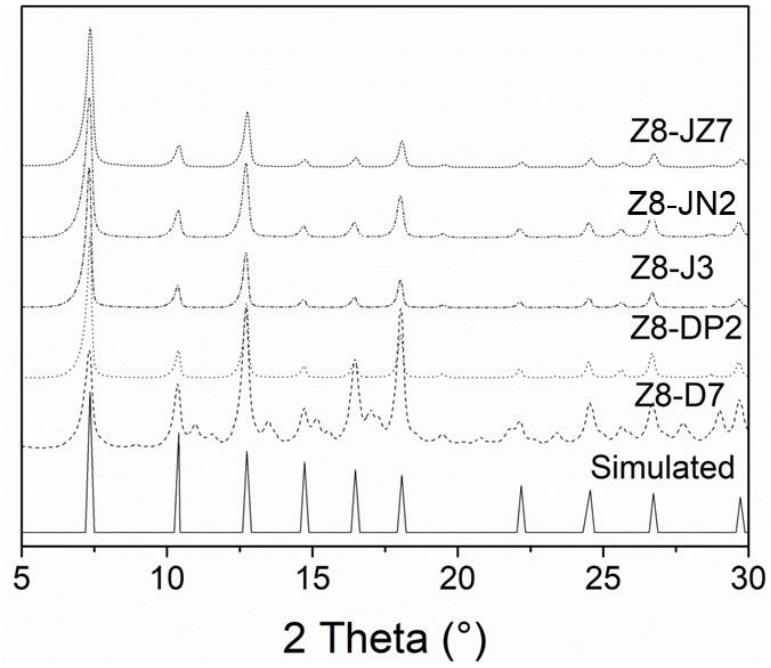

Fig. 3-8: XRD patterns of the ZIF-8 NPs, obtained from the different procedures, referring to the ZIF-8 simulated pattern

Z8-JZ7 FT-IR spectrum is presented in Fig. 3-9 where its primary functional groups are specified. The aromatic and aliphatic imidazole C–H stretching bands are at 3145 cm^{-1} and 2935 cm^{-1}, respectively [187]. The peak at 1579 cm^{-1} can be assigned to C=N stretching mode, while the intense and convoluted bands between 1380 – 1515 cm^{-1} is the entire aromatic ring stretching. The bands in 900 – 1380 cm^{-1} region are defined as aromatic in-plane bending while those below 800 cm^{-1} are for aromatic out-of-plane bending. ZIF-8's defining Zn–N stretching mode is indicated by the strong signal at 419 cm^{-1} [187].

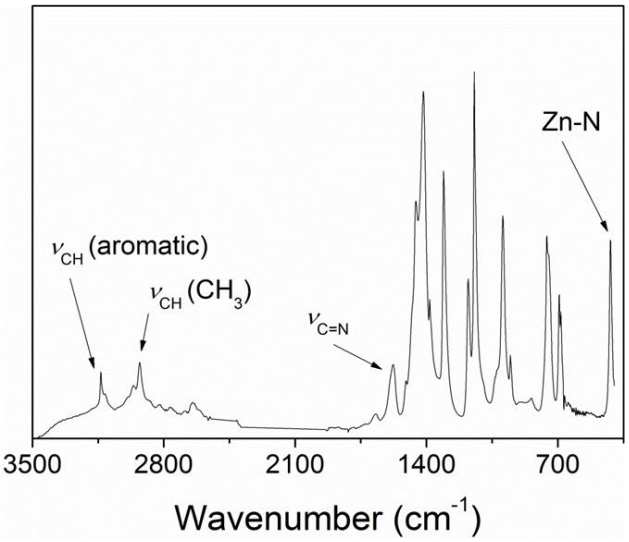

Fig. 3-9: FTIR spectra of Z8-JZ7 ZIF-8 nanoparticles, presented between 3500 – 350 cm^{-1}.

Particle size and crystallinity properties of ZIF-8 NPs are tabulated in Table 3-3. Both Z8-JZ7 and Z8-JN2 were chosen to prepare MMMs, due to their smaller particle sizes and high crystallinity (see Fig. 3-10: Z8-JZ7 and Z8-JN2). A bigger particle size obtained for Z8-JZ7 is attributed to its higher precursor concentrations in methanol during synthesis, and the concentrations influence the ZIF-8 particle size [189]. The initial focus of investigating ZIF-8 one-pot synthesis with 6FDA-bisP was discontinued due to the poor characteristics of Z8-D7 and Z8-DP2, both synthesized in DMF at elevated temperature (up to 110 °C). It is important to note that the ZIF-8 solvothermal synthesis requires an elevated temperature of ca. 140 °C in DMF [190], meanwhile 6FDA-bisP synthesis in the same solvent is needed to be conducted at a maximum temperature of ca. 60 °C. Bustamante *at al.* [208] reported no ZIF-8 presence even after 120 min of synthesis in DMF at room temperature. The pyridine addition as a nucleophilic catalyst was only able to reduce the synthesis temperature to 80 °C. Z8-J3 was withdrawn due to its larger particles (see Fig. 3-11: Z8-DP2 and Z8-J3).

Table 3-3: Particle size range of ZIF-8 NPs and their relative crystallinity.

Sample	Solvent	Zn^{2+}: Hmim: solvent molar ratios	Size range (nm)	Relative crystallinity (%)
Z8-D7	DMF	1:8:600	-	5.5
Z8-DP2	DMF + Pyridine	1:8(1)*:600	50-60	44.4
Z8-J3	MeOH	1:6:400	100-300	98.7
Z8-JN2	MeOH	1:8:1000	40-60	87.0
Z8-JZ7	MeOH	1:6:350	70-100	100**

*Ratio of 1-mole pyridine to 8-mole diamine monomer
**The reference peak.

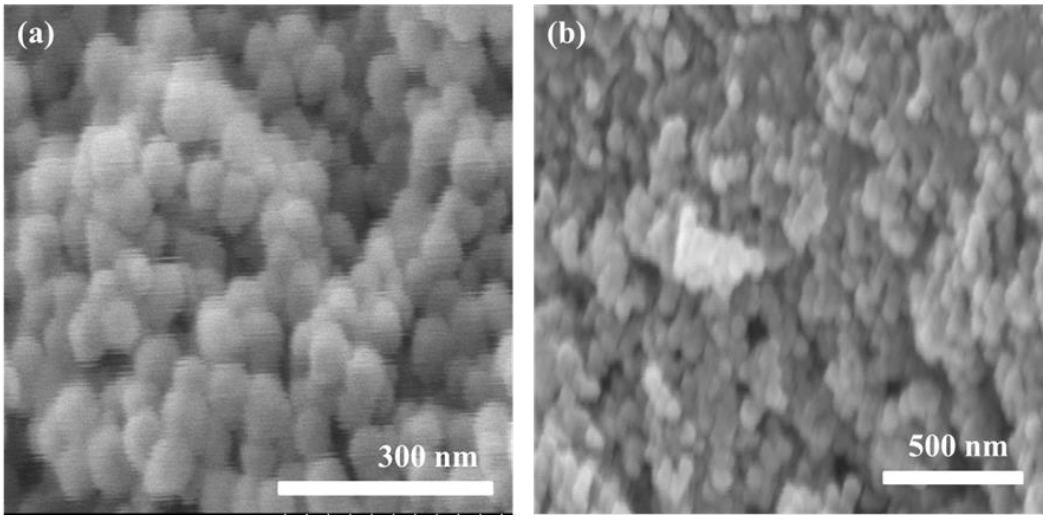

Fig. 3-10: SEM images of ZIF-8 nanoparticles (a) Z8-JZ7 and (b) Z8-JN2, synthesized at different Zn2+: Hmim: solvent molar ratios.

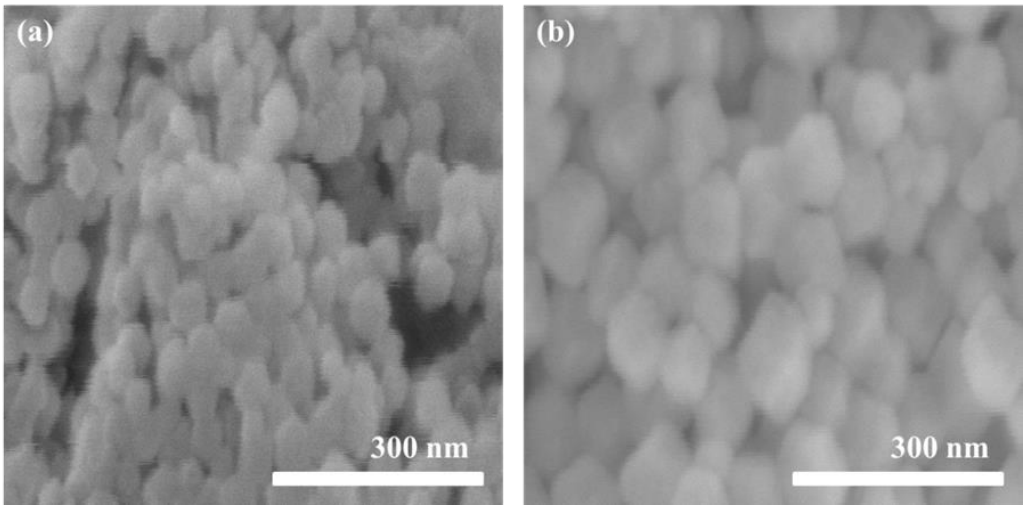

Fig. 3-11: SEM images of ZIF-8 nanoparticles (a) Z8-DP2 and (b) Z8-J3, synthesized in different $Zn^{2+;}$ Hmim: solvent molar ratios. The solvents used were DMF-pyridine mixture and methanol for Z8-DP1 and Z8-J3, respectively.

Fig. 3-12(a) and 3-12(b) display the N_2 adsorption-desorption for both ZIF-8 NPs obtained from BET analysis at -196 °C. The adsorption analysis presents a classic type I and IV isotherm, with the N_2 adsorbed quantity of 542 $cm^3(STP)\cdot g^{-1}$ for Z8-JN2 NPs and 495 $cm^3(STP)\cdot g^{-1}$ for Z8-JZ7 NPs at P/P_o = 0.9. The presence of hysteresis loop after P/P_o = 0.8 is due to capillary condensation phenomenon, normally occurs in between the smaller nanoparticles [55]. The NPs also show BET surface areas of 1463 $m^2\cdot g^{-1}$ and 1341 $m^2\cdot g^{-1}$ for Z8-JN2 and Z8-JZ7, with an external surface area of 176 $m^2\cdot g^{-1}$ and 161 $m^2\cdot g^{-1}$, respectively. The surface areas are comparable to those reported of between 1200 – 1700 $m^2\cdot g^{-1}$ for nano-sized ZIF-8 [118,190].

TGA curve in Fig. 3-13 reveals that Z8-JZ7 NPs are stable up to ca. 396 °C, close to the reported thermal stability values for nano-sized ZIF-8 in N_2 [112,191] before the zeolitic framework starts to decompose. The initial mass loss of ~ 1% below 200 °C is attributed to trapped moisture [188], the latter of ~ 5.8% is due to the removal of guest molecules and potentially the unreacted species from NP surfaces [112,209]. The following steep endothermic mass losses up to ca. 700 °C corresponds to the thermal decomposition of ZIF-8 due to organic linker molecules removal [191], and the combustion in air at the final stage produces ZnO_2.

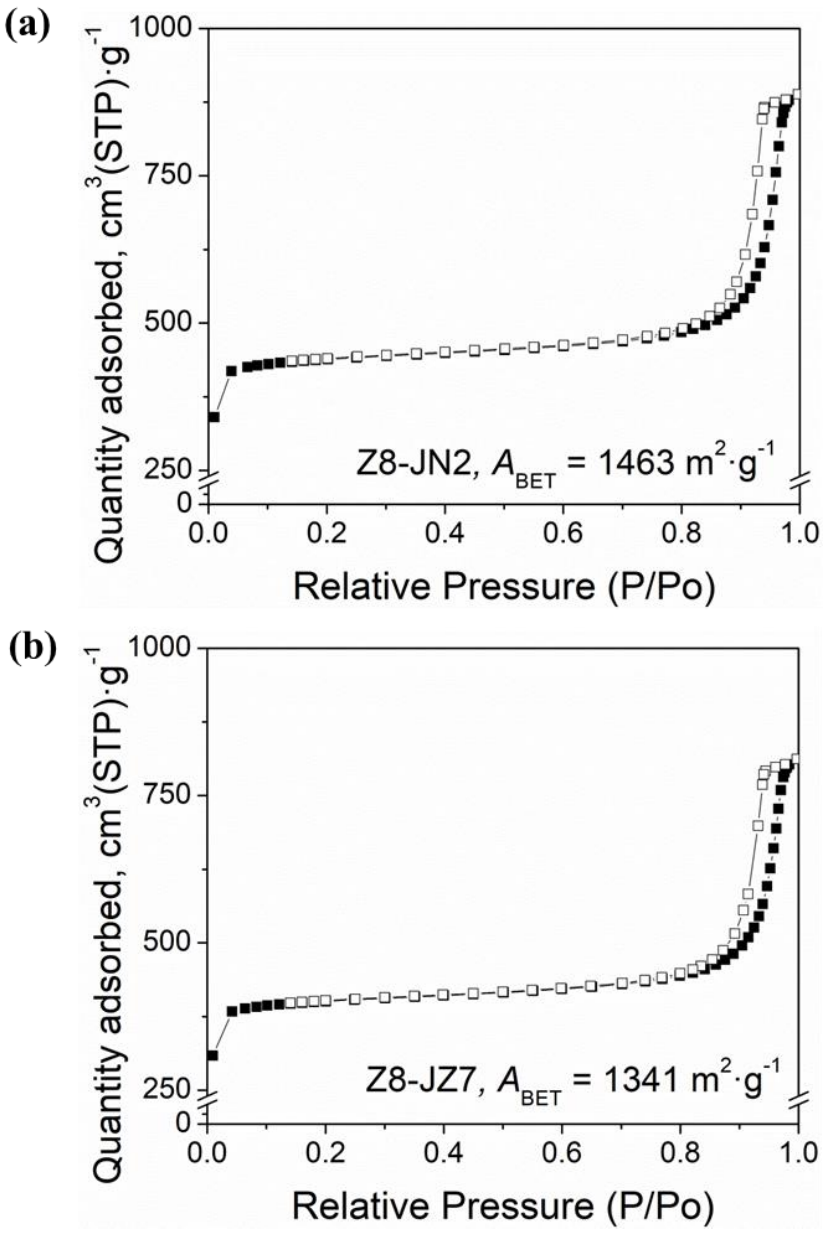

Fig. 3-12: N_2 adsorption (filled) and desorption (unfilled) isotherms measured at -196 °C for the ZIF-8 NPs (a) Z8-JN2 and (b) Z8-JZ7.

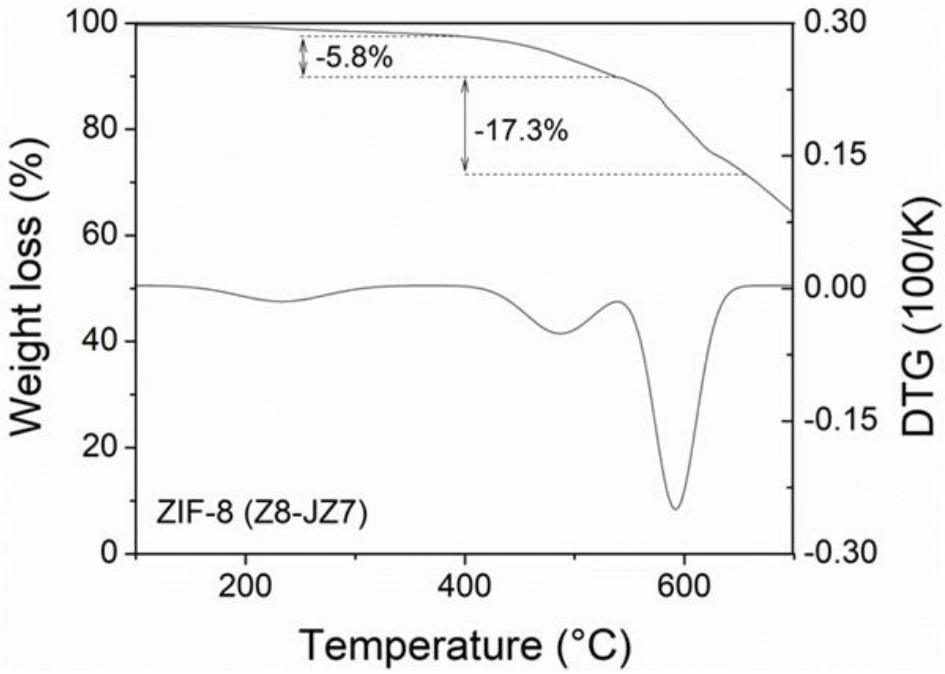

Fig. 3-13: TGA curve for ZIF-8 Z7-JZ7 and its DTG, measured up to 700 °C in N_2 flow of 20 mL·min^{-1}. Final combustion was conducted in 20 mL·min^{-1} of air, oxidizing the zinc residue into solid ZnO_2.

3.5.3. Membrane characterizations

Besides producing a better polymer-filler interfacial interaction, the introduction of un-agglomerated nanoparticles into the MMM is essential as it provides the desired additional surface areas [17,210]. A few studies reported the incorporation of smaller fillers produced a higher degree of agglomeration, particularly at high loadings [55]. The addition of Z8-JN2 (40 – 60 nm) into 6FDA-bisP through protocols M1 and M2, both produced MMMs with high particle agglomeration and several with interfacial voids (see. Fig. 3-14). In the presence of vast agglomeration, purportedly the polymer matrix will be unable to surround the agglomerates, leading to the void formation and resulted in non-selective gas diffusion [29,55]. The agglomerates also reduce the gas selectivity due to the presence of by-pass channels between the nanoparticles. These samples were not tested for gas separation performance. We investigated the phenomenon and found that the smaller (higher external surface area) Z8-JN2 possessed a bigger size distribution, up to >500 μm (94.4 %) and only 5.6 % for particle < 60 μm, 50 days after the synthesis (see Fig. 3-15). Demessence *et al.* [211] reported a positive zeta potential of ZIF-8 NPs suspension in ethanol, explaining the hydrogen bonding network of the protonated imidazole molecules in the NP surfaces and the solvent, leading to particle agglomeration. The Z8-JN2 polydispersity index (PdI) and

hydrodynamic diameter (dhy) were at 0.43 and 4.53 µm, respectively. The values are at least twice bigger than of Z8-JZ7 (PdI = 0.173; dhy = 2.31 µm) and indicate clear evidence of particle agglomeration in Z8-JN2.

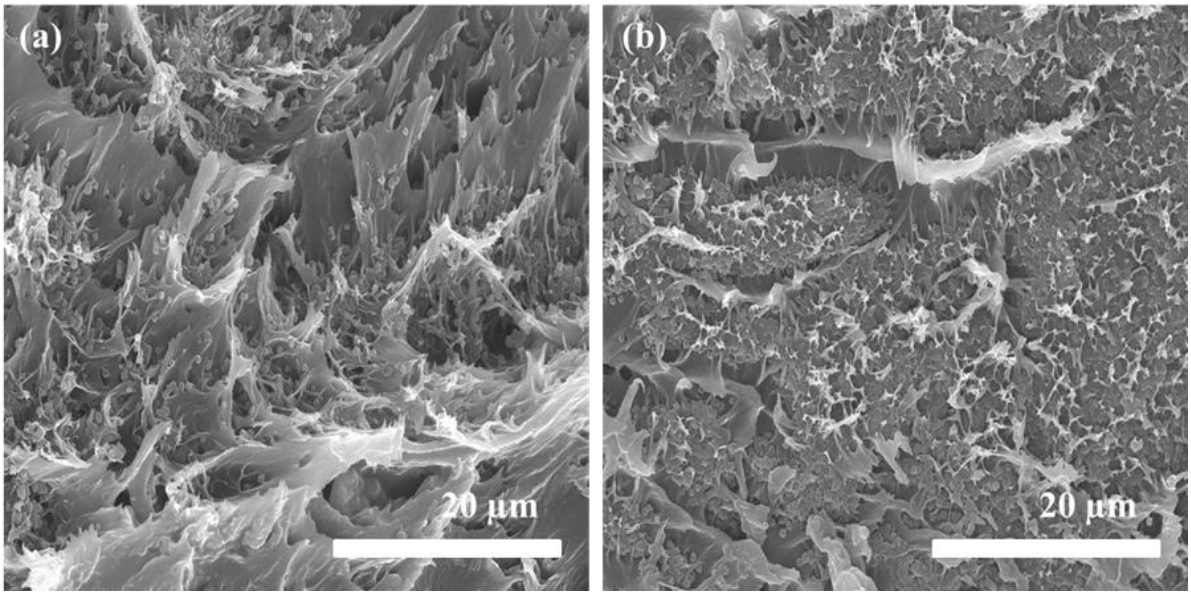

Fig. 3-14: FESEM images 6FDA-bisP MMMs with (a) 10 wt.% and (b) 15 wt.% of Z8-JN2 (40 – 60 nm) particle loadings. The agglomeration was more prominent compared to those MMMs using Z8-JZ7 (70 – 100 nm) ZIF-8 nanoparticles.

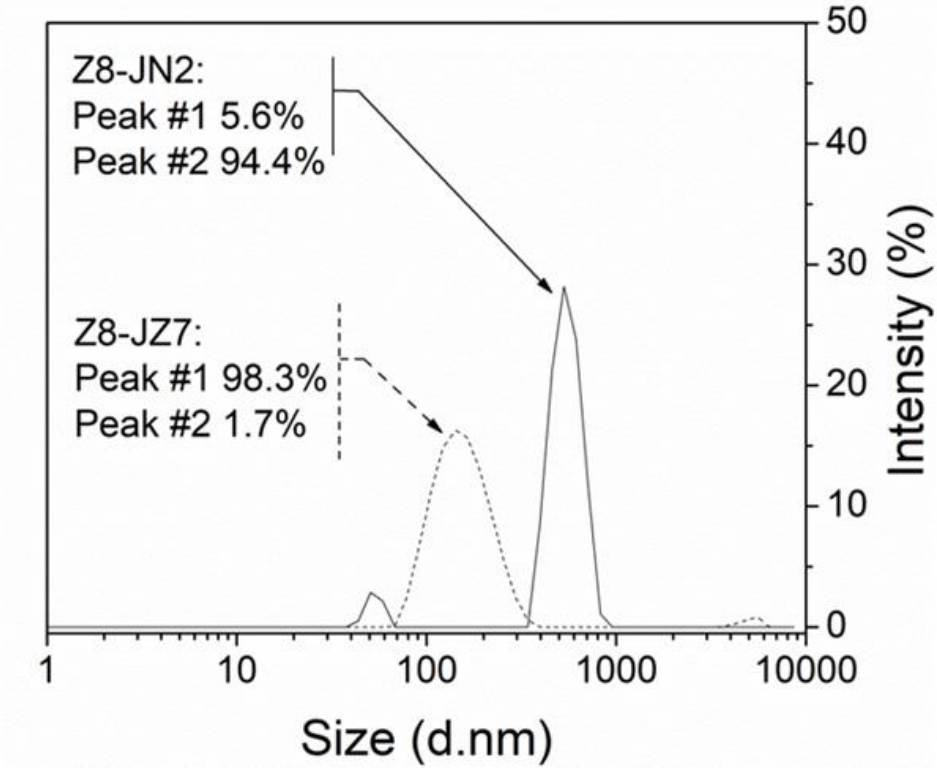

Fig. 3-15: Particle size distribution, obtained from DLS measurement of re-dispersed ZIF-8 NPs in absolute ethanol after 150 days of synthesis.

The MMMs prepared through protocol M1 and M2 with Z8-JZ7 (70 – 100 nm) are in the thickness range of 50 – 70 μm (see Fig. 3-6). The membranes also show a well dispersed and homogenous NPs distribution in the polymer matrix. The typical NP distributions are presented in SEM and EDX images (Fig. 3-17). The crater-like morphology, which typically presents in MMM can be observed, and the centers are formed by the inorganic particle [185]. As expected, the crater size reduces with loading increments. The presence of the convoluted crater and elongated region around the particles is due to interfacial stress as a result of polymer–filler de-bonding [185,212]. This region contributes to the additional free volume, consequently, gives rise to gas diffusion in the MMM [55]. Zinc distribution in the MMMs obtained from EDX also indicated homogenous ZIF-8 distribution well-agreeing to the SEM findings. The addition of 20 wt.% ZIF-8, however, produces a poorer filler dispersion and particle agglomeration.

Besides the known 'weaker' interaction between the filler and the polymer, i.e., H-bonding and π – π aromatic stacking in solid state [213], FTIR measurement were conducted on the MMMs to determine any 'stronger' chemical interaction between ZIF-8 and 6FDA-bisP. Fig. 3-16 shows neither additional peak nor a significant shift in the materials key functional groups, as observed at 1720 cm^{-1} for symmetric C=O stretching and at 1373 cm^{-1} for imide –CN– in 6FDA-bisP and most importantly ZIF-8 Zn–N stretching at 419 cm^{-1}. The result suggests no strong chemical interaction occurred. The intensity of Zn-N peak nonetheless increases, as expected with the ZIF-8 loading increment in MMMs.

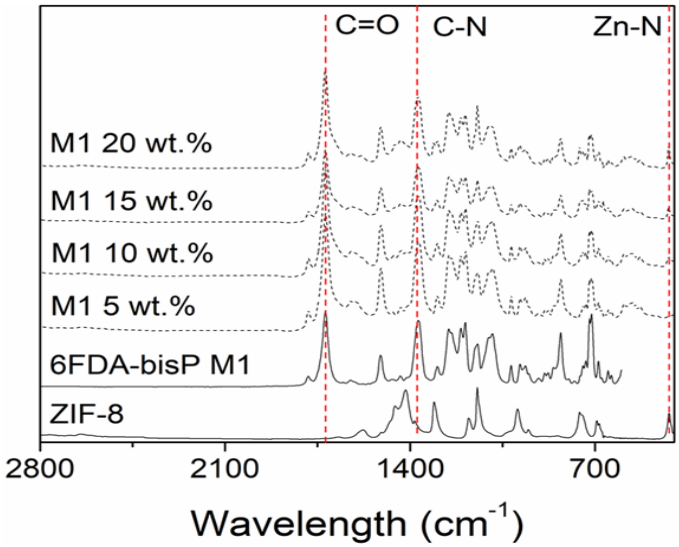

Fig. 3-16: FTIR spectra of pristine 6FDA-bisP and its M1 MMMs, containing Z8-JZ7 nanoparticles, observed at the wavelength of 3500 – 400 cm-1.

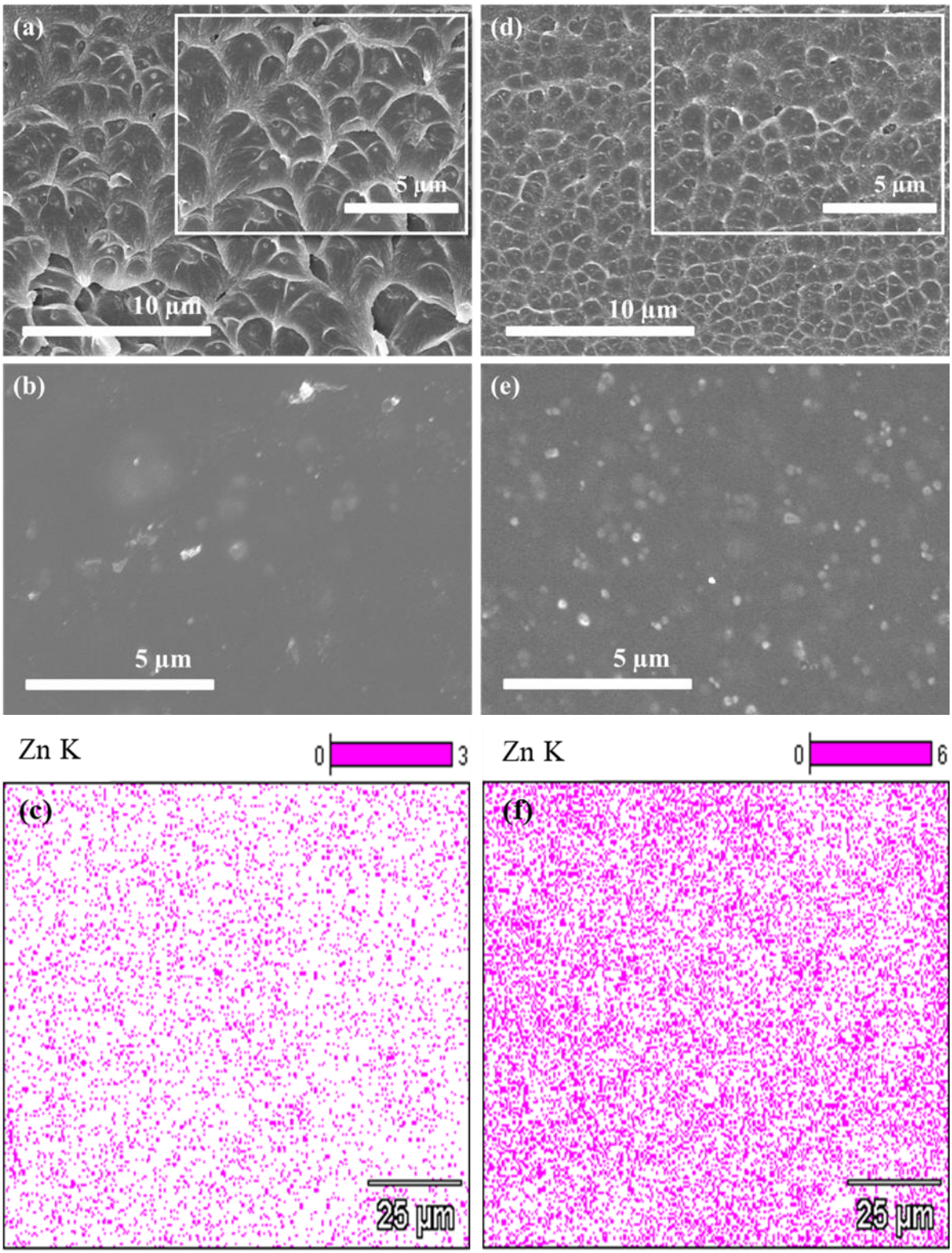

Fig. 3-17: Cross-section and surface images of 6FDA-bisP MMMs with Z8-JZ7, protocol M1 at (a, b) 10 wt.% and (d, e) 15 wt.%, obtained FESEM analysis. EDX images, indicated zinc distribution in the same membranes (c) 10 wt.% and (f) 15 wt.%.

Decomposition temperature (T_d) and glass transition temperature (T_g) of the MMMs were obtained from TGA and DSC analyses (Table 3-4) and provide insight on ZIF-8 addition influence on the MMM thermal stability and polymer chain flexibility. With every 5 wt.% addition of ZIF-8, the T_d for M1 MMM decreases by 7 – 21 °C and a similar reduction trend can be observed for M2 MMMs (between 11 to 13 °C). The reduced thermal stability is due to 6FDA-bisP polymer chain disruption upon the particle addition. Thus lower thermal energy is required for the polymer chain to mobile and decompose. The disruption also allows the amorphous polymer to transition to glassy at a lower temperature, as indicated by T_g reduction in both MMMs.

Table 3-4: The decomposition (T_d) and glass transition temperatures (T_g) for 6FDA-bisP and its ZIF-8 MMMs, fabricated using protocol M1 and M2.

ZIF-8 loading in 6FDA-bisP, wt.%	Decomposition temperature, T_d (°C)		Glass transition temperature *T_g (°C)	
	M1	M2	M1	M2
0	543	531	390	384
5	522	520	383	377
10	504	507	379	355
15	497	495	370	355
20	485	483	364	360

*Average measurement error, M1 samples = -0.522 %/K and M2 = -0.418 %/K

3.5.4. Gas transport properties

3.5.4.1. Gas permeability and CO_2/CH_4 selectivity

The mixed gas permeation properties of 6FDA-bisP and its MMMs were determined by feeding a 50:50 (vol: vol) CO_2/CH_4 binary mixture at a constant feed pressure of 5 bar, at 25 °C. M1 neat membrane presents separation performances of P_{CO2} = 24.9 ± 0.7 Barrer, $\alpha_{CO2/CH4}$ = 19.4 ± 2.8 while M2 neat membrane shows P_{CO2} = 35.3 ± 5.5 Barrer, $\alpha_{CO2/CH4}$ = 25.6 ± 1.6. Gas separation of small kinetic molecules (CO_2, CH_4) in the membrane is governed by a diffusion mechanism and the diffusion is enhanced in a higher free volume polymer membranes [29,155]. The different membrane preparation, i.e., granulation and re-dissolving in $CHCl_3$ in the case of M2, changes the 6FDA-bisP chain packing thus produces a less dense membrane with a higher free volume (FFV = 0.214). These structural changes increase the gas permeability coefficients [29,41], as observed in M2 membranes. The performances of our neat membranes on the other hand are comparable to some aromatic 6FDA-polyimides, 6FDA-HAB (P_{CO2} = 12.3 Barrer, $\alpha_{CO2/CH4}$ = 30) [214], 6FDA-APAF (P_{CO2} = 13.3 Barrer, $\alpha_{CO2/CH4}$ = 22) [214], 6FDA-BAPHF (P_{CO2} = 19.1 Barrer, $\alpha_{CO2/CH4}$ = 37) [215], 6FDA-BATPHF (P_{CO2} = 22.8 Barrer, $\alpha_{CO2/CH4}$ = 32) [215], at 35 °C, between 3 – 10 bar.

Fig. 3-18(a) and 3-18(b) show the gas separation performances of 6FDA-bisP and its ZIF-8 MMMs. The numeric values are summarized in Table 3-5. Both M1 and M2 5 wt.% Z8-JZ7 loading MMMs exhibit a less prominent permeability and selectivity increments. The higher performance in M2 membranes is due to the different physical properties (e.g., density, FFV), related to the preparation protocol as previously discussed. Further filler addition continuously improves the performances and the best performing membrane for M1 membranes are with 15 wt.% Z8-JZ7 loading showing 91% and 50% enhancements for CO_2 permeability and selectivity, respectively ($M1_{15\ wt.\%}$: P_{CO2} = 47.7 ± 2.5, $\alpha_{CO2/CH4}$ = 29.1 ± 1.5). Higher CO_2 permeability enhancement of 130% is recorded for M2 membrane at the same loading with 37% selectivity increase ($M2_{15\ wt.\%}$: P_{CO2} = 81.2 ± 3.3, $\alpha_{CO2/CH4}$ = 35.0 ± 2.9). The incorporation of ZIF-8, expected to enhance CO_2 permeability and ideally increase the CO_2/CH_4 selectivity tremendously, owing to its molecular sieving effect where the ZIF-8 pore aperture size of ca. 3.4 Å (kinetic diameters of CO_2 and CH_4 are 3.3 and 3.8 Å, respectively). Due to its not completely rigid structure and its flexibility to a certain extent [96,216], ZIF-8 adsorbs gasses with kinetic diameters of > 3.4 Å easily, causing CO_2/CH_4

selectivity to reduce [216]. Our MMMs show both good CO_2 permeability enhancement and less substantial selectivity improvement, supporting the above-mentioned information.

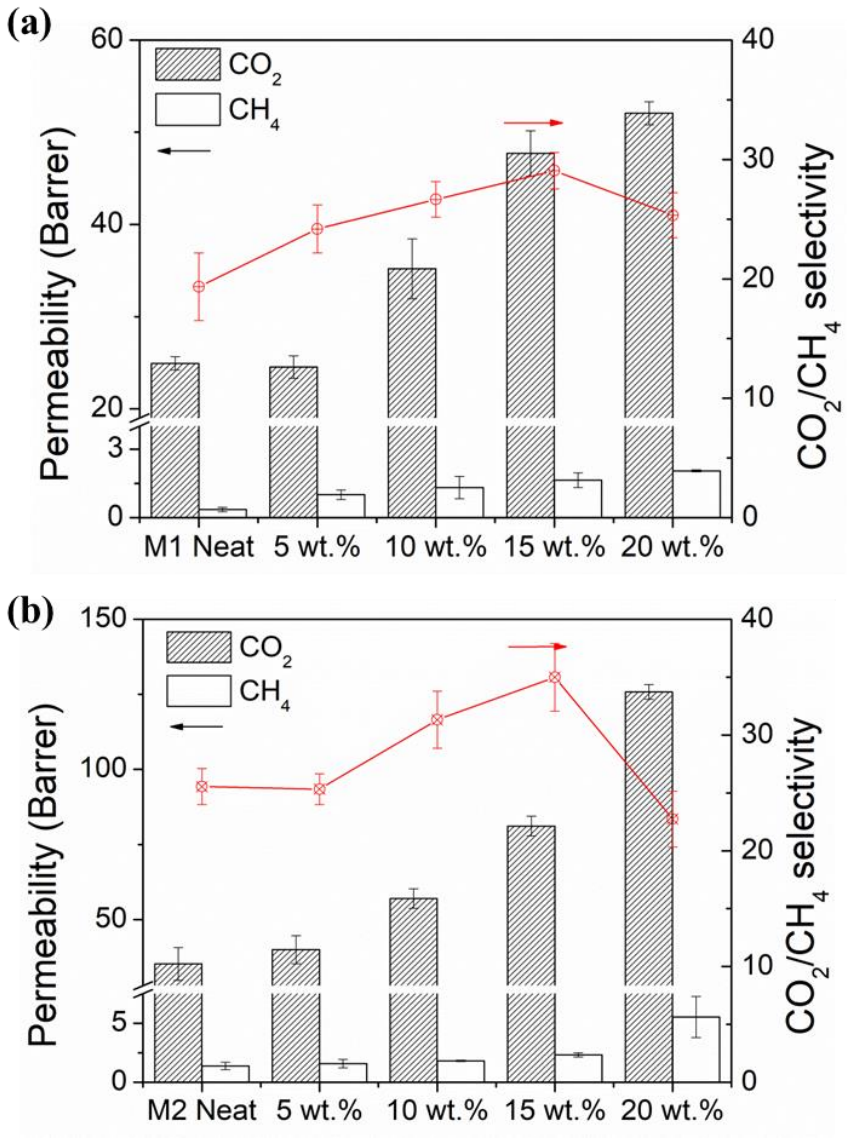

Fig. 3-18: CO_2 and CH_4 permeabilities, and CO_2/CH_4 selectivity of 6FDA-bisP and its ZIF-8 MMMs, (a) protocol M1 and (b) protocol M2; tested at 25 °C and 5 bar with an equimolar mixture of CO_2 and CH_4 feed content. Standard deviations were calculated based on 3 – 5 different membranes and error bars are represented accordingly.

Table 3-5: Mixed gas permeabilities and selectivity of pristine 6FDA-bisP and its ZIF-8 MMMs, measured with an equimolar CO_2 and CH_4 feed composition, at 25°C and 5 bar. The standard deviations were calculated based on several independent measurements of different samples.

6FDA-bisP membranes	ZIF-8 loading (wt.%)	Permeability (Barrer)		CO_2/CH_4 Selectivity
		CO_2	CH_4	
M1	0	24.9 ± 0.7	0.36 ± 0.09	19.4 ± 2.8
	5	24.5 ± 1.2	1.01 ± 0.21	24.2 ± 2.0
	10	35.2 ± 3.3	1.32 ± 0.49	26.7 ± 1.5
	15	47.7 ± 2.5	1.64 ± 0.32	29.1 ± 1.5
	20	52.1 ± 1.3	2.05 ± 0.04	25.3 ± 1.9
Neat M2	0	35.3 ± 5.6	1.38 ± 0.31	25.5 ± 1.6
	5	40.0 ± 4.7	1.58 ± 0.36	25.3 ± 1.3
	10	57.0 ± 3.2	1.82 ± 0.06	31.3 ± 2.5
	15	81.2 ± 3.3	2.32 ± 0.17	35.0 ± 2.9
	20	125.8 ± 2.5	5.53 ± 1.73	22.8 ± 2.4

At the highest loading (20 wt.%) M1 MMM loses 13% of its selectivity comparing to the previous loading (15 wt.%), whereas the M2 MMM indicates a 35% selectivity loss. We believe that the selectivity reduction is due to the presence of bypass channels in the particle agglomerates and the interfacial voids [29,55]. Others reported comparable amount of ZIF-8 loadings and achieved CO_2 permeability improvements without compromising CO_2/CH_4 selectivity in low permeable polymers (i.e. 10 wt.% in polyurethane [217]; 30 wt.% in Matrimid® 9725 [104]) and at lower loadings for high permeable polymers (i.e. 10 wt.% in PEBAX-1657 [186]; 5 wt.% in 6FDA-durene [62]).

Fig. 3-19(a) and 3-19(b) show the membrane FFV values calculated to the normalized solid density values to the actual particle loadings obtained from TGA. The differences of pristine membrane FFVs are as previously discussed. M1 MMM presents an FFV increment of 113% at the highest loading and gives rise to 109% of CO_2 permeability enhancement. Whereas in M2 MMM, 79% FFV increment is observed at the highest loading, adding to its already higher free volume in the pristine membrane, contributed to a 257% CO_2 permeability improvement. The additional FFV in MMM arises from the filler–polymer interfacial region [106], indicated by the convoluted crater in the SEM images (see Fig. 3-17), and occurs due to polymer chain disruption after the filler addition and the interfacial de-bonding [29]. The ‘new’ polymer arrangement possesses a higher free volume

and positively influences the gas permeability. These findings also well-agree to the established free volume–gas permeability correlation in low permeable glassy polymers by Park and Paul [218] as presented in Fig. 3-20(a) and 3-20(b), where a higher free volume glassy polymer gives a higher gas permeability.

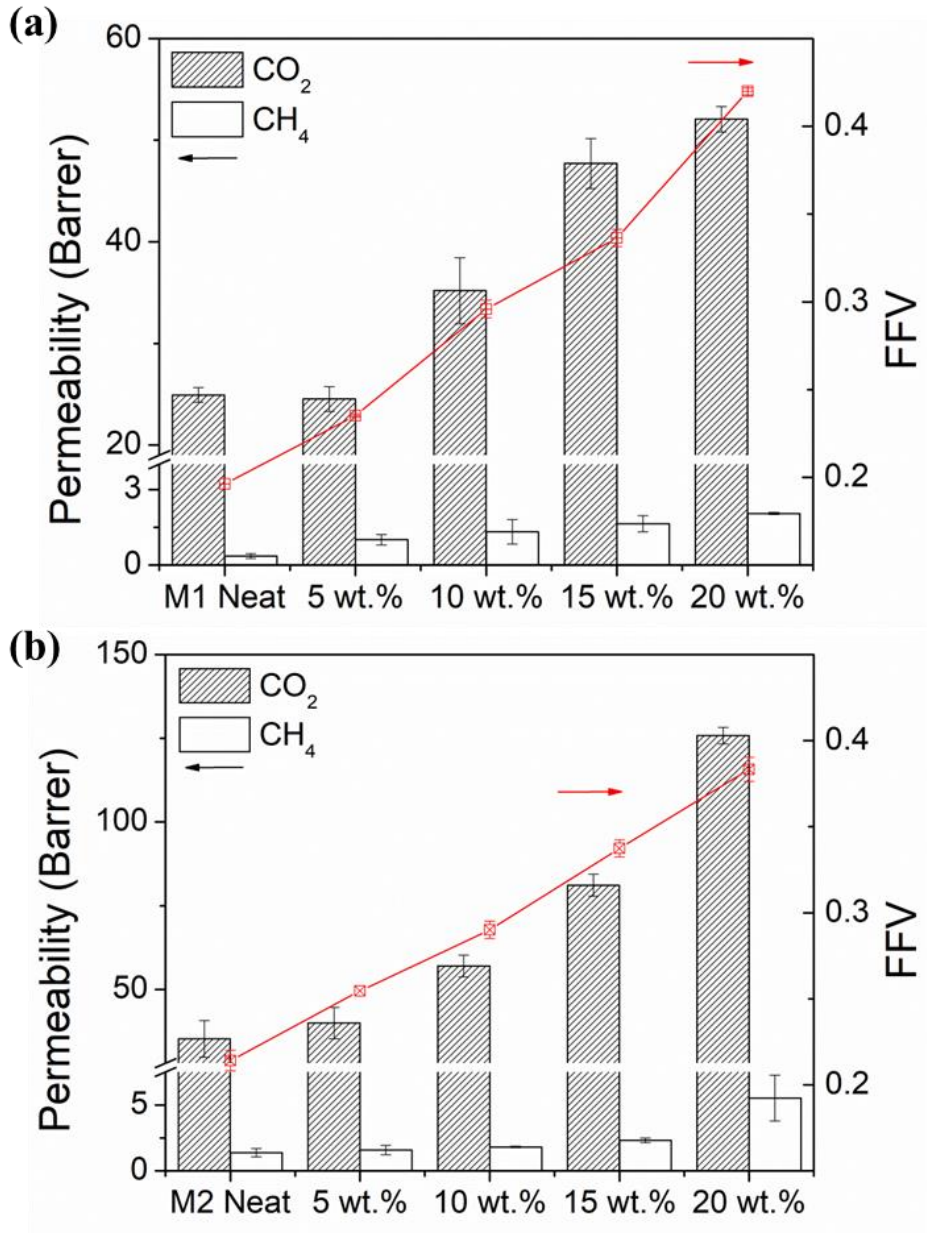

Fig. 3-19: CO_2 and CH_4 permeabilities from CO_2/CH_4 mixture measurement and FFV values for 6FDA-bisP and its MMMs (a) protocol M1 and (b) protocol M2, calculated from normalized solid density measured at 20 ºC with pressurized He cycles between 2 – 20 bar.

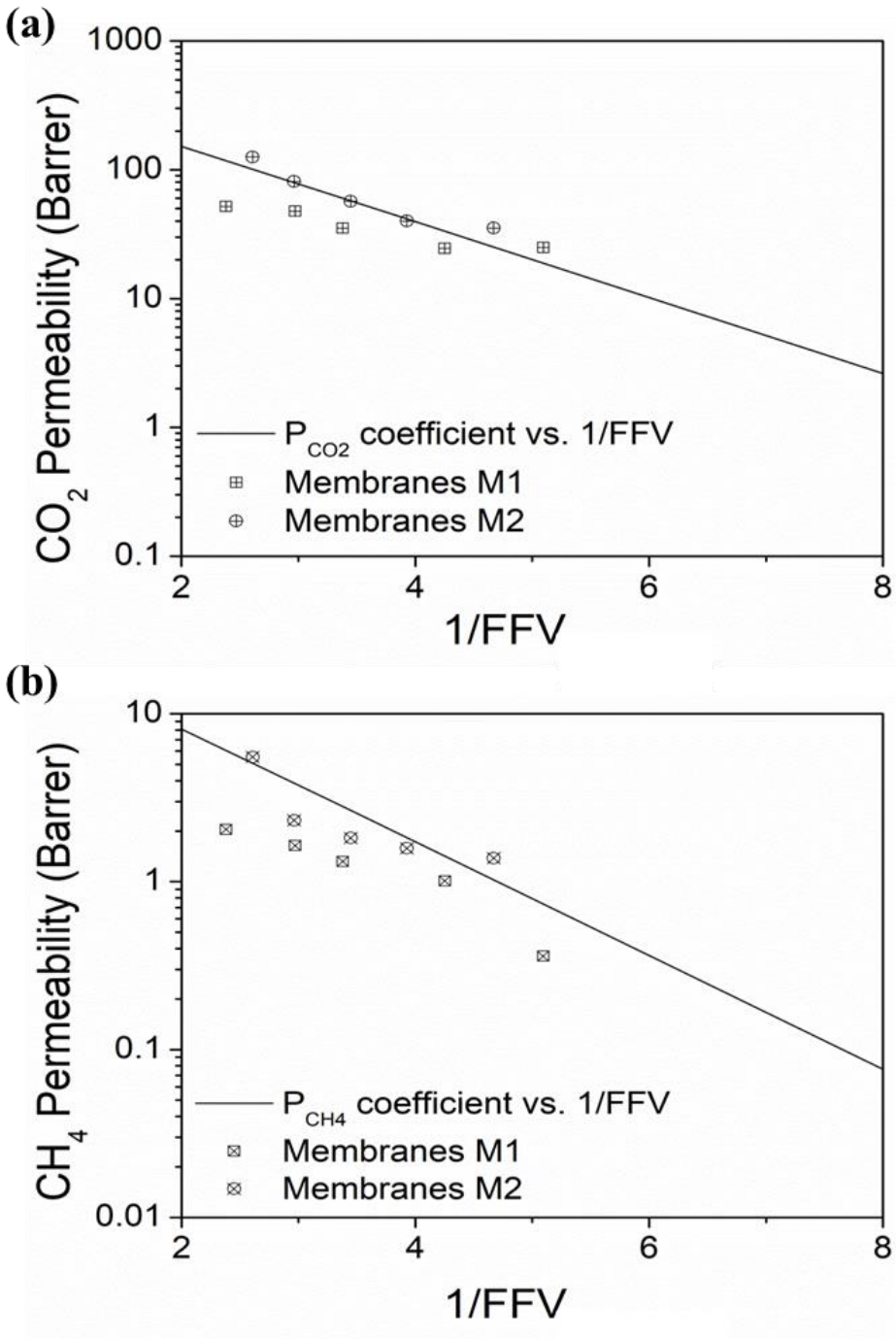

Fig. 3-20: (a) CO_2 and (b) CH_4 permeability against 1/FFV, in comparison with permeability coefficient correlations to 1/FFV for glassy polymers, presented by Park and Paul [218]

3.5.4.2. Separation performance comparisons with upper bounds

Fig. 3-21(a) and 3-21(b) show performances of the pristine 6FDA-bisP membranes (marked by black boxes) and its MMMs, obtained from both protocols, when measured with an equimolar of CO_2 and CH_4 feed mixture at 5 bar and 25 °C against the Robeson upper bounds [20,21].

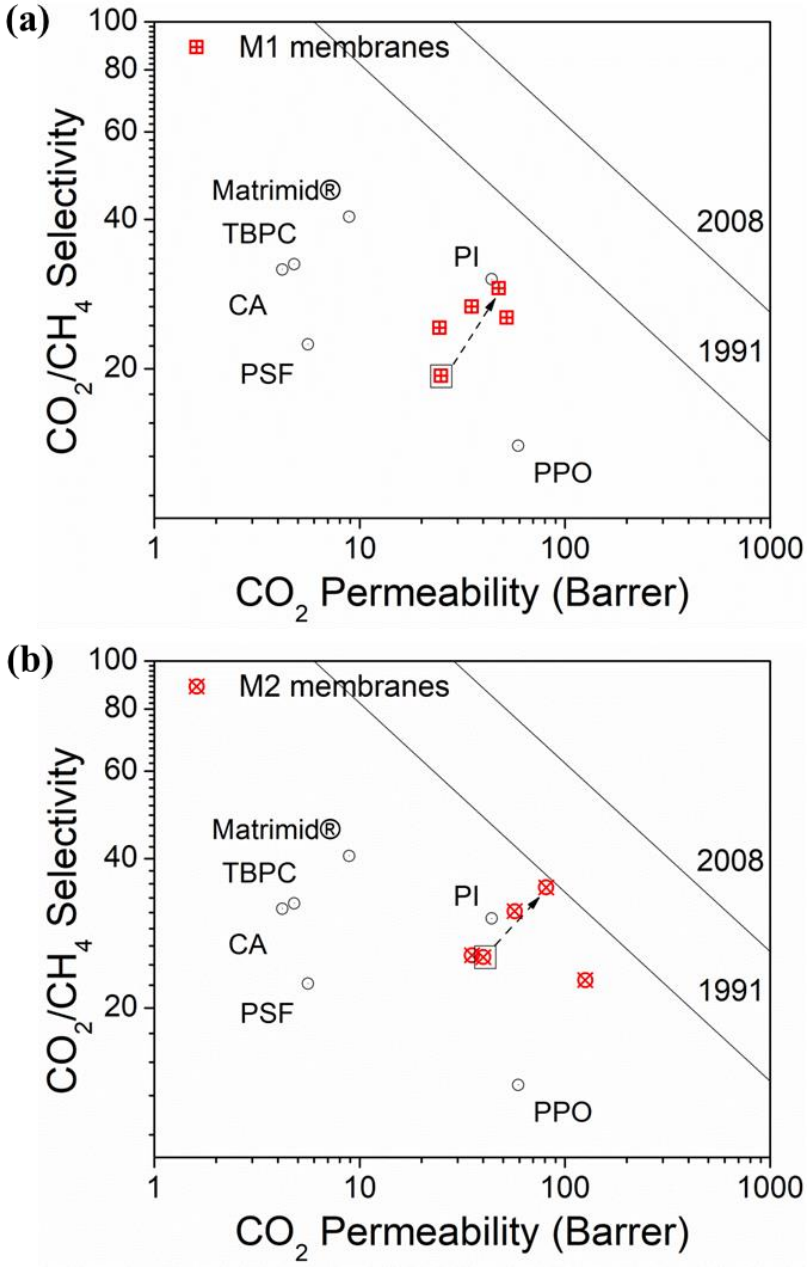

Fig. 3-21: The comparison of 6FDA-bisP and its (a) M1 and (b) M2 MMMs with 1991 [20] and 2008 [21] Robeson's plot. Unfilled circles are industrially relevant polymers, as highlighted in a review by Sanders et al. [41].

Indicated by the unfilled circles are industrially relevant polymers; tetrabromo polycarbonate (TBPC), cellulose acetate (CA), polysulfone (PSF), Matrimid®, and poly(2,6-dimethyl-1,4-phenylene oxide) (PPO), polyimide (PI), as highlighted in a review by Sanders *et al.* [41]. The neat 6FDA-bisP membrane demonstrates a higher CO_2 permeability compared to several commercial polymer membranes (Matrimid®, TBPC, CA and PSF) and only higher than PSF and PPO in term of CO_2/CH_4 selectivity. The performances nevertheless are improved by ZIF-8 additions, achieving an optimum loading of 15 wt.%.

Protocol M2 membranes prove to have superior performances, owing to the positive impact of its fabrication method on the polymer chain packing and free volume. To demonstrate the efficiency of the optimized MMM in gas separation we subjected two duplicate membranes with different CO_2 content (25% and 50%) in the binary feed mixture and varied its pressure between 2 – 8 bar, at a constant temperature. The results are presented in Fig. 3-22(a-d). As can be observed, a higher CO_2 partial pressure gives higher CO_2 permeability and evidently the continuous CO_2 permeability reduction with increasing pressure suggests the competitive sorption effect [219,220]. The trend is accordingly to the dual-mode sorption model [54]. The increase in CO_2 solubility and its transport through the membrane matrix inversely decreases CH_4 solubility and its ability to permeate, also resulting in a slight increase of selectivity over pressure. The different stabilization curves between at low and higher pressures can be explained by the different permeating gas saturation modes. At low pressure, the membranes usually achieve its saturation by gas diffusion and upon changing the pressure; an upward stabilization curve shows that the gas saturation is governed by its solubility in the membrane matrix. High CO_2-partial pressure, on the other hand, can plasticize a glassy polymer [221] and leads to an increase of diffusion of the lower permeable component, thus reducing the gas separation performance. We observe no CO_2-induced plasticization in both samples when tested up to 8 bar. Furthermore, at the highest pressure and high CO_2-partial pressure, M2 15 wt.% S1 sample demonstrated high selectivity stability for the test duration (Fig. 3-23). These results indicate that the new 6FDA-bisP, with an appropriate fabrication method and inorganic filler addition to forming mixed matrix membrane, has a good potential for CO_2/CH_4 gas separation applications.

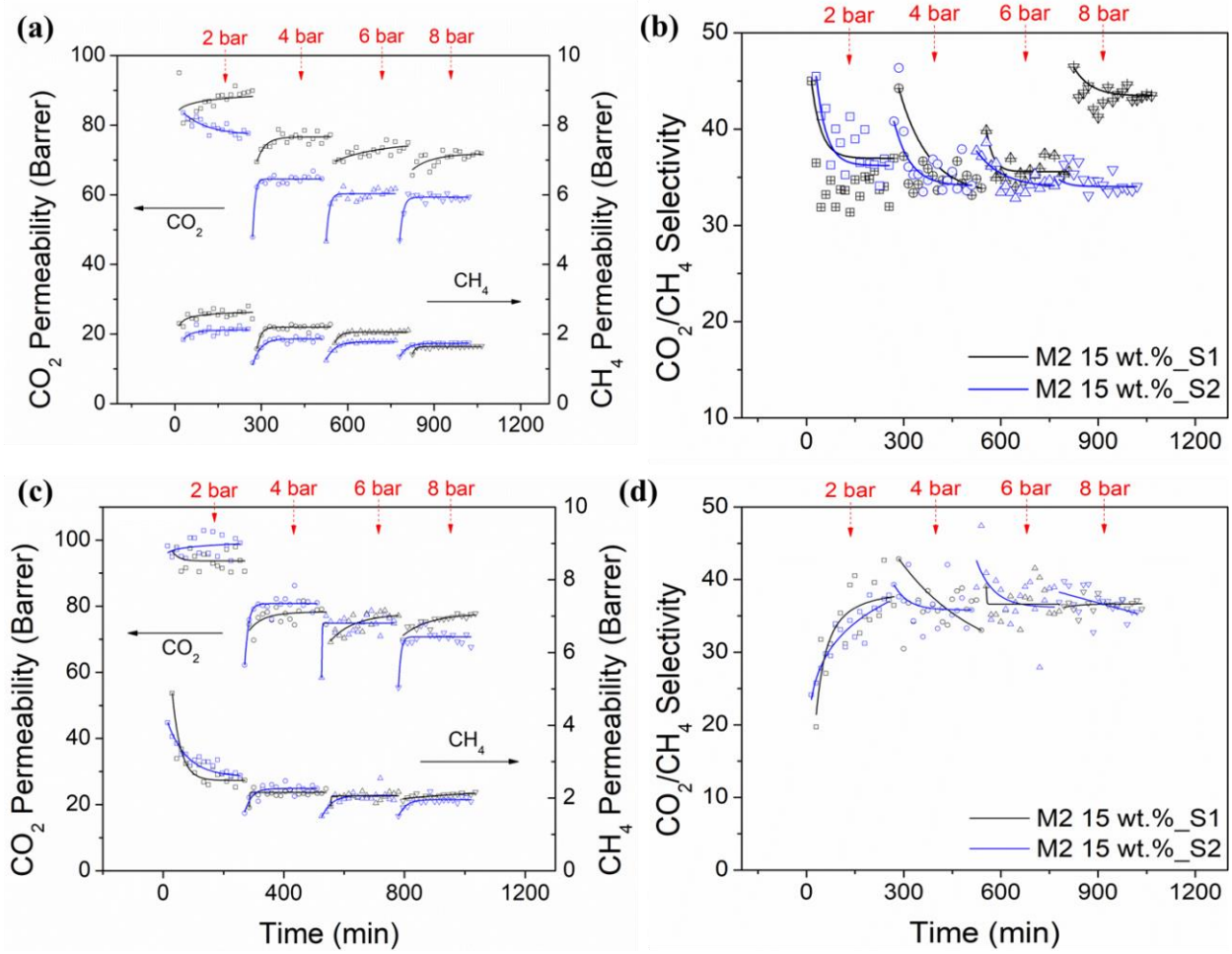

Fig. 3-22: Gas permeability and CO_2/CH_4 selectivity performance of two M2 15 wt.% samples, S1 and S2 when tested with (a-b) 25:75 and (c-d) 50:50 CO_2:CH_4 feed mixture at 2 – 8 bar, at a constant temperature of 25 °C.

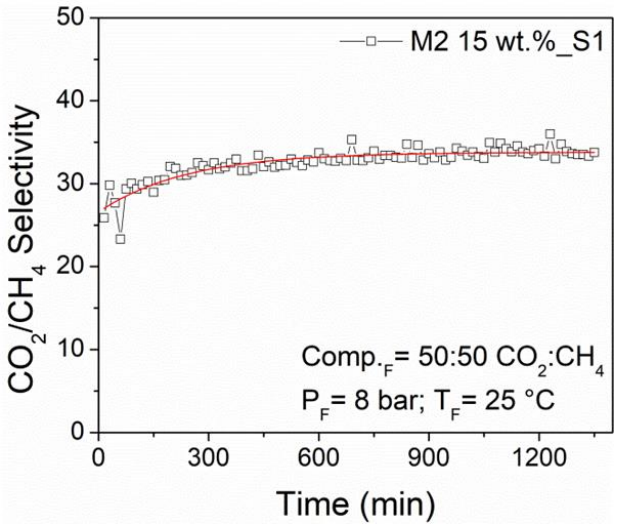

Fig. 3-23: The CO_2/CH_4 selectivity performance of M2 15 wt.% sample S1, at 8 bar when tested with an equimolar CO_2:CH_4 feed mixture at 25 °C, for more than 20 hours.

3.6. CHAPTER CONCLUSION

We report the successful synthesis of a new 6FDA-bisP polyimide, intended for natural gas separation, with a high free volume (FFV = 0.196 – 0.214) from two different fabrication protocols. Protocol M2 proves to be a more suitable fabrication method for the 6FDA-polyimide, and the membrane demonstrates CO_2/CH_4 gas separation performance of P_{CO2} = 35.3 Barrer and $\alpha_{CO2/CH4}$ = 25.6. The performances are further improved with the addition of ZIF-8 nanocrystals (particle size range of 70 – 100 nm, surface area of 1341 $m^2 \cdot g^{-1}$). An optimum loading is identified at 15 wt.% of ZIF-8, giving M2 MMM the P_{CO2} = 81.2 Barrer and $\alpha_{CO2/CH4}$ = 35 which correspond to the improvement of 130% and 37% for CO_2 permeability and CO_2/CH_4 selectivity, respectively. ZIF-8 NPs incorporation not only increases the CO_2 solubility and CO_2/CH_4 diffusion selectivity of the MMM but also contributes to the increase of polymer free volume. Referring to this study, we suggest the following scopes to be investigated; (1) gas separation performance at high pressure and high temperature, (2) in the presence of higher hydrocarbons (C_3 – C_5), and (3) the incorporation of the other inorganic fillers into the new 6FDA-bisP for gas separation applications.

CHAPTER 4: ENHANCED SEPARATION OF 6FDA-BASED CO-POLYIMIDES MIXED MATRIX MEMBRANES EMBEDDED WITH UiO-66 NANOPARTICLES

4.1. CHAPTER OVERVIEW

Metal-organic frameworks (MOFs) incorporation into mixed matrix membranes (MMMs) is gaining more attention due to the combined advantages of high separation performance and easy processability. The use of a relatively new zirconium-based MOF, UiO-66 (University of Oslo) into MMMs has increased very recently; to improve polymeric membrane's CO_2 permeability due to its CO_2-philic nature and large window apertures (ca. 6 Å) to its accessible permanent pores (ca. 8 Å and ca. 11 Å). In this chapter, we further investigate the potential of the new 6FDA-bisP in form of MMM, as well as two other 6FDA-based co-polyimides, namely 6FDA-ODA and 6FDA-DAM. The study includes the synthesis of the nano-sized UiO-66, synthesis of the co-polyimides, membrane fabrication and CO_2/CH_4 binary mixture separation performance. The effects of incorporation of higher particle size UiO-66 on membrane morphology and separation performance are also discussed.

4.2. CHAPTER CONTRIBUTIONS

In this chapter, CO_2-philic MOF UiO-66 (Zr-BDC) nanoparticles (NPs) were synthesized with high surface area and ca. 50 nm particle size (and also for comparison with 100 and 200 nm sizes). They were incorporated into three 6FDA-based co-polyimides (namely 6FDA-bisP, 6FDA-ODA, and 6FDA-DAM), forming MMMs with loadings in the 4 – 23 wt.% range (see Fig. 4-1). The NPs and MMMs were characterized accordingly. CO_2 and CH_4 isotherms on the NPs were measured by a static volumetric method at the pressure up to 10 bar. Fractional free volume (FFV) was calculated using solid density, measured by He pycnometer. Gas separation performance was evaluated using a feed composition of 50%:50% CO_2:CH_4 binary mixture at 35 °C and a pressure difference of 2 bar.

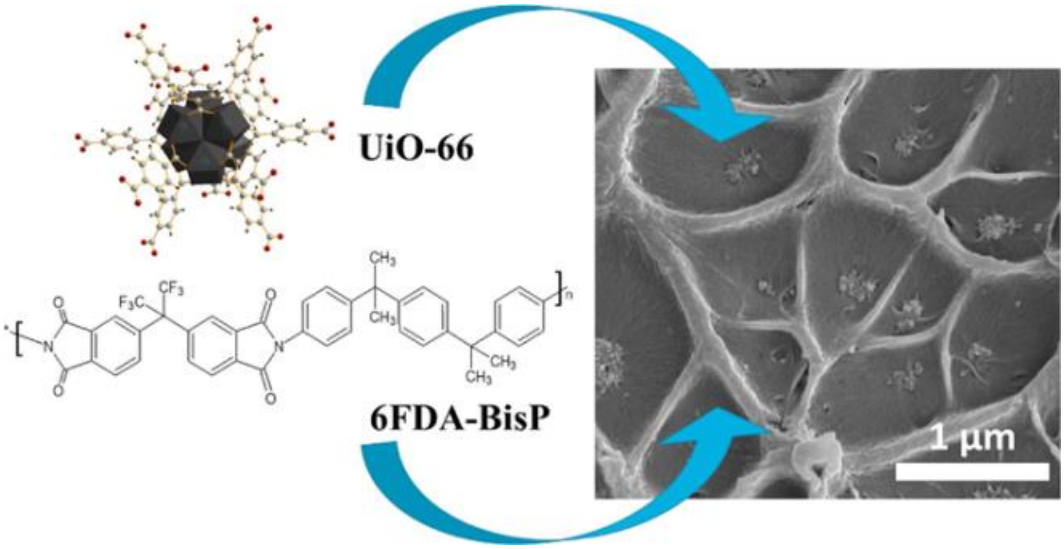

Fig. 4-1: Illustration of Zr-MOF, UiO-66 incorporation into 6FDA-based co-polyimide into a mixed matrix membrane.

4.3. INTRODUCTION

The number of investigations on metal-organic frameworks (MOFs) has grown rapidly in the past few years due to their promising applications in gas storage and separation. The potential application varies from the eminent purpose of natural gas sweetening and CO_2 post-combustion capture to the in-house air purification. MOFs can be classified by their three-dimensional crystalline frameworks with permanent porosity, formed with metal based clusters linked by organic ligands [26]. The infinite possibilities of metal and linker selections in the synthesis of MOFs give researchers a variety of coordination geometry choices, i.e. tetrahedral, pyramidal or bi-pyramidal, trigonal or octahedron [222]. This design flexibility

allows the MOFs to be attuned to their intended purposes. Additionally, their inherent properties are remarkable advantages, such as high CO_2 uptakes (e.g. HKUST-1 of 7.32 [22] and 10.71 mmol·g^{-1} [23], MIL-53 of 10.02 mmol·g^{-1} [23], MIL-100 of 9.98 mmol·g^{-1} [24], MIL-101 of 7.20 mmol·g^{-1} [25]), open porous framework structures with large accessible pore volumes, tuneable pore affinity and most importantly their relatively high chemical and thermal stabilities. Several reviews on MOFs for CO_2 separation [10,27–29] have been made available, and several others [26,222,223] comprehensively discussed on the MOF synthesis. The incorporation of these MOFs dispersed into the polymer continuous-phase as mixed matrix membranes (MMMs) has been reported using both low flux (e.g. PSF [30], PVAc [31] and PBI [32]) and high flux (e.g. rubbery PDMS [33] and glassy 6FDA-DAM [34,35]) polymers.

Scientific attention towards the relatively new class of highly crystalline zirconium-based MOFs, especially UiO-66 (UiO: University of Oslo) grows rapidly, as discussed in Section 2.2.4. The UiO-66 also posses low heat adsorption with the increase of CO_2 and CH_4 loading, due to its bulky and non-polar aromatic ring which sterically hinders the highly adsorptive metal cluster to adsorp the heat [43,135]. This is another added-value feature which is very desirable for thermal stability and lower cost regeneration.

Khdhayyer et al. [163] have recently published their findings regarding the incorporation of UiO-66 into the highly permeable polymer of intrinsic microporosity (PIM-1). The CO_2 permeability was increased to 7610 Barrer, obtaining a 60% improvement with 23 wt.% of UiO-66 loading. The CO_2/CH_4 selectivity, however, decreased with loading more than 9 wt.%. Castarlenas et al. [30] reported H_2/CH_4 and CO_2/CH_4 separation with UiO-66 MMMs, where the H_2/CH_4 selectivity improved by 6.5% in polysulfone Udel® 3500-P and 7.7% in polyimide Matrimid® with 32 wt.% loading. Remarkable H_2 permeability improvements of 475% and 148% were recorded for the stated MMMs, respectively. They also reported a 3-fold CO_2 permeability enhancement in the CO_2/CH_4 mixed gas separation, while the selectivity increased by 21% and 31%, respectively for Udel® 3500-P (32 wt.% UiO-66) and Matrimid® (16 wt.% UiO-66). Nik et al. [67] optimized 6FDA-ODA gas separation performance by incorporating 25 wt.% of the MOF. They improved the CO_2 permeability by 3.5 folds while maintaining the CO_2/CH_4 selectivity. Anjum et al. [134] also obtained an enhancement in membrane CO_2/CH_4 separation performance when embedding 30 wt.% UiO-66 in polyimide Matrimid®. Shen et al. [224] utilized polyether block amide (PEBAX MH 1657) for their CO_2/N_2 binary gas MMM and achieved the best selectivity with 7.5 wt.% UiO-66 loading. The selectivity and CO_2 permeability were improved by 31% and

73%, respectively. Higher loading addition, unfortunately, decreased the CO_2/N_2 selectivity, even to a lower performance than that of the bare polymer. Several publications have been made with regards to UiO-66 MMMs for different applications, such as pervaporation [139], nanofiltration [225] and reverse osmosis [164].

Our aim was to enhance CO_2/CH_4 gas separation of low (6FDA-bisP; 6FDA-ODA) and high fluxes (6FDA-DAM) polyimides, by making MMMs with different loadings of MOF UiO-66 nanoparticles. The nanoparticles, 50, 100 and 200 nm in size, were incorporated into three types of 6FDA based copolyimides with different aromatic diamine moieties, namely 6FDA-BisP, 6FDA-ODA and 6FDA-DAM. The chemical structures of the glassy polyimides are presented in Fig. 4-2.

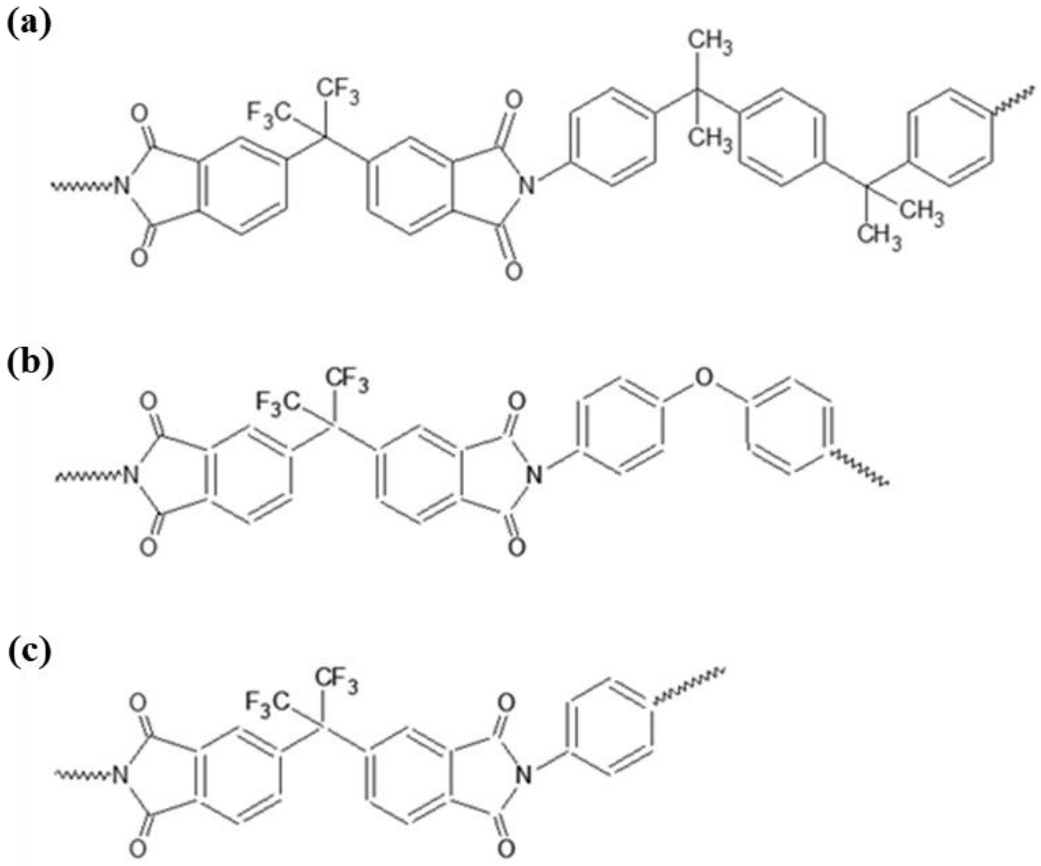

Fig. 4-2: Chemical structures of 6FDA co-polyimides presented are (b) 6FDA-BisP, (c) 6FDA-ODA and (d) 6FDA-DAM.

4.4. EXPERIMENTAL

4.4.1. UiO-66 synthesis

The synthesis of the UiO-66 nanoparticles (ca. 50 nm in size) was conducted accordingly to the literature [226], at 1 to 1 molar ratio of zirconium (IV) chloride ($ZrCl_4$, ≥99.5% trace metal basis, Sigma-Aldrich) to benzene-1,4-dicarboxylic acid (BDC, 98%, Sigma-Aldrich) in *N*,*N*-dimethylformamide (DMF, ≥99.9%, Sigma-Aldrich) with a small addition of water. Commonly, 1.71 mmol (0.40 g) of $ZrCl_4$ was dissolved in 100 mL of DMF at room temperature by sonication, prior to the addition of equimolar BDC (0.28 g) and 6.84 mmol (0.13 mL) of distilled water. Valenzano *et al.* [137] also reported a similar strategy to control the MOF particle size, instead of using other additives such as acetic acid, hydrochloric acid and formic acid [136,167,224]. The same amount of $ZrCl_4$ and BDC were also used to prepare UiO-66 of ca. 100 nm [139] in 100 mL of DMF, with an addition of 3.0 mL of acetic acid (≥99.8, Sigma Aldrich), instead of water. Whereas for UiO-66 of ca. 200 nm, 5 mmol (1.16 g) of $ZrCl_4$ was dissolved in 150 mL of DMF, followed by the addition of 5 mmol (0.83 g) of BDC, without any additive [45]. The solution was later transferred into a stainless steel Teflon-lined autoclave for a solvothermal process in a pre-heated oven at 120 °C for 24 h. After cooling to room temperature, the colloidal suspension was centrifuged at 10,000 rpm for 15 min. The precipitated MOF was rinsed with 25 mL of fresh DMF for three times, followed by washing with the same amount of methanol three times. For each washing step, the suspension was subjected to sonication for 2 – 3 min to re-disperse the possible agglomerated nanoparticles and to allow for a solvent exchange. The MOF was activated by thermal treatment in a muffled furnace at 300 °C for 3 h, with heating rates of 15 °C·min^{-1}.

4.4.2. 6FDA-bisP and 6FDA-ODA syntheses

We followed a classic two-step polymerization method by condensation, where one-to-one stoichiometry amount of dianhydride and diamine monomers were reacted in a polar aprotic solvent under N_2 atmosphere to produce poly(amic) acid (PAA) solution. A PAA solution of 10 wt.% polymer concentration was made by first dissolving the diamine, followed by addition of the dianhydride. The obtained PAA was thermally annealed at 70 – 250 ºC for 6FDA-BisP and 70 – 300 °C for 6FDA-ODA. The first annealing step was conducted at 70 ºC overnight, followed by a gradual temperature increment (50 ºC/h) before

maintaining at the highest temperature for 2 hours prior to cooling. The synthesis of 6FDA-ODA was conducted using 9 mmol (4.0 g) of 4,4'-(hexafluoroisopropylidene) diphthalic anhydride (6FDA, 99%, Sigma-Aldrich), 9 mmol (1.8 g) of 4,4′-oxydianiline (ODA, 97%, Sigma-Aldrich) in 58 g of DMF. Additional detail procedures for the polymer synthesis can be found elsewhere [64,68].

Whereas for 6FDA-BisP, the preparation is as per Section 3.4.2 and finally, 6FDA-DAM (Mw = 418,000) was purchased from Akron Polymer Systems, Inc. Both polymers were dried overnight at 100 ºC before use.

4.4.3. Membrane fabrication

Pure polymer membranes and MMMs were both fabricated by dissolving the corresponding amount of polyimide in chloroform, making a dope solution of 10 wt.%. For the MMMs, a pre-weighed amount of the UiO-66 nanoparticles was first re-dispersed in the chloroform under sonication for 2 h. To create a better filler-polymer interaction and thus produce an MMM with an optimal filler dispersion and lower agglomeration [210,227], a 10 – 15% of the total amount of polyimide was added under a rigorous magnetic-stirrer mixing for priming step. The remaining polyimide was added after 4 – 5 h of the priming step and the particle loading was calculated from Eq. 3.1.

The final solution was poured into a casting petri dish on a leveled surface to produce flat sheet membranes. The dense membranes were made under a controlled solvent evaporation rate overnight at room temperature, followed by a heat treatment at 180 ºC for 24 h to remove the remaining trapped solvent.

4.4.4. Characterizations

Scanning electron microscope (SEM), JEOL JSM 6400 operating at 20 kV was utilized to characterize the morphology of the UiO-66 crystals and the membranes. The MMMs cross-section was prepared by a freeze-fracturing method in liquid N_2. For an easier freeze-fracturing step, the membranes were first soaked in aqueous ethanol prior to immersion in the liquid N_2. UiO-66 nanoparticles were also imaged by transmission electron microscopy (TEM) using a FEI Tecnai T20 operated at 200 kV. The MOF crystals were first re-dispersed in ethanol and sonicated for a few minutes, and a couple of drops of the suspended particle solution were placed onto a holey carbon grid for the measurement.

N_2 sorption isotherms were determined using a Micromeritics Tristar 3000 porosity analyzer at -196 ºC. The specific surface area was calculated using the BET method

(P/P_0 = 0.08 – 0.16). CO_2 and CH_4 isotherms were obtained using an ASAP 2050 (Micromeritics), assessing Temkin and Freundlich adsorption in the 100 – 1000 kPa range, at 25 ºC. The samples were degassed for both methods at 100 ºC for 8 h prior to testing. X-ray diffraction (XRD) patterns of the nanoparticles and membranes were obtained using a PANanalytical Empyrean multipurpose diffractometer (40 kV, 20 mA) with a Cu-Kα (λ = 0.1542 nm) anode from 2θ of 2.5° to 40° with a 0.03º step·s^{-1}.

Thermogravimetric analysis (TGA) was conducted using a Mettler Toledo TGA/SDTA 851^e in the air flow of 40 mL(STP)·min^{-1} up to 750 ºC at a ramping of 10 ºC·min^{-1}. Differential scanning calorimetry (DSC) was conducted on a ca. 10 mg sample using a Mettler Toledo DSC822e system, measured in two cycles up to 450 ºC at the temperature ramping of 20 ºC·min^{-1}. ATR-FTIR was performed using a Bruker Vertex 70 spectrometer, equipped with a DTGS detector. The measurements were conducted from 600 to 4000 cm^{-1} at a resolution of 4 cm^{-1}. Both XRD and ATR-FTIR were also carried out on several MMMs to determine the MOF-polyimide chemical structure interactions.

The fractional free volume of the membranes was calculated from Eq. 3.4 and 3.5, and determined as explain in Section 3.4.5.

4.4.5. Gas separation performance

The membranes were tested with a 50:50 (v:v) CO_2 and CH_4 binary mixture, at a pressure difference of 2 bar and at 35 ºC. A 50 cm^3 (STP)·min^{-1} feed entered the permeation module with He as sweep gas (at 0.5 cm^3 (STP)·min^{-1} for 6FDA-BisP and 6FDA-ODA membranes, and at 1 cm^3 (STP)·min^{-1} for 6FDA-DAM membranes). The membranes were sealed with a Viton® O-ring in a stainless steel permeation module equipped with a microporous disk, 316LSS of 20 µm nominal pore size (Mott Corp.) as a support in the controlled temperature oven. The permeation set up was described in an earlier publication [189]. The permeate compositions were analyzed online by an Agilent 3000A micro-GC equipped with a thermal conductivity detector (TCD).

Gas permeation through a polymer is defined by the solution-diffusion theory due to the pressure difference and concentration gradient [70]. The permeability is described as the penetrated gas flux, normalized by the membrane thickness and the partial pressure drop across the membrane, and presented in Barrer (1 Barrer = 10^{-10} cm^3(STP)·cm·cm^{-2}·s^{-1}·cm·Hg^{-1}). The membrane evaluation performance was calculated as given in Section 3.4.6.

4.5. RESULTS AND DISCUSSION

4.5.1. Filler characterizations

UiO-66 nanoparticles with size ca. 50 nm and BET surface area of 951 ± 14 $m^2 \cdot g^{-1}$, close to the accessible theoretical surface of 1021 $m^2 \cdot g^{-1}$ [135], were synthesized. Fig. 4-3 (inserted) shows the XRD pattern of the UiO-66 in good agreement with the literature [137]. Fig. 4-3 corresponds to the TGA characterization, where the negligible weight loss below 100 ºC is suggested to be an initial solvent loss, while the latter drop until 300 ºC is attributed to the dehydration of the $Zr_6O_4(OH)_4$ nodes to Zr_6O_6 [167]. The second drop up to 500 ºC is related to the decomposition of organic linkers before the oxidation of the zirconium into ZrO_2 [137,167]. The formula of the framework between 300 and 500 ºC is $Zr_6O_6BDC_x$. The amount of BDC ligand, *x*, present in the MOF was estimated from the subsequent weight loss, as presented by Katz et al.[167] in their simulation and experimental work on UiO-66 and its derivatives. In fact, the MOF showed a mass loss of 42.4 % close to the 43.3% simulated mass loss corresponding to the 4-ligand UiO-66. Fig. 4-4 shows the crystal structure of UiO-66 containing 4 ligands, with colored spheres representing the tetrahedral (yellow) and octahedral (olive green) void regions in the framework.

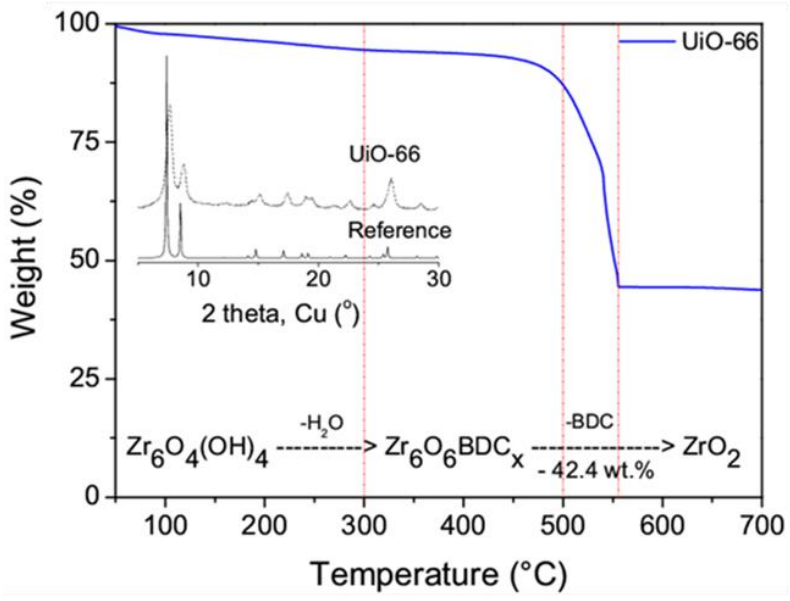

Fig. 4-3: The TGA profile of the UiO-66 nanoparticles and inserted, their XRD pattern with regards to the reference by Valenzano *et al.* [137]. Red dotted lines represented the dicussed temperatures for ease of viewing.

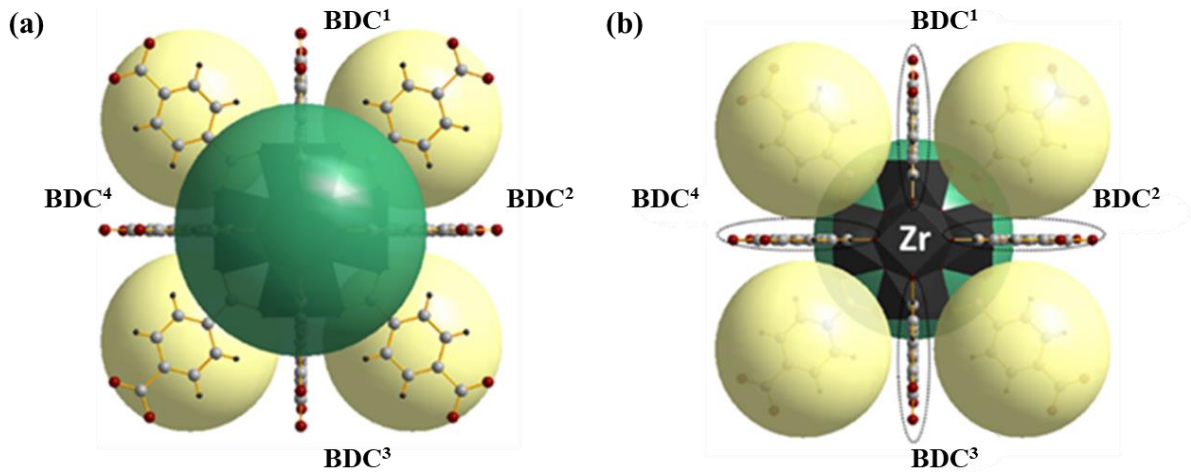

Fig. 4-4: The illustration of the 4-ligand UiO-66 crystalline structure based on a CIF on open-database CCDC [93], (Zr polyhedra, black; C, grey; O, red; and H, black), with benzene-1,4-dicarboxylic acid (BDC) as the ligand.

FTIR spectra of the pure UiO-66 also exhibited a very small O-H stretching peak at the wavelength of 3650 – 3700 cm^{-1} (Fig. 4-5), which indicated missing anionic BDC linkers, thus explaining the 0.9% lower mass loss in our UiO-66 compared to 4 ligands simulated for UiO-66 [167]. Unlike some UiO-66 synthesized following the conventional route using stronger acidic modulators, especially hydrochloric acid, the produced vacant sites were higher and sometimes resided by the stronger catalyst anion (chloride anion) to a certain extend [167]. Nevertheless, both FTIR and TGA findings complimented each other and suggested the presence of missing organic linkers in our UiO-66.

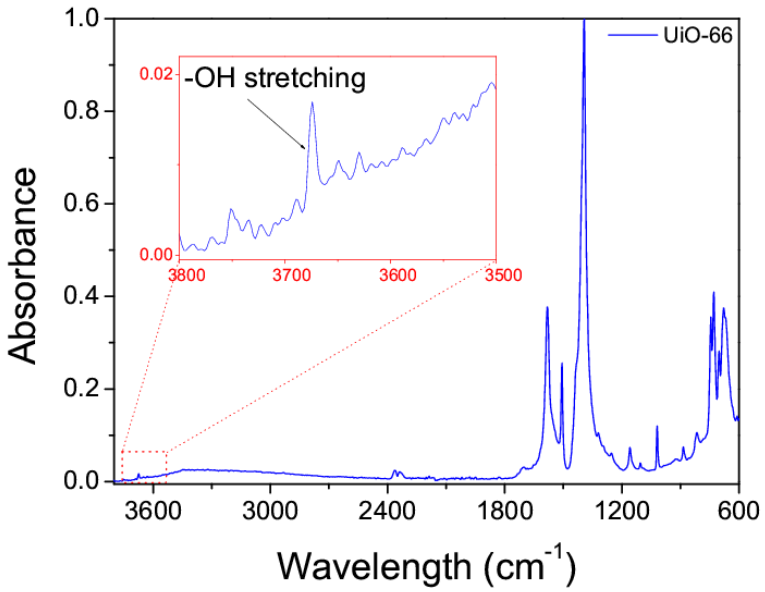

Fig. 4-5: FTIR spectra of the pure UiO-66, enlarged at the wavelength of 3800 – 3500 cm^{-1} is the free –OH stretching peak indicating the missing anionic BDC in the UiO-66 frameworks.

Fig. 4-6 displays TEM images of the UiO-66 nanoparticles, after being activated at 300 ºC and its SEM images can be referred in Fig. 4-7. The nanoparticles (ca. 50 nm) can be observed agglomerated to a certain degree, which presumably occurred during the drying process. However, individual particles are clearly visible and can be easily re-dispersed in highly polar solvents (i.e. ethanol) or low polarity solvents (i.e. chloroform).

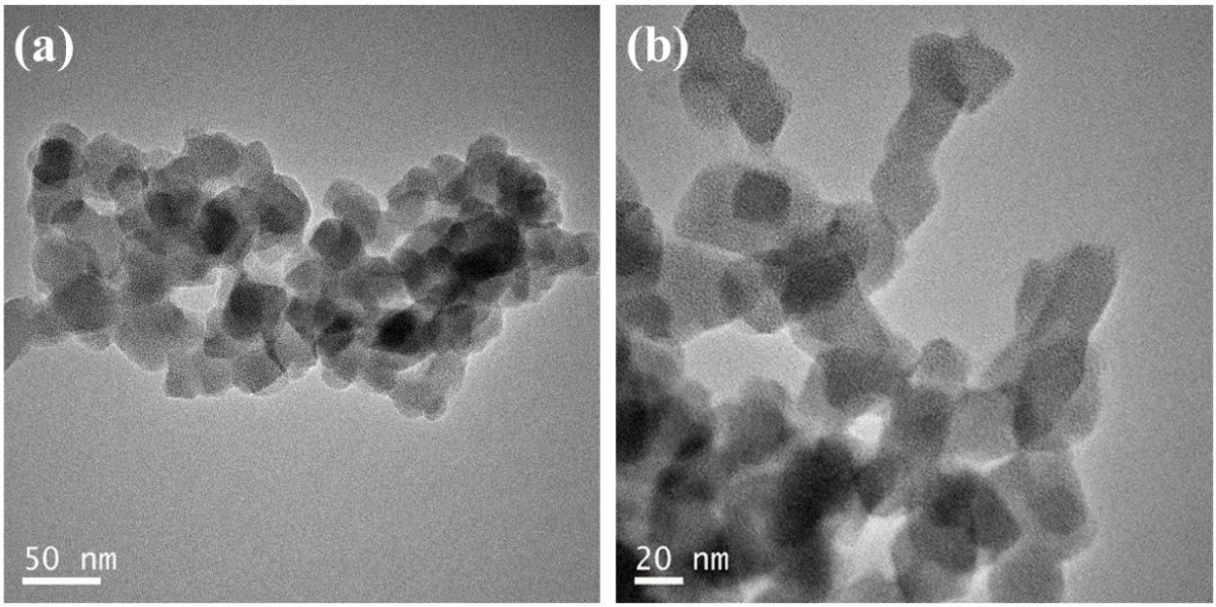

Fig. 4-6: TEM images of the as-synthesized UiO-66, with a particle size of < 50 nm.

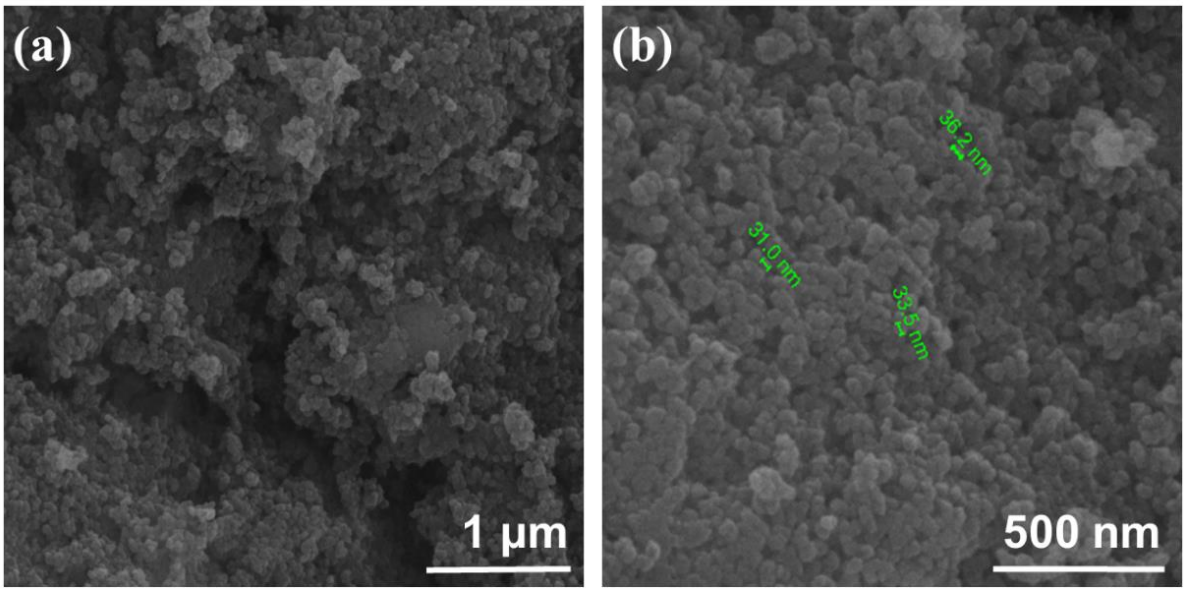

Fig. 4-7: SEM images of the as-synthesized UiO-66, with a particle size of < 50 nm.

Fig. 4-8(a) shows the N_2 adsorption – desorption obtained from the BET analysis. N_2 adsorption analysis showed a classic type I isotherm, with the N_2 adsorbed a quantity of ca. 430 $cm^3 \cdot g^{-1}$ at P/P_o = 0.9 and -196 ºC, comparable to the recently published data [167,228].

However, a hysteresis loop can be observed after P/P_o = 0.75 due to possible capillary condensation in between the small particles. Several researchers have reported a much lower N_2 adsorption between 250 and 350 cm^3 (STP)·g^{-1} [44,45,136]. The N_2 adsorption behavior in the MOFs is a localized adsorption, due to N_2 quadrupole moment interaction with the MOF monolayer polar sites; thus a lower N_2 uptake value indicates a lower cation distribution in the MOF.

The CO_2 and CH_4 adsorption capacities of the MOF display values of 1.13 and 0.28 mmol·g^{-1} (at 1 bar, 25 ºC), respectively (Fig. 4-8(b)). Yang *et al.* [135] showed that the UiO-66 internal tetrahedral and octahedral free volumes adsorb CO_2 and CH_4 preferentially where the CO_2 had higher adsorption in the tetrahedral cages due to the CO_2 higher affinity with the framework wall. The interaction between the pore affinity and the adsorbates greatly determines the capacity of the adsorption. Table 4-1 indicated the UiO-66 possess lower CO_2 and CH_4 adsorption capacities than those reported under the same conditions [43–45].The differences are believed to be contributed by the use of various activation methods, where lower activation temperature and chemical activation produce higher gas adsorptive UiO-66. Wu *et al.* [168] described that each hydroxylated UiO-66 framework consists of eight O-coordinated Zr ion (six of that cluster together forming the $Zr_6O_4(OH)_4$ metal cluster) and losses two H_2O molecules upon full activation at high temperature (~250 °C), reducing the Zr-O coordination to seven (de-hydroxylated). They demonstrated that the hydroxylated UiO-66 adsorbed 56% higher CO_2 comparing to the de-hydroxylated UiO-66 (CO_2 = 1.60 mmol·g^{-1}). The use of various catalyst modulator, i.e., acetic acid [43,168,229,230], benzoic acid [228,230], hydrochloric acid [231] or no modulator [44,45,67] also differed the gas adsorption properties, as the amount of missing organic linkers is influenced by the presence of the stronger anions [231]. Additionally, without modulation, Schaate *et al.* [230] presented a disordered UiO-66 phase with lower surface area comparing to those synthesized with the addition of acetic acid.

Table 4-1: The reported CO_2 and CH_4 adsorption capacities and BET surface area of UiO-66, compared to this study.

UiO-66	BET surface area ($m^2 \cdot g^{-1}$)	Adsorption capacities ($mmol \cdot g^{-1}$)			MOFs activation
		CO_2	CH_4	Measurement condition	
This work[1]	951	1.13	0.28	1 bar / 25 °C	Thermally at 300 °C / 3 h
[168][2]	1090	1.60	0.45*	1 bar / 30 °C	Thermally at 250 °C / 24 h
[44][3]	1057	1.96	0.50	1 bar / 25 °C	Thermally at 100 °C / vacuum
[45][3]	838	2.27	-	1 bar / 25 °C	Thermally at 120 °C overnight
[67][3]	857	1.57	0.40	1 bar / 35 °C	Chemically in MeOH / 4 days. Drying at 150 °C / 12 h
[43][2]	1105	1.79	0.49	1 bar / 25 °C	Chemically in MeOH / 1 days. Drying at 105 °C / vacuum

*Value is taken from their corresponding isotherms

MOF synthesis conducted with [1]water, [2]acetic acid or [3]no reaction modulator

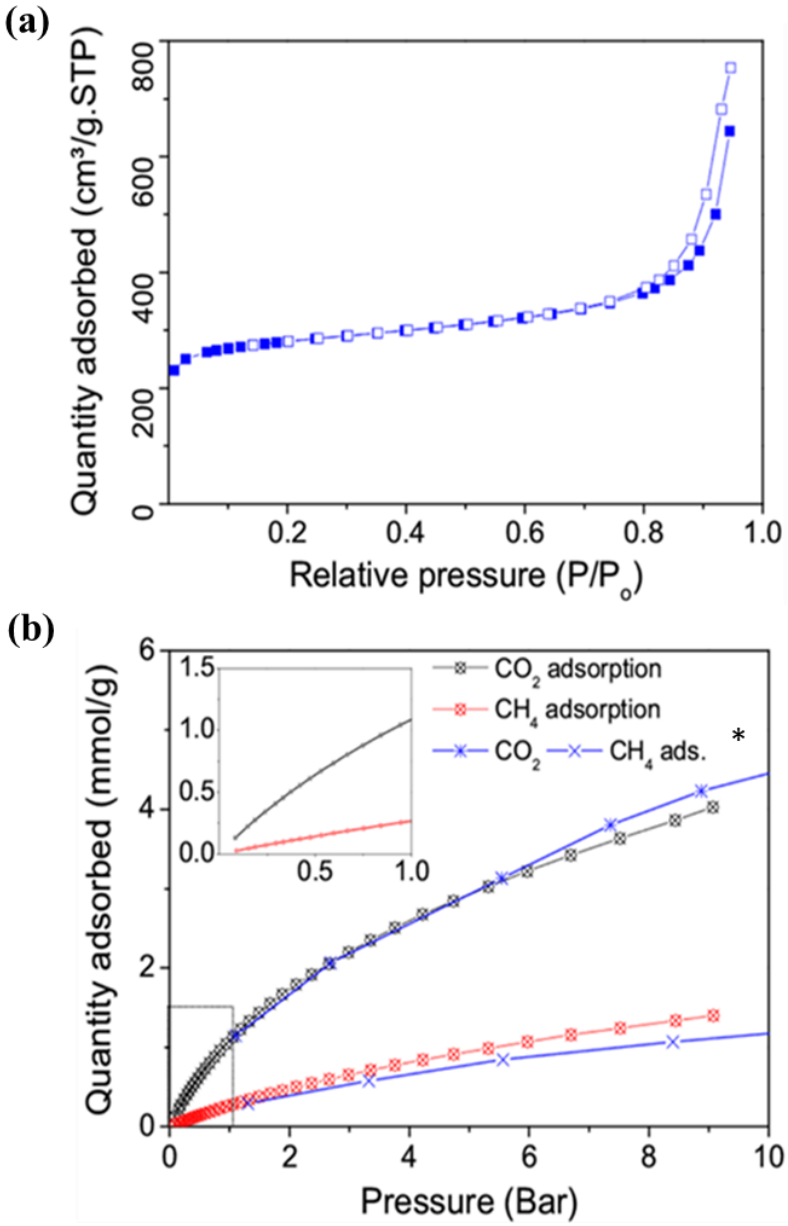

Fig. 4-8: (a) N_2 adsorption (filled) and desorption (empty symbols) isotherms measured at -196 ºC (b) CO_2 and CH_4 isotherms, measured at 1–10 bar and 25 ºC, compared to the literature (*) [166]. Inserted is CO_2 and CH_4 isotherms at low pressure (0.1–1.0 bar).

4.5.2. Membrane characterizations

Thermal stabilities of UiO-66 and the fabricated MMMs were characterized by TGA (Fig. 4-9).

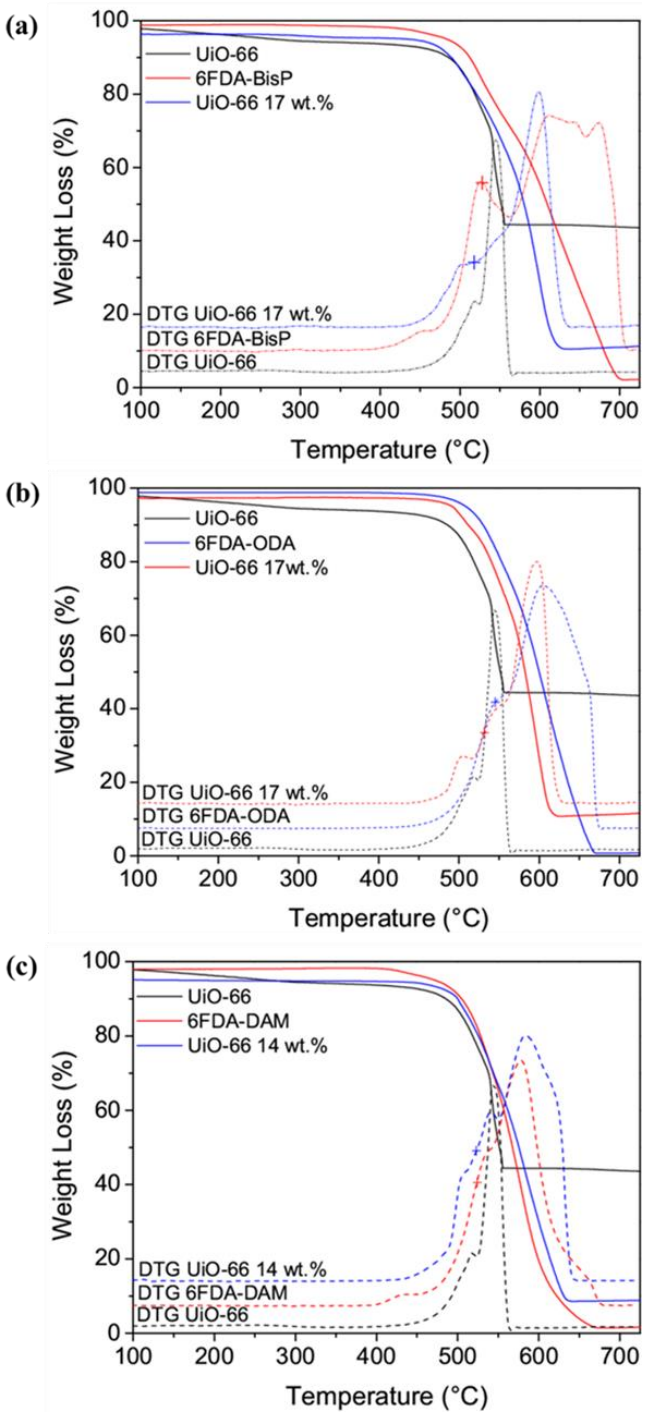

Fig. 4-9:The TGA curves and their respective first derivative for UiO-66 with (a) 6FDA-BisP, (b) 6FDA-ODA and (c) 6FDA-DAM and their respective MMM. Indicated (+) are the decomposition temperatures, T_d, calculated at 15% weight loss.

The decomposition temperature (T_d) was obtained by the minimum of the first derivative drops and presented in Table 4-2. UiO-66 was stable up to 544 °C, in good agreement with reported values [138,232]. For 6FDA-BisP ($T_{d,\ pure}$ = 528 ºC), the T_d reduced gradually up to 10 ºC with 21 wt.% loading. A similar trend was observed for 6FDA-ODA ($T_{d,\ pure}$ = 545 ºC), with a reduced temperature of 13 ºC with the highest loading. However, for 6FDA-DAM ($T_{d,\ pure}$ = 523 ºC), there were no remarkable differences between all the MMMs.

Table 4-2: The T_d (decomposition temperature) and T_g (glass transition temperature) values of the neat polymer membranes and their respective MMMs.

Polymer	Particle loading (wt.%)	T_d (ºC)	T_g (ºC)
6FDA-BisP	0	528	383
	14	522	387
	21	518	397
6FDA-ODA	0	545	306
	8	540	311
	23	532	315
6FDA-DAM	0	523	396
	8	526	395
	21	524	405

Glass transition temperatures (T_g) were determined for the pure polymer membrane and the MMMs by DSC, to investigate the influence of UiO-66 addition on the polymer chain flexibility. The T_g values of all neat membranes: 6FDA-ODA, 303 ºC [67,206] and 6FDA-DAM, 396 ºC [233,234] (Table 4-2) were in great agreement with previously published results. Nevertheless, 6FDA-BisP, with a T_g of 383 ºC, was for the first time tested in this work. Concerning MMMs, the T_g increase was less substantial at lower loadings. However, more significant increments were observed at higher loadings. 6FDA-BisP showed a temperature increase of 14 ºC, whereas 9 ºC increment for both 6FDA-ODA and 6FDA-DAM, for their highest loading MMMs. The T_g increase after the inclusion of the filler is usually caused by the rigidification of the polymer chain, which limits the chain movement. This disruption is believed to be caused by the interface interaction created between the polymer and the inorganic moieties of the MOF. Similar observations were reported on 6FDA based co-polyimides with other MOFs, such as Noria-Co^{t}BU [234] and ZIF-11 [124].

Fig. 4-10 shows the XRD patterns for all MMMs, revealing that the crystalline phase of the UiO-66 was preserved in the MMMs. These patterns are consistent with the afore-mentioned UiO-66 X-ray reference [137], indicated by dotted lines are some of the most important peaks at 7.4º, 8.5º, 12.0º, corresponding to (111), (002) and (022) planes, respectively.

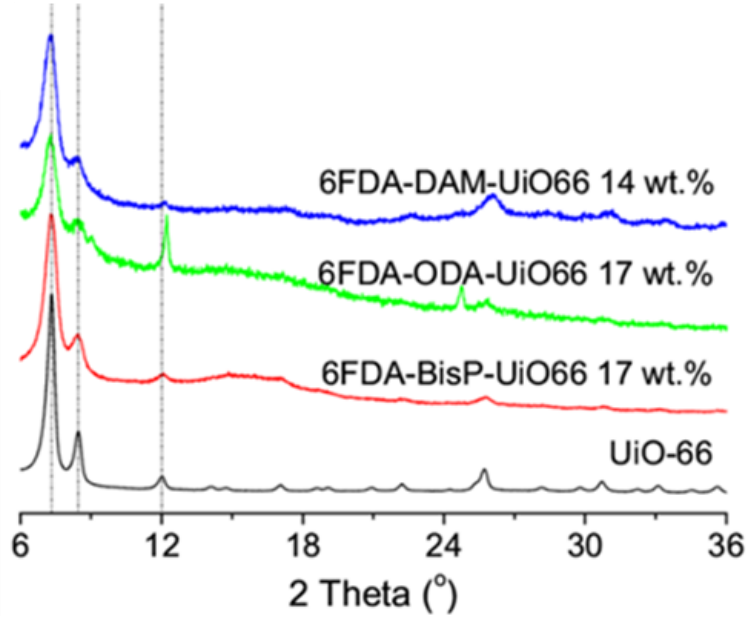

Fig. 4-10: XRD patterns of as-synthesized UiO-66 and their respective MMMs.

Additionally, we conducted FTIR analysis on the samples to determine the possible chemical interaction between the MOF and the polymer matrix. Fig. 4-11(a) – 4-11(c) show the FTIR spectra obtained. The absorbance of UiO-66 is described by the strong out-of-phase carboxylic -CO– peak at 1393 cm^{-1}, and –COO– stretching (in-of-phases) at 1570 cm^{-1}, indicating its strong reaction with the zirconium. The longitudinal and transverse mode of Zr-O_2 is presented by the marked (asterisk) triplet peaks at 730, 680 and 550 cm^{-1} [133,228]. The 550 cm^{-1} peak is not shown here. Other common absorbances are at 1018 cm^{-1} for C=C aromatic stretching and the multi-peaks between 750 and 690 cm^{-1} for the di-substituted benzene ring. The FTIR absorbance for all the membranes indicated that there was no significant shift in the key polyimide functional group signals; symmetric –C=O stretching at 1720 cm^{-1}, the imide –C-N– at 1373 cm^{-1} and also the most significant =COC= stretching at 1238 cm^{-1} in the diamine polyimide moiety of 6FDA-ODA.

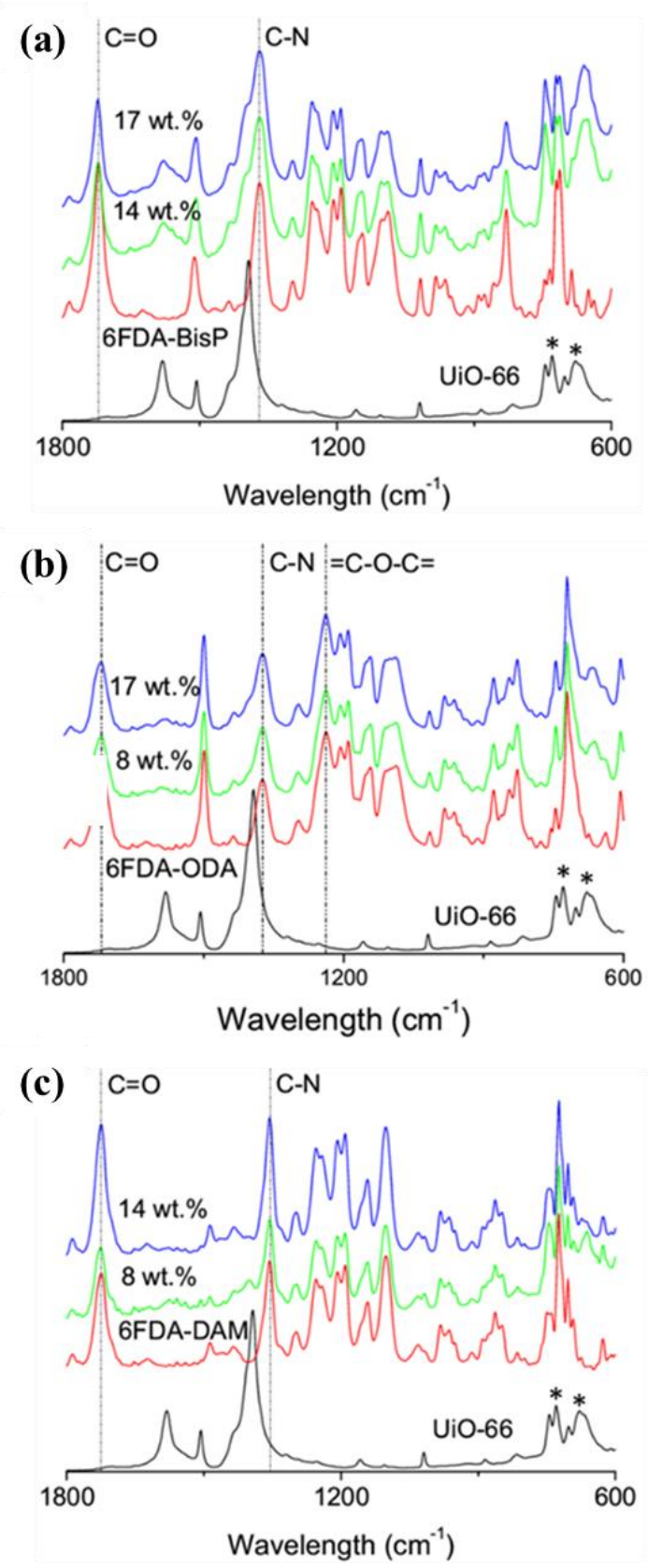

Fig. 4-11: FTIR spectra of UiO-66, 6FDA-polyimides and their respective MMMs: (a) 6FDA-BisP, (b) 6FDA-ODA, and (c) 6FDA-DAM. The asterisk marks represent the longitudinal and transverse mode of Zr-O_2.

The average thicknesses of the MMMs were about 30 – 60 μm for 6FDA-BisP and 6FDA-ODA and 80 – 110 μm for the 6FDA-DAM. Thinner 6FDA-BisP and 6FDA-ODA MMMs were prepared because of their lower gas permeabilities. Thus a thicker 6FDA-BisP or 6FDA-ODA membrane would require a longer stabilization period in the permeation test, comparing to the 6FDA-DAM. SEM images (Fig. 4-12) show a good interface interaction between the MOF and the polymeric matrix. However, the maximum size of the particle agglomerates increased with the increment in MOF loading, from ca. 0.28 μm at the lowest loading (6 wt.%) to ca. 1.3 μm at the highest loading (21 wt.%) for 6FDA-BisP. And from ca. 0.21 μm for the lowest (4 wt.%) to 0.60 μm for the highest (21 wt.%) loading 6FDA-DAM MMMs. The agglomeration, however, was more prominent in 6FDA-ODA MMMs where the agglomerate sizes ranged up from 0.5 to 1.5 μm, between the lowest (4 wt.%) and highest (23 wt.%) UiO-66 loadings. Gas permeabilities in MMMs occur in all the three present phases; continuous polymeric phase, the nanoparticles and the polymer-NPs interface. In the presence of NPs agglomeration, gas permeabilities may increase due to the formation of undesirable by-pass channels, connecting the voids between nanoparticles and may also reduce its selectivity [29,235]. The findings with regards to our MMMs are presented in the next section.

The presence of a high number of hydrogen bond donor and acceptor in both filler and polymer structures is believed to function as an interface compatibilizer by forming hydrogen bonding. In addition to that, the presence of other functional groups which are hydrogen bond acceptor and/or donor, such as $–CF_3$ (acceptor), –C=O (donor and/or acceptor), –CO– (acceptor) and –HCN– (donor and/or acceptor) in the 6FDA-polyimides, further enhanced the intermolecular hydrogen bond. The polyimide with a higher density of H-bond promoting groups in the diamine moieties (ODA > BisP > DAM) was anticipated to have a lesser particle agglomeration, as the promoting groups may increase the MOF-polymer interaction, thus reduces the MOF-MOF interaction which leads to the agglomeration. However, the behavior was not observed, and it may be attributed to a more favorable polymer-polymer H-bonding and presumably the charge-transfer complex (CTC) phenomena in the polyimides. The CTC [50] is a type of intra- and intermolecular bond, prominently occurs in aromatic polyimide membranes due to these electron acceptor/donor groups. The CTC phenomena in polyimide were exploited by many researchers in achieving higher gas selective membranes by thermal treatment, benefiting from CTC dependence on temperature [194,236].

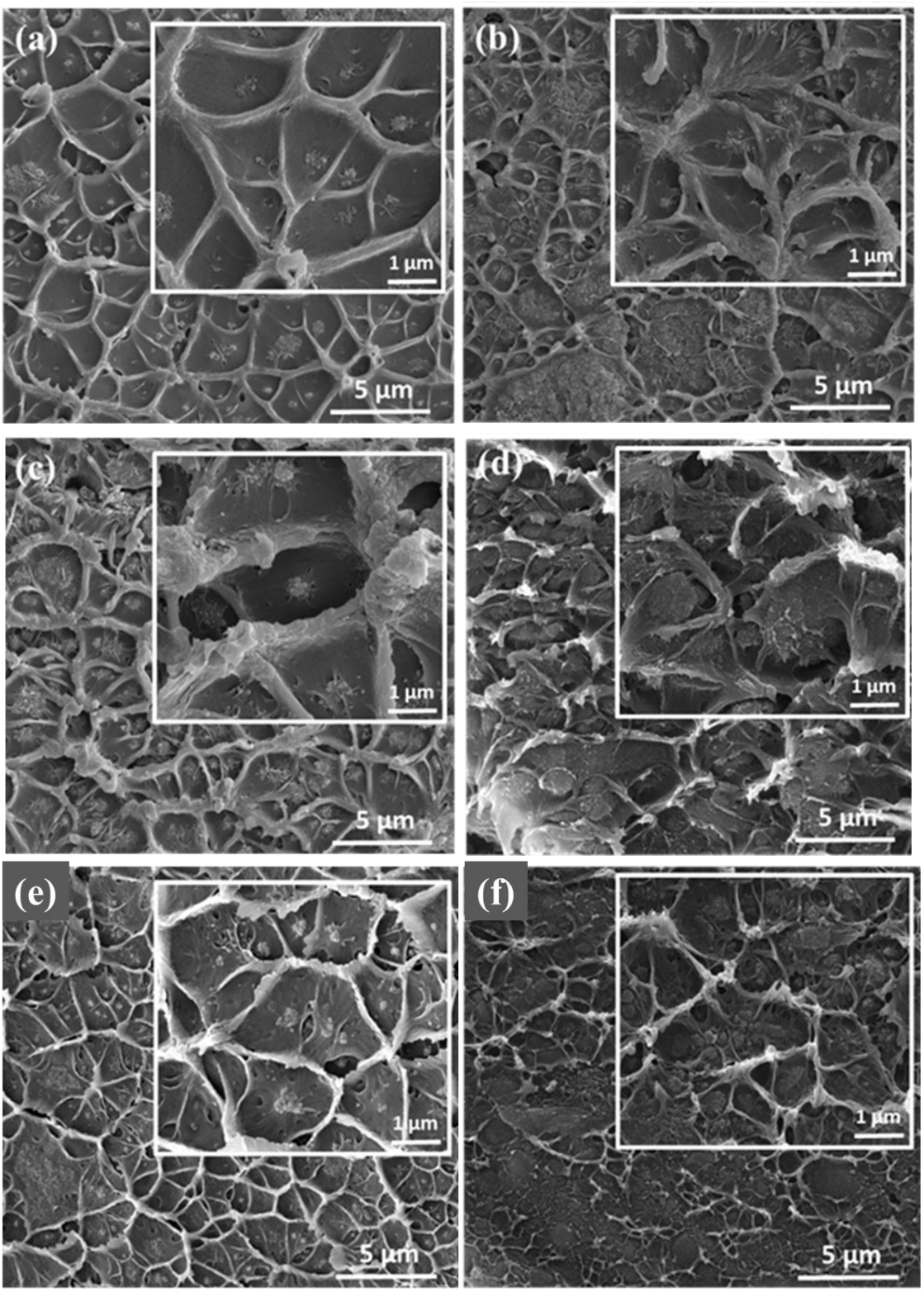

Fig. 4-12: SEM images of the cross-sections of the mixed matrix membranes containing UiO-66 at different loadings; 6FDA-BisP with (a) 6 wt.% and (b) 14 wt.%; 6FDA-ODA at (c) 4 wt.% and (d) 17 wt.%; 6FDA-DAM with (e) 4 wt.% and (f) 14 wt.%.

4.5.3. Gas transport properties

4.5.3.1. Mixed gas permeability and selectivity

Our used-as-purchased 6FDA-DAM possesses higher molecular weight (M_w = 418,000 g·mol^{-1}; FFV = 0.24; density = 1.26 g·cm^{-3}) comparing to the synthesized 6FDA-DAM previously tested (M_w = 81,000 g·mol^{-1}; FFV = 0.19; density = 1.35 g·cm^{-3}) [57]. The higher M_w 6FDA-DAM gave rise to P_{CO2} = 997 Barrer and $\alpha_{CO2/CH4}$ = 29.2, while that of the lower M_w showed P_{CO2} = 681 Barrer and $\alpha_{CO2/CH4}$ = 21.4 [57], measured with CO_2/CH_4 equimolar feed at a pressure difference of 2 bar.

Table 4-3: CO_2/CH_4 separation with pure 6FDA-polyimides with different physical properties.

Membrane	Physical properties			Drying temp. (ºC)	Pressure difference (bar)	Binary gas separation performance 50:50 (vol:vol)	
	T_g (ºC)	Density (g cm^{-1})	FFV			P_{CO2} (Barrer)	CO_2/CH_4 selectivity
6FDA-Bisp							
[this work*]	383	1.266	0.248	180	2	33.9	27.5
6FDA-ODA							
[this work]	303	1.435	0.161	180	2	25.9	20.1
[67]	294	1.455	0.169	230	10.2	14.4[a]	41.7
[206]	302	1.348	0.221	-	10	11.7	15.6
[151]	-	-	-	150	2	20.6[a]	33.1[b]
6FDA-DAM							
[this work]	396	1.259	0.238	180	2	997	29.2
[233]	395	-	-	-	6.9	817	17.6
[234]	383	-	-	200	1	426[a]	16.2[b]
[57]	325	1.35	0.19	180	2	681	21.4
[52]	372	1.334	0.190	382	2	299[a]	19.8
[237]	383	1.353	0.181	250	10	467[a]	15.9[b]

[a] Reported from single gas measurement
[b] Ideal selectivity
***First of this polymer for gas separation**

The difference in the molecular weight, even though has the lesser effect on gas permeability comparing to the free volume, evidently contributed to the higher gas separation performance. Xu *et al.* [233] investigated the influence of 6FDA-DAM molecular weight for hollow fiber gas separation and presented a similar behavior. Other observations were also

reported in different polymers such as polyimide Matrimid® [210] and polyacrylamide [238]. The differences in polymer physical properties certainly have an influence on the gas separation performance. Table 4-3 shows several studies on these polyimides, comparing their gas separation performances to those of our samples. Variation in the fabrication and treatment procedures (e.g. drying temperature) of the bare membranes also affected the gas separation performance. Nik *et al.* [67] on the other hand reported a two-fold higher CO_2/CH_4 selectivity for 6FDA-ODA ($\alpha_{CO2/CH4}$ = 41.7) to our neat membrane ($\alpha_{CO2/CH4}$ = 20.1), and this may be attributed to their higher annealing temperature, which usually produces a denser membrane with a lower gas permeability and higher separation factor [162].

For the three studied polymers, Fig. 4-13 and Table 4-4 present the gas separation performance of the bare polymer membranes and their respective UiO-66 MMMs. Gas permeability and selectivity increased accordingly to the increase of UiO-66 loading. 6FDA-BisP MMM with 17 wt.% UiO-66 (P_{CO2} = 108 Barrer; $\alpha_{CO2/CH4}$ = 41.9) performed the best, improved by 217% and 52%, respectively, the bare 6FDA-BisP performance (P_{CO2} = 33.9 Barrer; $\alpha_{CO2/CH4}$ = 27.5). However, the further addition of UiO-66 up to 21 wt.% decreased the selectivity to 24.6 with P_{CO2} = 155 Barrer. Similar observation was found for 6FDA-ODA MMMs, where the best performing MMM was that at 17 wt.% UiO-66 loading (P_{CO2} = 43.3 Barrer; $\alpha_{CO2/CH4}$ = 57.0) with 67% and 177% increments for CO_2 permeability and CO_2/CH_4 selectivity, respectively, comparing to the bare 6FDA-ODA (P_{CO2} = 25.9 Barrer; $\alpha_{CO2/CH4}$ = 20.6). Furthermore, the membrane showed the highest CO_2/CH_4 selectivity amongst the membranes prepared in this work. However, the further addition of UiO-66 to 23 wt.% did not improve the selectivity, even though the CO_2 permeability enhanced by 66% as compared to the 17 wt.% UiO-66 loading.

6FDA-DAM MMMs showed no significant increase in the selectivity, while the CO_2 permeability increased almost to 100% with 14 wt.% UiO-66 loading (P_{CO2} = 1912 Barrer; $\alpha_{CO2/CH4}$ = 30.9) compared to the bare 6FDA-DAM (P_{CO2} = 997 Barrer; $\alpha_{CO2/CH4}$ = 29.2). Further addition of UiO-66 up to 21 wt.% increased the CO_2 permeability to 2359 Barrer with a 56% decrease in CO_2/CH_4 selectivity.

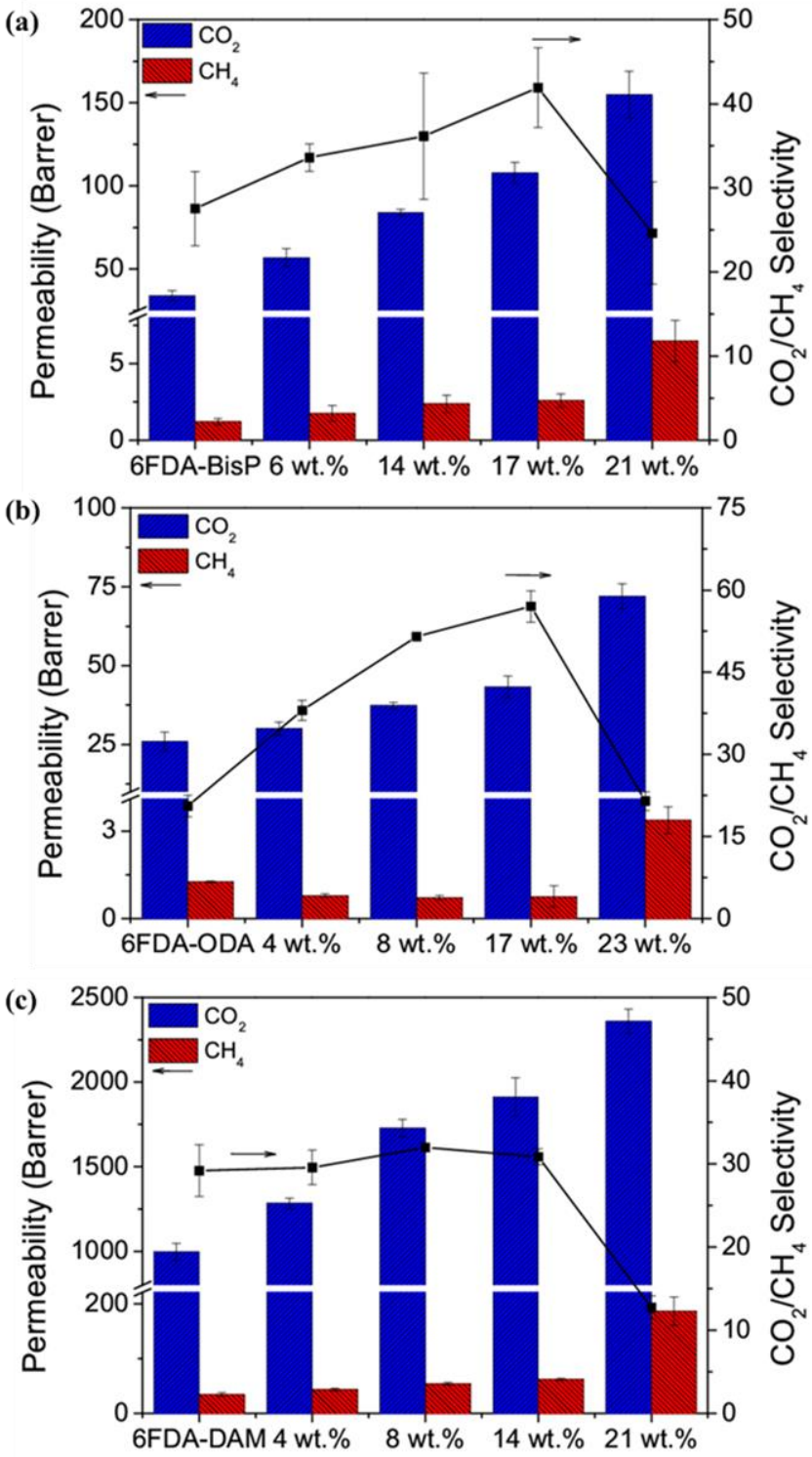

Fig. 4-13: CO_2 and CH_4 permeabilities and CO_2/CH_4 selectivity of (a) 6FDA-BisP, (b) 6FDA-ODA and (c) 6FDA-DAM MMMs containing UiO-66 as filler, tested at 35 ºC, a pressure difference of 2 bar with an equimolar binary mixture of CO_2 and CH_4. Standards deviations were calculated based on the results of at least 2-3 different membranes and error bars are represented accordingly.

Table 4-4: CO_2 and CH_4 permeabilities and CO_2/CH_4 selectivity of 6FDA-polyimides MMMs with UiO-66, measured at 35 ºC, a pressure difference of 2 bar with an equimolar binary mixture of CO_2 and CH_4.

Polymer	UiO-66 loading	Gas permeabilities (Barrer)		CO_2/CH_4 selectivity
		CO_2	CH_4	
6FDA-BisP	0 wt.%	33.9 ± 2.9	1.2 ± 0.2	27.5 ± 4.4
	6 wt.%	56.7 ± 5.5	1.8 ± 0.5	33.6 ± 1.6
	14 wt.%	83.9 ± 1.9	2.4 ± 0.5	36.2 ± 7.5
	17 wt.%	108 ± 7	2.6 ± 0.4	41.9 ± 4.7
	21 wt.%	155 ± 14	6.5 ± 1.4	24.6 ± 6.1
6FDA-ODA	0 wt.%	25.9 ± 3.0	1.3 ± 0.1	20.6 ± 2.0
	4 wt.%	30.1 ± 2.1	0.8 ± 0.1	38.0 ± 1.8
	8 wt.%	37.4 ± 1.1	0.7 ± 0.1	51.5 ± 0.2
	17 wt.%	43.3 ± 3.4	0.8 ± 0.4	57.0 ± 2.9
	23 wt.%	72.0 ± 4.0	3.4 ± 0.5	21.5 ± 1.7
6FDA-DAM	0 wt.%	997 ± 48	34 ± 3.2	29.2 ± 3.1
	4 wt.%	1283 ± 30	44 ± 2.3	29.6 ± 2.1
	8 wt.%	1728 ± 53	54 ± 2.1	32.0 ± 0.3
	14 wt.%	1912 ± 115	62 ± 1.9	30.9 ± 0.9
	21 wt.%	2358 ± 72	187 ± 25.8	12.7 ± 1.4

These results suggest that the incorporation of UiO-66 nanoparticles improved both gas diffusivity and adsorption of the MMMs. Gas diffusion was enhanced through the additional selective delaminated interface region [106] and the increase the polymer free volumes [29,239,240]. The influence of FFV is discussed in the next section. The CO_2 adsorption improved significantly in all samples, ought to be attributed to the CO_2-philic properties of the UiO-66 [136] These findings are consistent with the previously discussed adsorption results favoring CO_2 over CH_4 and the reported higher adsorption enthalpy for CO_2 (–26.2 $kJ \cdot mol^{-1}$) compared to CH_4 (–16.4 $kJ \cdot mol^{-1}$) on UiO-66 [135]. It has been suggested a stronger energetic interaction between CO_2 and the UiO-66 particle surface to occur at zero coverage, supported by the fact that CO_2 has a high quadrupole moment, thus causing it to adsorb stronger on UiO-66 than CH_4. Indeed, it has been reported that UiO-66 exhibits an intrinsic CO_2/CH_4 selectivity of 5.5 – 6.9 [44,135], measured at the temperature

of 25 – 50 ºC, with a 50/50 equimolar feed. Our as-synthesized UiO-66 possessed a lower selectivity of 4.1, calculated with single gas at 1 bar (from data corresponding to Fig. 4-8(b)). Considering the low CO_2/CH_4 selectivity and its triangular window of 6 Å as the point of gas entry, UiO-66 at a higher-than-optimum loading in polymers provided a less obstructive pathway to both CO_2 (3.3 Å) and CH_4 (3.8 Å) across the MMMs. The optimum loadings for our 6FDA-based MMM systems were in between 14 – 17 wt.% and further addition up to 21 – 23 wt.% decreased the selectivity by 41 – 62%. Zornoza *et al.* [29] described at higher loading; the polymer matrix is possibly unable to completely surround the particles thus producing interfacial voids, consequently increase the filler agglomeration. The tremendous increase in gas permeability and reducing gas selectivity is due to non-selective by-pass channels between the agglomerated particles [29,235] and the interfacial voids [155].

Similar observations were recently reported for CO_2/CH_4 gas pair in Matrimid® at 16 wt.%, polysulfone at 24 wt.% [30], and even at relatively low loadings especially in the highly permeable polymers, such as PIM-1 ($\alpha_{\text{bare polymer}} = 16.7$; $\alpha_{9\text{wt.\%}} = 16.0$) [163]. The high permeability PEBA polymer [224] also reported to produce its highest CO_2/N_2 selectivity only with 7.5 wt.% of UiO-66 loading.

Nonetheless, we further investigated the relationship between the degree of filler agglomeration and the gas separation performances by preparing additional MMMs using 6FDA-ODA with larger UiO-66 nanoparticles, at 17 and 23 wt.% loadings. The XRD patterns (Fig. 4-14) and SEM images (Fig. 4- 15) of the ca. 100 and 200 nm nanoparticles synthesized accordingly to Xu and Chung [139] and Cao *et al.* [45] are presented, with their respective MMMs cross sections (Fig. 4-16). It can be observed that UiO-66 ca. 100 nm were agglomerated to a higher degree than the ca. 50 nm nanoparticles. However, the ca. 200 nm nanoparticles agglomerated more prominently and produced poorer MOF-polymer interfaces. The gas performance of both MMMs with ca. 17 wt.% and ca. 23 wt.% loadings showed non-idealistic separation performances [155,241], as illustrated in Fig. 4-17. The incorporation of ca. 17 wt.% larger UiO-66 reduced the ideally enhanced 6FDA-ODA using ca. 50 nm nanoparticles, ($\alpha_{CO2/CH4,\ 17\ wt.\%} = 57.0$) to the ´leaking phenomenon` (represented by the formation of non-selective interface voids due to the poor filler-polymer interaction [17]), indicated by CO_2/CH_4 selectivity reductions in the 85 – 95% range. A similar ´leaking phenomenon´ was observed with the ca. 23 wt.% loading MMMs, where the selectivities were reduced by 50 – 75%, compared to the MMMs with the smallest UiO-66.

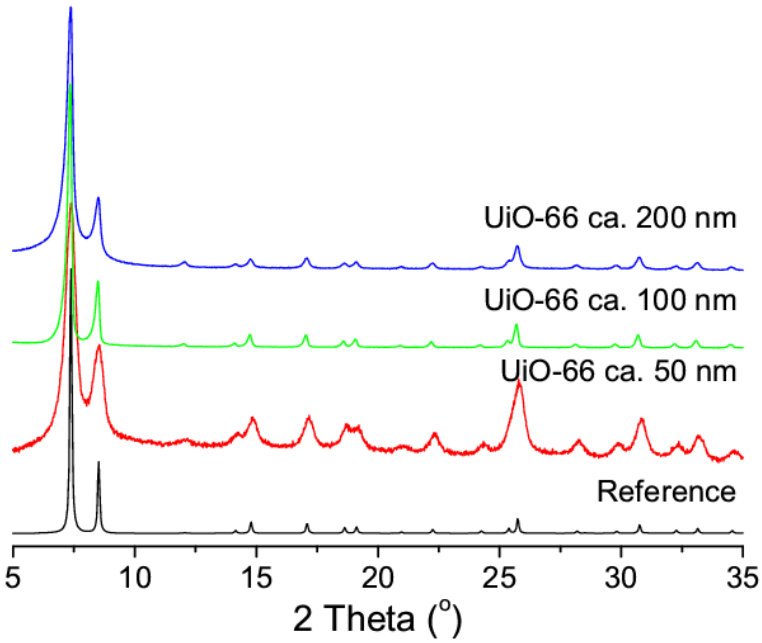

Fig. 4-14: The powder XRD of UiO-66 synthesized at different particles sizes of ca. 50 nm, ca. 100 nm and ca. 200 nm, prepared respectively to the procedures reported by Hou et al. [242], Xu and Chung [139] and Cao et al. [45].

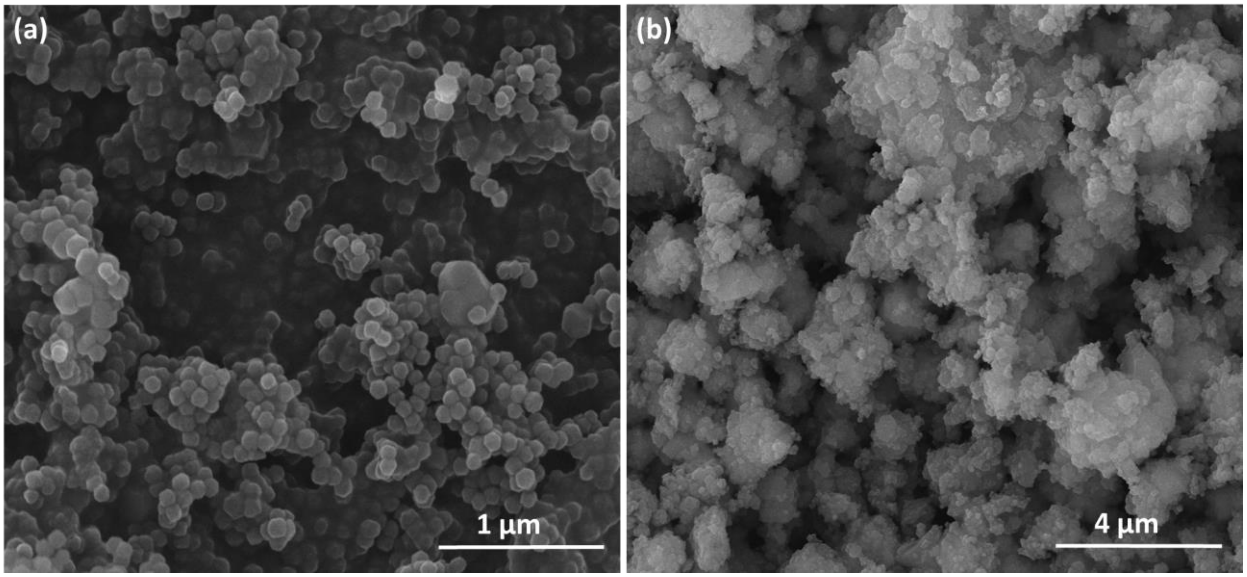

Fig. 4- 15: The SEM images of UiO-66 at (a) ca. 100 nm and (b) at ca. 200 nm.

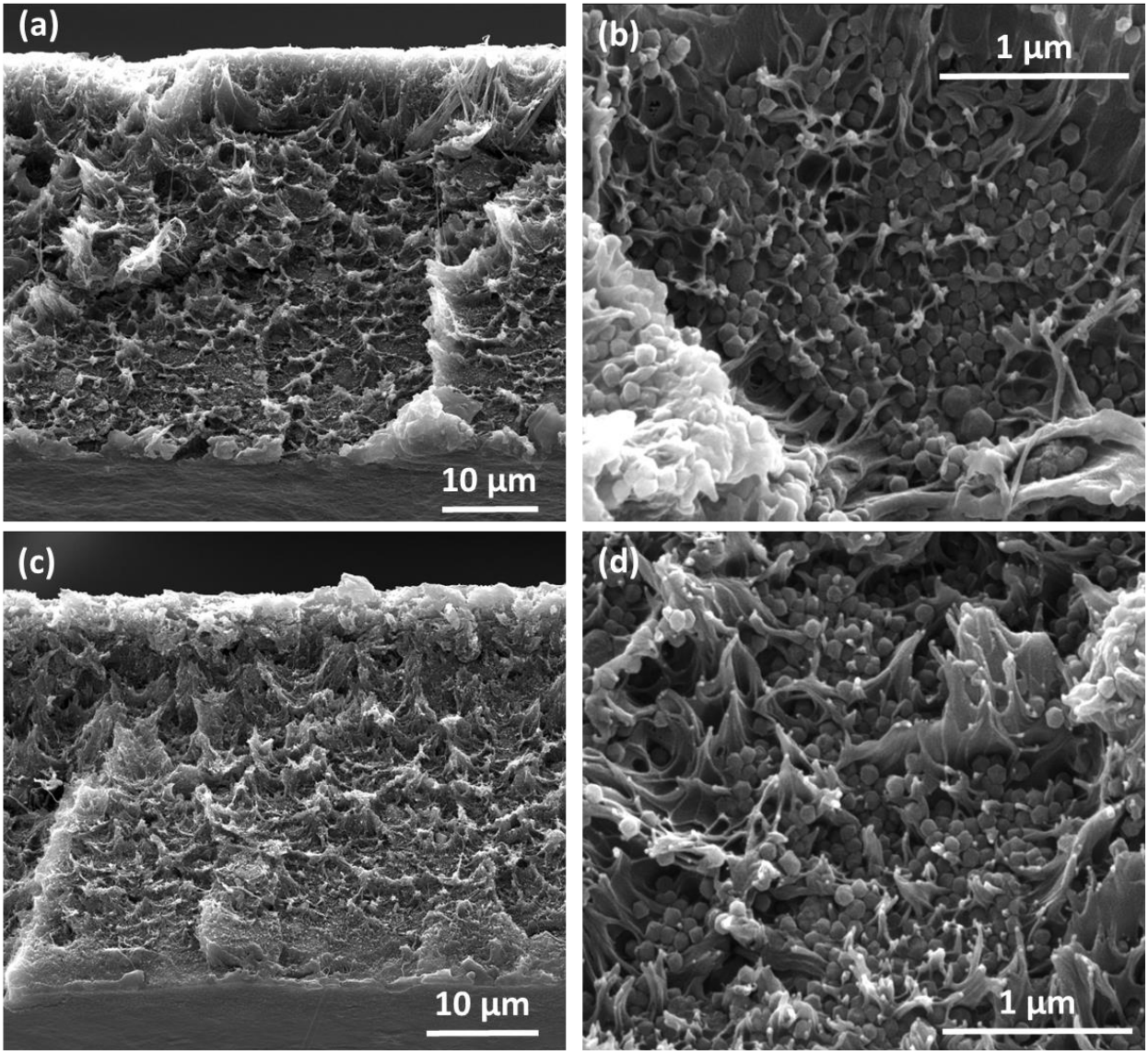

Fig. 4-16: SEM images of 6FDA-ODA MMMs with UiO-66 NPs, ca. 100 nm at (a, b) 17 wt.%; (b, c) 21 wt.% and NPs ca. 200 nm at (e, f) 17 wt.%; (g, h) 19 wt.% loadings.

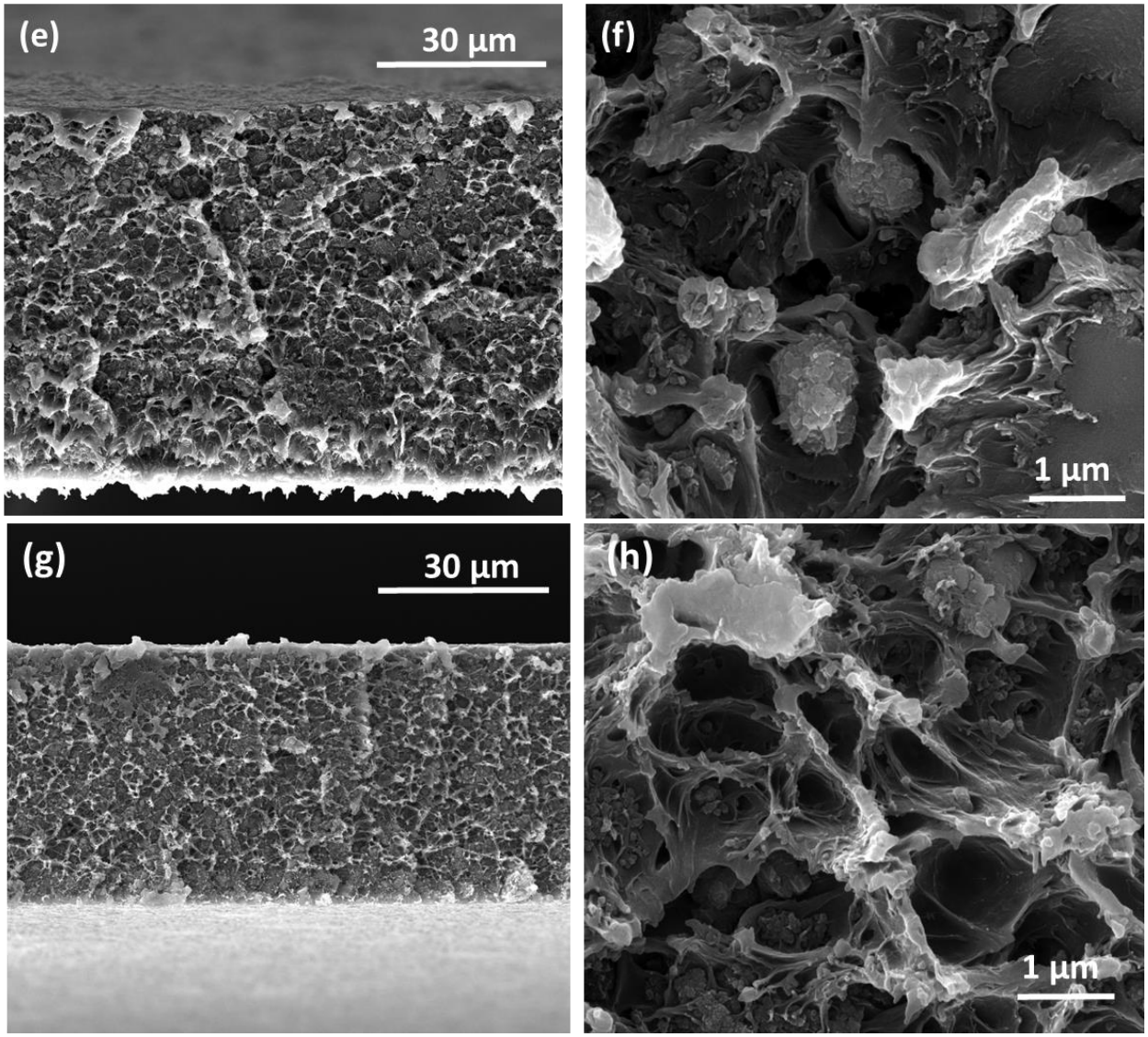

Fig. 4-16 (cont'd): SEM images of 6FDA-ODA MMMs with UiO-66 NPs, ca. 100 nm at (a, b) 17 wt.%; (b, c) 21 wt.% and NPs ca. 200 nm at (e, f) 17 wt.%; (g, h) 19 wt.% loadings.

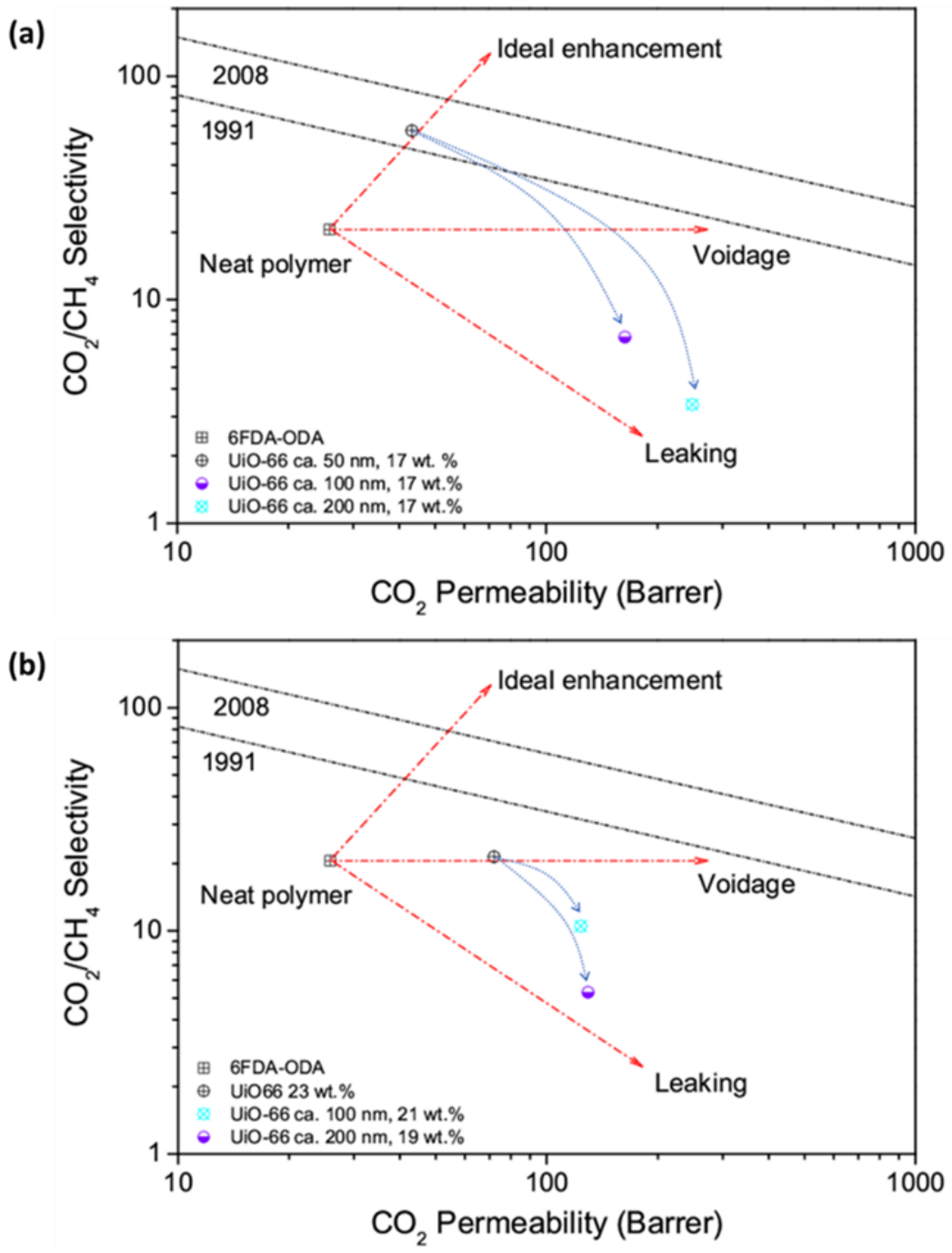

Fig. 4-17: The separation performance of 6FDA-ODA MMMs with different particle sizes of UiO-66 nanoparticles at (a) ca. 17 wt. % and (b) ca. 23 wt.% loadings. For proper comparison, 1991 [20] and 2008 [21] Robeson upper bounds are represented.

4.5.3.2. FFV vs. gas permeability

Fig. 4-18 shows the CO_2 and CH_4 permeabilities of the membranes together with their respective calculated FFVs. The studied 6FDA dianhydride-polyimide showed a relatively high free volume between 0.16 and 0.25 (6FDA-BisP = 0.248, 6FDA-ODA = 0.163 and 6FDA-DAM = 0.238) comparing to the other dianhydride-derived polyimides (i.e. 0.12 – 0.17 for BDPA and BTDA dianhydrides, and 0.11 – 0.19 for PMDA) [243]. FFV values were similar to those previously reported [52,67] and in the higher range of the free volume values (0.1 – 0.3) of most polymers [218,240]. Gas separation of the small kinetic diameter molecules (CO_2, 3.3 Å; CH_4, 3.8 Å) in this 6FDA-polyimide membranes were governed by the diffusion mechanism. The results corresponded to the relationship of the molecule kinetic diameters with the diffusion coefficient, where the smaller molecules have higher diffusion coefficients.

In 6FDA-BisP, the increment of the FFV was observed to be the highest at 85% with 21 wt.% UiO-66 loading, and contributed to the ± 3.5-fold CO_2 permeability rise. The 17 wt.% UiO-66 MMM demonstrated the best membrane performance, having an addition of >60% FFV and produced the highest CO_2/CH_4 selectivity of 41.9. For 6FDA-DAM, a 40% increase of FFV was observed with 14 wt.% UiO-66 loading while maintaining the selectivity of 31.0. A higher FFV enhancement for 6FDA-ODA with 17 wt.% loading was achieved (FFV of 0.364), and the CO_2/CH_4 selectivity was improved to 57.0 comparing to the bare polymer (20.6). The relationship of gas permeability coefficient with FFV is presented in Fig. 4-19, the straight lines obtained from Park and Paul correlation [218]. Both 6FDA-BisP and 6FDA-DAM behaved accordingly to the correlation. However, 6FDA-ODA did not follow the expected trend.

In relation to the SEM images of MOF-polyimide interfaces in Fig. 4-12, we suggested that a higher selective free volume was created in all polymer, while maintaining the ideal morphology of an MMM [17], except for MMMs with the highest loadings. At the highest loading, morphology with non-selective interface voids may have formed, as suggested from the gas selectivity reductions.

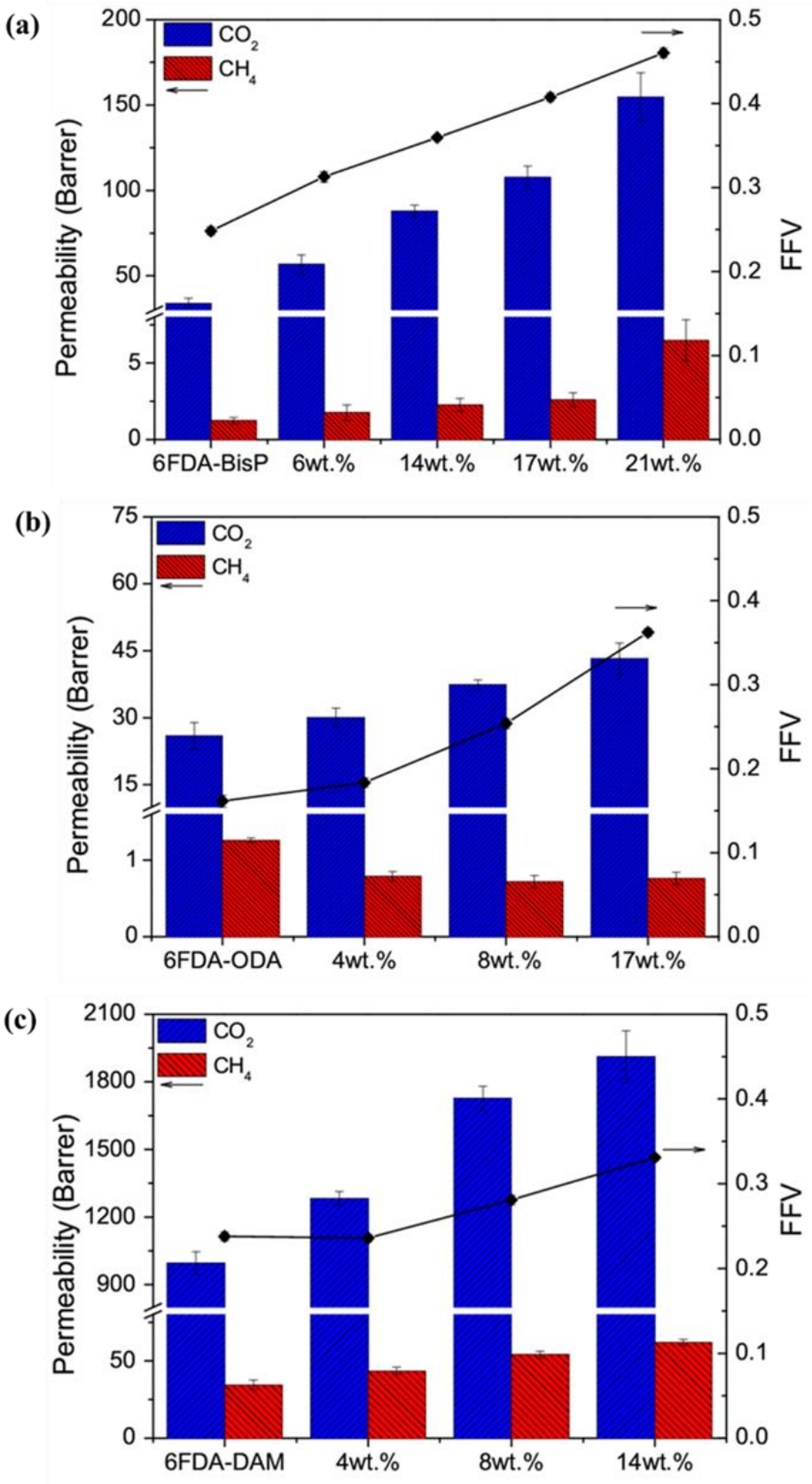

Fig. 4-18: CO_2 and CH_4 permeabilities from CO_2/CH_4 mixture and FFV values, calculated from solid density measured at 20 ºC with pressurized He cycles between 2 – 20 bar, for: (a) 6FDA-BisP, (b) 6FDA-ODA and (c) 6FDA-DAM and their respective UiO-66 MMMs.

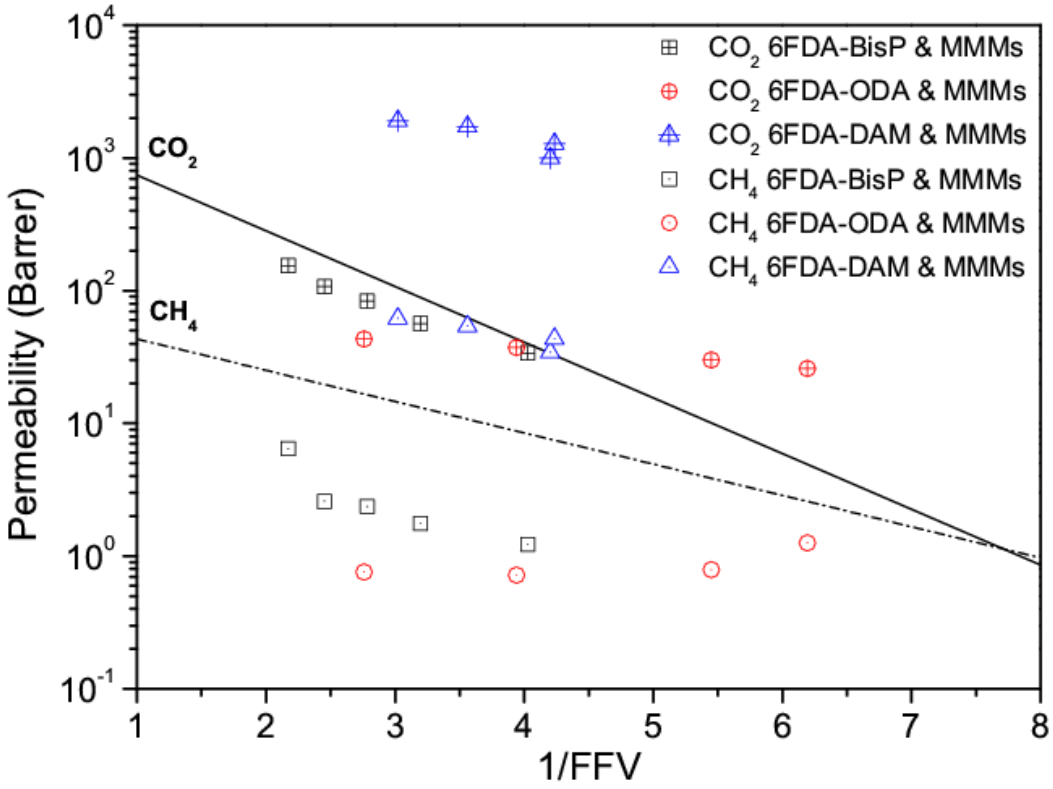

Fig. 4-19: Gas permeability obtained against 1/FFV in comparison with CO_2 and CH_4 permeability coefficient correlations to 1/FFV by Park and Paul [218]. MMMs values were estimated using their corresponding reduced density.

4.5.3.3. Performance comparisons with the upper bound

Fig. 4-20 shows the performances of all three studied 6FDA-based polyimide membranes and their MMMs with the CO_2/CH_4 1991 and 2008 Robeson upper bounds [20,21]. As depicted, 6FDA-BisP and 6FDA-ODA bare membranes resided below the upper bound. However, their respective MMMs with UiO-66 at 17 wt.% showed an improvement surpassed the 1991 upper-bound. Additional filler loading did not further improve the CO_2/CH_4 selectivity of both membranes. The bare polymer 6FDA-DAM, however, resided above the 2008 upper-bound and further improved inward in the targeted region due to the remarkable CO_2 permeability increase, while maintaining the CO_2/CH_4 selectivity with 14 wt.% UiO-66 loading. These findings show that the UiO-66 has a good potential in MMMs for gas separation applications.

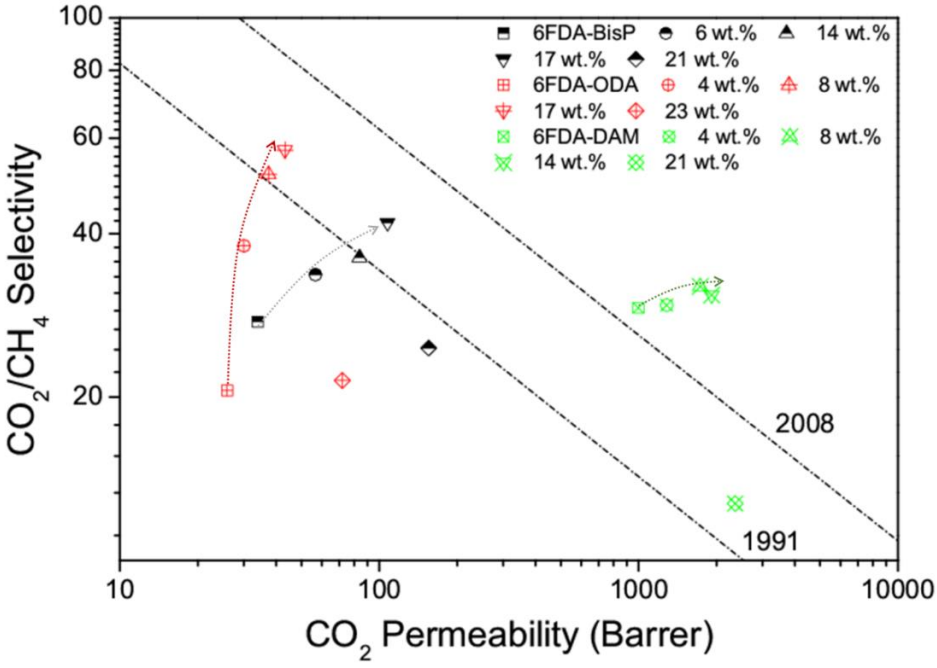

Fig. 4-20: Separation performances of the three types of 6FDA-polyimide MMMs containing UiO-66, measured with an equimolar feed of CO_2 and CH_4 at 35 ºC, at a pressure difference of 2 bar, against 1991 [20] and 2008 [21] Robeson upper bounds.

4.6. CHAPTER CONCLUSIONS

We report the successful synthesis of high surface area Zr-based MOF UiO-66, with a uniform particle size of ca. 50 nm, appropriate crystallinity, and excellent thermal stability, as well as the fabrication of UiO-66 mixed matrix membranes with three 6FDA-based co-polyimides. Upon obtaining excellent MOF-polymer interaction with ca. 50 nm UiO-66 (and less agglomeration than using 100 and 200 nm particles), the presence of the MOF contributed to the increase of the membrane free volumes. The gas separation performances showed significant CO_2 permeability and CO_2/CH_4 selectivity improvements. 6FDA-BisP (pristine performances of $_{\alpha CO2/CH4}$ = 27.5 ± 4.4, P_{CO2} = 33.9 ± 9.2 Barrer) were improved by 52% and 217%, while increments of 177% and 67% were obtained for 6FDA-ODA (pristine performances of $\alpha_{CO2/CH4}$ = 20.6 ± 2.0, P_{CO2} = 25.9 ± 3.0 Barrer), respectively, for selectivity and CO_2 permeability. In the case of 6FDA-DAM (pristine performances of $\alpha_{CO2/CH4}$ = 29.2 ± 3.1, P_{CO2} = 997 ± 48 Barrer), CO_2 permeability also increased by 92% while maintaining the CO_2/CH_4 selectivity. This work demonstrated that UiO-66 has the requisite advantages for fabricating mixed matrix membranes with high performance, thus making it a promising candidate for the future CO_2 capture membrane-based technologies.

CHAPTER 5: FURTHER SEPARATION ENHANCEMENT OF 6FDA-DAM BASED MIXED MATRIX MEMBRANE WITH UiO-66 AND ITS FUNCTIONALIZED DERIVATIVES

5.1. CHAPTER OVERVIEW

With regards to the excellent CO_2/CH_4 separation performance presented by 6FDA-based MMMs with UiO-66 (less than 50 nm), even surpassing the 2008 Robeson upper bounds in 6FDA-DAM MMMs, we continued to investigate its performance enhancement by incorporating 5 – 24 wt.% of the functionalized UiO-66 nanoparticles, e.g., UiO-66-NH_2 and UiO-66-NH-$COCH_3$. Amine-functionalized UiO-66-NH_2 was obtained through a direct synthesis using amino-containing organic ligand, whereas the acetamide-functionalized UiO-66-NH-$COCH_3$ was produced through a post-synthetic modification (PSM) of the amino UiO-66. It was expected that the functionalization endowed UiO-66-NH_2 and UiO-66-NH-$COCH_3$ nanoparticles with stronger CO_2 affinity compared to UiO-66 will produce a better CO_2/CH_4 separation, in addition to their expected better filler-polymer interfacial interaction. We investigated CO_2/CH_4 separation both at low (3 bar, at 35 °C) and high pressure (up to 40 bar, at 35 °C). The effects of CO_2 partial pressure in the feed stream, at both low and high pressures were also explored. Detail discussion on the nanoparticles and their respective MMMs are presented, which include their N_2, CO_2, CH_4 adsorption, cross-section morphologies and related changes in the physical properties upon the nanoparticle addition.

5.2. CHAPTER CONTRIBUTIONS

In this chapter, we synthesized UiO-66 ($Zr_6(\mu_3\text{-}O)_4(\mu_3\text{-}OH)_4(O_2C{-}C_6H_4{-}CO_2)_{12}$) and UiO-66-$NH_2$ ($Zr_6(\mu_3\text{-}O)_4(\mu_3\text{-}OH)_4(O_2C{-}C_6H_3(NH_2){-}CO_2)_{12}$). with less than 50 nm particle size. The UiO-66-NH-$COCH_3$ ($Zr_6(\mu_3\text{-}O)_4(\mu_3\text{-}OH)_4(O_2C{-}C_6H_3(COCH_3){-}CO_2)_{12}$) was obtained by acetamide-ligand PSM of a UiO-66-NH_2, with the aim of achieving better filler-polymer interactions, thus improving the CO_2 permeability and CO_2/CH_4 separation selectivity. The CO_2 uptakes at 10 bar in the two functionalized UiO-66s were improved by 44 and 58%, respectively, with respect to the pristine solid. The MOF nanoparticles were incorporated into the highly permeable polymer 6FDA-DAM (see Fig. 5-1), making MMMs with 5 to 24 wt.% particle loadings. Their gas separation performances were evaluated by feeding CO_2/CH_4 equimolar mixtures at 2 bar pressure difference at 35 °C. The measurement was also conducted with various binary compositions (CO_2 = 10 – 90%), both at low and high pressures up to 40 bar at 35 °C, showing no pressure-related CO_2-induced plasticization.

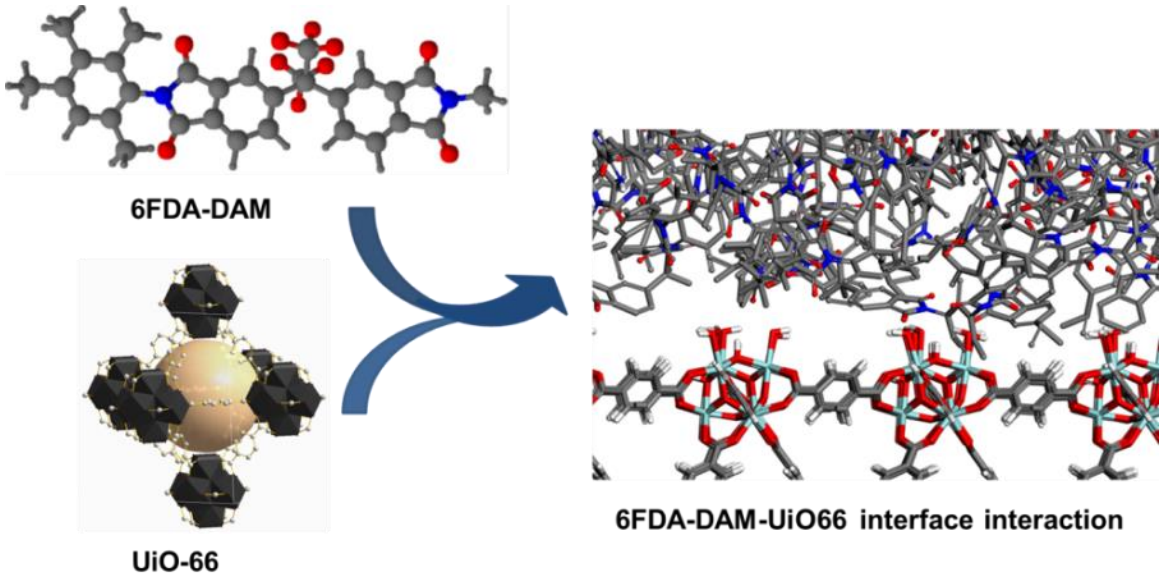

Fig. 5-1: Illustration of the atomistic modelling for the Zr-MOF/6FDA-DAM polymer interface.

5.3. INTRODUCTION

Natural gas sweetening by the removal of the acidic components (CO_2 and H_2S) has been discussed thoroughly over the years [244], including advantages and disadvantages of the established and competing technologies [10,11]. The process is crucial for natural gas production, before being made available for transportation. For this application, membrane technology seems of a practical interest mainly due to their lower cost and footprint, higher

energy efficiency and low environmental impact [12]. New strategies for developing membrane materials with improved permeation and selectivity have been described extensively, including the very promising approach of mixed matrix membranes (MMMs) [18]. MMM technology exploits the distinct and complementary properties of both polymer and inorganic materials with different physicochemical properties, selectivity and permeation flux for their selective separation.

Various materials, generally porous, such as carbon molecular sieves (CMS) [73,74], zeolites and silicas [74,75], metal oxides [76], carbon nanotubes (CNTs) [77], metal organic frameworks (MOFs) [55,56,79,186], graphene [81,82], etc. have been embedded in continuous polymer matrixes in the form of MMMs, thus leading to improved separation performances. The crystalline porous MOFs formed by the assembly of metal centers and organic ligands [26,222,245–247] are some of the emerging alternative fillers. They are gaining substantial attention due to their high CO_2 uptake (i.e., HKUST-1 of 7.2 $mmol \cdot g^{-1}$ [22], MOF-74 of 4.9 $mmol \cdot g^{-1}$ [23], at 1 bar, 273 – 298 K), large surface areas up to 7000 $m^2 \cdot g^{-1}$ [84], well-defined selective pores due their crystallinity, and superior thermal and chemical stability [10], among other features. Most importantly is their tunable pore geometries and flexible frameworks [248–251], giving rise to various gas separation purposes. Indeed, MOF-containing membranes have been reported to perform better than the current Robeson upper bounds [21] for several gas pairs of great interest: CO_2/CH_4 (e.g. ZIF-90 with 6FDA-DAM [86], ZIF-8 with PIM-1 [87], CO_2/N_2 (e.g. ZIF-7 in Pebax® 1657 [88], ZIF-8 in Pebax® 2533 [89], and H_2/CO_2 (e.g. NH_2-CAU-1 in PMMA [90], ZIF-8 in PBI [91]).

UiO-66 (UiO: University of Oslo), $Zr_6(\mu_3\text{-}O)_4(\mu_3\text{-}OH)_4(O_2C{-}C_6H_4{-}CO_2)_{12}$, is a highly crystalline zirconium-based MOF formed by octahedral $Zr_6O_4(OH)_4$, with 12-fold connections to the organic linker 1,4-benzene-dicarboxylate (BDC) (see Fig. 5-2(a)) [93,137]. This microporous framework is composed of centric octahedral cages (ca. 11 Å, Fig. 5-2(b)), cornered by eight tetrahedral cages (ca. 8 Å, Fig. 5-2(c)) and trigonal window openings (ca. 6 Å). This MOF of cubic symmetry possesses a significant porosity (theoretical accessible surface of 1021 $m^2 \cdot g^{-1}$ and pore volume of 0.40 $cm^3 \cdot g^{-1}$ [135]), high resistance to heat, (430 – 540 °C [136,137]), mechanical pressure and water adsorption [138,139]. The CO_2 uptake of UiO-66 was reported to be in the range of 1.8 – 2.3 $mmol \cdot g^{-1}$ (1 bar, 298 K) [43–45], while functionalization of the BDC organic ligand further increased its CO_2 capacity up to 2.6 $mmol \cdot g^{-1}$ with various alkanedioic acids ($HO_2HC(CH_2)_n\text{-}CO_2H$) [44], 3.0 $mmol \cdot g^{-1}$ with amino, $–NH_2$ [43], and 2.6 $mmol \cdot g^{-1}$ with dimethoxy, $–(OMe)_2$ [43].

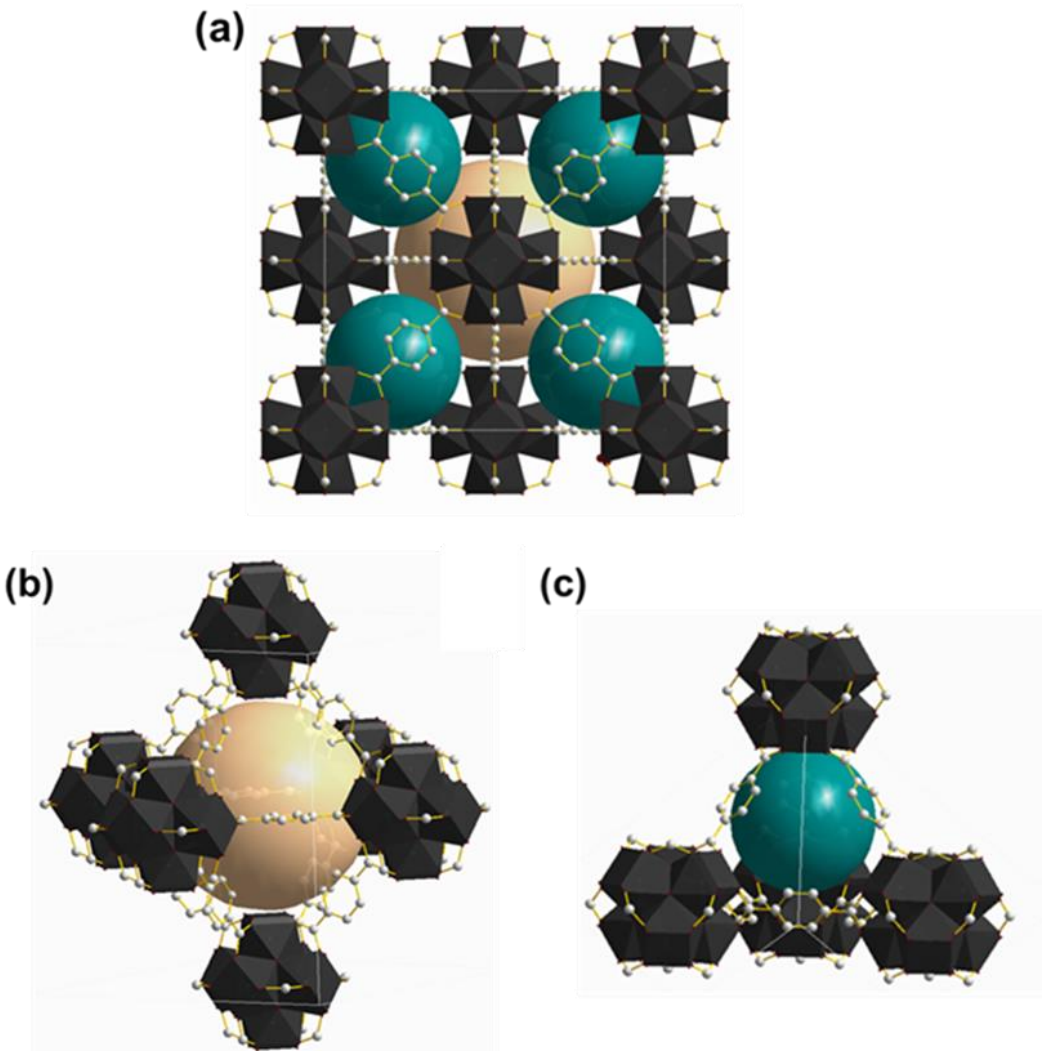

Fig. 5-2: Representation of UiO-66 three-dimensional is shown, (a) the iso-reticular framework with its Zr_6O_6 cuboctahedron polyhedral (dark gray cubes), emphasizing on (b) octahedron free volume (yellow ball), and (c) tetrahedron free volumes (blue ball). The drawing was done using Diamond 3.2 with CIF obtained from CDCC open database [93]. Hydrogen atoms are omitted for ease of viewing.

UiO-66-NH_2 was prepared by a direct synthesis route using amino-functionalized organic linker (UiO-66-NH_2 = $Zr_6(\mu_3\text{-}O)_4(\mu_3\text{-}OH)_4(O_2C{-}C_6H_3(NH_2){-}CO_2)_{12}$). The amino group is chemically inert in most solvents and does not participate in the coordination chemistry of the metal ions [85]. Post-synthetic modification (PSM) reactions of the amino functionality can be conducted through nucleophilic substitution, acid-base and condensation reactions [42]. This can simultaneously change the MOF properties such as pore accessibility and pore sorption behavior, depending on the orientation of the modified linkers [85]. The incorporation of functionalized-MOFs has been reported to improve the performance of the MMM compared to the pristine MOFs. As a typical illustration, Tien-Binh *et al.* [141] improved the CO_2 permeability (P_{CO2}) of polyimide 6FDA-DAM-HAB (P_{CO2} = 54 Barrer,

$\alpha_{CO2/CH4}$ = 18) by adding 10 wt.% MIL-53(Al) (P_{CO2} = 61 Barrer, $\alpha_{CO2/CH4}$ = 16) and obtained a much higher CO_2/CH_4 selectivity with 10 wt.% of NH_2-MIL(Al)-53 (P_{CO2} = 47 Barrer, $\alpha_{CO2/CH4}$ = 79). Anjum *et al.* [134] incorporated 30 wt.% of UiO-66 and UiO-66-NH_2 into polyimide Matrimid® 9725 and improved the CO_2 permeability by 160 - 200%. Xin *et al.* [142] enhanced both CO_2 permeability of sulfonated poly (ether ether ketone), SPEEK polymer by around 100%, using 40 wt.% of MIL-101(Cr) and MIL-101(Cr)-HSO_3.

5.4. EXPERIMENTAL

5.4.1. Syntheses of Zr-MOF nanoparticles (NPs)

All reactants were supplied by Sigma-Aldrich. The UiO-66 was synthesized as detailed in Section 4.4.1, whereas the UiO-66-NH_2 NPs (ca. 50 nm in size) was synthesized accordingly to Hou *et al.* [226], at 1 to 1 molar ratio of zirconium (IV) chloride ($ZrCl_4$, ≥99.5% trace metal basis) to 2-amino-1,4-benxenedicarboxylic acid (NH_2-BDC, 99%), in *N*,*N*-dimethylformamide (DMF, ≥99.9%). Similarly to UiO-66 synthesis, $ZrCl_4$ was first dissolved in DMF by sonication at room temperature before the addition of the corresponding organic ligand. Commonly for UiO-66-NH_2, 6.4 mmol (1.50 g) $ZrCl_4$ and 6.4 mmol (1.56 g) NH_2-BDC were dissolved in 180 mL of DMF. There was no reaction modulator was used.

The solutions were later transferred into stainless steel Teflon-lined autoclaves for a solvothermal process in a pre-heated oven at 80 °C / 14 h for UiO-66-NH_2. A second step heating was conducted for UiO-66-NH_2 at 100 °C / 24 h. After cooling to room temperature, the colloidal suspensions were centrifuged at 10,000 rpm for 15 min. A chemical activation was conducted for UiO-66-NH_2 NPs by washing in an absolute ethanol bath at 60 °C, three times in three days (ethanol was changed daily). After the complete cycle, the NPs were dried at room temperature. The reaction scheme is presented in Fig. 5-3.

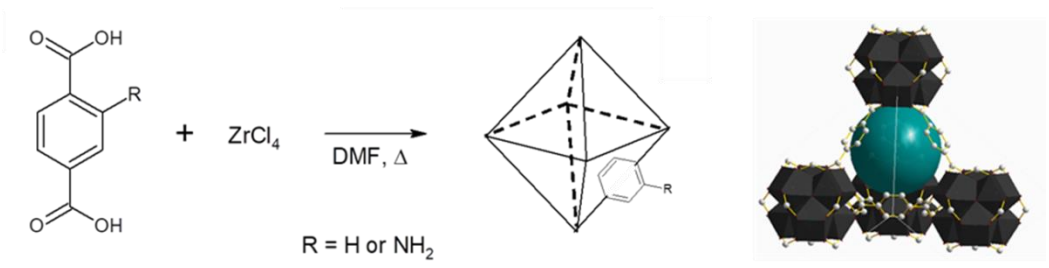

Fig. 5-3: The reaction schemes of (a) UiO-66 and UiO-66-NH_2 using $ZrCl_4$ and BDC and amino-BDC. Each iso-reticular framework forms the Zr-MOF permanent free volume, i.e. the tetrahedron free volumes (blue ball).

5.4.2. Modification of UiO-66-NH_2

All reactants were also supplied by Sigma-Aldrich. The synthesis of UiO-66-NH-$COCH_3$ cannot be achieved by a direct reaction between $ZrCl_4$ and 2-acetylamidobenzenedicarboxylic acid ($CH_3CONH–H_2BDC$) in DMF due to the formation of an amorphous gel [140]. Thus a covalent post-synthetic modification is needed. Normally, 0.2 mmol-NH_2 (~ 60 mg) was treated with a 0.2 mmol anhydride solution (2 mL chloroform ($CHCl_3$, anhydrous ≥ 99%), 20.4 mg acetic anhydride (AcO_2, ACS Reagent, ≥98.0%)) and heated under reflux at 55 °C / 24 h. Once completed, the colloidal solution was centrifuged, rinsed with fresh $CHCl_3$ (15 mL, 3x) and dried overnight at 150 °C before characterization and use. PSM using an acetic anhydride was reported to produce the highest conversion yield compared to the longer chain alkyl anhydrides [133], this reaction scheme is presented in Fig. 5-4.

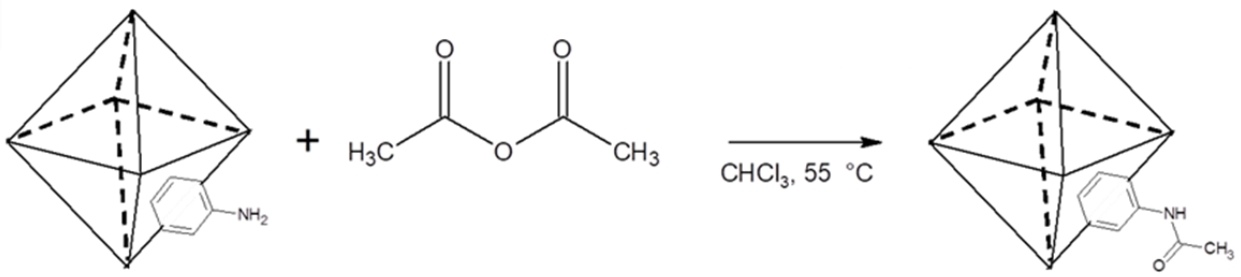

Fig. 5-4: The post-synthetic modification (PSM) of UiO-66-NH_2 with acetic anhydride in $CHCl_3$ at 55 °C.

The conversion yield was determined by the percentage of amide groups present in the modified NPs using proton nuclear magnetic resonance (^{1}H NMR). Samples of 10 mg of UiO-66-NH_2 and UiO-66-NH-$COCH_3$ were digested by sonication in 570 μL of deuterated dimethyl sulfoxide (d_6-DMSO, ≥99.96 atom % D) and 30 μL of hydrofluoric acid (HF, 48%), and their ^{1}H NMR spectra were acquired on a Bruker Avance III spectrometer (500 MHz). Similar digestion method was presented elsewhere [133,226].

5.4.3. Membrane fabrication, characterizations and gas separation evaluation

All the MMMs were fabricated using 6FDA-DAM (Mw = 418 kDa), which was purchased from Akron Polymer Systems, Inc. and the preparation procedure is as described in Section 4.4.3. The particle loading is calculated from Eq. 3.1. All the characterization and gas separation evaluation was conducted as presented in Section 4.4.4 and 4.4.5.

5.4.4. CO_2 and CH_4 permeabilities prediction using an extended Maxwell model

Different models for MMMs have been proposed in order to determine the effect of the incorporation of a dispersed phase into the continuous phase on mass transfer properties[51,252]. One of the most applied models for description of permeation through the MMMs is Maxwell-Wagner-Sillar model [146] developed initially to describe dielectric permittivity of heterogonous materials. Due to similarities between electric conductivity and the permeation of species through the MMMs this model can be applied for effective permeability (P_{eff}) calculation Eq. 5.1.

$$P_{eff} = P_c \frac{nP_d+(1-n)P_c-(1-n)\varphi(P_c-P_d)}{nP_d+(1-n)P_c+n\varphi(P_c-P_d)} \qquad \text{Eq. 5.1}$$

The n is the particle shape factor ranging between 0 and 1, P_c the permeability of continues phase (polymer), P_d the permeability of dispersed phase (particles) and φ the particle volumetric loading, respectively. The particle volumetric loading is defined by following equation:

$$\varphi = \frac{w_f/\rho_f}{w_f/\rho_f + w_p/\rho_p} \qquad \text{Eq. 5.2}$$

where w_f, w_p and ρ_f, ρ_p are the weight and density of the filler and polymer matrix, respectively.

Considering an ideal morphologies with a good dispersion of spherical particle without an additional phase (rigidification, void, and etc.) around the particle, n = 1/3 [51,252] and Maxwell extended model simplify to

$$P_{eff} = P_c \frac{P_d+2P_c-2\varphi(P_c-P_d)}{P_d+2P_c+\varphi(P_c-P_d)} \qquad \text{Eq. 5.3}$$

Due to the lack of experimental data, the particle permeability was estimated assuming the mass transfer in microporous material which is often referred to as configurational diffusion and is characterized by its activated nature. The molecules can either retain a gaseous character in the micropores or they adsorb in the micropore surface. Assuming Langmuir isotherm in the form

$$q_i = \frac{q_{mi} K_i p_i}{1+K_i p_i}, \qquad \text{Eq. 5.4}$$

the gas flux (J_i) through the microporous filler can be calculated by Eq. 5.5:

$$J_i = \rho_s q_{mi} \frac{D_{0i}}{L} \frac{\ln(1+K_i p_i^F)}{\ln(1+K_i p_i^P)} \qquad \text{Eq. 5.5}$$

Where the L and ρ_s are the thickness and density of the dispersed phase layer, p_i^F and p_i^P the partial pressures of component i on the feed and permeate sides, D_{0i} the corrected diffusion coefficient, q_{mi} and K_i, the Langmuir isotherm coefficients and ρ_s the density of the microporous layer (dispersed phase), respectively.

Due to limited experimental data about corrected CO_2 and CH_4 diffusivity values of UiO-66 and its functionalized derivatives, the Knudsen diffusion coefficient is assumed as D_{0i} (Eq. 5.6) to estimate the dispersed phase permeability [155]. In Eq. 5.6, r is the pore radius, M_i is the gas molecular weight, and T is the temperature.

$$D_{0i} = \frac{2r}{3}\sqrt{\frac{8RT}{\pi M_i}} \qquad \text{Eq. 5.6}$$

Particle permeability is then calculated using Eq. 5.7.

$$P_d = \frac{J_i L}{(p_i^F - p_i^P)} = \frac{D_{0i} q_{mi} \rho_s}{(p_i^F - p_i^P)} \frac{ln(1+K_i p_i^F)}{ln(1+K_i p_i^P)} \qquad \text{Eq. 5.7}$$

5.5. RESULTS AND DISCUSSIONS

5.5.1. Zr-MOF characterization

All the Zr-MOFs were found to be in a size range of below 50 nm, as shown in the corresponding TEM images (Fig. 5-5), where their distinctive cubic morphologies can be observed. Their small size makes these NPs suitable fillers for preparing thin and homogenous MMMs [80]. XRD patterns in Fig. 5-6(a) demonstrate the high crystallinity of the Zr-MOFs obtained after the activation treatment. Also, their corresponding XRD patterns are in good agreement with the simulated pattern for UiO-66 crystal structure [137]. It should be noted that the introduction of amine and amide groups into UiO-66 has a negligible influence on the crystal structure. The three Zr-MOF crystallite sizes estimated using Scherrer equation [253] were in the average of about 40 nm, in good agreement with TEM results.

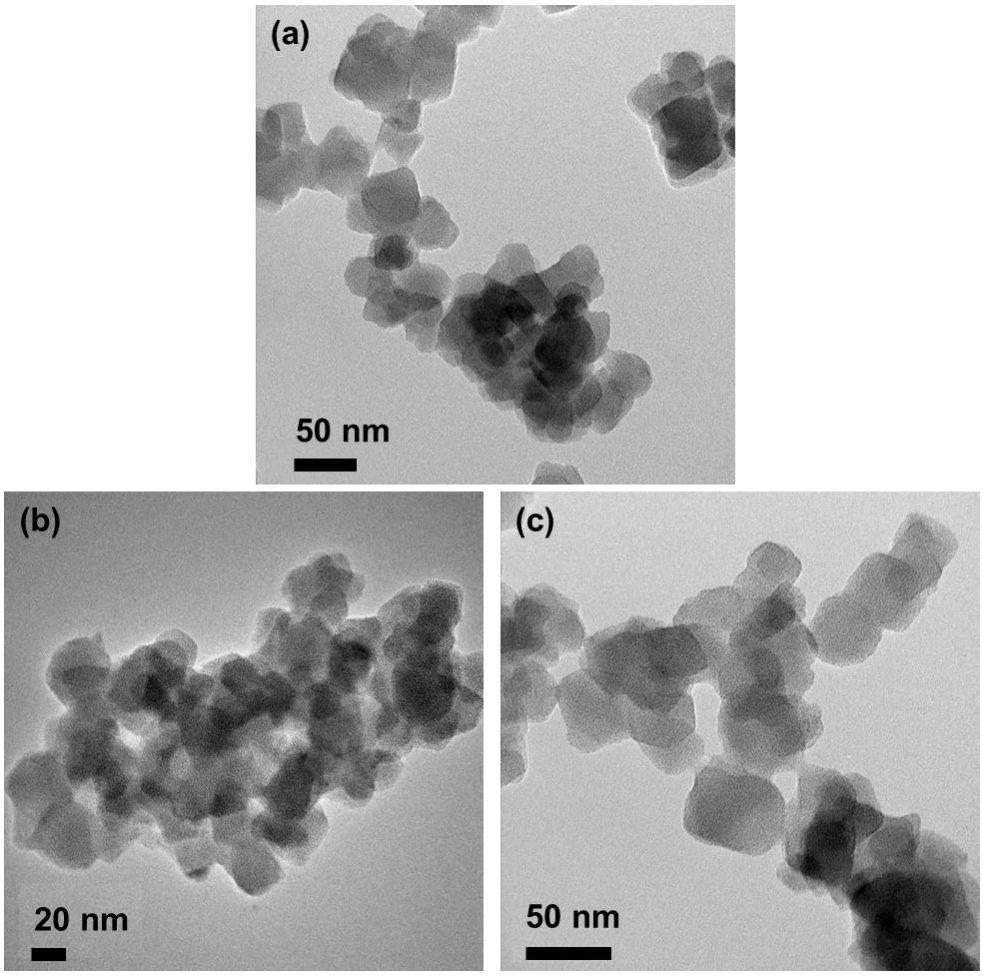

Fig. 5-5: TEM images of (a) UiO-66, (b) UiO-66-NH_2 and (c) the modified UiO-66-NH-$COCH_3$.

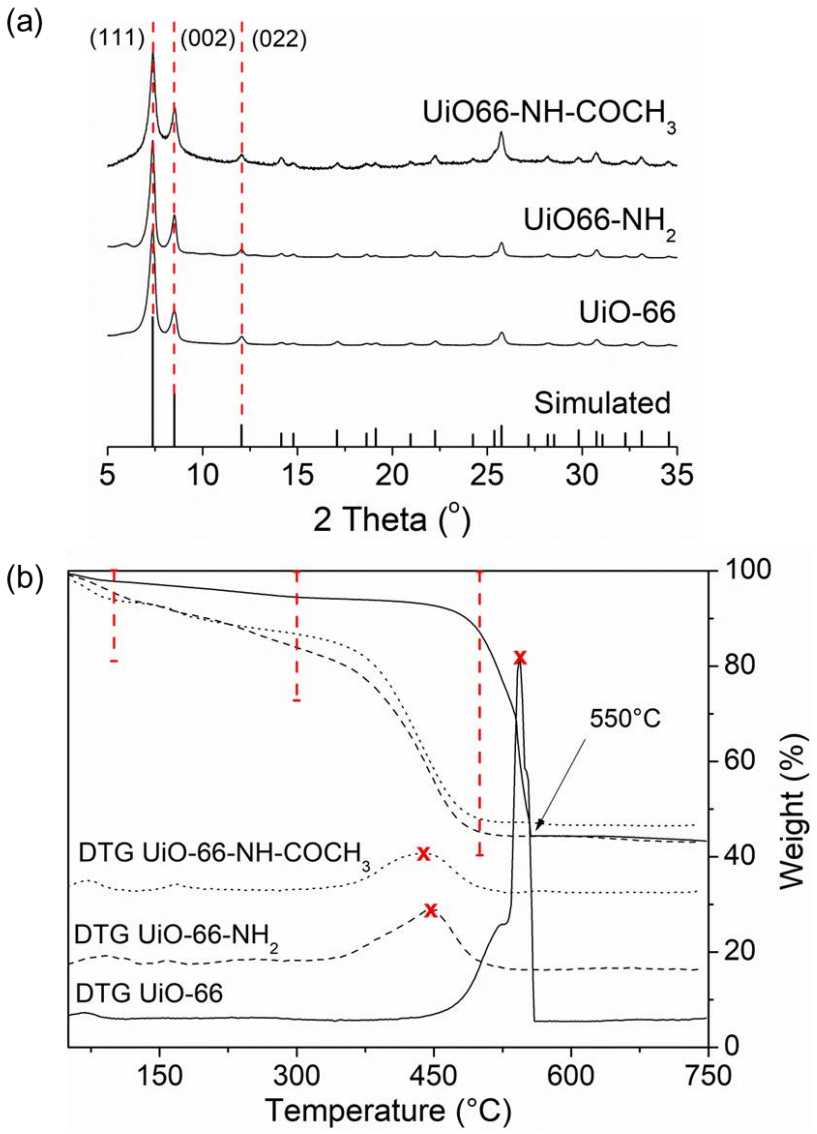

Fig. 5-6: XRD patterns of UiO-66, UiO-66-NH_2, and UiO-66-NH-$COCH_3$ NPs referring to the UiO-66 simulated pattern [137], (b) Weight loss curves and their corresponding derivatives (DTG) for the Zr-MOFs, obtained from TGA. Vertical dotted lines indicate the weight losses at discussed temperatures for ease of viewing.

Fig. 5-6(b) shows the weight loss curves of all prepared Zr-MOFs where the first drop below 100 ºC corresponds to the loss of remains of solvent. The next drop until 300 ºC corresponds to the dehydration of the $Zr_6O_4(OH)_4$ nodes to Zr_6O_6 [167]. The following drop up to 500 – 550 ºC is related to the decomposition of organic linkers before oxidation into ZrO_2 [43,137]. The higher mass losses observed in the functionalized UiO-66 NPs are due to their higher organic linker molecular masses. The MOF structure at the second stage is $Zr_6O_6L_x$ (L = BDC or BDC-NH_2 or BDC-NH-$COCH_3$, x = 1 – 6) where x indicates the stoichiometric ratio of the particular ligand present in the framework [167]. The as-

synthesized UiO-66 calculated to have 4-ligand with 2.1% missing organic linkers for every Zr atom [55], comparing to the simulated 4-ligand UiO-66 [167]. The decomposition temperatures (T_d, from the derivative maxima in Fig. 5-6(b)) of the Zr-MOFs confirm their high thermal stability in the range of 430 – 540 °C [136,137,242]: UiO-66 = 542 °C, UiO-66-NH_2 = 452 °C and UiO-66-NH-$COCH_3$ = 437 °C.

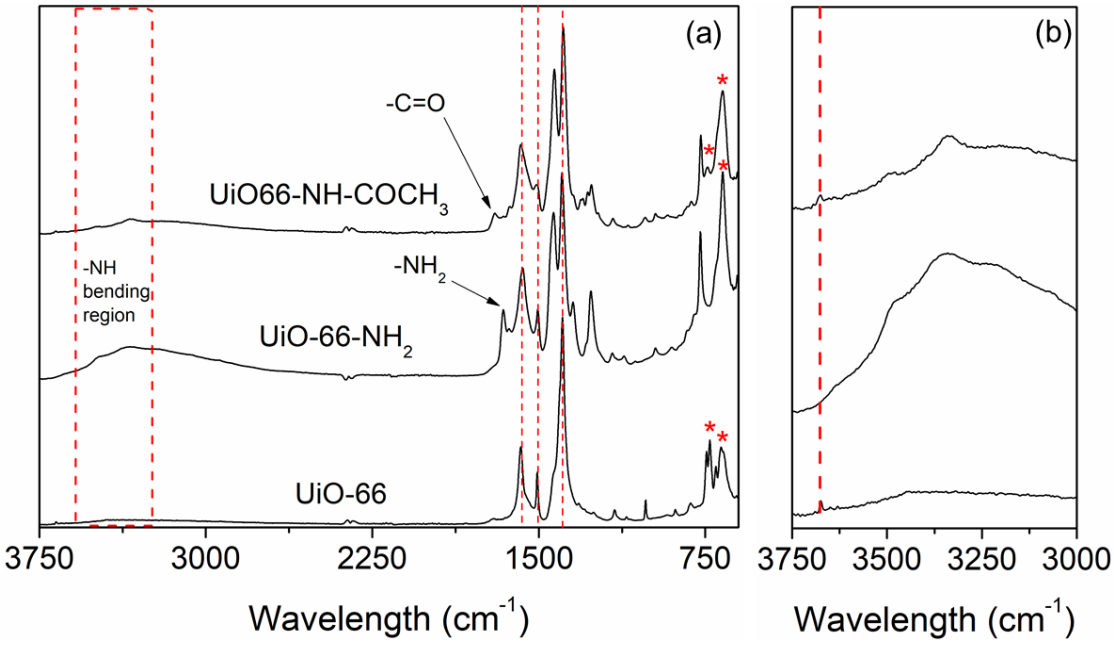

Fig. 5-7: FTIR spectra of the UiO-66 and its derivatives; (a) at the wavelength of 3750 – 600 cm^{-1}. The asterisk marks represent the longitudinal and transverse mode of Zr-O_2. Note: The 550 cm^{-1} peak is not presented here, and (b) The–NH bending region, between 3500 – 3000 cm^{-1} both primary R-NH_2 and secondary R_2-NH. The –OH peak at 3675 cm^{-1} is highlighted, indicating missing anionic BDC linkers [55,167].

Fig. 5-7 (a) shows the FTIR spectra of the Zr-MOFs, indicating the carboxylic –CO– (out-of-phase at 1393 cm^{-1}) and –COO– stretching (out-of-phase at 1503 cm^{-1} & in-of-phase at 1576 cm^{-1}) peaks for their strong reaction with zirconium. The longitudinal and transverse modes of Zr-O_2 are presented by the marked (asterisk) triplet peaks at 730, 680 and 550 cm^{-1} [133,228]. Especially for UiO-66-NH_2 and UiO-66-NH-$COCH_3$ the additional functional groups peaks can be ascribed to –NH wag at 770 cm^{-1} (both primary and secondary °N), –CN– stretching at 1266 cm^{-1} (primary °N), –NH_2 (primary °N) scissoring at 1680 cm^{-1} and acetamide –C=O vibration at 1690 cm^{-1}. The intensity of the peaks differs accordingly for UiO-66-NH_2 and UiO-66-NH-$COCH_3$ particularly for the broad –NH region between 3500 – 3000 cm^{-1}. Fig. 5-7(b) shows an –OH peak at 3675 cm^{-1}, indicating missing anionic BDC linkers on our 4-ligand Zr-MOFs [55].

The degree of PSM conversion of amino-functionalized UiO-66 to acetamide was determined by ^{1}H NMR, where the distinct downfield shift of C_2-position aromatic proton associated with the BDC ligand was calculated (Fig. 5-8). From the relative integration of these aromatic resonances between unmodified and modified UiO-66-NH_2 we estimated an amide conversion yield of 57% after a 24 h reaction at 55°C, lower than the reported yield of 88% for the same reaction period [133].

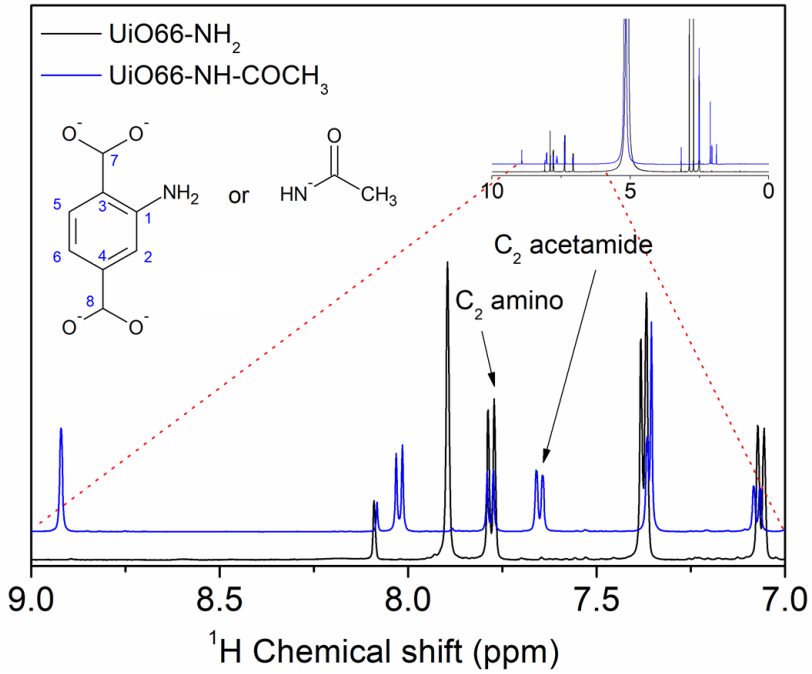

Fig. 5-8: ^{1}H NMR spectra of the digested solution of UiO-66-NH_2 and UiO-66-NH-$COCH_3$. Labeled are the C_2-position aromatic proton associated with BDC ligand and used as a reference in the conversion yield calculation.

The successful amine to amide conversion can also be observed by the additional –NH– peak at 9 ppm which only appears in the modified UiO-66-NH_2. Kandiah *et al.* [140] reported a 100% conversion of UiO-66-NH_2 with acetic anhydride on the 14th day of reaction at room temperature. The PSM reaction conversion is highly dependent on the reaction temperature, and for our study, we did not further optimize the PSM conditions. However, we believe our conversion level gave rise to functionalization enough to enhance both the filler-polymer interaction and the membrane CO_2 interaction regarding CO_2/CH_4 separation, both are discussed in Sec. 5.5.2 and Sec. 5.5.4.

The BET specific surface areas of the activated Zr-MOFs are (Table 5-1): UiO-66 = 951 $m^2 \cdot g^{-1}$, UiO-66-NH_2 = 965 $m^2 \cdot g^{-1}$ and UiO-66-NH-$COCH_3$ = 913 $m^2 \cdot g^{-1}$.

These values are consistent with the data previously reported for UiO-66 type materials [135].

Table 5-1: UiO-66 and its derivatives: BET specific surface areas from N_2 adsorption (P/P_o = 0.01 – 0.20) and N_2 adsorbed amounts at P/P_o = 0.2 and 0.9. Micropore volume and micropore and external surface areas have been calculated from the t-plot analysis, obtained with Harkins and Jura thickness equation in the 0.35 – 0.50 nm range.

Textural properties	*UiO-66*	*UiO-66-NH_2*	*UiO-66-NH-$COCH_3$*
A_{BET} $(m^2 \cdot g^{-1})$	951 ± 14	965 ± 13	913 ± 14
N_2 *adsorbed,* $cm^3(STP) \cdot g^{-1}$			
at P/Po = 0.2	281	285	270
at P/Po = 0.9	438	357	355
V_{PORE_micro}, $cm^3 \cdot g^{-1}$ *(at P/Po = 0.96)*	0.32	0.35	0.32
A_{PORE_micro}, $m^2.g^{-1}$	682	755	692
$A_{EXTERNAL}$, $m^2.g^{-1}$	269	210	222

Fig. 5-9 shows the N_2 adsorption and desorption isotherms of the Zr-MOFs obtained at 77 K. A combination of types I and IV isotherms is suggested in all samples. The presence of type IV isotherm is often due to capillary condensation between the smaller nanoparticles [55] and started to occur in our Zr-MOFs in the range of P/P_o = 0.5 – 0.8. No hysteresis was observed in larger particle sizes e.g. 60 – 80 nm UiO-66 [224] and ca. 200 nm UiO-66-NH_2 [67]. We found that the amino moieties did not have much effect on the UiO-66 system porosity as similarly observed in several publications [133,163,224]. A larger functional group (e.g., Br, –NO_2, – Naph [133]), however, does reduce the porosities. In agreement to this, the acetamide-PSM UiO-66-NH-$COCH_3$ presented the lowest BET specific surface area and possibly due to our lower conversion; it is still higher than the previously reported value of 818 $m^2 \cdot g^{-1}$ [133]. The consistent micropore volume values of 0.32 – 0.35 $cm^3 \cdot g^{-1}$ for the Zr-MOFs indicated no significant blockage of the pore system by the UiO-66 functionalization.

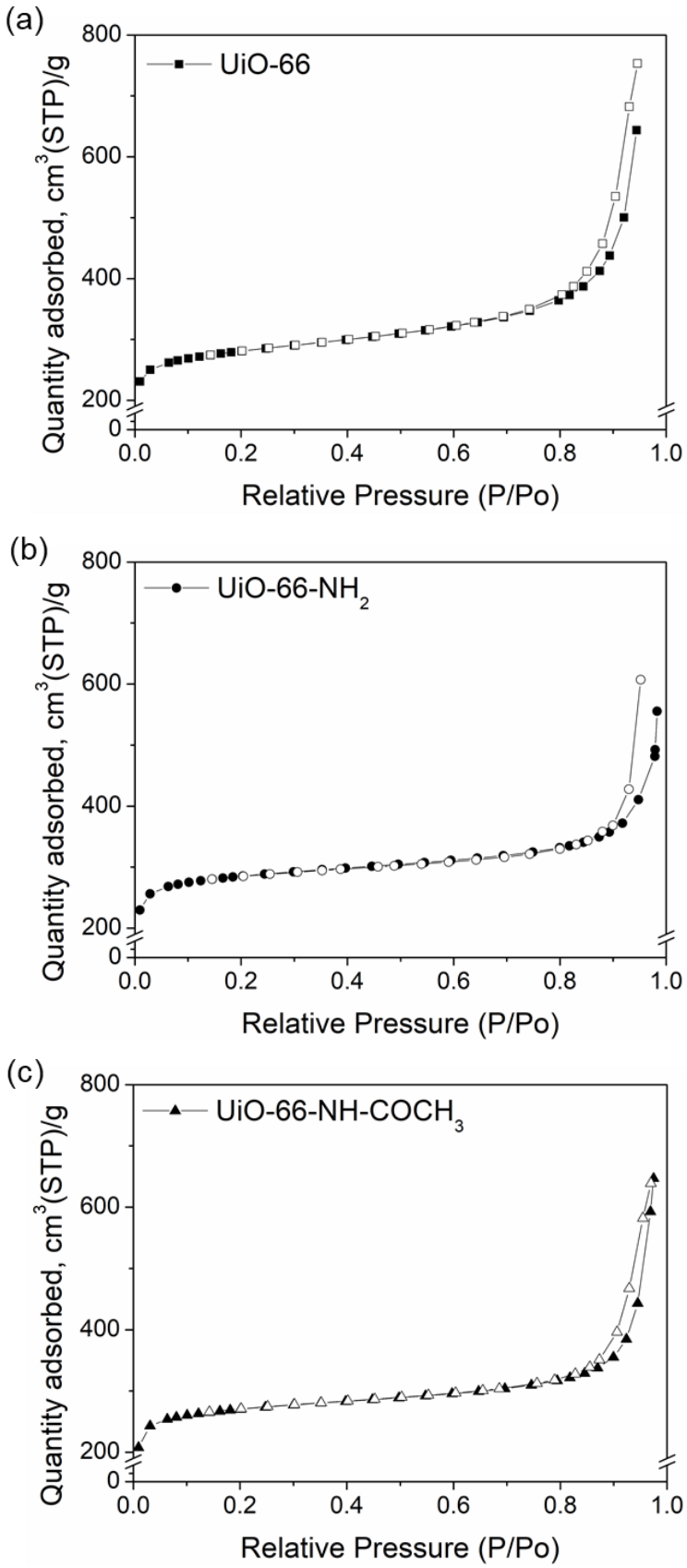

Fig. 5-9: N_2 adsorption (filled symbols) and desorption (empty symbols) isotherms measured at -196 °C for (a) UiO-66, (b) UiO-66-NH_2 and (c) UiO-66-NH-$COCH_3$.

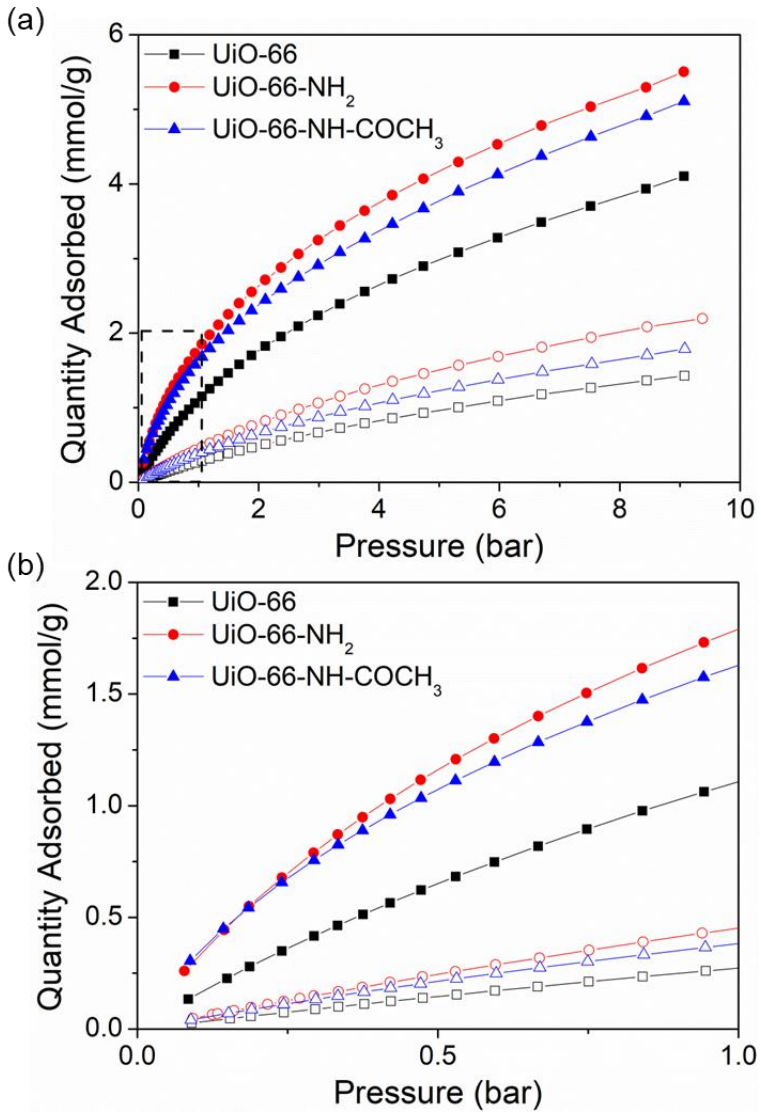

Fig. 5-10: CO_2 (filled symbols) and CH_4 (empty symbols) isotherms at (a) high pressure, 0.1 – 10 bar and (b) low pressure, 0.1 – 1.0 bar, measured at 25 °C.

Fig. 5-10(a) and Fig. 5-10(b) show the CO_2 and CH_4 adsorption isotherms of the Zr-MOFs measured at 25 °C between 0.1 – 10 bar and their resultant gas uptakes up to 1 bar. Table 5-2 presents the gas uptake values corresponding to Fig. 5-10(b). The UiO-66 functionalization increased the CO_2-philicity as expected. CO_2 adsorption capacities are in the following order (Table 5-2 at 1 bar and 25 ºC): UiO-66-NH_2 (1.79 mmol·g^{-1}) > UiO-66-NH-$COCH_3$
(1.63 mmol·g^{-1}) > UiO-66 (1.13 mmol·g^{-1}). The slightly lower adsorption capacities than the reported values (1.8 – 2.3 mmol CO_2·g^{-1}) measured under the same condition [43–45] can be due to the different activation methods used. At a higher activation temperature (>250 °C), dehydroxylated UiO-66 is produced and the resulting UiO-66 shows lower adsorption capacity [55,168]. The interaction between the framework pore affinity and the adsorbates

(CO_2, CH_4) greatly determines the capacity of the adsorption. The presence of an additional oxygen heteroatom in UiO-66-NH-$COCH_3$ increases the amide group polarity, thus making it more carbon-electron deficient. The amide group is more nucleophilic than the amine group and therefore expected to interact more strongly with CO_2. The slightly lower CO_2 adsorption capacity for UiO-66-NH-$COCH_3$ vs. its amino form (1.63 mmol·g^{-1} vs. 1.79 mmol·g^{-1}) is due to the higher steric hindrance created by the bulkier functional groups.

Table 5-2: UiO-66 and its derivatives: CO_2 and CH_4 uptakes obtained at 1 bar, corresponding to the measurements between 1 and 10 bar at 25 °C in Fig. 5-10(b).

MOF	***Adsorption properties (mmol·g^{-1})***		*****CO_2/CH_4 selectivity***
	CO_2	CH_4	
**UiO-66*	1.13	0.28	4.03
[43]	1.79	0.49	3.65
[44]	1.96	0.50	3.92
[45]	2.27	-	-
**UiO-66-NH_2*	1.79	0.45	3.98
**UiO-66-NH-$COCH_3$*	1.63	0.38	4.29

**This study*

***Calculated correspondingly from the CO_2 and CH_4 uptakes at 1 bar, 25 °C*

5.5.2. Membrane characterization

XRD and FTIR spectroscopy were used to determine any possible chemical interaction between the MOFs and polymer, while the flat sheet MMM microstructures (thickness of 100 – 150 μm) were imaged by SEM. Referring to the XRD patterns in Fig. 5-11(a), the pristine 6FDA-DAM shows a broad peak characteristic of an amorphous polymer with a *d*-spacing of 7.0 Å. The Zr-MOFs maintained their crystallinity in the polymer matrix, based on the comparison of MMM XRD patterns with UiO-66 characteristic diffraction peaks [137]. We found no evidence that the incorporation of functionalized UiO-66 altered the polymer *d*-spacing. In fact, this could occur due to polymer interpenetration into the NPs framework as previously reported in PEBA with UiO-66-NH_2 [224] and in 6FDA-DAM with mesoporous silica and hollow zeolite particles [57].

Additionally, FTIR absorbance of pristine 6FDA-DAM presented in Fig. 5-11(b) indicates the presence of the key functional group signals in diamine moiety. The symmetric –C=O stretching at 1720 cm^{-1} and the imide –C-N– at 1373 cm^{-1} remained unchanged. The spectra show no new additional peak, suggesting no strong chemical interaction between the MOF NPs and 6FDA-DAM. Nonetheless, a dominant presence of hydrogen bonding in the functionalized-MOF MMMs, in the following order; UiO-66-NH-$COCH_3$ > UiO-66-NH_2 > UiO-66 may have lessened filler agglomeration and improved MOF NPs-polymer interaction. The influence of hydrogen bonding can be observed in FTIR spectra (Fig. 5-10(c)) where upward shifts of the polymer carbonyl group by 3 cm^{-1} indicating a strong hydrogen bond interaction [254] were found in both functionalized-MOF MMMs. Their SEM images (Fig. 5-12) show smaller (up to ca. 500 nm, observed for 6 – 24 wt.% loading MMMs) and more uniform agglomerates compared to those of UiO-66 MMMs; ca. 200 – 600 nm, between the lowest to the highest loading (4 – 21 wt.%). This is due to the presence of an additional hydrogen donor/acceptor moieties (–NH_2 and –$NHCOCH_3$) in the functionalized Zr-MOFs, forming the intermolecular hydrogen bond with 6FDA-DAM bond/acceptor (–CF_3) and donor/acceptor (–C=O and –CN–).

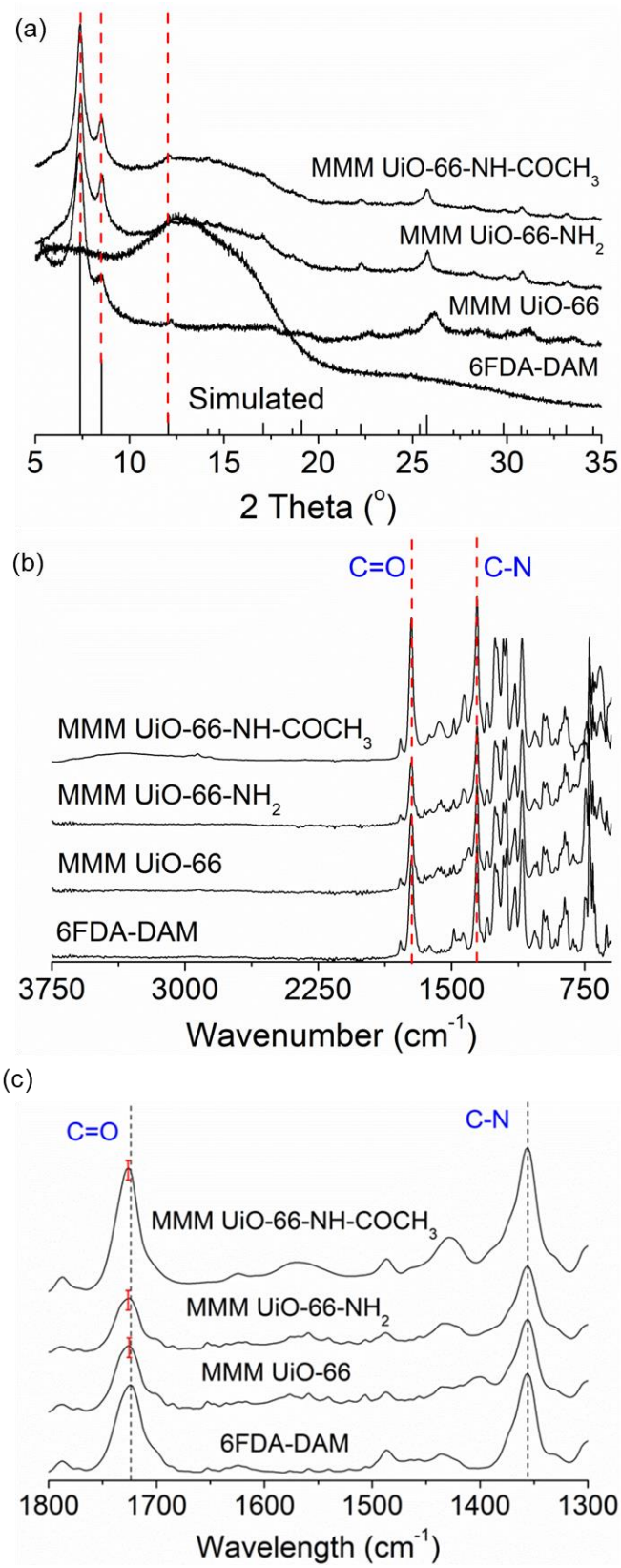

Fig. 5-11: (a) XRD patterns of UiO-66 (simulated [137]), polymer 6FDA-DAM and its Zr-MOF derived MMMs. (b) FTIR spectra of the 6FDA-DAM and Zr-MOF MMMs, with 14 – 16 wt.% of particle loadings.(c) the spectra focusing at the wavelength of 1300 – 1800 cm-1, showing a higher upward shift of ~3 cm-1, compared to the shift in UiO-66 MMM of only ~2 cm-1.

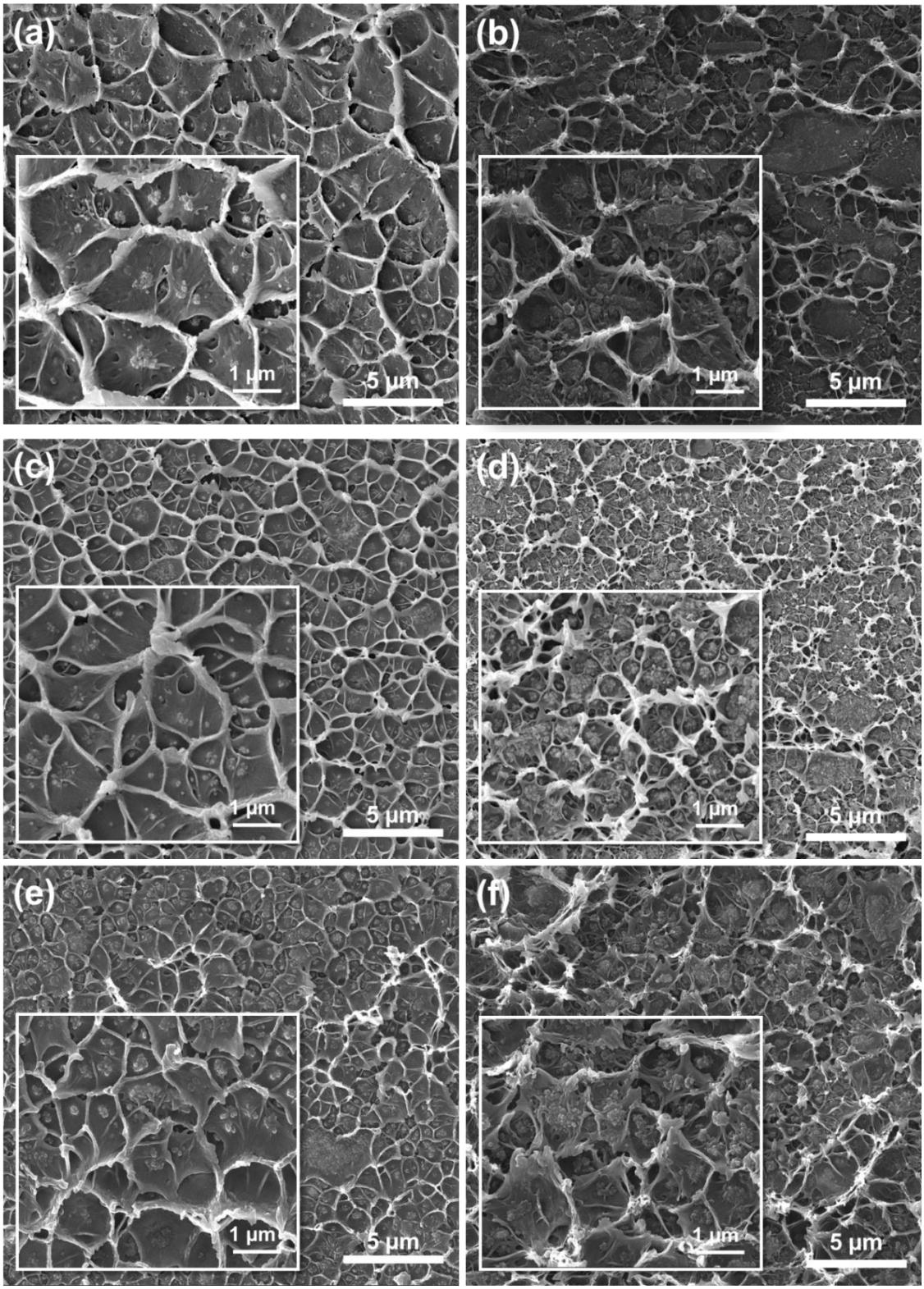

Fig. 5-12: SEM images of 6FDA-DAM MMMs with Zr-based MOFs at two different loadings: NPs UiO-66 (a) 4 wt.% and (b) 14 wt.%; UiO-66-NH_2 (c) 6 wt.% and (d) 16 wt.%; UiO-66-NH-$COCH_3$ (e) 6 wt.% and (f) 16 wt.%

DSC measurements (Table 5-3) showed that the as-purchased 6FDA-DAM transitioned to a rubbery polymer at 396 °C (glass transition temperature, T_g), close to the reported data at 372 – 395 °C [52,233,237]. The T_g increased by less than 10 °C in UiO-66 MMMs and by slightly more than 10 °C and around 20 °C in UiO-66-NH_2 and UiO-66-NH-$COCH_3$ MMMs, respectively.

Table 5-3: The glass transition temperature (T_g), decomposition temperature (T_d), calculated at 15% weight loss, solid density and free fractional value (FFV) values of the neat 6FDA-DAM and the respective Zr-MOFs MMMs.

Membrane	*Particle loading (wt.%)*	*Physical properties*			
		T_g (ºC)	T_d (ºC)	Density* (g cm^{-3})	FFV**
6FDA-DAM	-	396	522	1.259	0.238
UiO-66 MMM	8	395	525	1.188	0.281
	21	405	523	1.106	0.331
UiO-66-NH_2 MMM	6	398	527	1.237	0.251
	16	409	522	1.195	0.277
UiO-66-NH-$COCH_3$ MMM	6	399	536	1.299	0.214
	16	413	530	1.170	0.292

**Density for MMMs was normalized to the actual MOF loadings*
***FFV was calculated from the solid densities measured at 20 °C with pressurized He cycles between 2 – 20 bar*

In general, the inclusion of the MOF filler shows excellent interphase adhesion indicated by the filler-polymer stretched delamination segments (see Fig. 5-12). It also causes rigidification of polymer chains, thus limiting their movement and increasing the corresponding T_g values. MMM thermal stabilities were characterized by TGA and the corresponding decomposition temperature (T_d) values were calculated at 15% membrane weight loss (Fig. 5-13 and Table 5-3). As expected, the T_g changes were less substantial at lower loadings. The changes were most prominent in UiO-66-NH-$COCH_3$ MMMs due to the higher possibility of the hydrogen bonding to occur, leading to a stronger intermolecular interaction, as previously discussed. There were no remarkable differences in the UiO-66 and UiO-66-NH_2 MMMs T_d values compared to that of the pure 6FDA-DAM ($T_{d,\ pure}$ = 522 °C). The UiO-66-NH-$COCH_3$ MMMs (T_d = 530 °C), however, show T_d increment of around 8 °C. Regarding solid densities and FFV values it is important to note that the MMM densities were measured and normalized to the actual loadings of Zr-MOFs obtained from TGA analysis. The neat membrane showed a FFV of 0.238, higher than the 6FDA-DAM reported

values in the 0.181 – 0.190 interval [29,52,237] and in the upper range of most polymers (FFV = 0.1 – 0.3) [218,240].

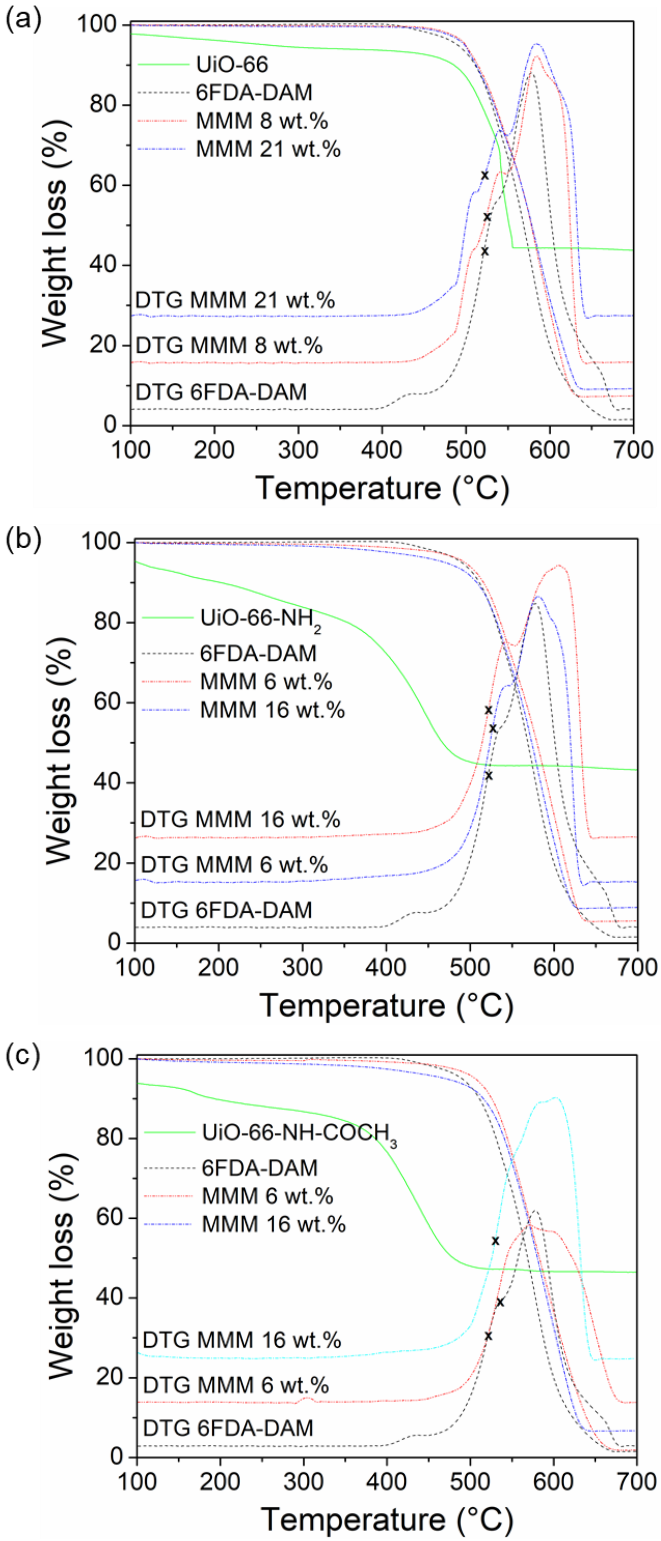

Fig. 5-13: The TGA curves and their respective first derivative for 6FDA-DAM with (a) UiO-66, (b) UiO-66-NH_2 and (c) UiO-66-NH-$COCH_3$ MMMs. Indicated (x) are the decomposition temperatures (T_d) calculated at 15% weight loss.

5.5.3. Gas transport properties

5.5.3.1. Mixed gas separation performances

Fig. 5-14(a-c) and Table 5-4 show the gas separation performances of 6FDA-DAM and its Zr-MOF MMMs with different wt.% loadings. The 6FDA-DAM neat membrane presented a higher CO_2 permeability and CO_2/CH_4 selectivity values (P_{CO2} = 997 Barrer, $\alpha_{CO2/CH4}$ = 29.2) than those recently reported with the same polymer [57,237]. This may be attributed to a few factors, such as higher polymer molecular weight (M_w = 418 kDa), higher free fractional volume (FFV = 0.24) and different post-treatment temperatures (180 °C). In fact, Zornoza *et al.* [57] reported P_{CO2} = 681 Barrer and $\alpha_{CO2/CH4}$ = 21.4 for membranes prepared from 6FDA-DAM with M_w = 81 kDa and FFV = 0.19, treated at the same temperature. Yeom *et al.* [237] reported P_{CO2} = 467 Barrer and $\alpha_{CO2/CH4}$ = 15.9 for membrane prepared from 6FDA-DAM with FFV = 0.18 and treated at 250 °C. FFV is a well-established factor that plays a major role in governing gas diffusivity within the polymer matrix [240]. Moreover, a higher annealing temperature produces a denser membrane thus affecting its free volume cavities and gas separation properties [162]. Several studies reported notable gas separation enhancement by optimizing the membrane thermal annealing procedure [255–257], optimizing the charge-transfer complex (CTC) phenomenon in aromatic polyimides, an inter- and intramolecular interaction which occurs more prominently at a high temperature [194,236].

In this study, the best performing 6FDA-DAM MMMs are with 14 – 16 wt.% Zr-MOF loadings. 14 wt.% UiO-66 and 16 wt.% UiO-66-NH_2 improved CO_2 permeability of 6FDA-DAM by 92% and 23%, respectively, while maintaining the CO_2/CH_4 selectivity at ~30. The addition of 16 wt.% of UiO-66-NH-$COCH_3$ improved both CO_2 permeability and CO_2/CH_4 selectivity by 27% and 13%, respectively. The higher permeability increment in the UiO-66 MMM is attributed to the easiness of CO_2 to diffuse into its frameworks, compared to the higher steric hindrance of functionalized-MOFs as discussed in the BET adsorption section. The significant improvement is also contributed by its higher FFV increment in the MMM and higher agglomeration degree of the UiO-66. The discussion follows accordingly in this section. Further Zr-MOF additions exhibited permeability-selectivity trade-off phenomenon more clearly where the selectivity reduced by 56% with 21 wt.% UiO-66, 31% with 22 wt.% UiO-66-NH_2 and 27% with 24 wt.% UiO-66-$NHCOCH_3$.

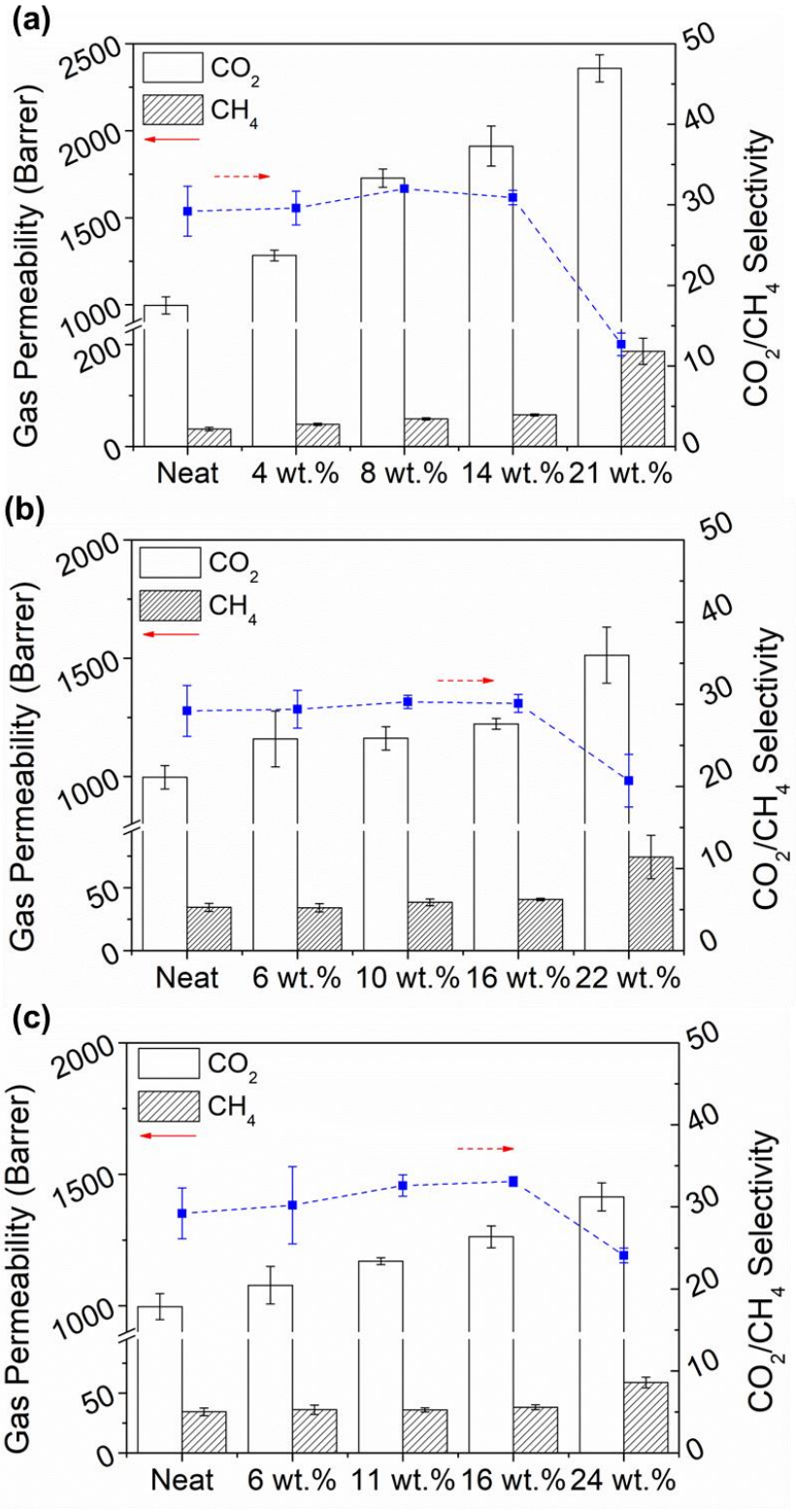

Fig. 5-14: CO_2 and CH_4 permeabilities and CO_2/CH_4 selectivities of 6FDA-DAM and the MMMs containing: (a) UiO-66, (b) UiO-66-NH_2 and (c) UiO-66-NH-$COCH_3$, tested at 35 °C, a pressure difference of 2 bar with an equimolar binary feed mixture of CO_2 and CH_4. Standard deviations were calculated based on at least 2 – 3 different membrane samples and error bars are presented.

Table 5-4: CO_2 and CH_4 permeabilities and CO_2/CH_4 selectivities of the neat 6FDA-DAM membrane and the Zr-MOFs MMMs, measured at 35 ºC, a pressure difference of 2 bar from an equimolar binary mixture of CO_2 and CH_4.

Polymer / Zr-MOFs	UiO-66 loading (wt.%)	Gas permeabilities (Barrer)		CO_2/CH_4 selectivity
		CO_2	CH_4	
6FDA-DAM	0	997 ± 48	34 ± 3.2	29.2 ± 3.1
UiO-66	4	1283 ± 30	44 ± 2.3	29.6 ± 2.1
	8	1728 ± 53	54 ± 2.1	32.0 ± 0.3
	14	1912 ± 115	62 ± 1.9	30.9 ± 0.9
	21	2358 ± 72	187 ± 25.8	12.7 ± 1.4
UiO-66-NH_2	6	1160 ± 118	34 ± 3.3	34.1 ± 0.3
	10	1162 ± 49	38 ± 2.7	30.3 ± 0.8
	16	1223 ± 23	41 ± 0.9	30.1 ± 1.1
	22	1514 ± 118	74.4 ± 17	20.7 ± 3.2
UiO-66-NH-$COCH_3$	6	1078 ± 71	36 ± 3.9	30.2 ± 4.7
	11	1170 ± 13	36 ± 1.7	32.6 ± 1.3
	16	1263 ± 42	38 ± 2.0	33.1 ± 0.6
	24	1414 ± 53	59 ± 4.4	24.1 ± 0.9

At the stated optimum loadings, the Zr-MOF addition was able to achieve ideal MMM morphology as presented in case 0 by Hashemifard *et al.* [155] and overcame the permeability-selectivity trade-off [258]. The enhanced permeability can be ascribed to the CO_2-philic characteristics of the Zr-MOFs [136] where a stronger energetic interaction between CO_2 (higher quadrupole moment than CH_4) and the nanoparticle surfaces to occur at zero coverage. Besides higher gas diffusion in the Zr-MOFs, the NPs addition improved the MMM gas diffusivity by creating a third selective interface region [106] and the additional free volume in the interfacial region [29,240]. The NPs agglomeration was more prominent at the highest loading as discussed, and the selectivity reduction ought to be caused by the formation of non-selective by-pass channels in the agglomerates [29] and possibly micro-voids in the interface region [155], although it cannot be evidenced by SEM.

Fig. 5-15 shows the gas permeabilities and the membrane FFV values calculated from the solid densities measured at 20 °C with pressurized He cycles between 2 and 20 bar and polymer van der Waals volume [203]. The FFV for 6FDA-DAM with 14 wt.% UiO-66

increased the highest by 40%, contributing to almost 100% increments for both CO_2 (from 997 to 1912 Barrer) and CH_4 (from 34 to 62 Barrer) permeabilities. Both 16 wt.% UiO-66-NH_2 and 16 wt.% UiO-66-NH-$COCH_3$ only increased their membrane FFVs by 16% and 23% and enhanced their CO_2 permeabilities by 23% and 27%, respectively. However, it is important to note that the CH_4 permeabilities in these membranes only increased by 11% and 18%, respectively. The additional FFV in the MMM was formed due to the polymer chain packing disruptions, especially in the NPs-polymer soft-delaminated interfacial region (refer to SEM images in Fig. 5-12). In the functionalized UiO-66 MMMs the FFV increments were lower which is in agreement with the expected stronger intermolecular interaction of polymer with the polar functional groups of these two MOFs.

Fig. 5-16 shows the as-prepared 6FDA-DAM neat membrane (P_{CO2} = 997 ± 50 Barrer, $\alpha_{CO2/CH4}$ = 29 ± 3) benchmarked to the 2008 Robeson upper bound [21]; positioned above the trade-off line and performed better than recently reported 6FDA-DAM MMMs with other MOFs. This outstanding performance was further enhanced by the incorporation of MOFs. 6FDA-DAM MMMs showed the best performance with 14 wt. % of UiO-66 (P_{CO2} = 1912 Barrer, $\alpha_{CO2/CH4}$ = 31), 16 wt.% of UiO-66-NH_2 (P_{CO2} = 1223 Barrer, $\alpha_{CO2/CH4}$ = 30) and 16 wt.% of UiO-66-NH-$COCH_3$ (P_{CO2} = 1263 Barrer, $\alpha_{CO2/CH4}$ = 33). Further addition of MOFs up to 21 – 24 wt.% particle loading decreased the CO_2/CH_4 selectivity and a permeability-selectivity trade-off phenomenon took place. The CO_2/CH_4 selectivities were lower than that of the neat membrane due to the intensive creation of defective transport paths. Overall, it's important to note that the use of UiO-66 and its functionalized derivatives are both beneficial to improve the separation shortcomings of a certain polymer depending on the improvement goals, i.e., to improve the CO_2 permeability of low permeable Matrimid® using UiO-66 and to improve the CO_2/CH_4 selectivity of using low selectivity PIMs.

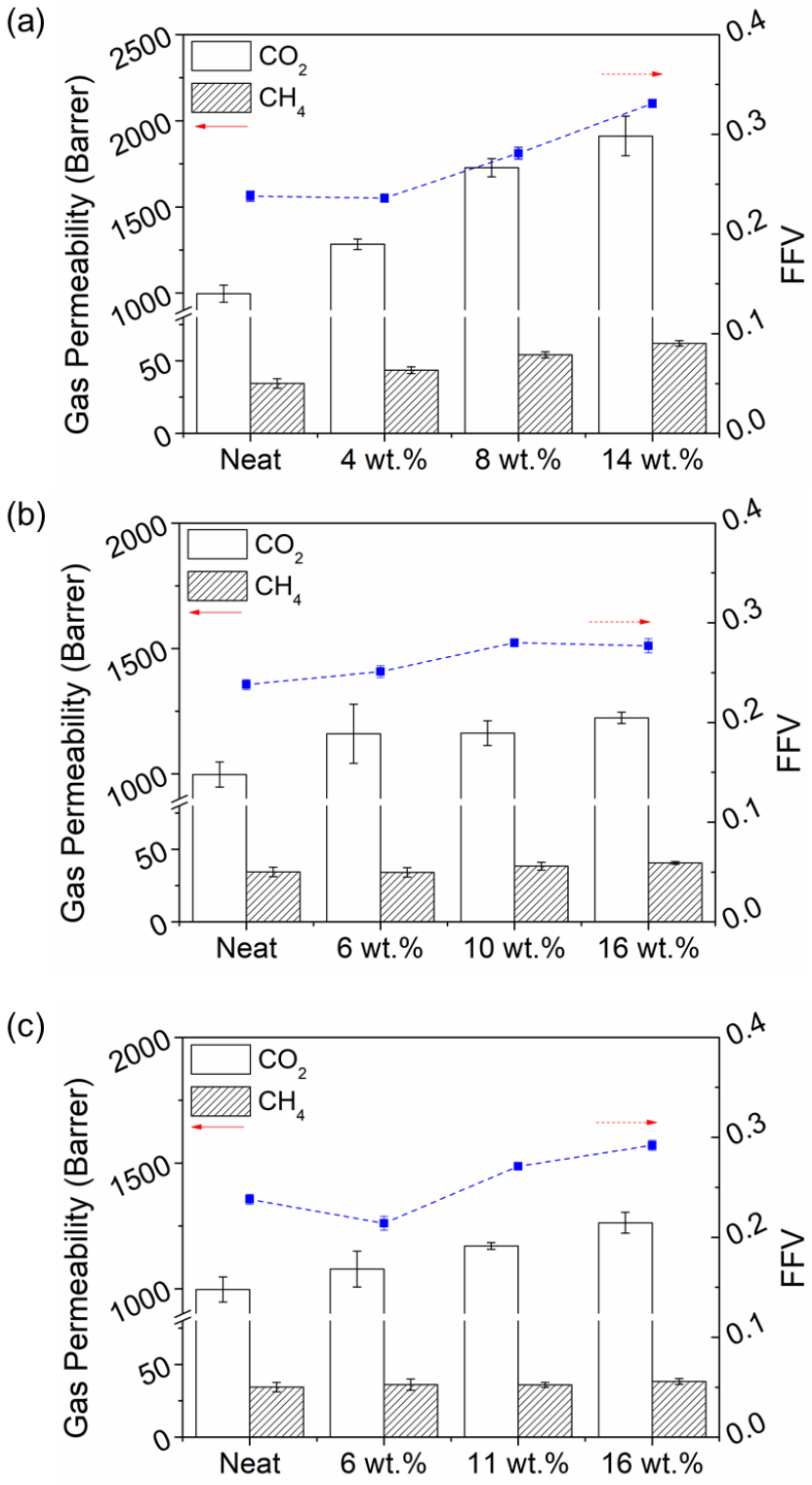

Fig. 5-15: CO_2 and CH_4 permeabilities and FFV values, calculated from solid densities measured at 20 °C with pressurized He cycles between 2 and 20 bar, of the neat 6FDA-DAM and its MMMs with (a) UiO-66 (a) UiO-66-NH_2 and (c) UiO-66-NH-$COCH_3$.

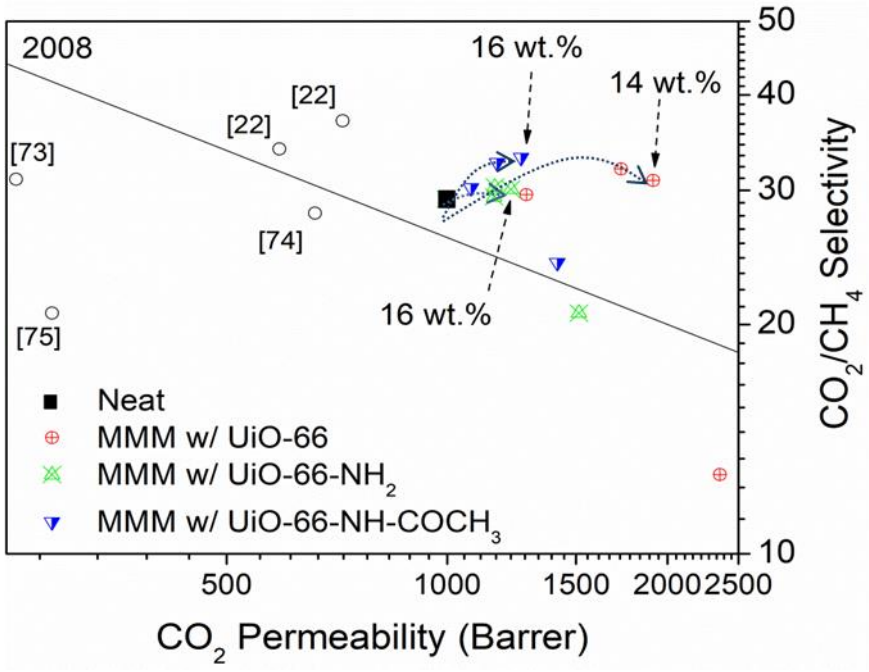

Fig. 5-16: CO_2 and CH_4 permeabilities and CO_2/CH_4 selectivities of 6FDA-DAM and the MMMs, compared to the several recently published 6FDA-DAM MMMs with other MOFs (unfilled circles); ZIF-11 [124], ZIF-90A [86], ZIF-90B [86], NH_2-MIL-53A [40] and Noria-CotBu [234], at their optimum loading of between 9.4 – 20 wt.%, measured at 25 – 35 °C and 1 – 4 bar. (*) indicates single gas permeation and its ideal selectivity, and (**) indicates binary CO_2:CH_4 mixture measurement at 1:1 volume ratio.

Langmuir coefficients for the Zr-MOFs are summarized in Table 5-5. The calculated permeabilities from an extended Maxwell model in comparison with experimental data are presented in Table 5-6, as presented in Section 5.4.4. The calculation was only conducted up to the optimum loading (14 – 16 wt.%) in all the MMM systems under assumption of ideal MMM morphologies. For UiO-66 MMM the model underestimated both CO_2 and CH_4 permeability with relative errors of between 15 – 30% and 13 – 26%, respectively (see Fig. 5-17(a)). In the case of UiO-66-NH_2 and UiO-66-NH-$COCH_3$ MMMs, the predicted CO_2 and CH_4 permeabilities are in good agreement with experimental data with only a slight overestimation of <12% relative error (Fig. 5-17(b) and Fig. 5-17(c)). However, the model underestimated the CH_4 permeability of UiO-66-NH-$COCH_3$ MMM at 16 wt.% loading by 20%.

Table 5-5: Calculated Langmuir coefficient parameters.

Zr-MOFs	Gas	Langmuir parameters		Knudsen
		q_{mi} (mmol·g^{-1})	K_i (1·bar^{-1})	D_{oi} (m^2·s^{-1})
UiO-66	CO_2	9.21	0.13	5.84 x 10^{-8}
	CH_4	3.87	0.08	4.24 x 10^{-8}
UiO-66-NH_2	CO_2	12.74	0.16	8.24 x 10^{-8}
	CH_4	5.06	0.10	5.66 x 10^{-8}
UiO-66-NH-$COCH_3$	CO_2	17.73	0.10	1.24 x 10^{-7}
	CH_4	4.95	0.08	5.81 x 10^{-8}

Table 5-6: Comparison of experimental data and calculated permeability from Maxwell model and their error deviation.

MMMs	Experimental data		Maxwell model data		Relative errors	
	P_{CO2} (Barrer)	P_{CH4} (Barrer)	P_{CO2} (Barrer)	P_{CH4} (Barrer)	CO_2 %RE	CH_4 %RE
UiO-66						
4 wt.%	1283	44	1094	38	-14.8	-13.3
8 wt.%	1728	54	1190	41	-31.1	-24.1
14 wt.%	1912	62	1335	46	-30.2	-25.7
UiO-66-NH_2						
6 wt.%	1160	34	1136	39	-2.0	+15.0
10 wt.%	1162	38	1229	42	+5.8	+10.5
16 wt.%	1223	41	1369	47	+11.9	+16.3
UiO-66-NH-$COCH_3$						
4 wt.%	1078	36	1131	39	+4.9	+8.1
8 wt.%	1170	38	1246	43	+6.3	+12.3
14 wt.%	1263	59	1356	47	+7.4	-20.4

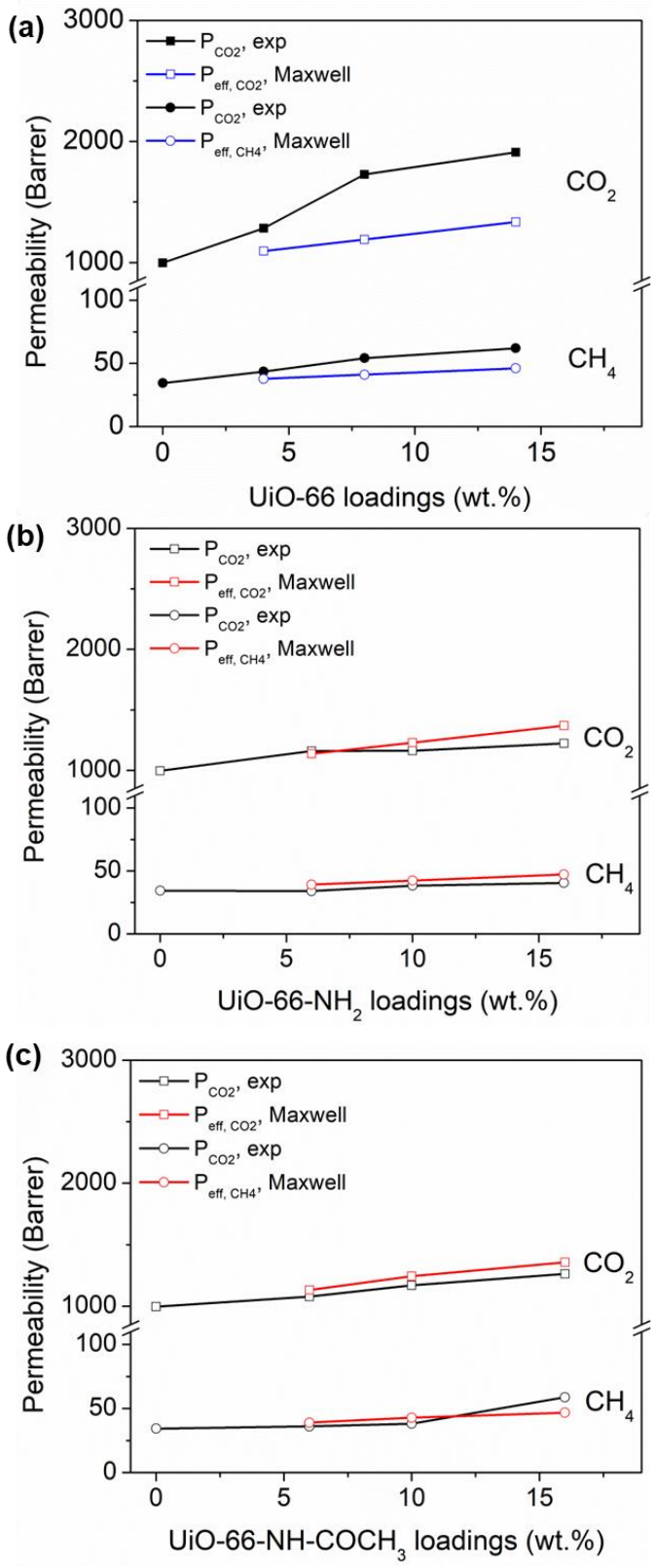

Fig. 5-17: The experimental CO_2 and CH_4 permeability data of (a) UiO-66, UiO-66-NH_2 and (c) UiO-66-NH-$COCH_3$ MMMs, measured with an equimolar CO_2:CH_4 binary mixture at 2 bar pressure difference at 35 °C, in comparison to the calculated effective permeability of MMM using an extended Maxwell model.

Overall, the relative error increases with the increasing loading. A similar trend was also revealed in other MMM systems [51,259,260]. This behaviour can be influenced by a several factors which is not taken into account, such as: (i) the model does not consider the competitive sorption of CO_2 and CH_4; (ii) the model assumes an ideal morphology between both phases with homogeneous dispersion, and referring to Sec. 5.5.2, we are aware that the agglomeration of different degree is present in the Zr-MOFs, and (iii) the model assumes spherical shapes particles, while our Zr-MOFs are in octahedral form.

5.5.3.2. Performance at various CO_2 partial pressures

One of the advantages of membrane technology in natural gas processing is its high adaptability to various gas volumes and CO_2 concentrations. To demonstrate the efficiency of the prepared MMMs in gas separation, we subjected each of the best-performing MMMs for binary gas separation with different CO_2 content (10 – 50%) in the feed gas at 2 bar pressure difference and 35 °C.

Fig. 5-18 shows the effect of CO_2 partial pressure on the MMMs separation properties where CO_2 permeability increased with an increasing CO_2 partial pressure in the feed gas. Conversely, it decreased the CH_4 permeability and directly translated into an improvement in the CO_2/CH_4 selectivity. The addition of Zr-MOFs to 6FDA-DAM polymer matrix assuredly increased its FFV and affected the gas diffusivity as well as the gas solubility, simultaneously affecting the competitive sorption effects [53,219].

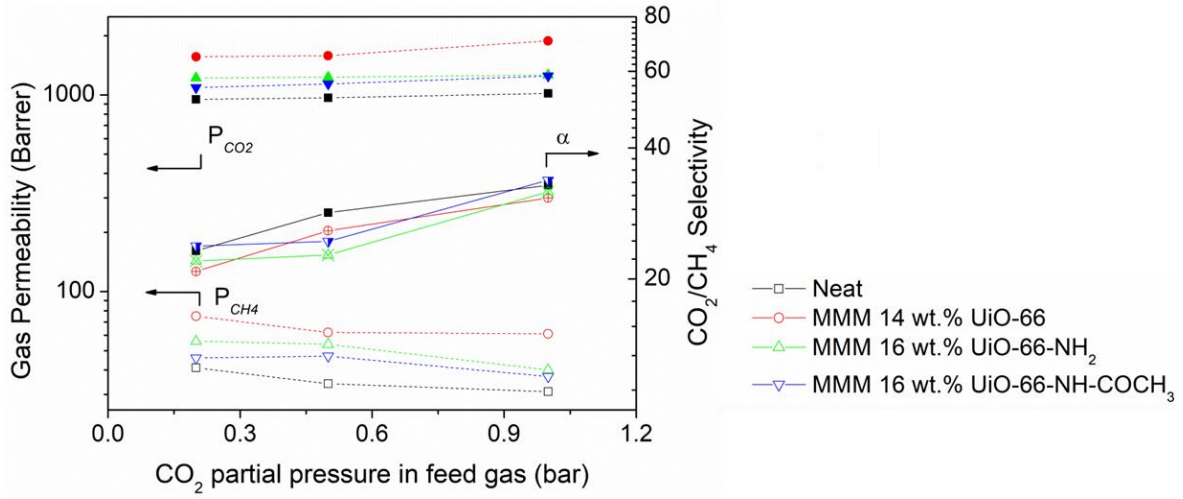

Fig. 5-18: Effect of CO_2 feed partial pressure on CO_2/CH_4 separation properties of the Zr-MOFs, measured at 2 bar pressure difference at 35 °C.

Interestingly the CO_2 permeability in the UiO-66 MMMs increased more than in the functionalized UiO-66 MMMs. This would suggest that competitive sorption is more prominent in the membrane matrix and it may be also influenced by different filler-polymer interactions. The CO_2-philicity of filler which is proportional to the CO_2 adsorption capacities (Table 5-2) that would favor MMMs containing functionalized UiO-66 has probably lower effect. The differences may also be influenced by the Zr-MOF pore opening towards CO_2 adsorption in the presence of the bulkier organic linkers with higher space steric hindrance and polarity, promoting selective CO_2 transport over that of CH_4. Fig. 5-19(a) shows their performances with regards to the 2008 Robeson upper bound for ease of comparison [21].

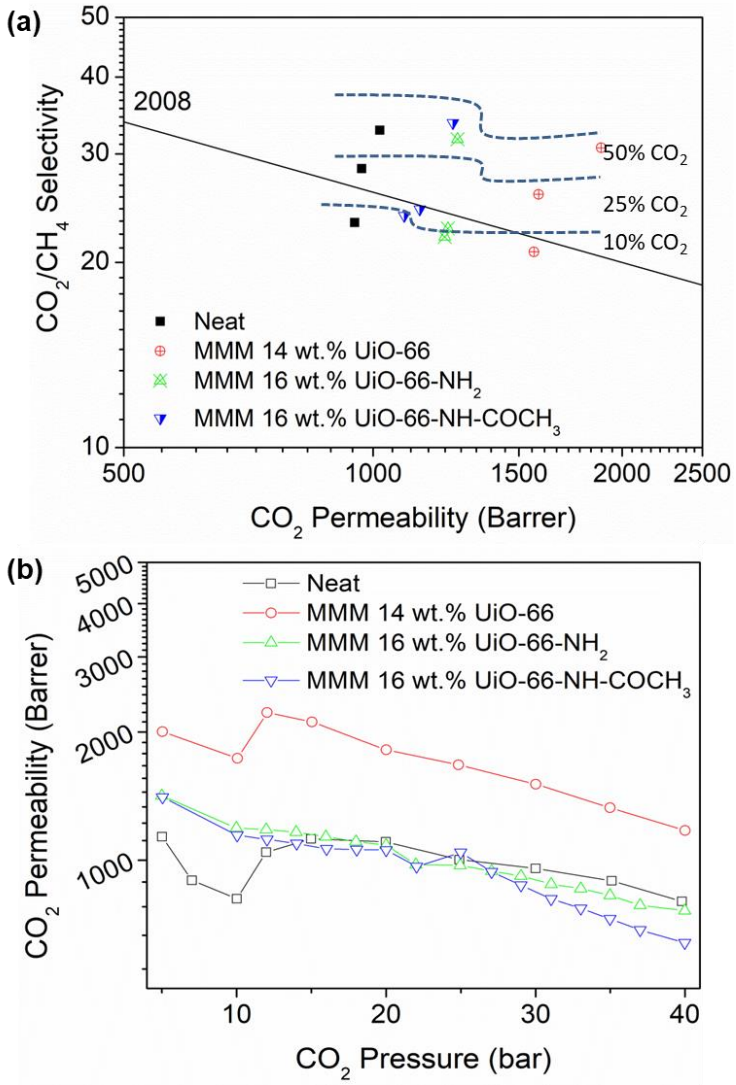

Fig. 5-19: CO_2/CH_4 separation performances of the Zr-MOFs 6FDA-DAM MMMs against 2008 Robeson upper bound [21]. (b) CO_2 single gas permeability vs. CO_2 pressure for the neat 6FDA-DAM and its best performing Zr-MOFs MMMs, measured at 5 – 40 bar. All measurements were conducted at 35°C.

5.5.3.3. Pure CO_2 and mixed gas high-pressure separation performance

High CO_2 partial pressure can plasticize a glassy polymer [48,52] and leads to an increase of the lower permeable component flux thus reducing the gas separation performance. We investigated the phenomenon by feeding pure CO_2 and CO_2/CH_4 binary mixtures (10:90 vol.% and 50:50 vol.%, see Fig. 5-20) up to 40 bar at 35 °C and the permeability and selectivity were measured. Fig. 5-19(b) and Fig. 5-21 show the CO_2 permeability as a function of CO_2 pressure and its CO_2 fluxes against the pressure difference.

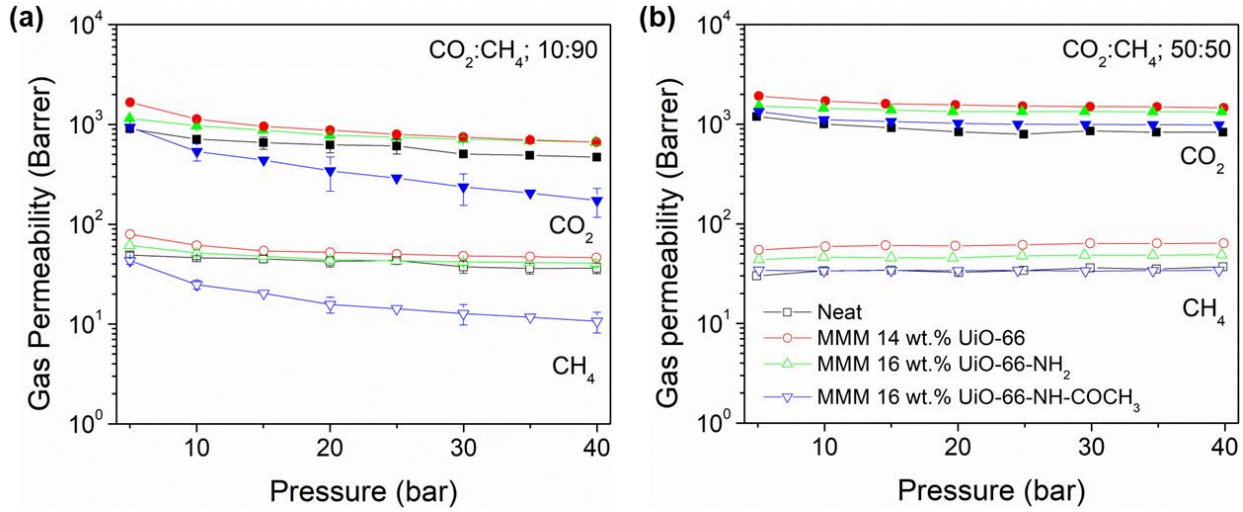

Fig. 5-20: CO_2/CH_4 selectivity vs. pressure for 6FDA-DAM and its best performing Zr-MOFs MMMs, measured between 5 – 40 bar at 35 °C with (a) 10%:90% and (b) 50%:50% CO_2:CH_4 binary mixture.

We observed a continuous decrease in permeability with increasing pressure, following the predicted behavior of the dual-mode sorption model [261,262]. Accordingly to our stabilization and measurement practice no CO_2-induced plasticization effect was observed for the neat 6FDA-DAM up to 40 bar, conflicting with the reported plasticization pressure for the same polymer in the 10 – 20 bar range [57,263]. The difference here could be attributed to their different polymer physical properties, i.e., molecular weight, density, and free volume, as previously discussed in Section 5.5.2 and 5.5.3.1. A similar observation was reported in a Matrimid® 5218 MIL-53(Al) MMM during a high-pressure single gas measurement [106]. Both functionalized MMMs showed a continuous decrease in CO_2 permeability from 5 to 40 bar, demonstrating the competitive sorption effects and the gradual saturation of the permeating gas in the membrane with increasing pressure. For 10:90 vol.% and 50:50 vol.% CO_2:CH_4 gas mixture separations, we witnessed no upward inflection in CO_2 permeability in all membranes when measured between 5 and 40 bar at 35 °C (Fig. 5-22 and

Fig. 5-23) and only gradual CO_2/CH_4 selectivity reduction (Fig. 5-24(a–b)). However, there is a slight increase in CH_4 permeability when tested with the 50 vol.% of CO_2 in feed content for the neat membrane, UiO-66 and UiO-66-NH_2 MMMs.

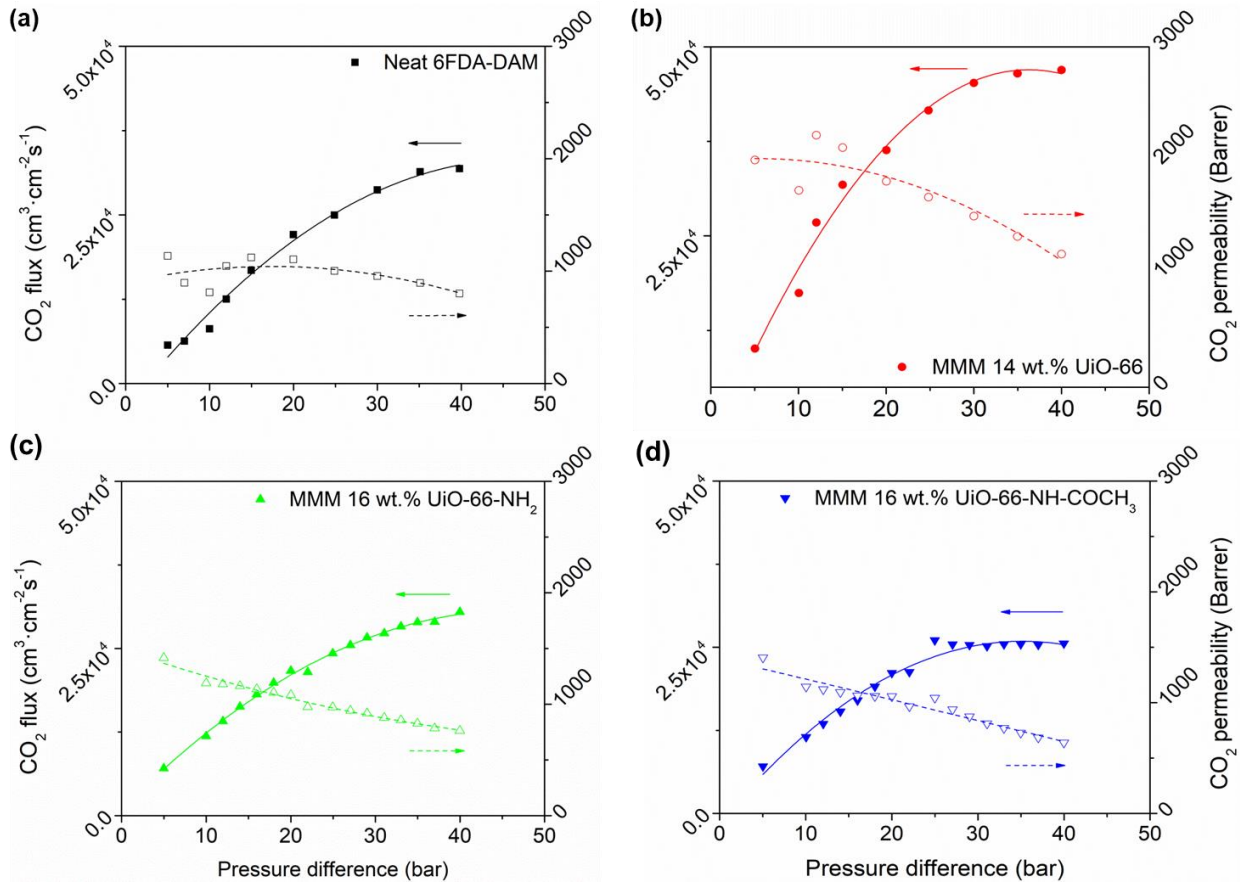

Fig. 5-21: Gas fluxes and permeabilities of 6FDA-DAM and its Zr-MOF MMMs as a function of the pressure difference, measured with pure CO_2 at 35 °C between 5 – 40 bar.Lines are drawn to illustrate the trends and not theoretical predictions.

The change in gas permeability with increasing feed pressure is influenced by either dual-mode adsorption transport or plasticization and the trend, in the case of binary feed mixture can be observed by comparing CO_2 and CH_4 permeabilities at the lowest (5 bar) and the highest feed pressure (40 bar) [264]. For our membranes, CO_2 permeability decreases with increasing pressure when tested with pure CO_2 and CO_2:CH_4 binary mixture, which indicated the dominance of dual-mode adsorption [264,265]. The net reduction effects are significant as can be observed in Fig. 5-25. As presented in Fig. 5-22 and Fig. 5-23, the continuous reduction of CO_2 permeability in all measurement indicated the absence of CO_2-induced plasticization in the thick membrane [265]. Despite the flux increments, permeability reduction also indicated decreasing diffusion and permeation coefficient in the

membrane matrixes as a function of pressure. This is a good indication that the membrane showed no CO_2-induced plasticization in the tested pressure range. Despite the known fact that the permeating gasses are adsorbed higher into the polymer matrix at elevated pressure, causing the increase in chain mobility and plasticization, we observed no such behavior [53,54,221]. Interestingly, Bachman *et al.* [263] also reported 6FDA-DAM with 25 wt.% Ni_2(dobdc), when tested with an equimolar of CO_2: CH_4 gas mixture, plasticization at 47 bar, despite the polymer CO_2-induced plasticization pressure at 10 bar in CO_2 pure gas.

The increase of CH_4 permeability in the neat polymer, UiO-66 and UiO-66-NH_2 MMMs is shown in Fig. 5-25(e) when tested with an equimolar CO_2:CH_4 binary mixture. The increment is also observable in Fig. 5-23. Such behavior was explained by Bachman and Long [264], where the occurrence is due to a lower Langmuir solubility component, as compared to its Henry's Law component. Thus, the observation was concluded to be plasticization and most likely to be contributed by its higher competitive sorption effect in the case of an equimolar feed mixture separation. Higher functionalization of UiO-66 seems to reduce the plasticization effect (almost zero net permeability reduction effect) and its permeability is dominated by dual-mode transport over the entire pressure range. Additionally, both neat 6FDA-DAM and UiO-66 membranes displayed a slight increase of CO_2 permeability at ~ 10 – 12 bar (Fig. 5-19(b) and Fig. 5-21). These inflections, however, do not correspond to the plasticization points as the CO_2 permeability further decreases with higher pressure. Thus there was no CO_2-induced plasticization at the reported pressures (~ 10 – 20 bar).

Additionally, we can observe that the CH_4 permeability decreased more than that of CO_2, indicating that CH_4 adsorption into the polymer matrix was suppressed at the high pressure. This may be explained by competitive sorption [219]: CO_2 would penetrate faster into the membrane adsorption sites which associated with the nonequilibrium free volume in glass polymer and hindered the CH_4 transport through the membrane. Furthermore, the extent of CO_2-induced plasticization depends on a few factors including the membrane thickness [266] whose influence on our membranes (thickness range of 100 – 150 μm) was not investigated.

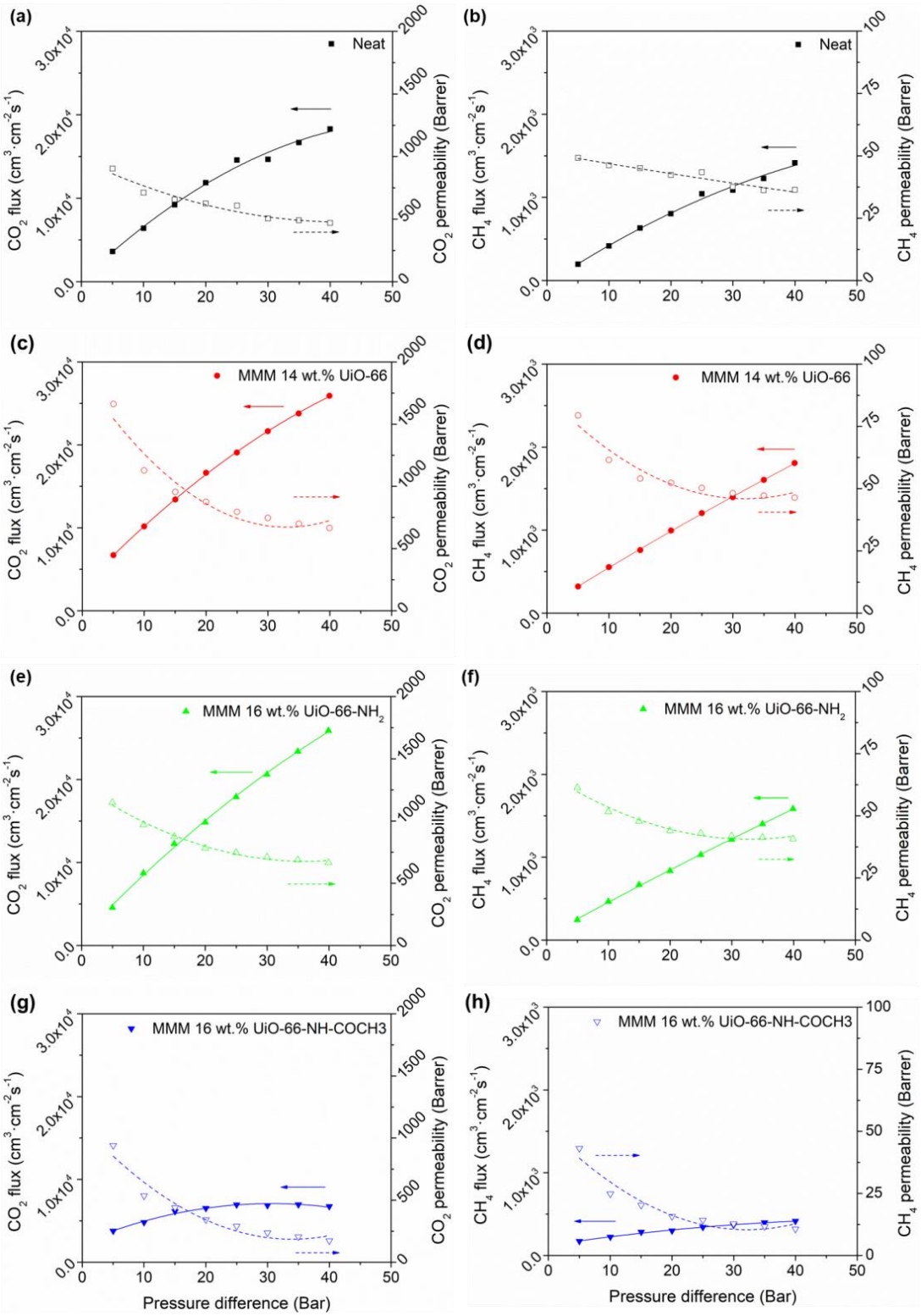

Fig. 5-22: Gas fluxes and permeabilities of 6FDA-DAM and its Zr-MOF MMMs as a function of the pressure difference, measured with 10:90 vol:vol CO_2:CH_4 at 35 °C between 5 – 40 bar.Lines are drawn to illustrate the trends and not theoretical predictions. Lines are drawn to illustrate the trends and not theoretical predictions.

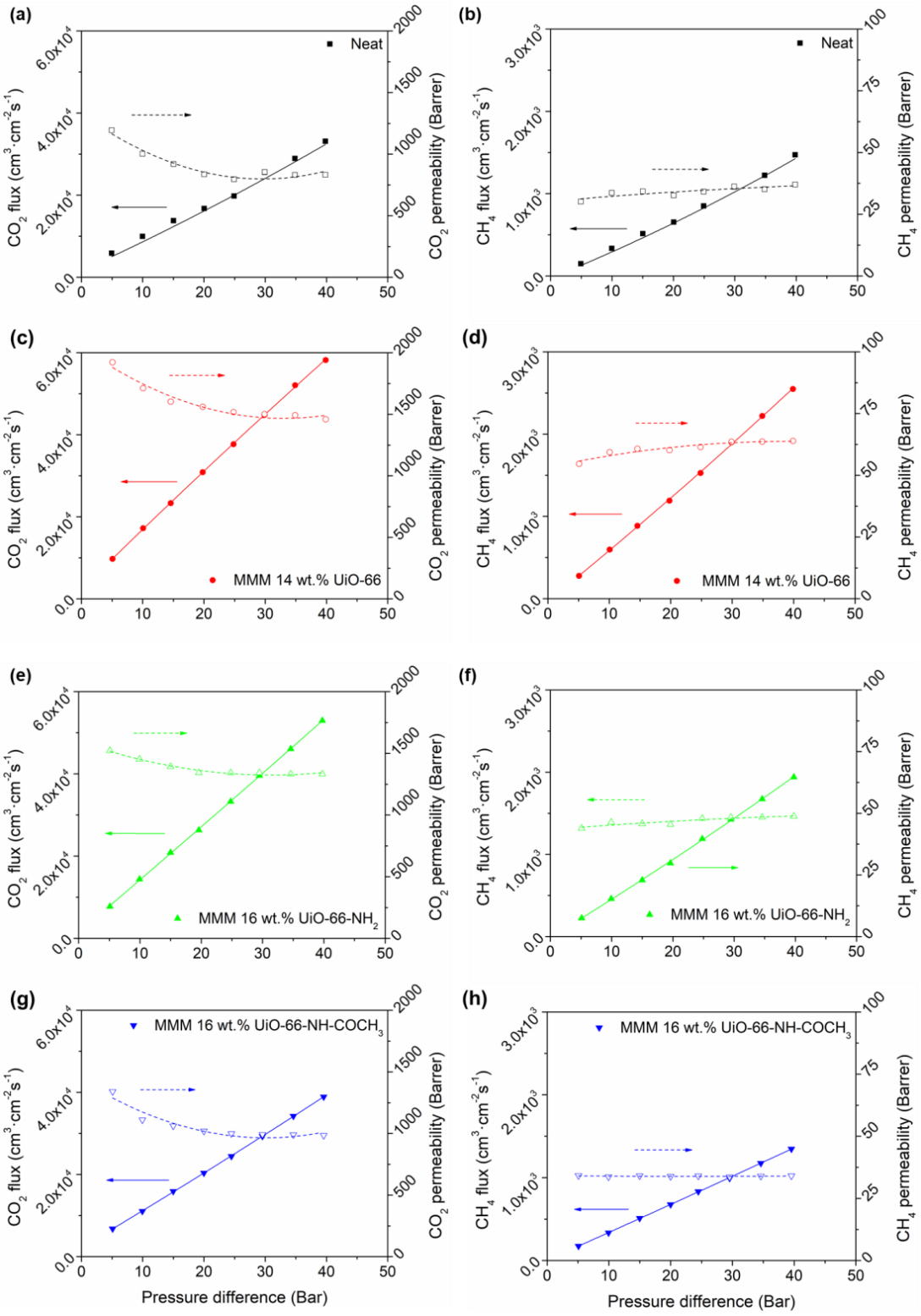

Fig. 5-23: Gas fluxes and permeabilities of 6FDA-DAM and its Zr-MOF MMMs as a function of the pressure difference, measured with 50:50 vol:vol CO_2:CH_4 at 35 °C between 5 – 40 bar.Lines are drawn to illustrate the trends and not theoretical predictions. Lines are drawn to illustrate the trends and not theoretical predictions.

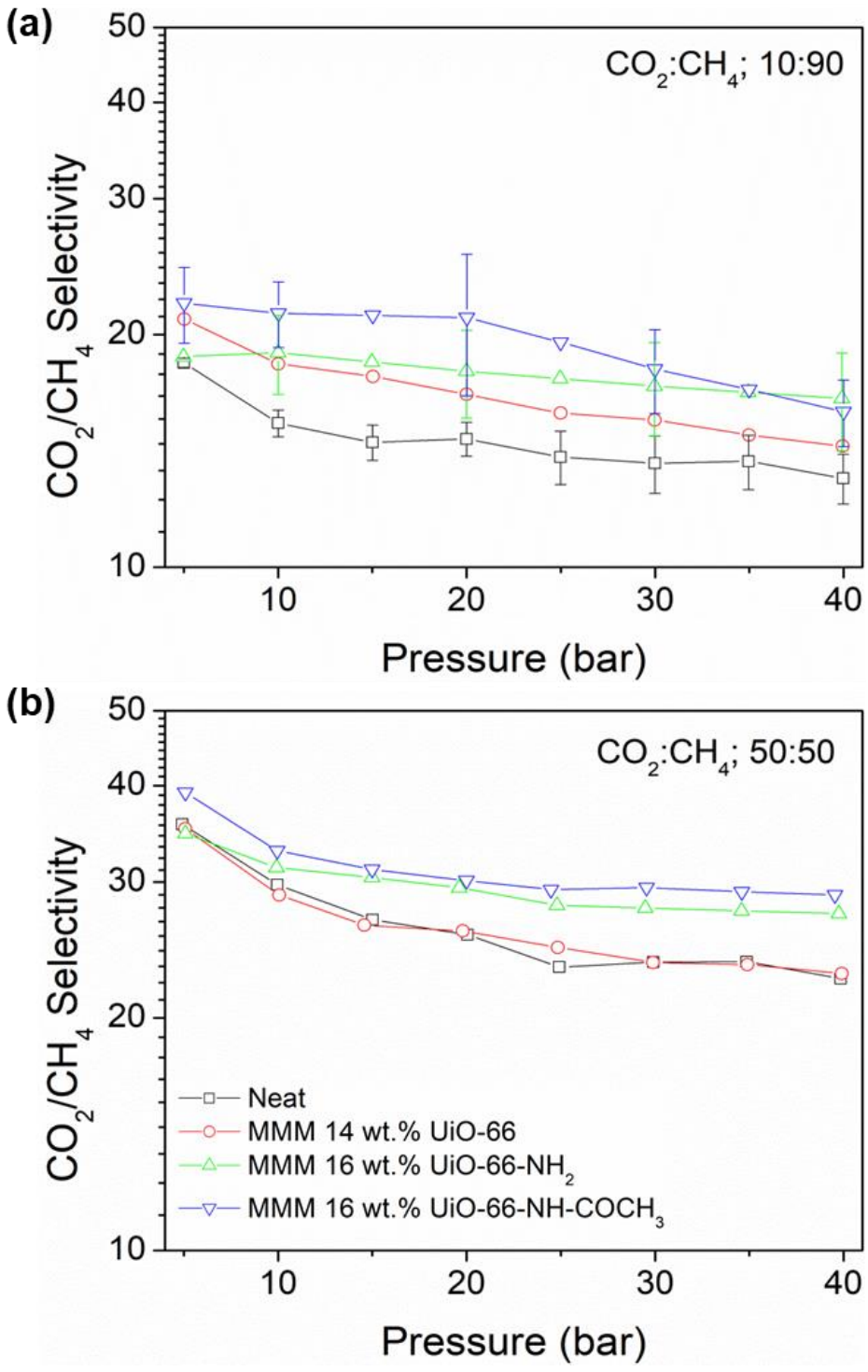

Fig. 5-24: CO_2/CH_4 selectivity vs. pressure for 6FDA-DAM and its best performing Zr-MOFs MMMs, measured between 5 – 40 bar at 35 °C with (a) 10%:90% and (b) 50%:50% CO_2/CH_4 gas mixtures. In (c), the data are represented against 2008 Robeson upper bound.

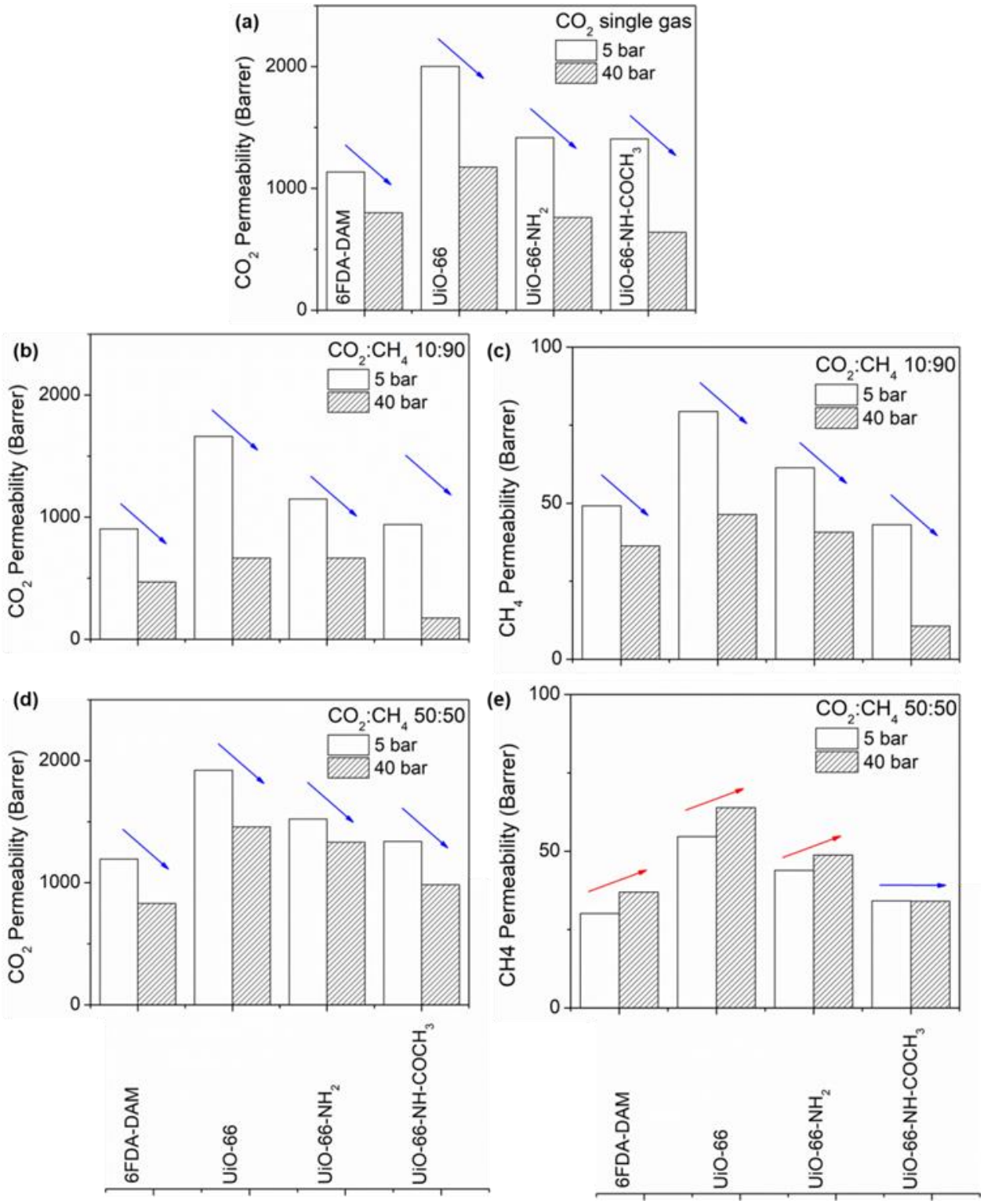

Fig. 5-25: Gas permeability values for 6FDA-DAM and its respective Zr-MOF MMMs when measured at elevated pressure of between 5 – 40 bar, at 35 °C with (a) pure CO_2 single gas, (b & c) 10:90 CO_2:CH_4 binary mixture and (d & e) 50:50 CO_2:CH_4 binary mixture.

Fig. 5-26 shows the performances with regards to the 2008 Robeson upper bound [21] and shows that CO_2 permeability and CO_2/CH_4 selectivity were both higher when tested with greater CO_2 content in the feed mixture. This is related to the higher CO_2 partial pressure and competitive adsorption as previously discussed.

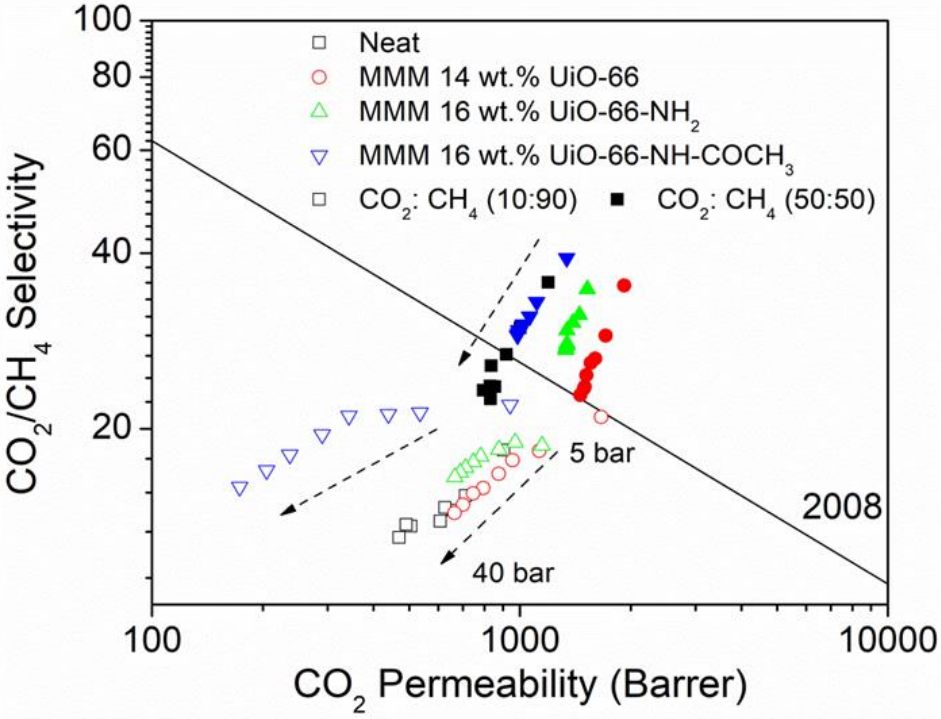

Fig. 5-26: CO_2/CH_4 selectivity vs. pressure for 6FDA-DAM and its best performing Zr-MOFs MMMs, measured between 5 – 40 bar at 35 °C with (a) 10%:90% and (b) 50%:50% CO_2/CH_4 gas mixtures. In (c), the data are represented against 2008 Robeson upper bound.

5.6. CHAPTER CONCLUSION

The syntheses of crystalline, high thermal stability Zr-based MOF nanoparticles, namely UiO-66 and UiO-66-NH_2 in a uniform size of less than 50 nm, were carried out. A post-synthetic modification of UiO-66-NH_2 was successfully conducted to produce acetamide-functionalized UiO-66. 6FDA-DAM-based MMMs with the three Zr-MOFs at different loadings (5 – 24 wt.%) were fabricated and investigated for CO_2:CH_4 mixture separation. A significant CO_2 permeability improvement of 6FDA-DAM to almost 100% was achieved with 14 wt.% UiO-66 MMMs while maintaining the selectivity when tested with an equimolar CO_2:CH_4 binary mixture at 2 bar pressure difference and 35 °C. MMMs with 16 wt.% of both UiO-66-NH_2 and UiO-66-NH-$COCH_3$ improved the CO_2 permeability by 23% and 27%, respectively. The UiO-66-NH-$COCH_3$ MMMs presented a small but significant improvement in selectivity of 13%, at the similar measurement conditions. High-pressure CO_2 single gas and CO_2:CH_4 (10 – 90% CO_2) binary mixed gas measurement at 35 °C showed highly promising results, where CO_2-induced plasticization was not observed up to 40 bar, for all the membranes. The enhanced membrane performance was mirrored by its improved physical properties; i.e., free fractional volumes and glass transition temperatures. Therefore, the developed membranes have demonstrated their potential for natural gas purification process and are substantially beneficial for industrial scale gas separation.

CHAPTER 6: UNDERSTANDING HIGH PRESSURE CO_2/CH_4 SEPARATION OF Zr-MOFs BASED MMMs TO VARIOUS SEPARATION PARAMETERS VARIANCES AND IN THE PRESENCE OF HYDROGEN SULFIDE.

6.1. CHAPTER OVERVIEW

The findings in Chapter 5 further demonstrated the effectiveness of Zr-MOFs incorporation into 6FDA-DAM as mixed matrix membranes for CO_2/CH_4 separation. Despite of the known facts that actual natural gas processing is conducted at high pressure (between 30 – 60 bar), the presence of CO_2- and H_2S-induced plasticization and the non-ideal gas behavior in a gas mixture especially at the high pressure, many publications only focused on low pressure single gas permeation thus presenting significant shortcomings of the presented MMM systems. Having said that, we collaborated with SINTEF Materials and Chemistry, Oslo Norway for an extensive high pressure separation study our 6FDA-DAM Zr-MOFs MMM systems. In this chapter we discuss the CO_2/CH_4 separation behavior of the said MMMs as a function of feed pressure of between 2 – 20 bar. At the highest pressure we investigated the effects of different CO_2 concentration in the feed content (between 10 – 50 vol.%), operating temperature (between 35 – 55 °C) and also the separation of a tertiary feed mixture of CO_2:H_2S:CH_4. The latter study was to understand H_2S effects to the penetrating molecules competitive sorption and possibly H_2S-induced plasticization in the 6FDA-DAM Zr-MOFs MMMs.

6.2. CHAPTER CONTRIBUTION

In this chapter, the gas separation properties of 6FDA-DAM mixed matrix membranes (MMMs) with three types of zirconium-based metal organic framework nanoparticles (MOF NPs, ca. 40 nm) have been investigated up to 20 bar. Both NPs preparation and MMMs development are as presented in the previous chapter that reported outstanding CO_2/CH_4 separation performances (50:50 vol.% CO_2/CH_4 feed at 2 bar pressure difference, 35 °C) and this subsequent study is to demonstrate its usefulness to the natural gas separation application. In the current -chapter, CO_2/CH_4 separation has been investigated at high pressure (2 – 20 bar feed pressure) with varying CO_2 content in the feed (10 – 50 vol.%) in the temperature range 35 – 55 °C. Moreover, the plasticization, competitive sorption effects and separation of the acid gas hydrogen sulfide (H_2S) has been investigated in a ternary feed mixture of CO_2:H_2S:CH_4 (vol.% ratio of 30:5:65) at 20 bar and 35 °C.

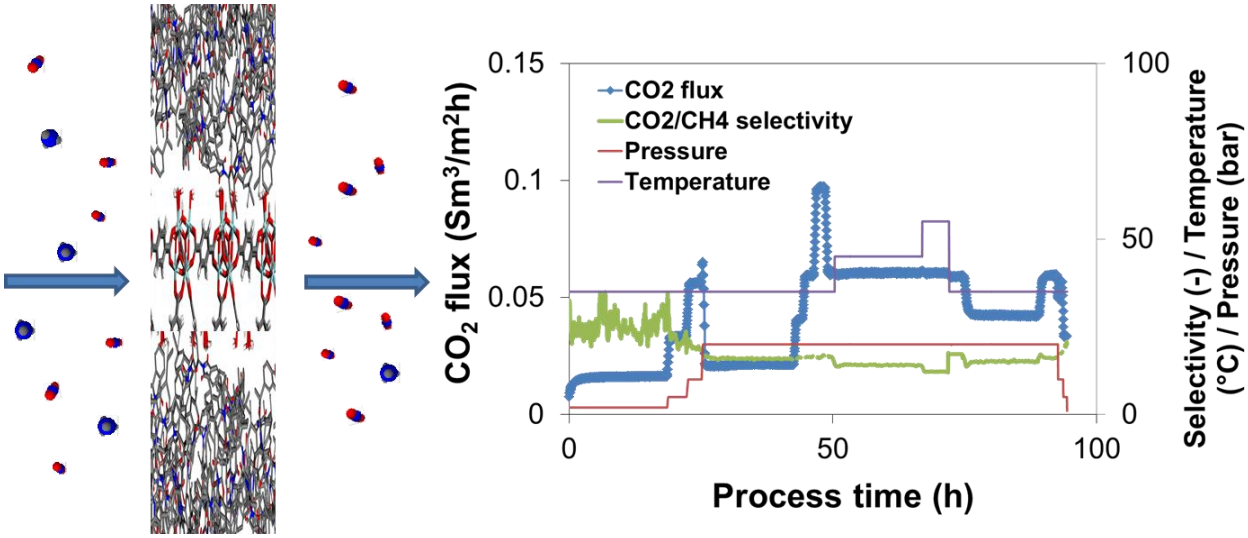

Fig. 6-1: the CO_2/CH_4 separation of 6FDA-DAM Zr-MOF MMM with various separation parameter variances over time.

6.3. INTRODUCTION

The acid gas content (carbon dioxide, CO_2; hydrogen sulfide, H_2S) in raw natural gas varies accordingly to the hydrocarbon geo-origins [1–3] and is commonly in the range of 25 – 55 mol.% for CO_2 and below 2 mol.% for H_2S (≥ 5 mol.% in several regions) [4,267,268]. CO_2, the most undesirable diluent aside from H_2S, is essential to be discarded from the gas stream as it corrodes transmission pipelines in the presence of water [5,6]. Additionally, CO_2 lowers the natural gas caloric value and causes atmospheric pollution [3–6]. Consequently, the content of these impurities must be reduced to meet the industrial processing and pipeline distribution requirements, e.g., maximum allowable contents of 2 – 3 mol.% CO_2 and 0.0004 – 0.0005 mol.% (4.3 – 5.0 ppm) H_2S (see Table 6-1) [269]. In the last decades, the advances in gas separation membranes have allowed the technology to increase its share of the total membrane market, comprising over 1,000 – 1,500 million US dollar per year [270] and appear to be the most viable alternative to substitute the conventional highly energy consuming processes, including the solvent-based absorption processes [5,9]. However, due to challenges such as plasticization especially at high-pressure operation and degradation, membrane processes only represents <5% of the natural gas sweetening market [7,8].

Table 6-1: Specification of pipeline quality gas [269].

Major component	Minimum Mol.%	Maximum Mol.%
Methane	75	None
Ethane	None	10
Propane	None	5
Butanes	None	2
Pentanes and heavier	None	0.5
Nitrogen and other inert gasses	None	3
Carbon dioxide	None	2 – 3
	Trace Components	
Hydrogen sulfide	0.25 – 0.3 g/100 scf (6 – 7 $mg \cdot m^{-3}$)	
Water vapor	4.0 – 7.0 lb/MM scf (60 – 110 $mg \cdot m^{-3}$)	
Oxygen	1.0%	

Both plasticization and degradation effects can be suppressed by polymer blending and cross-linking [271–274], but a more promising method to for the suppression is the

combination of polymeric and inorganic materials as mixed matrix membranes (MMMs) [185,275–277]. Yong *et al.* [275] reported the effectiveness of 2 wt.% POSS (polyhedral oligomeric silsesquioxane) nanoparticles into the highly permeable PIM-1 to suppress the neat polymer CO_2-induced plasticization pressure of 15 bar in the range of tested pressure (30 bar) with 50:50 vol.% CO_2:CH_4 feed mixture, at 35 °C. Additionally, the MMM presented 40.8% CO_2 permeability and 11.4% CO_2/CH_4 selectivity improvements. Adams *et al.* [276] reported a more than five times increase of CO_2 partial pressure needed to plasticize PVAc-50 wt.% zeolite 4A at 30 bar, also measured with 50:50 vol.% CO_2:CH_4 feed mixture, at 35 °C. Both Shahid and Nijmeijer [185] and Samadi and Navarchian [277] reported higher CO_2-plasticization pressures of Matrimid® 5218 (neat $P_{plasticization.}$ of ~10 bar) by incorporating 30 wt.% mesoporous Fe-BTC [185], 5 wt.% MgO [277] and 10 wt.% modified clay mineral with polyaniline [277], up to 21, 15 and 30 bar, respectively.

Permeation of a mixture of gases through a membrane can depend strongly on the operating parameters, for example the feed pressure and temperature, amongst others due to the gases' non-ideal behavior [265,278,279] and their competitive sorption [262,265,279,280]. Moreover, in a MMM system, the presence of a porous filler and the new filler-polymer interfacial phase created need to be understood as they further influence the gas mobility and sorption through the membrane. Metal organic frameworks (MOFs), formed with metal-based clusters linked by organic ligands [26] in three-dimensional crystalline frameworks with permanent porosity, are an emerging class of porous fillers [83]. They have gained substantial attention due to their high CO_2 uptake (i.e., HKUST-1 of 7.2 $mmol \cdot g^{-1}$ [22], MOF-74 of 4.9 $mmol \cdot g^{-1}$ [23], at 1 bar, 273 – 298 K), large surface areas up to 7000 $m^2 \cdot g^{-1}$ [84], well-defined selective pores due to their crystallinity, amongst other features. Many researchers observed that the incorporation of a MOF into the polymer continuous phase not only improved its separation properties but also its physical properties [51,55,195,275], due to interfacial interactions between the polymer and the MOFs. The polymer in some cases penetrates into the MOF open pores or rigidifies and forms microvoids at the interface [220,281], thereby affecting the membrane's physical properties and gas separation performance.

Zr-based MOF UiO-66 is a highly stable new material and has recently been applied as part of a MMM [55,134,282]. The synthesis of three types of Zr-MOFs, namely UiO-66 and its functionalized derivatives, UiO-66-NH_2 and UiO-66-NH-$COCH_3$, as well as MMM fabrication with 6FDA-DAM have been presented earlier [220,226].

6.4. EXPERIMENTAL

6.4.1. Materials and membrane fabrications

The syntheses of UiO-66, UiO-66-NH_2 and the covalent post-synthetic modification (PSM) onto UiO-66-NH_2 to produce UiO-66-NH-$COCH_3$ NPs are as described in Section 5.4.1 and 5.4.2. All the used nanoparticles are approximately ca. 40 nm in size. The membrane preparation on the other hand is described in Section 5.4.3, using 6FDA-DAM (Mw = 418 kDa) which was purchased from Akron Polymer Systems, Inc. The flat sheet mixed matrix membranes were in the thickness range of 100 – 150 μm.

6.4.2. Standard permeation measurement

To assess the gas separation performance of the membranes, a 25/25 $cm^3(STP)\cdot min^{-1}$ CO_2/CH_4 binary feed mixture was used at a pressure difference of 2 bar at 35 ºC applying He as sweep gas at 1 cm^3 $(STP)\cdot min^{-1}$. The permeate composition was analyzed online by an Agilent 3000A micro-GC equipped with a thermal conductivity detector (TCD) at the Institute Nanoscience of Aragon (INA), University of Zaragoza. The permeability was calculated as the penetrated gas flux, normalized for the membrane thickness and the partial pressure drop across the membrane, and presented in Barrer (1 Barrer = 10^{-10} $cm^3(STP)\cdot cm\cdot cm^{-2}\cdot s^{-1}\cdot cmHg^{-1}$ (see Eq. 3.6 and 3.7 in Section 3.4.6). The mixed gas separation performance was discussed in section 5.5.3 and presented the best performing MMMs with 14 – 16 wt.% Zr-MOF particle loadings in Fig. 5-16**.**

6.4.3. High pressure performance evaluation

The membranes were placed in a proprietary high-pressure permeation module obtained from the European Membrane Institute (EMI, The Netherlands). The membrane was supported with an S&S 589/1 black ribbon ash-less filter paper on a perforated plate to avoid membrane deformation during the high-pressure testing. The sample was sealed with an o-ring system providing for an effective membrane area of 0.78 cm^2. Both feed and retentate sides were connected by high-pressure Swagelok quick-connects whereas the permeate gas was collected using a 1/8 inch Swagelok connector.

The permeation module was placed inside a Memmert UF450 forced air circulation oven, connected to a proprietary permeation set-up at SINTEF Materials and Chemistry, Oslo for high-pressure gas separation measurement (Fig. 6-2). The permeation set-up is designed to

withstand pressures up to 92 bar with a forced air temperature control up to 300 °C. The feed (150 $cm^3(STP)\cdot min^{-1}$) and permeate (10 $cm^3(STP)\cdot min^{-1}$) flow rates were controlled by automated Bronkhorst High-Tech mass controllers (MFC), equipped with a back pressure controller (Bronkhorst High-Tech, P-512C equipped with an F-033C control valve, max of 92 bars) on the feed side for pressure regulation. The atmospheric-pressure permeate gas analyzed by a two-channel column (MolSieve 5A, MS5 and PoraPLOT U, PPU) Agilent 490 micro-GC, coupled with thermal conductivity detectors (TCD). The micro-GC was calibrated for low CO_2 (0 – 12 vol.%), CH_4 (0 – 5 vol.%) and H_2S (0 – 0.5 vol.%) concentrations in argon. Good correlation coefficients of $R^2 = \geq 0.999$ were obtained for the µ-GC response as a function of CO_2, CH_4, and H_2S concentration. The fluxes were calculated from the measured permeate concentrations and the calibrated flow of Ar sweep gas.

High-pressure gas permeation measurements were conducted accordingly to the following experimental sequence, and the separation performances were calculated correspondingly to Eq. 3.6 and Eq. 3.7 (see Section 3.4.6).

1. Pressure variation with 50:50 vol.% CO_2: CH_4 feed mixture: Preliminary measurement at 2 bar and at 35 °C was conducted to validate the initial membrane performances, and the pressure was subsequently increased to 5 and 10 bar. Before proceeding to 20 bar, the CO_2 feed content was decreased to 10 vol.% for the second step measurements.
2. CO_2 feed content variation at the feed pressure of 20 bar: At 20 bar, the 10 vol.% CO_2 feed content was subsequently increased to 20 vol.%, 30 vol.%, and 50 vol.% with CH_4.
3. The effect of temperature variation on the separation performance, with 30:70 vol.% CO_2:CH_4 feed mixture at 20 bar: The temperature increase was conducted by stepwise increments from 35 °C to 45 °C and 55 °C, and followed by a reduction back to 35 °C prior to the H_2S introduction (step no. 4).
4. Investigation of separation performance in the presence of H_2S with 30:5:65 vol.% CO_2:H_2S:CH_4 feed mixture was conducted at 20 bar and 35 °C.

It is important to note that the samples were allowed to equilibrate overnight, after each pressure or feed composition change. Specific attention was given to Health, Safety and Environmental (HSE) matters, and the lab was equipped with preventive safety measures which include H_2, CO and H_2S detection systems, personal portable gas detectors and separate floor level ventilation suction.

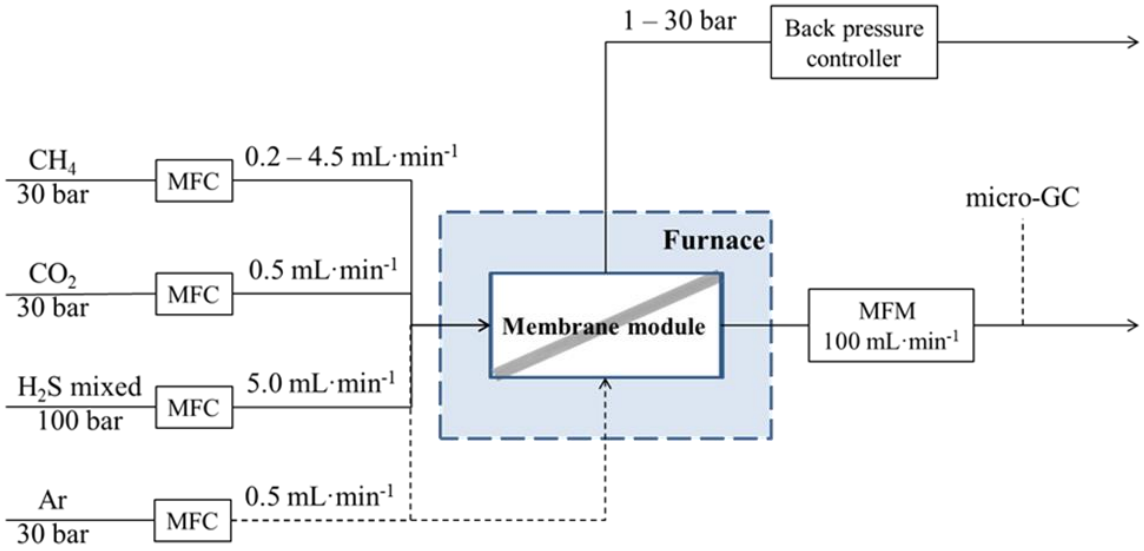

Fig. 6-2: Schematic representation of the high-pressure experimental set-up. The mass flows are calibrated at standard temperature and pressure condition.

6.5. RESULTS AND DISCUSSIONS

In the previous chapter, we found very promising performance indicators for several 6FDA-DAM MMMs with Zr-MOFs when tested at low pressure (2 bar), with the best performance observed for membranes that contain 14 – 16 wt.% Zr-MOF. An increase in the Zr-MOF loading shows a clear permeability-selectivity trade-off and selectivity reductions have been observed [220,258]. Table 6-2 shows the re-measured gas separation performance of the duplicate membranes, at 35 °C, with a pressure difference of 2 bar with an equimolar binary mixture of CO_2 and CH_4. The values are in good agreement with the published data and similar improvement behaviors were observed after incorporation of the Zr-MOF. The presence of 14 wt. % UiO-66, 16 wt. % UiO-66-NH_2 and 16 wt. % UiO-66-NH-$COCH_3$ improves the CO_2 permeability of 6FDA-DAM (P_{CO2} = 335 Barrer) by 165%, 56% and 37%, respectively. These enhancements are well-related to the CO_2-philic nature of the Zr-MOFs where a stronger energetic interaction between CO_2 (higher quadrupole moment than CH_4) and the nanoparticle surfaces at zero coverage, and to the increments in free fractional volume (FFV) in the MMMs (Neat 6FDA-DAM, FFV = 0.238). 14 wt. % UiO-66 MMM presents the highest increment value of 39%, followed by 16 wt. % UiO-66-NH_2 and 16 wt. % UiO-66-NH-$COCH_3$ with 16% and 22%, respectively. The CO_2/CH_4 selectivity of the samples also increased by 23 – 32%.

At these observed optimum loadings the Zr-MOFs addition enhances both CO_2 permeability and CO_2/CH_4 selectivity to beyond the permeability-selectivity trade-off [258]. Besides a higher gas diffusion in the Zr-MOFs, the NPs addition improved the MMM gas diffusivity by inducing an ancillary selective interface phase [106] with additional free volume [29,240]. Agglomeration of the NPs was more prominent at the highest loadings, and the concurrent reduction of the selectivity reduction is likely due to the formation of non-selective by-pass channels in the filler agglomerates [29] and possibly micro-voids in the filler-polymer interface region [155], although such morphological features are not observed by SEM analyses.

Table 6-2: CO_2 and CH_4 permeability and CO_2/CH_4 selectivity of the neat 6FDA-DAM and its Zr-MOF MMMs, measured at 35 °C and a pressure difference of 2 bar with an equimolar binary mixture of CO_2 and CH_4.

Membrane	Gas permeability (Barrer)		CO_2/CH_4 Selectivity
	CO_2	CH_4	
INA, UNIZAR			
Neat	997.0	34.4	29.2
MMM UiO-66 14 wt.%	1911.8	62.0	30.9
MMM UiO-66-NH_2 16 wt.%	1223.2	40.6	30.1
MMM UiO-66-NH-$COCH_3$ 16 wt.%	1262.5	38.2	33.1
SINTEF MLAB			
Neat	334.9	17.7	19.3
MMM UiO-66 14 wt.%	887.7	35.9	25.1
MMM UiO-66-NH_2 16 wt.%	520.9	21.9	23.8
MMM UiO-66-NH-$COCH_3$ 16 wt.%	459.4	18.1	25.4

6.5.1. Effect of feed pressure variation to mixed gas separation

Most of the fundamental studies on Zr-MOF polyimide MMMs related to Matrimid and 6FDA-copolyimides have been conducted at low pressures where CO_2-induced plasticization is expected to be of minor importance [30,55,67]. Here, we have investigated the gas separation performance of 6FDA-DAM and its Zr-MOF MMMs at a pressure ranging between 2 to 20 bar in a 50:50 vol. % CO_2:CH_4 feed mixture at 35 °C. The obtained mixed gas permeability and CO_2/CH_4 selectivity behavior as a function of pressure are shown in Fig. 6-3.

The CO_2-induced plasticization pressure is defined to occur at the minimum observed in the CO_2-permeability as a function of CO_2-partial feed pressure. In the case of mixed gases, the permeation rate of all gases is affected due to swelling of the polymer matrix and the increased chain mobility caused by the high CO_2 concentration. The enhancement in permeation is more pronounced for the least permeable gases, resulting in a decrease of the selectivity as a function of pressure. In contrast, for all samples in the present study, a monotone decrease in CO_2 permeability with increasing pressure is observed (see Fig. 6-4), which indicates no substantial plasticization [265]. The decrease in CO_2 permeability reduction is a result of competitive sorption and the concave shape of the sorption isotherm [261,262]. This constitutes a reduction in driving force for transport with increasing pressure and, in addition, gradual saturation of the material may result in lower mobility. Overall, this results in a decrease in permeation coefficient in the polymer matrices (see Fig. 6-4). The CO_2 permeability continuously decreases with increasing pressure indicating there is no apparent CO_2-induced plasticization in the thick membrane [265], opposite to the reported single-gas CO_2-plasticization pressure of neat 6FDA-DAM membrane between ~ 10 – 20 bar, at 35 °C [57,263]. The plasticization pressure differences may be attributed to different physical properties, i.e., molecular weight, density and polymer free volume, as previously discussed [55,220].

The pressure dependence of the CH_4 permeability (Fig. 6-3(b)) over the measured pressure range, however, suggests that the neat 6FDA-DAM starts to swell immediately after the first pressure increment. It can be explained by dynamic swelling of the polymer matrices upon exposure to the CO_2 at high pressure [283], where the penetrating CO_2 causes the material dilation and subsequently increases its macromolecular mobility. Several researchers have reported the thermodynamics of swollen glassy polymers by a penetrant [284,285], and a thorough discussion was recently presented by Ogieglo et al. [283] when studying the glassy polymer relaxation in this films. The phenomenon, to the function of pressure, causes extensive dilation of the matrices, influencing the penetrants' permeation. Here, the effect is more apparent in CH_4 permeability increase compared to the readily high-permeability CO_2. In the case of UiO-66-NH_2 MMM, the high CO_2-affinity amino functional group increases the CO_2 adsorption in the polymer matrixes and directly further influences the molecular dynamic dilation. Even though it is not the membranes' plasticization pressure, their CO_2/CH_4 selectivity reduced by 55% and 58% respectively. This behavior also defined as swelling-induced perm-selectivity losses [220] was observed in several other co-polyimides, such as 6FDA-APAF and TPDA-APAF, when measured with CO_2/CH_4 binary mixture

up to 25 bar feed pressure, at 35 °C [286]. Heck *et al.* [201] also observed similar behavior in (6FDA-mPDA)-(6FDA-durene) block co-polyimide, for which they reported an increase in CH_4 permeability with pressure (up to 20 bar feed pressure), causing CO_2/CH_4 and He/CH_4 selectivity reductions.

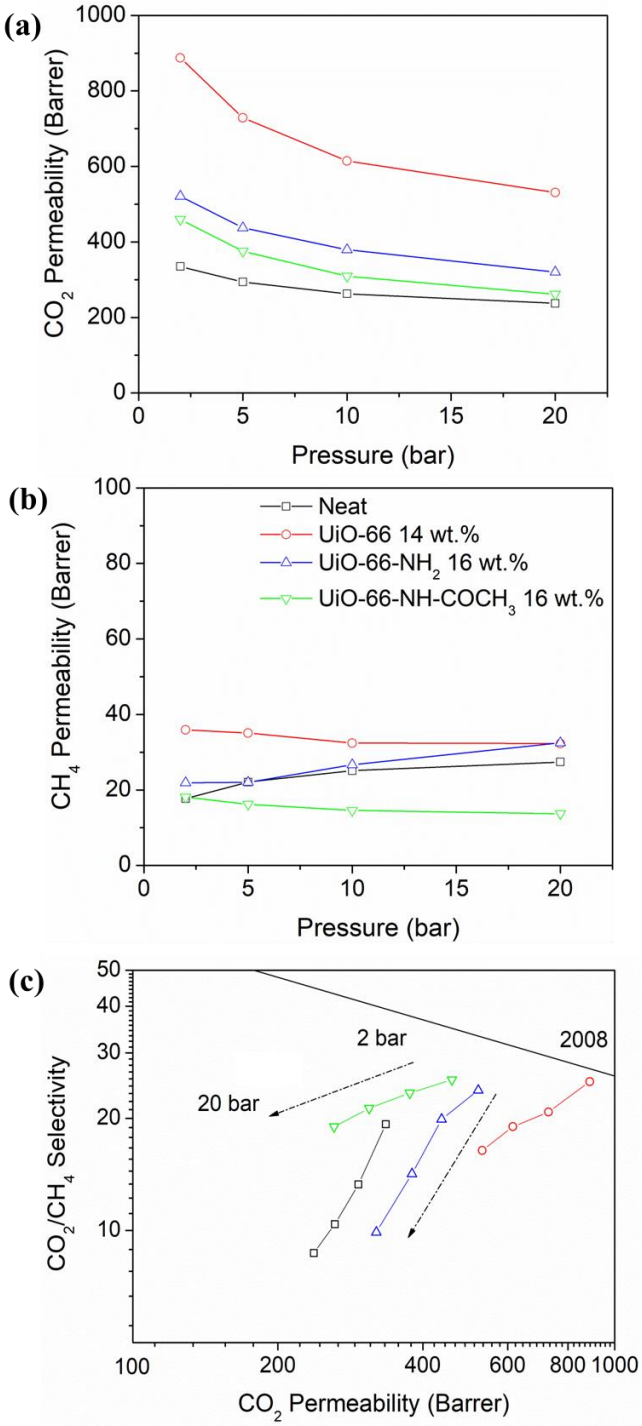

Fig. 6-3: (a) CO_2 and (b) CH_4 permeabilities of 6FDA-DAM and its Zr-MOFs as a function of feed pressure, measured with 50:50 vol.% CO_2: CH_4 feed mixture at 35 °C. Their corresponding CO_2/CH_4 selectivity values are presented in (c), against the 2008 Robeson upper bound [21].

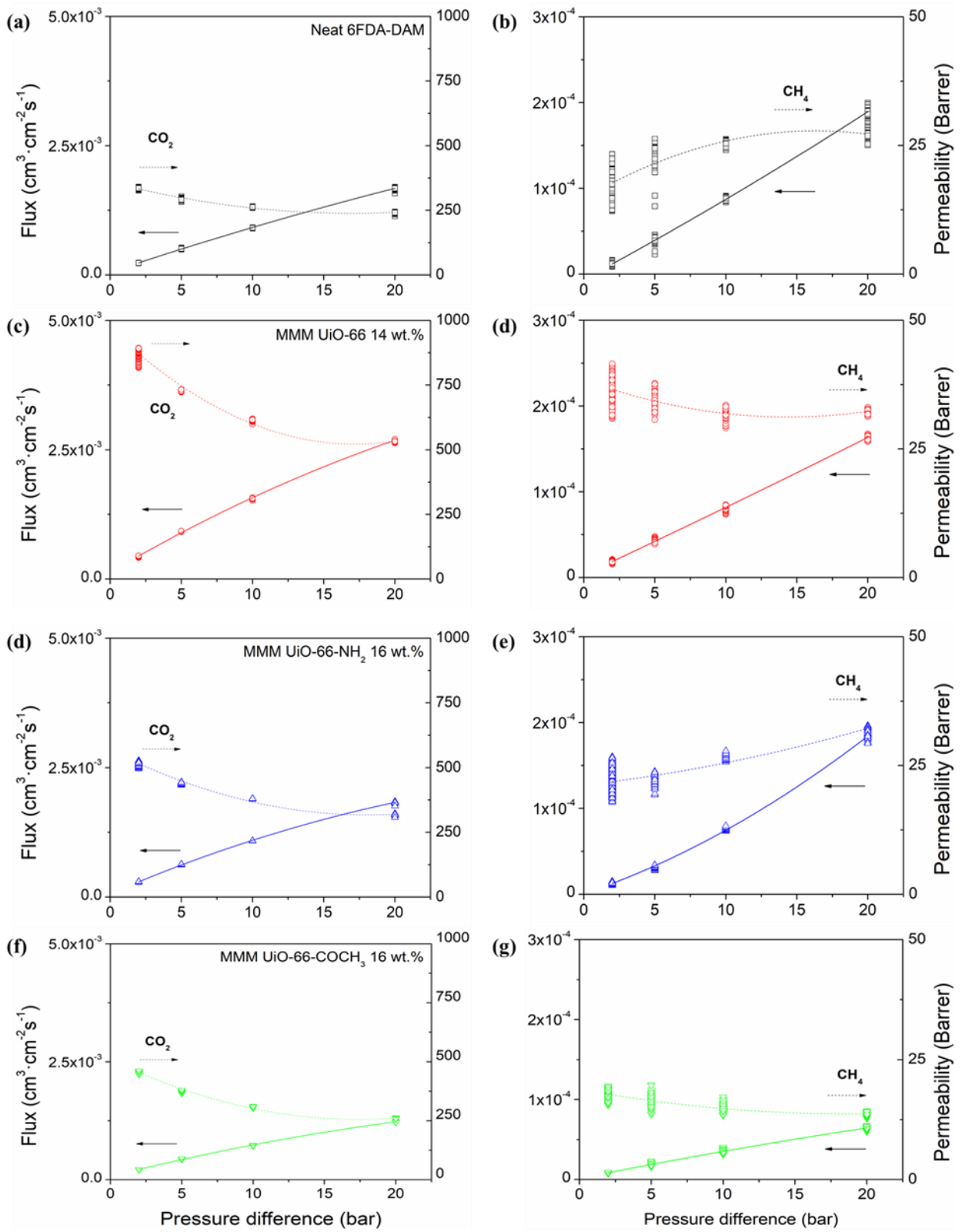

Fig. 6-4: Gas fluxes and permeabilities of (a, b) 6FDA-DAM and (c-g) its Zr-MOF MMMs as a function of pressure difference, measured with 50:50 vol.% CO_2:CH_4 feed mixture at 35 °C between 2 – 20 bar.

6.5.2. Effect of CO_2 feed composition in high pressure separation

Fig. 6-5(a) and Fig. 6-5(b) show the CO_2 and CH_4 permeability of the neat 6FDA-DAM and Zr-MOF MMMs, measured at 20 bar feed pressure and 35 °C, with a varying CO_2 feed content between 10 to 50 vol.%. The significant differences in the initial CO_2 permeabilities between the membranes were discussed previously in Section 5.5.3. ; higher CO_2 permeability in the UiO-66 MMM is attributed to the easiness of CO_2 to diffuse into its frameworks, compared to the higher steric hindrance functionalized-MOFs, and also its higher FFV. The CO_2 permeability decreases for the neat 6FDA-DAM and its Zr-MOF MMMs, with an increase of the CO_2 content between 9 and 22%, with the lowest reduction observed for the UiO-66 MMM. The observation, however, is opposite to the previously reported CO_2 permeability relationship with CO_2 partial pressure at low-pressure measurements, i.e., 6FDA-DAM Zr-MOF MMMs (at 2 bar) [220] and PES/SAPO-34/2-hydroxyl 5-methyl aniline MMMs (at 3 bar) [177]. At the low pressure, a higher CO_2 partial pressure produced a more prominent competitive sorption effect, where an increase in CO_2 solubility and transport through the membrane medium was observed and inversely decreased the second component's ability to permeate, in this case, CH_4.

Evidently, the continuous CO_2 permeability reduction with increasing pressure suggests that the competitive sorption effect at high pressure is less influenced by the CO_2 partial pressure (see Fig. 6-6). Instead, it is merely related to gradual saturation of the permeating gases inside the polymer micro-voids [185]. Nevertheless, a slight increase in the CH_4 permeability for the neat membrane (9%) and UiO-66-NH_2 MMM (21%) is observed, indicating the possibility of CO_2-induced plasticization that started to take effect [48,52]. These samples exhibited the highest CO_2/CH_4 selectivity reductions of between 28 and 33% in all the samples (shown in Fig. 6-5(c), relative to 2008 Robeson's upper bound [21]). Despite this CH_4 permeability increment, the behavior can be explained as swelling-induced perm-selectivity losses, an early stage in polymer plasticization [286].

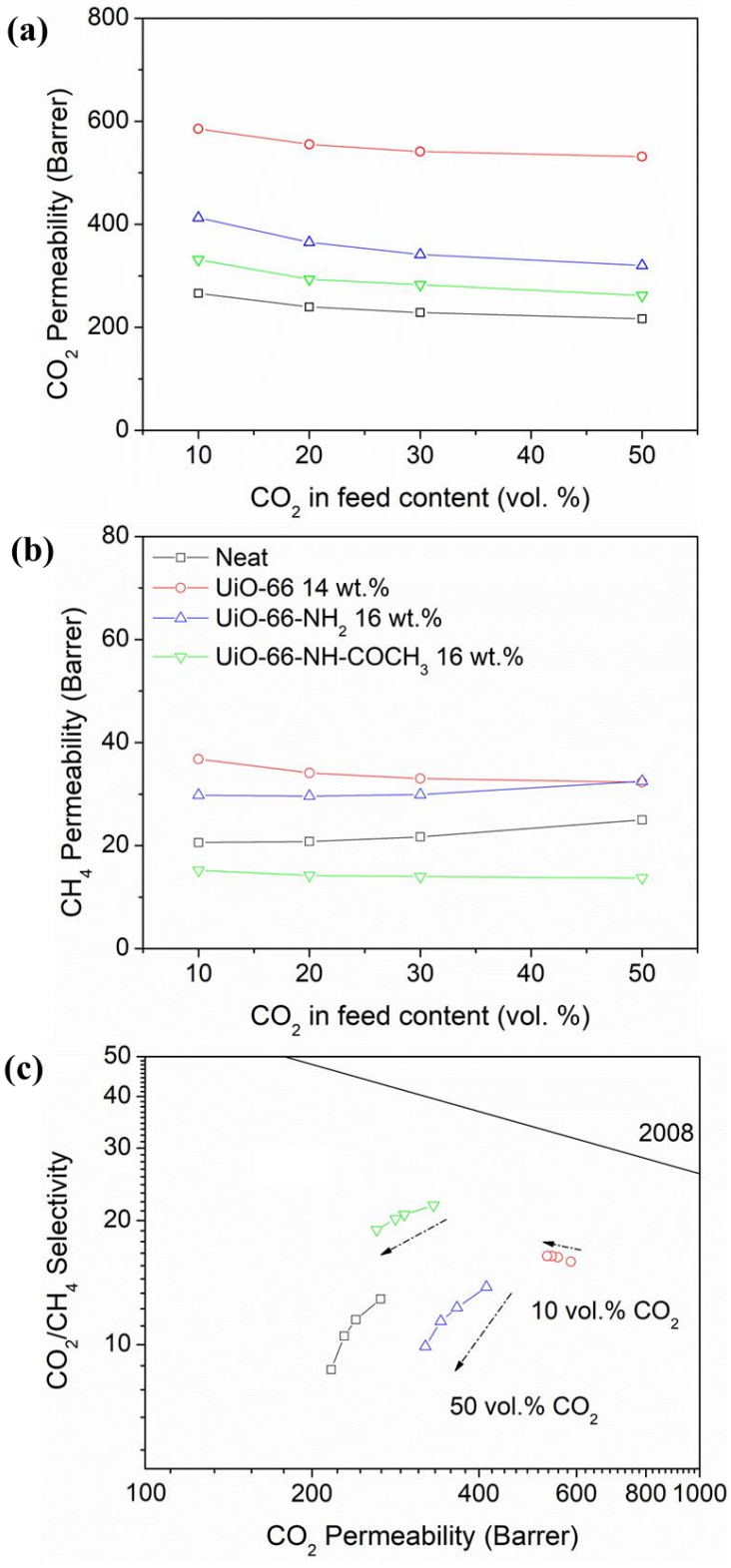

Fig. 6-5: (a) CO_2 and (b) CH_4 permeabilities of 6FDA-DAM and its respective Zr-MOF MMMs, measured at 20 bar feed pressure and 35 °C. Their corresponding CO_2/CH_4 selectivity values are presented in (c) against 2008 Robeson upper bound [21].

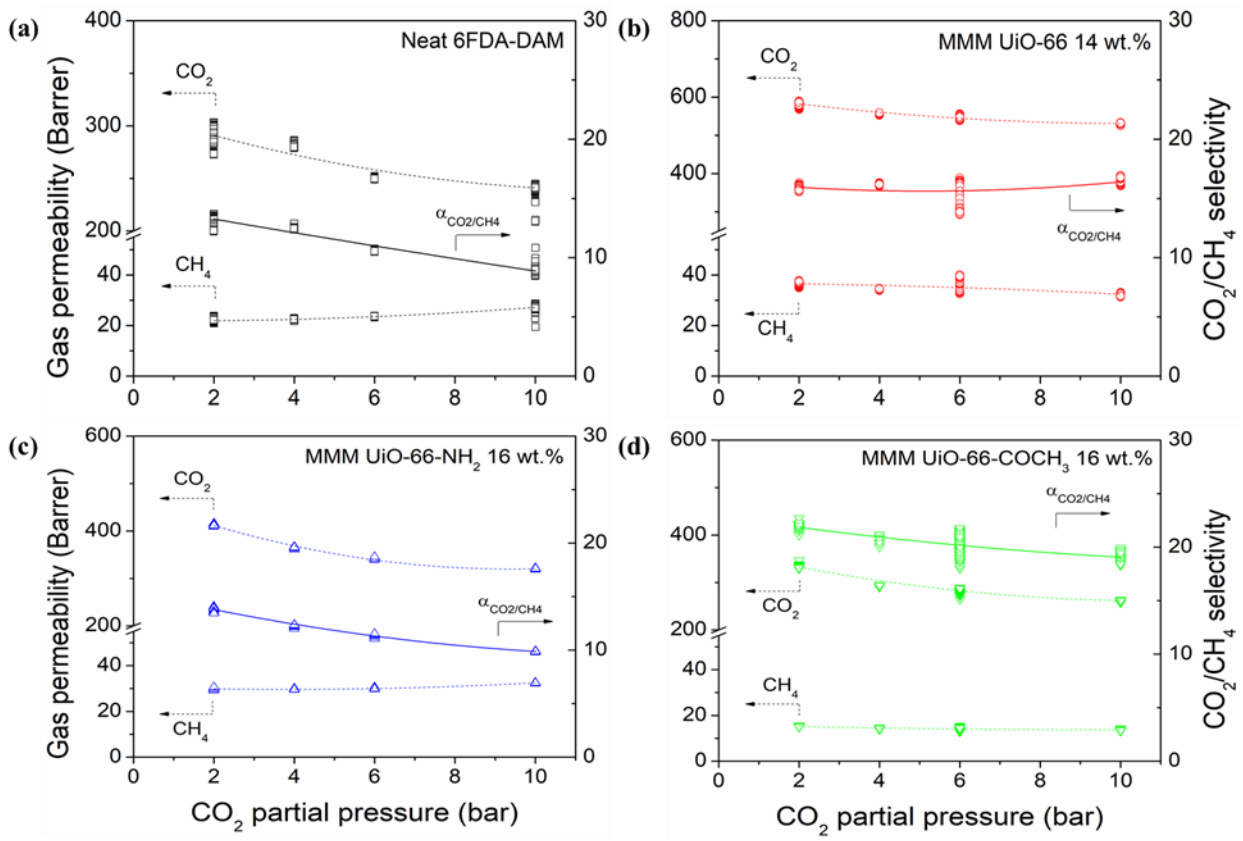

Fig. 6-6: CO_2 and CH_4 permeabilities, and CO_2/CH_4 selectivity of 6FDA-DAM and its Zr-MOF MMMs against CO_2 partial pressure, at 20 bar and 35 °C.

With regard to the initial separation performance (with 10 vol.% CO_2), similarly to the previous discussion, neat 6FDA-DAM showed a lower CO_2/CH_4 selectivity than that of MMMs (UiO-66-NH_2 < UiO-66 < UiO-66-$COCH_3$). The proportional selectivity increase in MMMs to the increasing CO_2 partial pressure [15,54,130], which only observed in UiO-66 MMM at the tested feed pressure of 20 bar (3% selectivity increment) represents the membrane's extended CO_2 sorption capability due to the CO_2-induced plasticization or swelling at constant pressure [15]. Its reduction conversely was explained based on CO_2 self-inhibition as a consequence of saturation of the filler active sites at a high CO_2 concentration in a feed mixture [177,287]. Referring to that hypothesis, a lower reduction exhibited by UiO-66-NH-$COCH_3$ MMM (13%) compared to UiO-66-NH_2 MMM (28%), represented by its lesser concave shape in the permeability isotherm, may be due to a higher CO_2 affinity towards acetamide functional groups, with a higher number of adsorption sites compared to UiO-66-NH_2 NPs. Moreover, constant selectivity values demonstrate no dependency of an MMM system towards the increasing CO_2 partial pressure, as also revealed in the PES/SAPO-34/HMA MMM system, measured at 3 bar [177]. This hypothesis implies that only a minor amount of the active sites is occupied at low pressure.

6.5.3. Effect of operating temperature at high-pressure separation

Fig. 6-7(a-c) shows the CO_2 and CH_4 permeability and the CO_2/CH_4 selectivity as a function of the operating temperature applying a 30:70 vol. % CO_2:CH_4 feed mixture at 20 bar. A minor increase in CO_2 permeability of <6% was recorded for all samples, whereas for CH_4 permeability, the increments were higher in between 28 and 37%, as the operating temperature increased from 35 to 55 °C.

The effect of temperature on the gas permeability can be quantitatively observed in their activation energy for permeability, following Arrhenius rule using Eq. 6.1 [288]:

$$P = P_0 e^{\frac{-E_p}{RT}} \qquad \text{Eq. 6.1}$$

Where;

P_0	pre-exponential factor of permeation, Barrer
E_p	activation energy for permeability, $J \cdot mol^{-1}$
R	universal gas constant, 8.314 $J \cdot mol^{-1}$ K^{-1}
T	temperature in Kelvin

Using CO_2/CH_4 selectivity expression of the permeability coefficient ratio of CO_2 over CH_4 and applying Eq. 6.1 the gas selectivity is defined:

$$\alpha_{CO_2/CH_4} = \frac{P_{CO2}}{P_{CH4}} = \frac{P_0\,(CO_2)}{P_0\,(CH_4)} \exp\left(-\frac{E_p\,(CO_2) - E_p(CH_4)}{RT}\right) \qquad \text{Eq. 6.2}$$

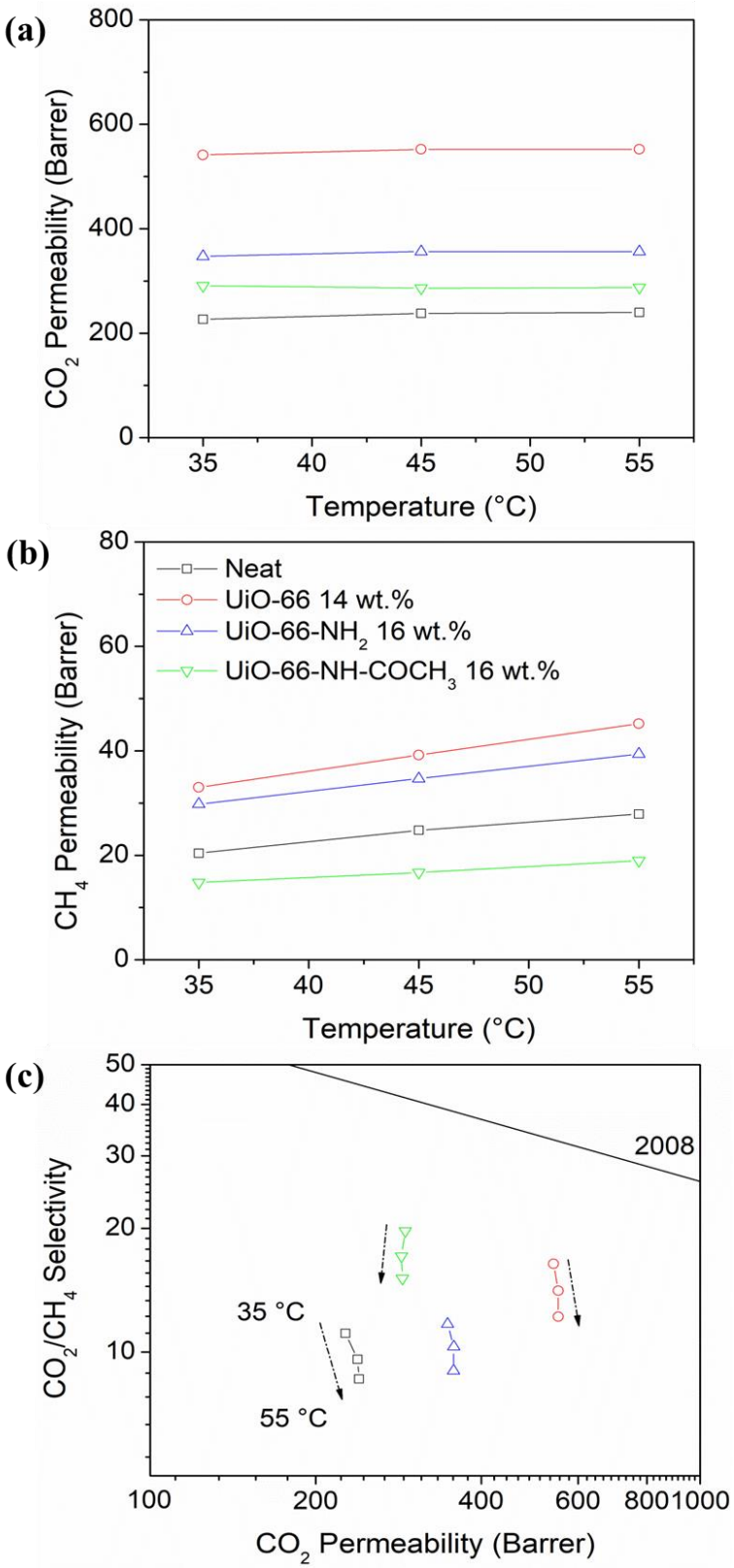

Fig. 6-7: (a) CO_2 and (b) CH_4 permeabilities of 6FDA-DAM and its respective Zr-MOF MMMs, as a function of temperature with 30:70 vol. % CO_2: CH_4 feed mixture. Data obtained at a feed pressure of 20 bar. Their corresponding (c) CO_2/CH_4 selectivity values are presented against 2008 Robeson upper bound [21].

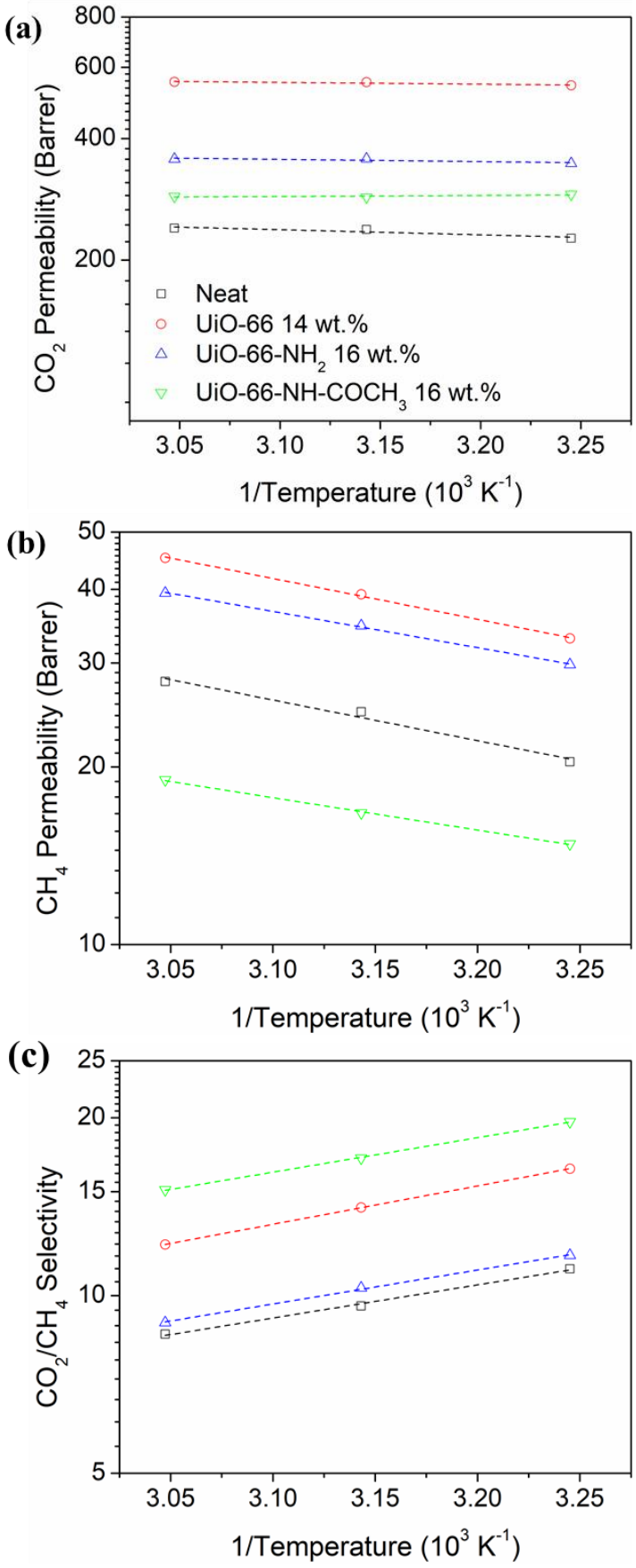

Fig. 6-8: (a) CO_2 and (b) CH_4 permeability and its (c) perm-selectivity to temperature dependence, for neat 6FDA-DAM and its Zr-MOFs membranes at the measurement temperature of 35 – 55 °C.

Fig. 6-8 indicates that CH_4 permeability in the 6FDA-DAM neat membrane and its Zr-MOF MMMs followed Arrhenius rule in the temperature range of 35 – 55 °C, while the CO_2 permeability was less influenced by the temperature and thus shows a large relative error. A lower fit for CO_2 at this high-pressure separation indicated that the molecule's non-ideal behavior in a gas mixture was more influenced by both pressure and temperature, compared to CH_4. Their permeability activation energy are summarized in Table 6-3.

Table 6-3: Activation energy of permeation for CO_2 and CH_4 in neat 6FDA-DAM and its Zr-MOF MMMs, calculated for the temperature operating range of 35 – 55 °C, with 30:70 vol. % CO_2/CH_4 at 20 bar.

Gas	**Membrane**	**Permeability activation energy, kJ·mol^{-1}**
		E_a, (35 – 55 °C)
CO_2	Neat	0.16
	MMM UiO-66 14 wt.%	0.05
	MMM UiO-66-NH_2 16 wt.%	0.07
	MMM UiO-66-NH-$COCH_3$ 16 wt.%	-0.03
CH_4	Neat	0.85
	MMM UiO-66 14 wt.%	0.86
	MMM UiO-66-NH_2 16 wt.%	0.76
	MMM UiO-66-NH-$COCH_3$ 16 wt.%	0.68

The permeability dependency is a combination of the diffusion and solubility coefficients temperature dependencies, and the lower CO_2 and CH_4 activation energies in MMMs as compared to the neat polymer indicate gas transport through filler porosity [30]. Regarding 6FDA-DAM, in addition to polymer matrix compression at the high pressure, the overall CO_2 activation energy trend does not show a clear correlation to the membrane FFVs (MMMs (UiO-66; 0.331 > UiO-66-$COCH_3$, 0.292 > UiO-66-NH_2; 0.277) > neat 6FDA-DAM, 0.238). Instead, the activation energy seems profoundly influenced by the presence of Zr-MOF nanoparticles in MMMs, in the order of their group functionalities (UiO-66-NH-$COCH_3$ > UiO-66-NH_2 > UiO-66 > neat 6FDA-DAM). It also concludes that the CO_2 permeation is predominately influenced by its solubility (sorption) in the membrane systems, and less depended on temperature. The higher activation energies presented by the non-polar CH_4 also indicated that its transport was more influenced compared to CO_2 molecules, giving higher CH_4 permeability increments and consequently reduced the CO_2/CH_4 selectivity by 22 – 26%. This observation is consistent with activated diffusion of non-polar molecules in

glassy polymers (related to chain mobility and polymer free volumes) [289], where the least permeable gas often possesses a higher activation energy and realizes a more substantial permeability increase with increasing temperature. In any event, the activation energies (temperature-dependent) are low for both the neat polymer membrane and the MMMs, compared to the other 6FDA-based polyimides in the literature (seeTable 6-4). This suggests a low penetrant-membrane interaction perhaps because there is a relatively large difference between the CO_2 and CH_4 kinetic diameter and the membrane controlling pore size.

Table 6-4: CO_2 and CH_4 temperature-dependent permeation properties of 6FDA-based co-polyimides flat sheet membranes, unless indicated.

Membrane	Temperature range and pressure °C / bar	Permeability activation energy E_a, kJ·mol^{-1}		Ref
		CO_2	CH_4	
6FDA-DAM	35 – 55 / 20	0.16	0.85	This study
6FDA-DAM:DABA (4:1)	30 – 50 / 6.9	6.2	-	[290]
6FDA-TAB	35 – 80 / 10	0.6	4.1	[291]
6FDA:PMDA (1:1) -TAB	35 – 80 / 10	1.0	3.1	[291]
6FDA-Dureen	30 – 50 / 10	0.2	7.3	[292]

Abbreviation:

6FDA: 2,2-bis(3,4-dicarboxyphenyl)hexafluoropropane diandydride; DAM: 2,4,6-trimethyl-1,3-diaminobenzene; DABA: 3,5-diaminobenzoic acid; TAB: 3,3',4,4'-tetraamino biphenyl; PMDA: pyromellitic dianhydride; Dureen: 2,3,5,6-tetramethyl-1,4-phenylenediamine;

Besides that, the CH_4 permeability increase was also influenced by the increase of polymer free volume (as a function of polymer chain packing and intersegmental motion) by the effect of elevated temperature. The activated diffusion often proves to be a significant advantage in the separation of non-polar H_2 from CO_2, giving enhanced H_2/CO_2 selectivity at higher temperatures as demonstrated in 6FDA-*m*PBI [289] and PBI-ZIF8 MMMs [174].

$$\log P_0 = \frac{E_p}{R} \times 10^{-3} + Z \qquad \text{Eq. 6.3}$$

Regardless of common polymer chemical structures, Van Krevelen [293] presented a positive slope of 1 x 10^{-3} for log P_0 and E_p/R plot (Eq. 6.3), with Z values of -7.0 and -8.2 for rubbery and glassy polymers respectively, for permeability measurement below their glass transition temperatures. Fig. 6-9 indicates that the addition of Zr-MOFs into 6FDA-DAM

altered CO_2 permeability-temperature dependency significantly, giving a negative E_p/R slope of -0.15 x 10^{-3}, while only reduced CH_4 permeability-temperature dependency by roughly 70% (CH_4 permeability E_p/R slope = 0.32 x 10^{-3}).

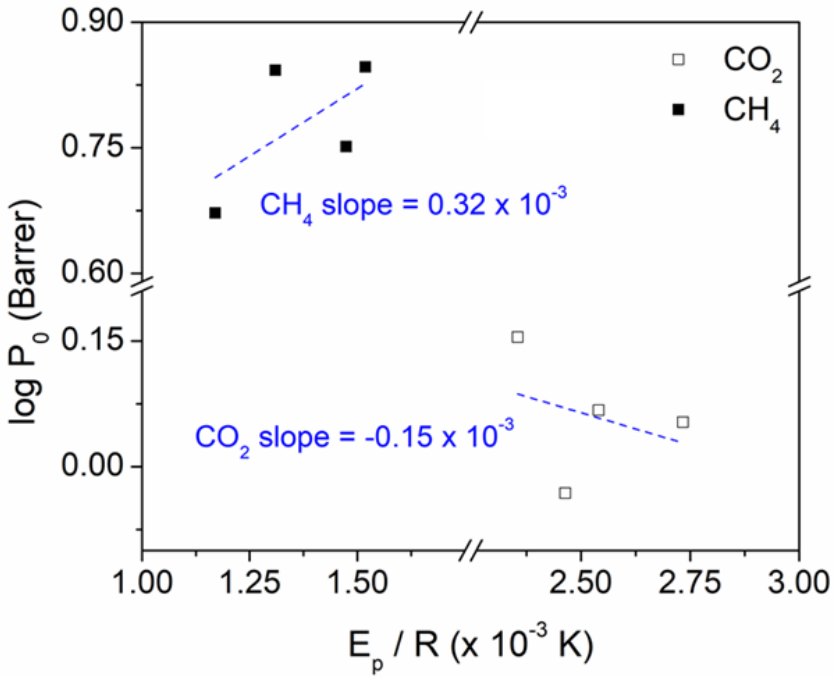

Fig. 6-9: CO_2 and CH_4 permeability dependence on temperature, for 6FDA-DAM and its Zr-MOF MMMs at the measurement range of 35 – 55 °C, with 30:70 vol. % CO_2:CH_4 feed mixture at 20 bar.

6.5.4. Effect of the presence of H_2S on membrane separation

The concentration of H_2S in natural gas mixture varies depending on the geo-origin and can be more than 5 vol. % [267,268]. As aforementioned, besides investigating the 6FDA-DAM and its Zr-MOF MMMs performances for H_2S separation, it is important to understand the H_2S effect on membrane performance. We studied the gas separation performance of 6FDA-DAM and its Zr-MOF MMMs with 30:70 vol. % CO_2:CH_4 feed mixture at 20 bar and 35 °C, before switching to 30:5:65 vol. % CO_2:H_2S:CH_4. The separation performance after H_2S exposure were also investigated and summarized in Table 6-5.

Table 6-5: Gas separation performances of 6FDA-DAM and its 14 – 16 wt.% Zr-MOFs MMMs, tested with binary (30:70 vol.%; CO_2: CH_4) and tertiary (30:5:65 vol.%; CO_2: H_2S: CH_4) feed mixture at 20 bar, 35 °C.

Feed mixture	**Separation performances**	**6FDA-DAM membranes**			
		Neat	MMM UiO-66	MMM UiO-66-NH_2	MMM UiO-66-NH-$COCH_3$
CO_2:CH_4 (30:70 vol. %) Before exposure	Gas permeability (Barrer)				
	CO_2	231	541	359	291
	CH_4	21.7	33.0	33.1	14.8
	CO_2/CH_4 selectivity	10.6	16.4	10.8	19.7
CO_2:H_2S:CH_4 (30:5:65 vol. %)	Gas permeability (Barrer)				
	CO_2	167	385	243	193
	H_2S	137	352	224	172
	CH_4	18.5	25.4	25.7	10.6
	CO_2/CH_4 selectivity	9.1	15.2	9.5	18.2
	H_2S/CH_4 selectivity	7.4	13.6	8.7	16.2
CO_2:CH_4 (30:70 vol. %) After exposure	Gas permeability (Barrer)				
	CO_2	227	543	347	284
	CH_4	20.4	33.7	29.8	14.3
	CO_2/CH_4 selectivity	11.1	16.1	11.7	19.8

In the presence of 5 vol. % H_2S in the mixed gas, CO_2 permeability in all samples decreased by an average of 28 – 34%, according to their functionality order: MMMs (UiO-66-NH-$COCH_3$ > UiO-66-NH_2 > UiO-66) > neat 6FDA-DAM. Besides the competitive sorption of a two-component gas mixture, the presence of a third component intensifies the gas mixtures non-ideal behavior and influences each penetrant permeation rate, especially at elevated pressures [265]. 6FDA-DAM MMMs showed a higher CO_2 permeability reduction in the presence H_2S, compared to the neat membrane. The observation exhibited the influence of Zr-MOFs addition into the polymer, where it increased H_2S sorption due to its active metal sites and well-agreed to the order of isosteric adsorption heat in UiO-66 (CO_2; 25.7 kJ·mol^{-1} > H_2S; 23.8 kJ·mol^{-1} > CH_4; 18.8 kJ·mol^{-1}, reported at 30 °C [282]).

Functionalized UiO-66 derivatives presented higher values, in the same order. The gas physical properties; dipole moment (Debye), quadrupole moment (au) and polarizability (a_0^3), also greatly contributed to the competitive sorption outcomes and H_2S high polarizability explained its higher permeability despite of its relatively low content in the feed mixture compared to CO_2; CH_4: 5.4 x 10^{-6} Debye, 0 au, 17.3 a_0^3; CO_2: 0 Debye, 3.2 au, 18 a_0^3; H_2S: 0.978 Debye, 0 au, 25 a_0^3 [294]. Hence, the observed CO_2/CH_4 selectivity reduction can be explained by a larger competitive sorption effect induced by H_2S, as the solubility of H_2S is larger than that of CH_4 in the membrane systems. Furthermore, the effect on selectivity reduction was proven to be more prominent in the neat membranes (-30%) compared to the 6FDA-DAM Zr-MOFs MMMs (-17 – 19%).

In the presence of H_2S, all MMMs presented higher CO_2/CH_4 and H_2S/CH_4 selectivities compared to the neat 6FDA-DAM ($\alpha_{CO2/CH4}$ = 9.1; $\alpha_{H2S/CH4}$ = 7.4) with the highest values presented in UiO-66-NH-$COCH_3$ MMM ($\alpha_{CO2/CH4}$ = 18.2; $\alpha_{H2S/CH4}$ = 16.2). The UiO-66-NH-$COCH_3$ MMM presented similar or higher H_2S/CH_4 selectivity than several membranes, such as in 6FDA-PAI-3/TmPDA (ideal $\alpha_{H2S/CH4}$ = 10.9) and Torlon® 4000T (ideal $\alpha_{H2S/CH4}$ = 14.8), both tested at 4.5 bar, 35 °C [295], and in a rigid (6FDA-mPDA)-(6FDA-durene) block co-polyimide, ($\alpha_{H2S/CH4}$ = ca. 15), when tested with 1 vol. % H_2S in a CO_2:H_2S:N_2:CH_4 quaternary mixture at 3.8 bar, 22 °C [296]. The performance is also comparable to the commercial poly(ester urethane) urea, PEUU, $\alpha_{H2S/CH4}$ = 16 [297] (CO_2:H_2S:CH_4 feed ratio of 5.4:3:remaining, at 55 °C, 20 bar) and cellulose acetate, CA, $\alpha_{H2S/CH4}$ = 19 [298] (CO_2:H_2S:CH_4 feed ratio of 29:6:65, at 35 °C, 10 bar). In the separation of an actual natural gas sample containing 5008 ppm H_2S, water vapor, C_1-*n*C_5, and mercaptan, commercial polyphenylene oxide hollow fibers presented $\alpha_{H2S/CH4}$ = 2.9, while a commercial poly (ester urethane) urea (PEUU) flat sheet membrane gave $\alpha_{H2S/CH4}$ = 3.4, measured at 40 °C and 23 °C, respectively [299]. The separation performances of several other dense membranes to the ternary gas mixture with H_2S at 35 °C are presented in Table 6-6 for comparison.

Interestingly, after the H_2S exposure for a period of 20 – 40 h, both CO_2 permeability and CO_2/CH_4 selectivity of all membranes were regained to pre-H_2S exposure values, indicating the presence of H_2S only caused a reversible competitive sorption between the permeating molecules and no H_2S-induced plasticization or other permanent effect. These remarkable results confirmed the capability of polymer 6FDA-DAM and its Zr-MOF MMMs for simultaneous acid gases (CO_2, H_2S) separation from CH_4.

6.6. CHAPTER CONCLUSIONS

6FDA-DAM co-polyimide offers an attractive opportunity in gas separation application, and the incorporation of the highly stable zirconium-based UiO-66 and its functionalized derivatives as MMM further enhanced the separation properties. The membranes possessed excellent CO_2/CH_4 separation performance and presented high-performance stability at conditions relevant to actual gas processing (pressure, CO_2 content, temperature). The Zr-MOFs improved not only 6FDA-DAM gas separation properties but also deterred CO_2-induced plasticization and swelling. Additionally, in the presence of high H_2S content (50,000 ppm in feed mixture) at high total pressure, both CO_2- and H_2S-induced plasticization were suppressed and only reversible competitive sorption effect was observed. This successful high-pressure testing of 6FDA-DAM MMMs with Zr-MOFs is encouraging and industrially relevant for natural gas sweetening at high pressure. Nevertheless, the separation understanding in the presence of water vapor and condensable hydrocarbons needs to be addressed beforehand. These impurities are not only suspected to reduce the separation performance but could also deteriorate the physical integrity of a membrane system.

Table 6-6: Separation comparison of 6FDA-DAM and its Zr-MOF MMMs with several other dense membranes, when tested with ternary mixed gas feeds containing ≤ 15 mol.% of H_2S at 35 °C.

Polymer	Pressure (bar)	Feed compositions mol.% (CO_2:H_2S:CH_4)	Permeability (Barrer)		Selectivity		Ref
			CO_2	H_2S	CO_2/CH_4	H_2S/CH_4	
6FDA-DAM	20	30:5:65	167	137	9.1	7.4	
MMM UiO-66	20	30:5:65	385	352	15.2	13.6	This
MMM UiO-66-NH_2	20	30:5:65	243	224	9.5	8.7	study
MMM UiO-66-NH-$COCH_3$	20	30:5:65	193	172	18.2	16.2	
Cellulose acetate	10	29:6:65	2.4	2.1	22.0	19.0	[298]
Pebax 1074	10	18.1:12.5:69.4	155	695	11.0	50.0	[298]
PU2	10	18.1:12.5:69.4	195	618	5.6	18.0	[298]
PIM-6FDA-OH	34.5	15:15:70	54.7	36.0	27.8	18.3	[300]
6FDA-DAM:DABA (3:2)							
Annealed at 180 °C	48	20:10:70	55.6	25.4	32.1	14.7	[301]
Annealed at 180 °C	48	20:10:70	50.8	23.6	31.1	14.4	[301]
6FDA-PAI-1	63	20:10:70	8.1	4.2	32	11	[302]

Abbreviation:

6FDA: 2,2-bis(3,4-dicarboxyphenyl)hexafluoropropane diandydride; DAM: 2,4,6-trimethyl-1,3-diaminobenzene; PEBAX: polyether block amide; PU: polyurethane; PIM: polymers of intrinsic microporosity; DABA: 3,5-diaminobenzoic acid; PAI: poly(amide-imide)

CHAPTER 7: CONCLUSIONS AND RECOMMENDATIONS

This study successfully produced new 6FDA-copolymides MMMs, in corporation with MOFs and their gas separation performances have been presented accordingly. The optimized MMM systems have demonstrated excellent separation properties, either surpassing 1991 or 2008 Robeson upper bounds. Fig. 7-1 summarizes their performances in comparison to the industrially relevant polymeric membranes and several of the highly studied polymers.

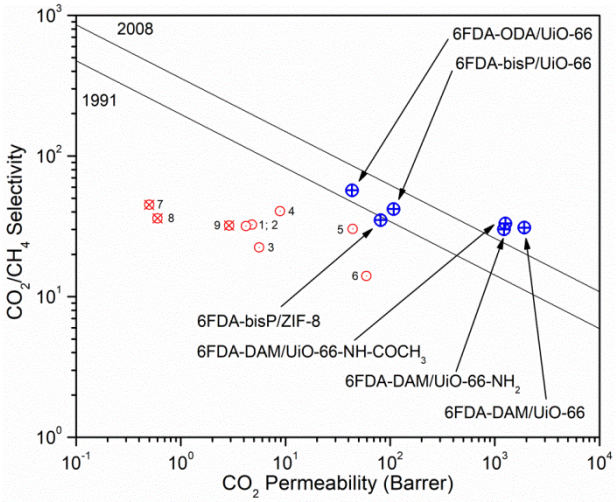

Fig. 7-1: The performances of the developed 6FDA-copolyimide MMMs in this thesis, highlighted against the industrially relevant polymeric membranes (tetra-bromo-polycarbonate, TBPC (1); cellulose acetate, CA (2); polysulfone, PSF (3); Matrimid® (4); polyimide, PI; poly(2,6-dimethyl-1,4-phenylene oxide, PPO) [41] and several of easily accessible and most intensively studied polymers (Torlon® polyamide-imide, PAI (7); polyetherimide, PEI (8); polyethersulfone, PES (9)) in the last decade, in comparison to the Robeson permeability-selectivity 1991 and 2008 upper bounds [20,21].

7.1. CONCLUSIONS

This research was set out to investigate a novel 6FDA-copolyimide and its fabrication into mixed matrix membrane with nano-sized metal organic frameworks (MOFs) for CO_2/CH_4 separation. Based on the set goals and the studies conducted within this thesis, the following conclusions could be drawn:

1. The synthesis of a new 6FDA-copolyimide membrane, namely 6FDA-bisP with high free volume (FFV = 0.196 – 0.214), for CO_2/CH_4 separation was achieved. The membrane was best prepared with an additional step of dissolving step after the polyimide was fully imidized (P_{CO2} = 33.9 – 35.3 Barrer and $\alpha_{CO2/CH4}$ = 25.6 – 27.5), and not directly obtained from thermal imidization of its constituents poly(amic acid). The preparation was highly reproducible and conducted at two different universities.
2. The guided methodology of the 6FDA-bisP and other 6FDA-copolyimides (6FDA-ODA, 6FDA-DAM) preparation into mixed matrix membranes was presented, with the nano-sized MOFs (ZIF-8, < 100 nm; UiO-66, < 50 nm). At the optimum loadings, 6FDA-bisP presented an enhanced performance of 130% and 37% for CO_2 permeability and CO_2/CH_4 selectivity with ZIF-8, whereas 52% and 217% improvements were achieved with UiO-66. 6FDA-ODA (pristine performances of P_{CO2} = 25.9 ± 3.0 Barrer, $_{\alpha CO2/CH4}$ = 20.6 ± 2.0) on the other hand presented CO_2 permeability and selectivity improvements of 67% and 177% with UiO-66. In the case of 6FDA-DAM (pristine performances of $\alpha_{CO2/CH4}$ = 29.2 ± 3.1, P_{CO2} = 997 ± 48 Barrer), CO_2 permeability also increased by 92% while maintaining the CO_2/CH_4 selectivity.
3. The investigation of a MMM with an optimized interface interaction to systematically improve the gas separation performance led the study to the preparation of amino-and acetamide-functionalized UiO-66 (< 50 nm). The latter was produced through a post-synthesis modification (PSM). We demonstrated small but significant CO_2 permeability improvements of 6FDA-DAM of 23% and 27% with UiO-66-NH_2 and UiO-66-NH-$COCH_3$, with an improvement in selectivity for the UiO-66-NH-$COCH_3$ MMMs by 13%, at their optimum loading. The incorporation of functionalized UiO-66 has overcome the difficult task of

enhancing the selectivity of a highly permeable polymer membrane. High-pressure CO_2 single gas and CO_2/CH_4 mixed gas measurement showed highly promising results, where CO_2-induced plasticization was not observed up to 40 bar, for all the membranes. The enhanced membrane performance was mirrored by its improved physical properties; i.e., free fractional volumes and glass transition temperatures, indicated good compatibility between the Zr-MOFs and 6FDA-DAM.

4. The stability of MMM systems was demonstrated in high-pressure CO_2/CH_4 separation, with various parameter variants including in the presence hydrogen sulfide (H_2S). The membranes presented high-performance stability at the relevant separation conditions to an actual gas processing (pressure, CO_2 content, temperature). The Zr-MOFs not only improved 6FDA-DAM gas separation properties but proven to deter induced plasticization and swelling. Additionally, in the presence of high H_2S content (50,000 ppm in feed mixture) at high pressure, both CO_2- and H_2S-induced plasticization were suppressed and only presented reversible competitive sorption effect.

7.2. RECOMMENDATION: FUTURE OUTLOOKS

The effectiveness of the studied 6FDA-copolyimide mixed matrix membranes, especially with the Zr-based MOFs has been demonstrated to be promising candidates for an industrial application. However, there are several other aspects need to be addressed beforehand as they present significant effects on the mixed matrix membrane's overall performances.

1. Besides the mostly studied CO_2 and H_2S gasses, which are instituting the highest portion of contaminants by concentration in the natural gas, the presence of water vapour and condensable hydrocarbons (nC_3 – nC_7, especially benzene) should be thoroughly investigated. These condensable components can cause a reduction in the membrane gas separation performance due condensation at the membrane boundary layer, competitive sorption effect and occupation of the polymer matrix free volume. The investigation also should address the transport behavior of the condensable vapour especially the polar water vapour in the hydrophilic MOFs (ZIF-8, UiO-66 and UiO-66 derivatives) and at the polymer-filler interfaces. Hence, understanding their effects to the overall membrane performances, as well

as maintaining the material structural integrity and stability is crucial for the MMM further development.

2. The gas diffusion mechanism in the MOF-based MMMs needs to be determined as well as distinguishing the rate-limiting step involved in the separation process. Understanding the mechanism would provide the improvement guidance in terms of MOF and/or membrane modification (if needed) to improve the separation and physical performance.
3. Provided the above-mentioned studies were concluded, the development of asymmetric membrane is needed to maximize the separation potential of the MMM system, either in form of a hollow fiber or a flat sheet membrane. An asymmetric membrane, with a thin mixed matrix selective layer will increase the permeation flux as the bulk diffusion resistance in the membrane will significantly decrease. Thus, an asymmetric membrane will reduce the need for a larger effective surface area in a membrane module. Nevertheless the development will present a new set of challenges particularly to produce un-defective thin membrane layer and the ideal filler-polymer morphology. The unselective diffusion through the thin layer and interfacial defects should be eliminated.
4. And last but not least, the application of the studied MMMs, especially the hydrophilic Zr-MOF MMM systems can be extended to other applications, especially in pervaporation and organic vapour removal.

REFERENCES

[1] S. Faramawy, T. Zaki, A.A.E. Sakr, J. Nat. Gas Sci. Eng. 34 (2016) 34–54.
[2] V.A. Skorobogatov, V.S. Yakushev, E.M. Chuvillin, in:, Permafr. - Sevent Int. Conf., 1998, pp. 1001–1007.
[3] B. Shimekit, H. Mukhtar, Adv. Nat. Gas Technol. (2012) 235–270.
[4] X.Y. Chen, H. Vinh-Thang, A.A. Ramirez, D. Rodrigue, S. Kaliaguine, RSC Adv. 5 (2015) 24399–24448.
[5] Z.A. Manan, W.N.R. Mohd Nawi, S.R. Wan Alwi, J.J. Klemeš, J. Clean. Prod. 167 (2017) 1–13.
[6] E.D. Bates, R.D. Mayton, I. Ntai, J.H. Davis, J. Am. Chem. Soc. 124 (2002) 926–927.
[7] R.W. Baker, in:, Adv. Membr. Technol. Appl., John Wiley & Sons, Inc., 2008, pp. 557–580.
[8] T. Rodenas, I. Luz, G. Prieto, B. Seoane, H. Miro, A. Corma, F. Kapteijn, F.X. Llabrés i Xamena, J. Gascon, Nat. Mater. 14 (2014) 48–55.
[9] R.W. Baker, K. Lokhandwala, Ind. Eng. Chem. Res. 47 (2008) 2109–2121.
[10] E. Adatoz, A.K. Avci, S. Keskin, Sep. Purif. Technol. 152 (2015) 207–237.
[11] Y. Alcheikhhamdon, M. Hoorfar, Chem. Eng. Process. Process Intensif. 120 (2017).
[12] R.W. Baker, Ind. Eng. Chem. Res. 41 (2002) 1393–1411.
[13] J.K. Fink, High Performance Polymers: 2nd Edition, William Andrew Publishing, Norwich, NY, 2008.
[14] C.A. Scholes, G.W. Stevens, S.E. Kentish, Fuel 96 (2012) 15–28.
[15] S. Sridhar, B. Smitha, T.M. Aminabhavi, Sep. Purif. Rev. 36 (2007) 113–174.
[16] W.J. Koros, R. Mahajan, J. Memb. Sci. 175 (2000) 181–196.
[17] T.S. Chung, L.Y. Jiang, Y. Li, S. Kulprathipanja, Prog. Polym. Sci. 32 (2007) 483–507.
[18] M. Vinoba, M. Bhagiyalakshmi, Y. Alqaheem, A.A. Alomair, A. Pérez, M.S. Rana, Sep. Purif. Technol. 188 (2017) 431–450.
[19] X.-L. Ma, J.Y.-S. Lin, in:, Mod. Inorg. Synth. Chem. (Second Ed., Elsevier, Amsterdam, 2017, pp. 669–686.
[20] L.M. Robeson, J. Memb. Sci. 62 (1991) 165–185.
[21] L.M. Robeson, J. Memb. Sci. 320 (2008) 390–400.
[22] X. Yan, S. Komarneni, Z. Zhang, Z. Yan, Microporous Mesoporous Mater. 183 (2014) 69–73.
[23] A.R. Millward, O.M. Yaghi, J. Am. Chem. Soc. 127 (2005) 17998–17999.
[24] P.L. Llewellyn, S. Bourrelly, C. Serre, A. Vimont, M. Daturi, L. Hamon, G. De Weireld, J. Chang, D. Hong, Y.K. Hwang, S.H. Jhung, Langmuir (2008) 7245–7250.
[25] M. Montazerolghaem, S.F. Aghamiri, M.R. Talaie, S. Tangestaninejad, J. Taiwan Inst. Chem. Eng. 72 (2017) 45–52.
[26] O.M. Yaghi, M. O'Keeffe, N.W. Ockwig, H.K. Chae, M. Eddaoudi, J. Kim, Nature 423 (2003) 705–714.
[27] S.R. Venna, M.A. Carreon, Chem. Eng. Sci. 124 (2015) 3–19.
[28] B. Seoane, J. Coronas, I. Gascon, M.E. Benavides, O. Karvan, J. Caro, F. Kapteijn, J. Gascon, Chem. Soc. Rev. 44 (2015) 2421–2454.
[29] B. Zornoza, C. Tellez, J. Coronas, J. Gascon, F. Kapteijn, Microporous Mesoporous Mater. 166 (2013) 67–78.
[30] S. Castarlenas, C. Tellez, J. Coronas, J. Memb. Sci. 526 (2017) 205–211.
[31] J. Ahmad, M.B. Hågg, J. Memb. Sci. 445 (2013) 200–210.
[32] T. Yang, T.-S. Chung, Int. J. Hydrogen Energy 38 (2013) 229–239.

[33] H. Yin, C.Y. Lau, M. Rozowski, C. Howard, Y. Xu, T. Lai, M.E. Dose, R.P. Lively, M.L. Lind, J. Memb. Sci. 529 (2017) 286–292.
[34] C. Zhang, Y. Dai, J.R. Johnson, O. Karvan, W.J. Koros, J. Memb. Sci. 389 (2012) 34–42.
[35] R. Mueller, V. Hariharan, C. Zhang, R. Lively, S. Vasenkov, J. Memb. Sci. 499 (2016) 12–19.
[36] Z. Xie, T. Li, N.L. Rosi, M.A. Carreon, J. Mater. Chem. A 2 (2014) 1239–1241.
[37] X. Zou, F. Zhang, S. Thomas, G. Zhu, V. Valtchev, S. Mintova, Chem. - A Eur. J. 17 (2011) 12076–12083.
[38] Y. Liu, G. Zeng, Y. Pan, Z. Lai, J. Memb. Sci. 379 (2011) 46–51.
[39] H. Bux, C. Chmelik, J.M. Van Baten, R. Krishna, J. Caro, Adv. Mater. 22 (2010) 4741–4743.
[40] A. Sabetghadam, B. Seoane, D. Keskin, N. Duim, T. Rodenas, S. Shahid, S. Sorribas, C. Le Guillouzer, G. Clet, C. Tellez, M. Daturi, J. Coronas, F. Kapteijn, J. Gascon, (2016) 3154–3163.
[41] D.F. Sanders, Z.P. Smith, R. Guo, L.M. Robeson, J.E. McGrath, D.R. Paul, B.D. Freeman, Polym. (United Kingdom) 54 (2013) 4729–4761.
[42] K.K. Tanabe, S.M. Cohen, Chem. Soc. Rev. 40 (2011) 498–519.
[43] G.E. Cmarik, M. Kim, S.M. Cohen, K.S. Walton, Langmuir 28 (2012) 15606–15613.
[44] D.H. Hong, M.P. Suh, Chem. - A Eur. J. 20 (2014) 426–434.
[45] Y. Cao, Y. Zhao, Z. Lv, F. Song, Q. Zhong, J. Ind. Eng. Chem. 27 (2015) 102–107.
[46] J.D. Wind, D.R. Paul, W.J. Koros, J. Memb. Sci. 228 (2004) 227–236.
[47] S.V. Kumar, H.C. Yu, J. Choi, K. Kudo, Y.H. Jang, C.M. Chung, J. Polym. Res. 18 (2011) 1111–1117.
[48] L. Cui, W. Qiu, D.R. Paul, W.J. Koros, Polymer (Guildf). 52 (2011) 5528–5537.
[49] H. Seo, B. Chae, J.H. Im, Y.M. Jung, S.W. Lee, J. Mol. Struct. 1069 (2014) 196–199.
[50] H. Kawakami, M. Mikawa, S. Nagaoka, J. Memb. Sci. 118 (1996) 223–230.
[51] V. Martin-Gil, A. Lopez, P. Hrabanek, R. Mallada, I.F.J. Vankelecom, V. Fila, J. Memb. Sci. 523 (2017) 24–35.
[52] J.H. Kim, W.J. Koros, D.R. Paul, J. Memb. Sci. 282 (2006) 21–31.
[53] T. Visser, N. Masetto, M. Wessling, J. Memb. Sci. 306 (2007) 16–28.
[54] A. Bos, I.G.M. Pünt, M. Wessling, H. Strathmann, J. Memb. Sci. 155 (1999) 67–78.
[55] M. Zamidi Ahmad, M. Navarro, M. Lhotka, B. Zornoza, C. Téllez, V. Fila, J. Coronas, Sep. Purif. Technol. 192 (2018) 465–474.
[56] A. Perea-Cachero, J. Sánchez-Laínez, Á. Berenguer-Murcia, D. Cazorla-Amorós, C. Téllez, J. Coronas, J. Memb. Sci. 544 (2017) 88–97.
[57] B. Zornoza, C. Téllez, J. Coronas, O. Esekhile, W.J. Koros, AIChE J. 61 (2015) 4481–4490.
[58] S.-H. Park, K.-J. Kim, W.-W. So, S.-J. Moon, S.-B. Lee, Macromol. Res. 11 (2003) 157–162.
[59] W. Qiu, L. Xu, C.-C. Chen, D.R. Paul, W.J. Koros, Polymer (Guildf). 54 (2013) 6226–6235.
[60] N. Alaslai, B. Ghanem, F. Alghunaimi, E. Litwiller, I. Pinnau, J. Memb. Sci. 505 (2016) 100–107.
[61] N. Jusoh, Y.F. Yeong, W.L. Cheong, K.K. Lau, A. M. Shariff, J. Ind. Eng. Chem. 44 (2016) 164–173.
[62] V. Nafisi, M.B. Hägg, Sep. Purif. Technol. 128 (2014) 31–38.
[63] C. Fuhrman, M. Nutt, K. Vichtovonga, M.R. Coleman, J. Appl. Polym. Sci. 91 (2004) 1174–1182.
[64] O.G. Nik, X.Y. Chen, S. Kaliaguine, J. Memb. Sci. 379 (2011) 468–478.

[65] K.L. Gleason, Z.P. Smith, Q. Liu, D.R. Paul, B.D. Freeman, J. Memb. Sci. 475 (2015) 204–214.
[66] D.F. Sanders, Z.P. Smith, C.P. Ribeiro Jr, R. Guo, J.E. McGrath, D.R. Paul, B.D. Freeman, J. Memb. Sci. 409–410 (2012) 232–241.
[67] O.G. Nik, X.Y. Chen, S. Kaliaguine, J. Memb. Sci. 413–414 (2012) 48–61.
[68] S. Xiao, R.Y.M. Huang, X. Feng, Polymer (Guildf). 48 (2007) 5355–5368.
[69] A.I. Wozniak, A.S. Yegorov, V.S. Ivanov, S.M. Igumnov, K. V. Tcarkova, J. Fluor. Chem. 180 (2015) 45–54.
[70] Y. Xiao, B.T. Low, S.S. Hosseini, T.S. Chung, D.R. Paul, Prog. Polym. Sci. 34 (2009) 561–580.
[71] S. Velioğlu, S.B. Tantekin-Ersolmaz, J.W. Chew, J. Memb. Sci. 543 (2017) 233–254.
[72] A. Shimazu, T. Miyazaki, T. Matsushita, M. Maeda, K. Ikeda, J. Polym. Sci. Part B Polym. Phys. 37 (1999) 2941–2949.
[73] M. Farnam, H. Mukhtar, A. Shariff, Procedia Eng. 148 (2016) 1206–1212.
[74] M.Y. Wey, H.H. Tseng, C. kai Chiang, J. Memb. Sci. 446 (2013) 220–229.
[75] N. Jusoh, Y.F. Yeong, K.K. Lau, A. M. Shariff, J. Memb. Sci. 525 (2017) 175–186.
[76] H. Zhao, Q. Xie, X. Ding, J. Chen, M. Hua, X. Tan, Y. Zhang, J. Memb. Sci. 514 (2016) 305–312.
[77] D. Zhao, J. Ren, Y. Wang, Y. Qiu, H. Li, K. Hua, X. Li, J. Ji, M. Deng, J. Memb. Sci. 521 (2017) 104–113.
[78] S.J.D. Smith, B.P. Ladewig, A.J. Hill, C.H. Lau, M.R. Hill, Sci. Rep. 5 (2015) 7823.
[79] Q. Huang, J. Ding, X. Huang, X. Wei, W. Wang, Energy Procedia 105 (2017) 4395–4401.
[80] L.H. Wee, Y. Li, K. Zhang, P. Davit, S. Bordiga, J. Jiang, I.F.J. Vankelecom, J.A. Martens, Adv. Funct. Mater. 25 (2015) 516–525.
[81] L.J. van Rooyen, H. Bissett, M.C. Khoathane, J. Karger-Kocsis, Carbon N. Y. 109 (2016) 30–39.
[82] H. Ha, J. Park, S. Ando, C. Bin Kim, K. Nagai, B.D. Freeman, C.J. Ellison, J. Memb. Sci. 518 (2016) 131–140.
[83] H.B. Tanh Jeazet, C. Staudt, C. Janiak, Dalt. Trans. 41 (2012) 14003.
[84] O.K. Farha, I. Eryazici, N.C. Jeong, B.G. Hauser, C.E. Wilmer, A.A. Sarjeant, R.Q. Snurr, S.T. Nguyen, A.Ö. Yazaydin, J.T. Hupp, J. Am. Chem. Soc. 134 (2012) 15016–15021.
[85] T. Ahnfeldt, D. Gunzelmann, J. Wack, J. Senker, N. Stock, CrystEngComm 14 (2012) 4126–4136.
[86] T. Bae, J.S. Lee, W. Qiu, W.J. Koros, C.W. Jones, (2010) 9863–9866.
[87] A.F. Bushell, M.P. Attfield, C.R. Mason, P.M. Budd, Y. Yampolskii, L. Starannikova, A. Rebrov, F. Bazzarelli, P. Bernardo, J. Carolus Jansen, M. Lanč, K. Friess, V. Shantarovich, V. Gustov, V. Isaeva, J. Memb. Sci. 427 (2013) 48–62.
[88] T. Li, Y. Pan, K.-V. Peinemann, Z. Lai, J. Memb. Sci. 425–426 (2013) 235–242.
[89] V. Nafisi, M.B. Hägg, J. Memb. Sci. 459 (2014) 244–255.
[90] L. Cao, F. Lv, Y. Liu, W. Wang, Y. Huo, X. Fu, R. Sun, Z. Lu, Chem. Commun. (Camb). 51 (2015) 1–4.
[91] G.M. Shi, T. Yang, T.S. Chung, J. Memb. Sci. 415–416 (2012) 577–586.
[92] S.C. Xiang, W. Zhou, J.M. Gallegos, Y. Liu, B.L. Chen, J. Am. Chem. Soc. 131 (2009) 12415–12419.
[93] S. Øien, D. Wragg, H. Reinsch, S. Svelle, S. Bordiga, C. Lamberti, K.P. Lillerud, Cryst. Growth Des. 14 (2014) 5370–5372.
[94] B.C. Hughes, C.R. Murdock, D.M. Jenkins, Inorg. Chem. Front. 2 (2015) 1001–1005.

[95] C.R. Murdock, N.W. McNutt, D.J. Keffer, D.M. Jenkins, J. Am. Chem. Soc. 136 (2014) 671–678.
[96] L. Zhang, G. Wu, J. Jiang, J. Phys. Chem. C 118 (2014) 8788–8794.
[97] H. Yehia, T.J. Pisklak, J.P. Ferraris, K.J. Balkus Jr., I.H. Musselman, in:, Adv. Membr. Challenging Appl., 2004.
[98] I.H. Musselman, K.J. Balkus Jr., J.P. Ferraris, Mixed-Matrix Membranes for CO2 and H2 Gas Separations Using Metal-Organic Frameworks and Mesoporous Hybrid Silicas, Richardson, Texas, 2008.
[99] A. Car, C. Stropnik, K.V. Peinemann, Desalination 200 (2006) 424–426.
[100] E.V. Perez, K.J. Balkus Jr, J.P. Ferraris, I.H. Musselman, in:, PMSE Prepr. 2006, 2006, pp. 815–816.
[101] Y. Zhang, I.H. Musselman, J.P. Ferraris, K.J. Balkus, J. Memb. Sci. 313 (2008) 170–181.
[102] R. Adams, C. Carson, J. Ward, R. Tannenbaum, W. Koros, Microporous Mesoporous Mater. 131 (2010) 13–20.
[103] S.S.Y. Chui, S.M.F. Lo, J.P.H. Charmant, a G. Orpen, I.D. Williams, Science (80-.). 283 (1999) 1148–1150.
[104] S. Basu, A. Cano-Odena, I.F.J. Vankelecom, Sep. Purif. Technol. 81 (2011) 31–40.
[105] B. Zornoza, B. Seoane, J.M. Zamaro, C. Téllez, J. Coronas, ChemPhysChem 12 (2011) 2781–2785.
[106] S. Shahid, K. Nijmeijer, J. Memb. Sci. 470 (2014) 166–177.
[107] H. Li, M. Eddaoudi, M. O'Keeffe, O.M. Yaghi, Nature 402 (1999) 276–279.
[108] S. Gadipelli, Z. Guo, Chem. Mater. 26 (2014) 6333–6338.
[109] M. Arjmandi, M. Pakizeh, J. Ind. Eng. Chem. 20 (2014) 3857–3868.
[110] N. Lock, Y. Wu, M. Christensen, L.J. Cameron, V.K. Peterson, A.J. Bridgeman, C.J. Kepert, B.B. Iversen, J. Phys. Chem. C 114 (2010) 16181–16186.
[111] J.A. Thompson, K.W. Chapman, W.J. Koros, C.W. Jones, S. Nair, Microporous Mesoporous Mater. 158 (2012) 292–299.
[112] K.S. Park, Z. Ni, A.P. Côté, J.Y. Choi, R. Huang, F.J. Uribe-Romo, H.K. Chae, M. O'Keeffe, O.M. Yaghi, Proc. Natl. Acad. Sci. U. S. A. 103 (2006) 10186–91.
[113] W. Morris, C.J. Doonan, H. Furukawa, R. Banerjee, O.M. Yaghi, J. Am. Chem. Soc. 130 (2008) 12626–12627.
[114] V.M. Aceituno Melgar, J. Kim, M.R. Othman, J. Ind. Eng. Chem. 28 (2015) 1–15.
[115] J. Cravillon, C.A. Schröder, H. Bux, A. Rothkirch, J. Caro, M. Wiebcke, CrystEngComm 14 (2012) 492–498.
[116] J. McEwen, J.D. Hayman, A. Ozgur Yazaydin, Chem. Phys. 412 (2013) 72–76.
[117] S.R. Venna, M. Zhu, S. Li, M.A. Carreon, J. Porous Mater. 21 (2014) 235–240.
[118] S. Tanaka, K. Fujita, Y. Miyake, M. Miyamoto, Y. Hasegawa, T. Makino, S. Van Der Perre, J. Cousin Saint Remi, T. Van Assche, G. V. Baron, J.F.M. Denayer, J. Phys. Chem. C 119 (2015) 28430–28439.
[119] H. Bux, A. Feldhoff, J. Cravillon, M. Wiebcke, Y.S. Li, J. Caro, Chem. Mater. 23 (2011) 2262–2269.
[120] N. Hara, M. Yoshimune, H. Negishi, K. Haraya, S. Hara, T. Yamaguchi, J. Memb. Sci. 450 (2014) 215–223.
[121] D. Liu, X. Ma, H. Xi, Y.S. Lin, J. Memb. Sci. 451 (2014) 85–93.
[122] W.S. Chi, S. Hwang, S.J. Lee, S. Park, Y.S. Bae, D.Y. Ryu, J.H. Kim, J. Kim, J. Memb. Sci. 495 (2015) 479–488.
[123] D. Eiras, Y. Labreche, L.A. Pessan, Mater. Res. 19 (2016) 220–228.
[124] M. Safak Boroglu, A.B. Yumru, Sep. Purif. Technol. 173 (2017) 269–279.
[125] K. Self, M. Telfer, H.F. Greer, W. Zhou, Chem. - A Eur. J. 21 (2015) 19090–19095.

[126] L. Li, J. Yao, X. Wang, Y.B. Cheng, H. Wang, J. Appl. Polym. Sci. 41056 (2014) 1–7.
[127] Q. Zhang, S. Luo, J.R. Weidman, R. Guo, Polymer (Guildf). 131 (2017) 209–216.
[128] M. Meilikhov, K. Yusenko, R. a Fischer, Dalton Trans. 53 (2009) 600–602.
[129] F. Dorosti, M. Omidkhah, R. Abedini, Chem. Eng. Res. Des. 92 (2014) 2439–2448.
[130] E. V. Perez, K.J. Balkus, J.P. Ferraris, I.H. Musselman, J. Memb. Sci. 328 (2009) 165–173.
[131] J.O. Hsieh, K.J. Balkus, J.P. Ferraris, I.H. Musselman, Microporous Mesoporous Mater. 196 (2014) 165–174.
[132] M. Krüger, A.K. Inge, H. Reinsch, Y.H. Li, M. Wahiduzzaman, C.H. Lin, S.L. Wang, G. Maurin, N. Stock, Inorg. Chem. 56 (2017) 5851–5862.
[133] S.J. Garibay, S.M. Cohen, Chem. Commun. (Camb). 46 (2010) 7700–2.
[134] M.W. Anjum, F. Vermoortele, A.L. Khan, B. Bueken, D.E. De Vos, I.F.J. Vankelecom, ACS Appl. Mater. Interfaces 7 (2015) 25193–25201.
[135] Q. Yang, A.D. Wiersum, H. Jobic, V. Guillerm, C. Serre, P.L. Llewellyn, G. Maurin, J. Phys. Chem. C 115 (2011) 13768–13774.
[136] S. Biswas, P. Van Der Voort, Eur. J. Inorg. Chem. (2013) 2154–2160.
[137] L. Valenzano, B. Civalleri, S. Chavan, S. Bordiga, M.H. Nilsen, S. Jakobsen, K.P. Lillerud, C. Lamberti, Chem. Mater. 23 (2011) 1700–1718.
[138] J.H. Cavka, S. Jakobsen, U. Olsbye, N. Guillou, C. Lamberti, S. Bordiga, K.P. Lillerud, 6 (2008) 13850–13851.
[139] Y.M. Xu, T.S. Chung, J. Memb. Sci. 531 (2017) 16–26.
[140] M. Kandiah, S. Usseglio, S. Svelle, U. Olsbye, K.P. Lillerud, M. Tilset, J. Mater. Chem. 20 (2010) 9848.
[141] N. Tien-Binh, H. Vinh-Thang, X.Y. Chen, D. Rodrigue, S. Kaliaguine, J. Mater. Chem. A 3 (2015) 15202–15213.
[142] Q. Xin, T. Liu, Z. Li, S. Wang, Y. Li, Z. Li, J. Ouyang, Z. Jiang, H. Wu, J. Memb. Sci. 488 (2015) 67–78.
[143] M. Rezakazemi, A. Ebadi Amooghin, M.M. Montazer-Rahmati, A.F. Ismail, T. Matsuura, Prog. Polym. Sci. 39 (2014) 817–861.
[144] H. Cong, M. Radosz, B.F. Towler, Y. Shen, Sep. Purif. Technol. 55 (2007) 281–291.
[145] P.S. Goh, A.F. Ismail, S.M. Sanip, B.C. Ng, M. Aziz, Sep. Purif. Technol. 81 (2011) 243–264.
[146] M.A. Aroon, A.F. Ismail, T. Matsuura, M.M. Montazer-Rahmati, Sep. Purif. Technol. 75 (2010) 229–242.
[147] R.D. Noble, J. Memb. Sci. 378 (2011) 393–397.
[148] M. Khayet, Chem. Eng. Sci. 58 (2003) 3091–3104.
[149] H. Hasbullah, S. Kumbharkar, A.F. Ismail, K. Li, J. Memb. Sci. 366 (2011) 116–124.
[150] P. Pandey, R.S. Chauhan, Prog. Polym. Sci. 26 (2001) 853–893.
[151] R. Lin, L. Ge, L. Hou, E. Strounina, V. Rudolph, Z. Zhu, ACS Appl. Mater. Interfaces 6 (2014) 5609–5618.
[152] T.H. Weng, H.H. Tseng, M.Y. Wey, Int. J. Hydrogen Energy 35 (2010) 6971–6983.
[153] T.T. Moore, W.J. Koros, J. Mol. Struct. 739 (2005) 87–98.
[154] M.F.A. Wahab, A.F. Ismail, S.J. Shilton, Sep. Purif. Technol. 86 (2012) 41–48.
[155] S.A. Hashemifard, A.F. Ismail, T. Matsuura, J. Memb. Sci. 347 (2010) 53–61.
[156] Y. Li, H.M. Guan, T.S. Chung, S. Kulprathipanja, J. Memb. Sci. 275 (2006) 17–28.
[157] S. Kim, E. Marand, J. Ida, V. V. Guliants, Chem. Mater. 18 (2006) 1149–1155.
[158] C. Casado-Coterillo, J. Soto, M.M. Jimaré, S. Valencia, A. Corma, C. Téllez, J. Coronas, Chem. Eng. Sci. 73 (2012) 116–122.
[159] G. Khanbabaei, E. Vasheghani-Farahani, A. Rahmatpour, Chem. Eng. J. 191 (2012) 369–377.

[160] J.R. Johnson, W.J. Koros, J. Taiwan Inst. Chem. Eng. 40 (2009) 268–275.
[161] J. Dechnik, C.J. Sumby, C. Janiak, Cryst. Growth Des. 17 (2017) 4467–4488.
[162] F. Cacho-Bailo, G. Caro, M. Etxeberria, O. Karvan, C. Tellez, J. Coronas, RSC Adv. (2016) 5881–5889.
[163] M.R. Khdhayyer, E. Esposito, A. Fuoco, M. Monteleone, L. Giorno, J.C. Jansen, M.P. Attfield, P.M. Budd, Sep. Purif. Technol. 173 (2017) 304–313.
[164] X. Liu, N.K. Demir, Z. Wu, K. Li, J. Am. Chem. Soc. 137 (2015) 6999–7002.
[165] K. Vellingiri, P. Kumar, A. Deep, K.H. Kim, Chem. Eng. J. 307 (2017) 1116–1126.
[166] C.L. Luu, T.T. Van Nguyen, T. Nguyen, T.C. Hoang, Adv. Nat. Sci. Nanosci. Nanotechnol. 6 (2015) 025004.
[167] M.J. Katz, Z.J. Brown, Y.J. Colón, P.W. Siu, K. a Scheidt, R.Q. Snurr, J.T. Hupp, O.K. Farha, Chem. Commun. (Camb). 49 (2013) 9449–51.
[168] H. Wu, Y.S. Chua, V. Krungleviciute, M. Tyagi, P. Chen, T. Yildirim, W. Zhou, J. Am. Chem. Soc. 135 (2013) 10525–10532.
[169] A. Ebadi Amooghin, M. Omidkhah, H. Sanaeepur, A. Kargari, J. Energy Chem. 25 (2016) 450–462.
[170] A.F. Ismail, S.A. Hashemifard, T. Matsuura, J. Memb. Sci. 379 (2011) 378–385.
[171] Y. Li, T.-S. Chung, S. Kulprathipanja, AIChE J. 53 (2007) 610–616.
[172] F. Li, Y. Li, T.S. Chung, S. Kawi, J. Memb. Sci. 356 (2010) 14–21.
[173] K. Zahri, K.C. Wong, P.S. Goh, A.F. Ismail, RSC Adv. 6 (2016) 89130–89139.
[174] J. Sánchez-Laínez, B. Zornoza, S. Friebe, J. Caro, S. Cao, A. Sabetghadam, B. Seoane, J. Gascon, F. Kapteijn, C. Le Guillouzer, G. Clet, M. Daturi, C. Téllez, J. Coronas, J. Memb. Sci. 515 (2016) 45–53.
[175] N.T. Dintcheva, F.P. La Mantia, V. Malatesta, Express Polym. Lett. 5 (2011) 923–935.
[176] E. Karatay, H. Kalıpçılar, L. Yılmaz, J. Memb. Sci. 364 (2010) 75–81.
[177] U. Cakal, L. Yilmaz, H. Kalipcilar, J. Memb. Sci. 417–418 (2012) 45–51.
[178] J. Jaafar, A.F. Ismail, T. Matsuura, J. Memb. Sci. 345 (2009) 119–127.
[179] H.H. Yong, H.C. Park, Y.S. Kang, J. Won, W.N. Kim, J. Memb. Sci. 188 (2001) 151–163.
[180] V.M. Aceituno Melgar, H.T. Kwon, J. Kim, J. Memb. Sci. 459 (2014) 190–196.
[181] V.M. Aceituno Melgar, H. Ahn, J. Kim, M.R. Othman, J. Ind. Eng. Chem. 21 (2015) 575–579.
[182] Y.-S. Li, F.-Y. Liang, H. Bux, A. Feldhoff, W.-S. Yang, J. Caro, Angew. Chemie 122 (2010) 558–561.
[183] H.K. Chae, D.Y. Siberio-Perez, J. Kim, Y. Go, M. Eddaoudi, A.J. Matzger, M. O'Keeffe, O.M. Yaghi, Nature 427 (2004) 523–527.
[184] B. Chen, L. Wang, Y. Xiao, F.R. Fronczek, M. Xue, Y. Cui, G. Qian, Angew. Chemie - Int. Ed. 48 (2009) 500–503.
[185] S. Shahid, K. Nijmeijer, J. Memb. Sci. 459 (2014) 33–44.
[186] P.D. Sutrisna, J. Hou, H. Li, Y. Zhang, V. Chen, J. Memb. Sci. 524 (2017) 266–279.
[187] Y. Hu, H. Kazemian, S. Rohani, Y. Huang, Y. Song, Chem. Commun. 47 (2011) 12694.
[188] H. Kaur, G.C. Mohanta, V. Gupta, D. Kukkar, S. Tyagi, J. Drug Deliv. Sci. Technol. 41 (2017) 106–112.
[189] F. Cacho-Bailo, B. Seoane, C. Téllez, J. Coronas, J. Memb. Sci. 464 (2014) 119–126.
[190] Y.R. Lee, M.S. Jang, H.Y. Cho, H.J. Kwon, S. Kim, W.S. Ahn, Chem. Eng. J. 271 (2015) 276–280.
[191] J. Cravillon, S. Münzer, S. Lohmeier, A. Feldhoff, K. Huber, Chem. Mater. 21 (2009) 1–21.

[192] J. Cravillon, R. Nayuk, S. Springer, A. Feldhoff, K. Huber, M. Wiebcke, Chem. Mater. 23 (2011) 2130–2141.
[193] L.S. Lai, Y.F. Yeong, N.C. Ani, K.K. Lau, A.M. Shariff, Part. Sci. Technol. 32 (2014) 520–528.
[194] M. Askari, T.-S. Chung, J. Memb. Sci. 444 (2013) 173–183.
[195] E.M. Mahdi, J.C. Tan, J. Memb. Sci. 498 (2016) 276–290.
[196] P. Küsgens, M. Rose, I. Senkovska, H. Fröde, A. Henschel, S. Siegle, S. Kaskel, Microporous Mesoporous Mater. 120 (2009) 325–330.
[197] D.J. Liaw, K.L. Wang, Y.C. Huang, K.R. Lee, J.Y. Lai, C.S. Ha, Prog. Polym. Sci. 37 (2012) 907–974.
[198] S. Liu, R. Wang, T.S. Chung, M.L. Chng, Y. Liu, R.H. Vora, J. Memb. Sci. 202 (2002) 165–176.
[199] G. Ragosta, M. Abbate, P. Musto, G. Scarinzi, J. Mater. Sci. 47 (2012) 2637–2647.
[200] R. Wang, S.S. Chan, Y. Liu, T.S. Chung, J. Memb. Sci. 199 (2002) 191–202.
[201] R. Heck, M.S. Qahtani, G.O. Yahaya, I. Tanis, D. Brown, A.A. Bahamdan, A.W. Ameen, M.M. Vaidya, J.P.R. Ballaguet, R.H. Alhajry, E. Espuche, R. Mercier, Sep. Purif. Technol. 173 (2017) 183–192.
[202] S.R. Venna, M. a Carreon, Synthesis (Stuttg). 40292 (2010) 1–8.
[203] N.R. Horn, J. Memb. Sci. 518 (2016) 289–294.
[204] P. Hrabánek, A. Zikánová, B. Bernauer, V. Fíla, M. Kočiřík, Desalination 245 (2009) 437–443.
[205] B. Ghanem, N. Alaslai, X. Miao, I. Pinnau, Polym. (United Kingdom) 96 (2016) 13–19.
[206] S. Velioğlu, M.G. Ahunbay, S.B. Tantekin-Ersolmaz, J. Memb. Sci. 417–418 (2012) 217–227.
[207] R. Recio, L. Palacio, P. Prádanos, A. Hernández, Á.E. Lozano, Á. Marcos, J.G. de la Campa, J. de Abajo, J. Memb. Sci. 293 (2007) 22–28.
[208] E.L. Bustamante, J.L. Fernández, J.M. Zamaro, J. Colloid Interface Sci. 424 (2014) 37–43.
[209] J. Yao, M. He, K. Wang, R. Chen, Z. Zhong, H. Wang, CrystEngComm 15 (2013) 3601.
[210] S. Japip, H. Wang, Y. Xiao, T.S. Chung, J. Memb. Sci. 467 (2014) 162–174.
[211] A. Demessence, C. Boissière, D. Grosso, P. Horcajada, C. Serre, G. Férey, G.J.A.A. Soler-Illia, C. Sanchez, J. Mater. Chem. 20 (2010) 7676.
[212] Y. Zhang, K.J. Balkus, I.H. Musselman, J.P. Ferraris, J. Memb. Sci. 325 (2008) 28–39.
[213] T. Steiner, Angew. Chem. Int. Ed. 41 (2002) 49–76.
[214] Z.P. Smith, G. Hernández, K.L. Gleason, A. Anand, C.M. Doherty, K. Konstas, C. Alvarez, A.J. Hill, A.E. Lozano, D.R. Paul, B.D. Freeman, J. Memb. Sci. 493 (2015) 766–781.
[215] T. Koley, P. Bandyopadhyay, A.K. Mohanty, S. Banerjee, Eur. Polym. J. 49 (2013) 4212–4223.
[216] R. Banerjee, H. Furukawa, D. Britt, C. Knobler, M.O. Keeffe, O.M. Yaghi, J. Am. Chem. Soc. 131 (2009) 3875–3877.
[217] H.R. Amedi, M. Aghajani, J. Nat. Gas Sci. Eng. 35 (2016) 695–702.
[218] J. Park, D.R. Paul, J. Memb. Sci. 125 (1997) 23–39.
[219] W.J. Koros, R.T. Chern, V. Stannett, H.B. Hopfenberg, J. Polym. Sci. Polym. Phys. Ed. 19 (1981) 1513–1530.
[220] M.Z. Ahmad, M. Navarro, M. Lhotka, B. Zornoza, C. Téllez, W.M. De Vos, N.E. Benes, N.M. Konnertz, T. Visser, R. Semino, G. Maurin, V. Fila, J. Coronas, J. Memb. Sci. 558 (2018) 64–77.

[221] S. Kanehashi, T. Nakagawa, K. Nagai, X. Duthie, S. Kentish, G. Stevens, J. Memb. Sci. 298 (2007) 147–155.
[222] G. Férey, Chem. Soc. Rev. 37 (2008) 191–214.
[223] J.R. Long, O.M. Yaghi, Chem. Soc. Rev. 38 (2009) 1213–1214.
[224] J. Shen, G. Liu, K. Huang, Q. Li, K. Guan, Y. Li, W. Jin, J. Memb. Sci. 513 (2016) 155–165.
[225] D.X. Trinh, T.P.N. Tran, T. Taniike, Sep. Purif. Technol. 177 (2017) 249–256.
[226] L. Hou, L. Wang, N. Zhang, Z. Xie, D. Dong, Polym. Chem. 7 (2016) 5828–5834.
[227] T. Yang, Y. Xiao, T.-S. Chung, Energy Environ. Sci. 4 (2011) 4171.
[228] X. Zhu, J. Gu, Y. Wang, B. Li, Y. Li, W. Zhao, J. Shi, Chem. Commun. (Camb). (2014) 8779–8782.
[229] S. Wang, W. Morris, Y. Liu, C.M. McGuirk, Y. Zhou, J.T. Hupp, O.K. Farha, C.A. Mirkin, Angew. Chemie - Int. Ed. 54 (2015) 14738–14742.
[230] A. Schaate, P. Roy, A. Godt, J. Lippke, F. Waltz, M. Wiebcke, P. Behrens, Chem. - A Eur. J. 17 (2011) 6643–6651.
[231] M.J. Katz, Z.J. Brown, Y.J. Colón, P.W. Siu, K.A. Scheidt, R.Q. Snurr, J.T. Hupp, O.K. Farha, Chem. Commun. 49 (2013) 9449.
[232] S. Xian, Y. Wu, J. Wu, X. Wang, J. Xiao, Ind. Eng. Chem. Res. 54 (2015) 11151–11158.
[233] L. Xu, C. Zhang, M. Rungta, W. Qiu, J. Liu, W.J. Koros, J. Memb. Sci. 459 (2014) 223–232.
[234] H. Mao, S. Zhang, J. Colloid Interface Sci. 490 (2017) 29–36.
[235] M.J.C. Ordoñez, K.J. Balkus, J.P. Ferraris, I.H. Musselman, J. Memb. Sci. 361 (2010) 28–37.
[236] C. Zhang, P. Li, B. Cao, J. Memb. Sci. 528 (2017) 206–216.
[237] C.K. Yeom, J.M. Lee, Y.T. Hong, K.Y. Choi, S.C. Kim, J. Memb. Sci. 166 (2000) 71–83.
[238] B. Huang, W. Zhang, R. Xu, Z. Shi, C. Fu, Y. Wang, K. Song, Energies 10 (2017) 951.
[239] M. Moaddeb, W.J. Koros, J. Memb. Sci. 125 (1997) 143–163.
[240] H. Lin, M. Yavari, J. Memb. Sci. 475 (2015) 101–109.
[241] K.W. Moore TT, Mahajan R, Vu DQ, AIChE J 50 (2004) 311–21.
[242] L. Hou, L. Wang, N. Zhang, Z. Xie, D. Dong, Polym. Chem. 7 (2016) 5828–5834.
[243] M.L. Cecopieri-Gómez, J. Palacios-Alquisira, J.M. Domínguez, J. Memb. Sci. 293 (2007) 53–65.
[244] G. George, N. Bhoria, S. Alhallaq, A. Abdala, V. Mittal, Sep. Purif. Technol. 158 (2016) 333–356.
[245] G. Férey, Chem. Mater. 13 (2001) 3084–3098.
[246] G. Maurin, C. Serre, A. Cooper, G. Férey, Chem. Soc. Rev. 46 (2017) 3104–3107.
[247] B.F. Hoskins, R. Robson, J. Am. Chem. Soc. 111 (1989) 5962–5964.
[248] K. Adil, Y. Belmabkhout, R.S. Pillai, A. Cadiau, P.M. Bhatt, A.H. Assen, G. Maurin, M. Eddaoudi, Chem. Soc. Rev. 46 (2017) 3402–3430.
[249] G. Férey, C. Serre, Chem. Soc. Rev. 38 (2009) 1380.
[250] G. Férey, C. Serre, T. Devic, G. Maurin, H. Jobic, P.L. Llewellyn, G. De Weireld, A. Vimont, M. Daturi, J.-S. Chang, Chem. Soc. Rev. 40 (2011) 550–562.
[251] A. Schneemann, V. Bon, I. Schwedler, I. Senkovska, S. Kaskel, R.A. Fischer, Chem. Soc. Rev. 43 (2014) 6062–6096.
[252] H. Vinh-Thang, S. Kaliaguine, Chem. Rev. 113 (2013) 4980–5028.
[253] T.-H. Bae, J.R. Long, Energy Environ. Sci. 6 (2013) 3565.
[254] M. Loloei, A. Moghadassi, M. Omidkhah, A. Ebadi Amooghin, Greenh. Gases Sci. Technol. 2 (2015) 530–544.

[255] R.J. Swaidan, X. Ma, E. Litwiller, I. Pinnau, J. Memb. Sci. 495 (2015) 235–241.
[256] J.T. Vaughn, W.J. Koros, J.R. Johnson, O. Karvan, J. Memb. Sci. 401–402 (2012) 163–174.
[257] C. Hibshman, C.J. Cornelius, E. Marand, J. Memb. Sci. 211 (2003) 25–40.
[258] B.D. Freeman, Macromolecules 32 (1999) 375–380.
[259] B. Seoane, J.M. Zamaro, C. Téllez, J. Coronas, RSC Adv. 1 (2011) 917.
[260] M. Etxeberria-Benavides, O. David, T. Johnson, M.M. Łozińska, A. Orsi, P.A. Wright, S. Mastel, R. Hillenbrand, F. Kapteijn, J. Gascon, J. Memb. Sci. 550 (2018) 198–207.
[261] V. Stannett, J. Memb. Sci. 3 (1978) 97–115.
[262] M. Saberi, A.A. Dadkhah, S.A. Hashemifard, J. Memb. Sci. 499 (2016) 164–171.
[263] J.E. Bachman, Z.P. Smith, T. Li, T. Xu, J.R. Long, Nat. Mater. 15 (2016) 845–849.
[264] J.E. Bachman, J.R. Long, Energy Environ. Sci. 9 (2016) 2031–2036.
[265] T. Visser, G.H. Koops, M. Wessling, J. Memb. Sci. 252 (2005) 265–277.
[266] M. Wessling, M. Lidon Lopez, H. Strathmann, Sep. Purif. Technol. 24 (2001) 223–233.
[267] A. Kazemi, M. Malayeri, A. Gharibi kharaji, A. Shariati, J. Nat. Gas Sci. Eng. 20 (2014) 16–22.
[268] A. Kazemi, A.G. Kharaji, A. Mehrabani-Zeinabad, V. Faizi, J. Kazemi, A. Shariati, J. Unconv. Oil Gas Resour. 14 (2016) 6–11.
[269] A.J. Kidnay, W.R. Parrish, in:, L.L. Faulkner (Ed.), Fundam. Nat. Gas Process., CRC Press, Taylor & Francis Group, Boca Raton, FL, 2006, pp. 1–21.
[270] M. Galizia, W.S. Chi, Z.P. Smith, T.C. Merkel, R.W. Baker, B.D. Freeman, Macromolecules (2017) 7809–7843.
[271] N.L. Le, Y. Wang, T.S. Chung, J. Memb. Sci. 415–416 (2012) 109–121.
[272] K. Vanherck, G. Koeckelberghs, I.F.J. Vankelecom, Prog. Polym. Sci. 38 (2013) 874–896.
[273] J.D. Wind, C. Staudt-Bickel, D.R. Paul, W.J. Koros, Macromolecules 36 (2003) 1882–1888.
[274] M.L. Chua, Y.C. Xiao, T.S. Chung, Chem. Eng. Sci. 104 (2013) 1056–1064.
[275] W.F. Yong, K.H.A. Kwek, K.S. Liao, T.S. Chung, Polym. (United Kingdom) 77 (2015) 377–386.
[276] R.T. Adams, J.S. Lee, T.H. Bae, J.K. Ward, J.R. Johnson, C.W. Jones, S. Nair, W.J. Koros, J. Memb. Sci. 367 (2011) 197–203.
[277] S. Akbar, A.H. Navarchian, Gas Process. J. 4 (2016) 1–18.
[278] S. Lee, M. Binns, J.H. Lee, J.-H. Moon, J. Yeo, Y.-K. Yeo, Y.M. Lee, J.-K. Kim, J. Memb. Sci. 541 (2017).
[279] M. Scholz, T. Harlacher, T. Melin, M. Wessling, Ind. Eng. Chem. Res. 52 (2013) 1079–1088.
[280] C.A. Scholes, G.W. Stevens, S.E. Kentish, J. Memb. Sci. 350 (2010) 189–199.
[281] R. Semino, J.C. Moreton, N.A. Ramsahye, S.M. Cohen, G. Maurin, Chem. Sci. 00 (2018) 1–10.
[282] Z. Li, F. Liao, F. Jiang, B. Liu, S. Ban, G. Chen, C. Sun, P. Xiao, Y. Sun, Fluid Phase Equilib. 427 (2016) 259–267.
[283] W. Ogieglo, M. Wessling, N.E. Benes, Macromolecules 47 (2014) 3654–3660.
[284] J.S. Vrentas, C.M. Vrentas, Macromolecules 24 (1991) 2404–2412.
[285] F. Doghieri, G.C. Sarti, Macromolecules 29 (1996) 7885–7896.
[286] R. Swaidan, B. Ghanem, E. Litwiller, I. Pinnau, J. Memb. Sci. 475 (2015) 571–581.
[287] T. Battal, N. Baç, L. Yilmaz, Sep. Sci. Technol. 30 (1995) 2365–2384.
[288] T. Komatsuka, K. Nagai, Polym. J. 41 (2009) 455–458.

[289] R.P. Singh, X. Li, K.W. Dudeck, B.C. Benicewicz, K.A. Berchtold, Polymer (Guildf). 119 (2017) 134–141.
[290] R.P. Lively, M.E. Dose, L. Xu, J.T. Vaughn, J.R. Johnson, J.A. Thompson, K. Zhang, M.E. Lydon, J.S. Lee, L. Liu, Z. Hu, O. Karvan, M.J. Realff, W.J. Koros, J. Memb. Sci. 423–424 (2012) 302–313.
[291] C.M. Zimmerman, W.J. Koros, J. Polym. Sci. Part B Polym. Phys. 37 (1999) 1251–1265.
[292] W.H. Lin, T.S. Chung, J. Memb. Sci. 186 (2001) 183–193.
[293] D.W. Van Krevelen, K. Te Nijenhuis, in:, D.W. Van Krevelen, K. Te Nijenhuis (Eds.), Prop. Polym. (Fourth Ed., Fourth Edi, Elsevier, Amsterdam, 2009, pp. 189–227.
[294] A.A. Radzig, B.M. Smirnov, in:, Ref. Data Atoms, Mol. Ions. Springer Ser. Chem. Phys., Springer, Berlin, Heidelberg, 1985, pp. 317–315.
[295] J. Vaughn, W.J. Koros, Macromolecules 45 (2012) 7036–7049.
[296] G.O. Yahaya, M.S. Qahtani, A.Y. Ammar, A.A. Bahamdan, A.W. Ameen, R.H. Alhajry, M.M.B. Sultan, F. Hamad, Chem. Eng. J. 304 (2016) 1020–1030.
[297] T. Mohammadi, M.T. Moghadam, M. Saeidi, M. Mahdyarfar, Ind. Eng. Chem. Res. 47 (2008) 7361–7367.
[298] G. Chatterjee, A.A. Houde, S.A. Stern, J. Memb. Sci. 135 (1997) 99–106.
[299] S.M.S. Niknejad, H. Savoji, M. Pourafshari Chenar, M. Soltanieh, Int. J. Environ. Sci. Technol. 14 (2017) 375–384.
[300] S. Yi, X. Ma, I. Pinnau, W.J. Koros, J. Mater. Chem. A 3 (2015) 22794–22806.
[301] B. Kraftschik, W.J. Koros, J.R. Johnson, O. Karvan, J. Memb. Sci. 428 (2013) 608–619.
[302] J.T. Vaughn, W.J. Koros, J. Memb. Sci. 465 (2014) 107–116.

BIOGRAPHY

Mohd Zamidi Ahmad was born on May 28th, 1984 in Kelantan, Malaysia. He attended Royal Military College, Kuala Lumpur from the tender age of 14, and finished the high school certification in 2001. He later moved to the north of Malaysia, to Kolej Matrikulasi Kulim for a one-year pre-university program in Life Science.

After, he studied chemistry in National University of Malaysia and awarded Bachelor of Science with Honors (Chemistry) in 2006. Soon after, he joined PETRONAS Research Sdn Bhd as a Researcher (Chemist). His first project was on the crude preheat train energy recovery optimization in PETRONAS Melaka Refinery Complex, focusing on the development of fouling mitigation suite. In this period too, he pursued an MSc in Chemical Engineering by research, in the University of Technology PETRONAS. The thesis was titled 'Fouling characteristics of Malaysian sweet crude oils.' After its completion in 2010, he worked on the de-acidification of high acid crude oil and mercury removal in gas and condensate, using ionic liquid technology. These projects allowed him to work in close collaborations with local and international experts (Queen's University of Belfast, Universiti Teknologi PETRONAS, Cameron, Intertek).

In 2012, he was promoted to Senior Researcher (Chemist) and began working in upstream CO_2 Management Department, focusing on the membrane development for high CO_2 separation. He worked in both polymeric and mixed matrix membrane (TRL 1–6). The highlight was by achieving technology field testing (TRL 6) in Tangga Barat Central Processing Platform (TBCP-A, Malaysia. The project was in collaboration with PETRONAS Upstream Division and several contractors (UTM, GENERON). He also led PRSB Membrane Lab Centre and directly involved in the assembly and commissioning of Membrane Performance Test Rig (MPTR) pilot plant.

In 2014, Zamidi was awarded a European Union Joint Doctorate Program in Membrane Engineering and began his Ph.D. research in University of Chemistry and Technology Prague, Czech Republic. His study focuses on the development of mixed matrix membrane based on newly synthesized or modified polyimide with metal-organic frameworks (MOFs) for natural gas separation. He later conducted his mobility collaborations with University of Zaragoza, Spain, and University of Twente, Netherlands. He was employed by European Membrane Institute Twente, Netherlands in 2018 as a researcher for a short period, before deciding to continue with his scientific career in oil and gas industry.

Zamidi is a membrane of European Membrane Society, ASEAN Membrane & Technology Society, and Malaysian Institute of Chemistry (a member of Federation of Asian Chemical Societies).

LIST OF PUBLICATIONS

Peer-reviewed journal articles, as per June 2018:

1. Joanna Cookney, Mark E. Light, **Mohd Zamidi Ahmad**, Vlastimil Fila, Nieck E. Benes **CCDC 1554678: Experimental Crystal Structure Determination**, 2017. DOI: https://dx.doi.org/10.5517/ccdc.csd.cc1p5rxj
2. Roberto Castro-Muñoz, Violeta Martin-Gil, **Mohd Zamidi Ahmad**, Vlastimil Fíla, **Current state-of-the-art of Matrimid® 5218 in membrane preparation for gas separation**, Chem. Eng. Commun. 2018 (205), 2, 161-196. DOI: https://doi.org/10.1080/00986445.2017.1378647
3. **Mohd Zamidi Ahmad**, Marta Navarro, Miloslav Lhotka, Beatriz Zornoza, Carlos Téllez, Vlastimil Fila, Joaquín Coronas, **Enhancement of CO_2/CH_4 separation performances of 6FDA-based co-polyimides mixed matrix membranes embedded with UiO-66 nanoparticles**, Sep. Purif. Technol., 2018 (192), 465-474. DOI: https://doi.org/10.1016/j.seppur.2017.10.039
4. **Mohd Zamidi Ahmad**, Marta Navarro, Miloslav Lhotka, Beatriz Zornoza, Carlos Téllez, Wiebe M. De Vos, Nieck E. Benes, Nora M. Konnertz, Tymen Visser, Rocio Semino, Guillaume Maurin, Vlastimil Fila, Joaquín Coronas, **Enhanced gas separation performance of 6FDA-DAM based mixed matrix membranes by incorporating MOF UiO-66 and its derivatives**, J. Memb. Sci. 558 (2018), 64–77. DOI: https://doi:10.1016/j.memsci.2018.04.040
5. **Mohd Zamidi Ahmad**, Violeta Martin-Gil, Viacheslav Perfilov, Petr Sysel, Vlastimil Fila; **Investigation of a new co-polyimide, 6FDA-bisP and its ZIF-8 mixed matrix membranes for CO_2/CH_4 separation**. Sep. Purif. Technol. 2018 (207), 523-534. DOI: https://doi.org/10.1016/j.seppur.2018.06.067
6. **Mohd Zamidi Ahmad**, Henri Pelletier, Roberto Castro-Muñoz, Violeta Martin-Gil, Vlastimil Fila; **Chemical crosslinking of 6FDA-ODA and 6FDA-ODA: DABA membranes for improved CO_2/CH_4 separation**. Membranes, 2018, 8(3), 67 DOI: https://doi.org/10.3390/membranes8030067

Submitted articles:

1. V. Martin-Gil, **M. Z. Ahmad**, R. Castro-Muñoz, V. Fila Membrane technologies for natural gas applications. **A complete review of natural gas status and membrane technologies potential**, Sep. Purif. Review, 2017. Revised manuscript submitted in June 2018.
2. Srabani Majumdar, Violeta Martin-Gil, Roberto Castro-Muñoz, **Mohd Zamidi Ahmad**, James Campbell, Vlastimil Fila, Begum Tokay; **CO_2 separation performance of Mg–MOF–74/Poly (vinyl acetate) mixed matrix membranes**. Submitted to Microporous & Mesoporous Materials, March 2018
3. **Mohd Zamidi Ahmad**, Thijs Peters, Nora M. Konnertz, Tymen Visser, Carlos Téllez, Joaquín Coronas, Vlastimil Fila, Wiebe M. de Vos, Nieck E. Benes; High-pressure CO_2/CH_4 separation of Zr-MOFs based mixed matrix membranes, submitted to J. Memb. Sci, June 2018.
4. Roberto Castro-Muñoz, Vlastimil Fíla, **Mohd Zamidi Ahmad**; **Enhancement of CO_2 capture in Matrimid® 5218 membranes through PEG 200 addition**. Submitted to Chemical Engineering Science, February 2018.

Selected conference abstracts:

1. **Mohd Zamidi Ahmad**, Thijs Peters, Nora M. Konnertz, Tymen Visser, Carlos Téllez, Joaquín Coronas, Vlastimil Fila, Wiebe M. de Vos, Nieck E. Benes; **High-pressure CO_2/CH_4 separation of Zr-MOFs based mixed matrix membranes**
   EUROMEMBRANE 2018, July 2018, Valencia, SPAIN (oral presentation).
2. **Mohd Zamidi Ahmad**, Marta Navarro, Miloslav Lhotka, Beatriz Zornoza, Carlos Téllez, Wiebe M. De Vos, Nieck E. Benes, Vlastimil Fila, Joaquín Coronas, **Enhanced CO_2/CH_4 separation performances of 6FDA-DAM incorporated with Zr-UiO66 and its derivatives. Part 1: Mixed matrix membrane development.**
   10^{th} WCCE 2017, Oct. 2017, Barcelona, SPAIN (oral presentation).
3. **Mohd Zamidi Ahmad**, Marta Navarro, Miloslav Lhotka, Beatriz Zornoza, Carlos Téllez, Vlastimil Fila, Joaquín Coronas; **Gas Separation Performances of 6FDA-based Polyimide Mixed Matrix Membranes with High Surface Area UiO-66 (Zr-BDC) Nanoparticles**.
   ICOM 2017, July 2017. SF, USA (Oral presentation)

4. **Mohd Zamidi Ahmad**, Henri Pelletier, Roberto Castro-Muñoz, Violeta Martin-Gil, Vlastimil Fila; **Chemical crosslinking of 6FDA-ODA and 6FDA-ODA: DABA membranes for an improved CO_2/CH_4 separation**.
   ICOM 2017, July 2017. SF, USA (poster presentation)
5. Martín-Gil, **Mohd Zamidi Ahmad**, R. Castro-Muñoz, D. Dlouhy, J. Ullsperger, V. Fíla., **Membranes for gas separation applications**.
   8th Czech-Austrian workshop: New trends in photo and electro catalysis, Hnanice, 30.11-2.12.2016 (oral presentation)
6. **M. Z. Ahmad**, V. Fila, W. N. F. Mustapa, L. S. Nazir, Y. S. Yeo, Y. Said, M. H. Shafiai, M. F. Habarudin; **High-pressure gas separation performance of PEI/HNT mixed matrix membranes: A pilot study**.
   CHISA 2016, Aug 2016, Prague CR (poster presentation)
7. **M. Z. Ahmad**, V. Fila, P. Sysel; **Gas transport properties of a novel polyimide and its enhanced polyimide-zeolitic imidazolate framework: ZIF-8 mixed matrix membrane**.
   PERMEA & MELPRO 2016, May 2016, Prague, CR (poster presentation)
8. Friess Karel, LANČ Marek, PILNÁČEK Kryštof, ČÍHAL Petr, VOPIČKA Ondřej, RADOTÍNSKÝ Daniel, FÍLA Vlastimil, **ZAMIDI Ahmad**, ŠTĚPÁNEK František, ŠOLTYS Marek, SARVAŠOVÁ Nina, VU Nguyen Hong, SYSEL Petr, MALÝ David, VYŠOHLÍD Jan, IZÁK Pavel, KÁRÁSZOVÁ Magda, SEDLÁKOVÁ Zuzana: **Tailor-made nano-scale additives for CO_2/CH_4 gas separation mixed matrix membranes**.
   NANOCON 2015, Oct. 2015, Brno, CR (oral presentation)
9. **M. Z. Ahmad**, V. Fila, P. Sysel; **Gas Transport Properties of A Novel Polyimide and Its Enhanced Polyimide – Zeolitic Imidazolate Framework: ZIF-8 Mixed Matrix Membrane**.
   EMS Summer Membrane School 2015, June 2015, Liberec, CR (poster presentation).

GRATITUDE

First and foremost, I would like to thank my precious mother for all the support you have given, without any hesitation and for always being there for me. I would like to apologize too for missing many of your smiles, giggles, and tears. Know that I cannot do this without you and I love you very much. To my siblings, who have been very supportive all these years. You too have done too much and sacrificed too many times, each in your own way to be there for mum during my absence. I cannot thank you enough for that. I love all of you too.

To my 'bestest' of friends Jimmy Najeem, Shamin Yusof, Shahrezzan Ezani and Alia Bastamam (and our parents; mummy Zara, Auntie Zaimah, Auntie Patimah, uncle Din and Uncle Bastamam), you know what you have done to have me succeed this journey and thank you too. To others (Jaity Adrina, Farah Mior, Azri Aznan, Iko Ira Tanya, Lissa Firdaus, W. Azri Jaafar, Priscilla Tan, Natalie Kniese, Natrah Omar, Fairul and many more) I have missed you, and you should be glad that I am not around to annoy you all the time.

Secondly, I would like to thank my supervisors from UCTP (Vlastimil Fila), UNIZAR (Joaquin Coronas and Carlos Tellez) and UTwente (Nieck Benes and Wiebe de Vos). Not forgetting the key personnel in Instituto de Nanociencia de Aragón (INA); Beatriz Zornoza and Marta Navarro, from the European Membrane Institute Twente (EMI); Tymen Visser, Nora Konnertz, Denys Pavlenko and in Membrane Science and Technology (MST) group; Antoine Kemperman, Herman Teunis, and Harmen Zwijnenberg. You have helped me a lot and thank you for your continuous support and guidance. I appreciate and enjoy every moment, despite the hardship – the journey teaches me to a lot of new things, and I pray it will make me a better scientist and most importantly a better person.

To all my colleagues in UTCP; Violeta Martin, Roberto Castro, Viacheslav Perfilov, Milan Bernauer, Joanna Cookney and Henri Pelletier, thank you for making my stay challenging and interesting. I wish everyone great successes. Also to all the colleagues in both UNIZAR and UTwente, thank you. I won't be able to list all of your names here, but you guys rock. I love every moment and laughter we had. And finally, Xavier Cruz (also mama Loli and Papa Francesc), thank you for all your help and kindness during my early days in Europe. And my utmost appreciation to Michal Kasparek and mummy Dasha for amazing years we have so far, you have given me the support and care far more than I could ever imagine. Love you guys.

ANNEX 1. CONCLUSIONES Y RECOMENDACIONES

En esta Tesis Doctoral se ha realizado exitosamente el desarrollo de nuevas membranas de matriz mixta (MMMs) basadas en copoliimidas de 6FDA y la incorporación de MOFs. Además, se han presentado los rendimientos de estas MMMs en la separación de gases. Las MMMs optimizadas han demostrado excelentes propiedades de separación ya sea superando los límites de Robeson en 1991 o en 2008. La figura A-1 resume sus rendimientos en comparación con las membranas poliméricas industrialmente relevantes y membranas estudiadas en la bibliografía.

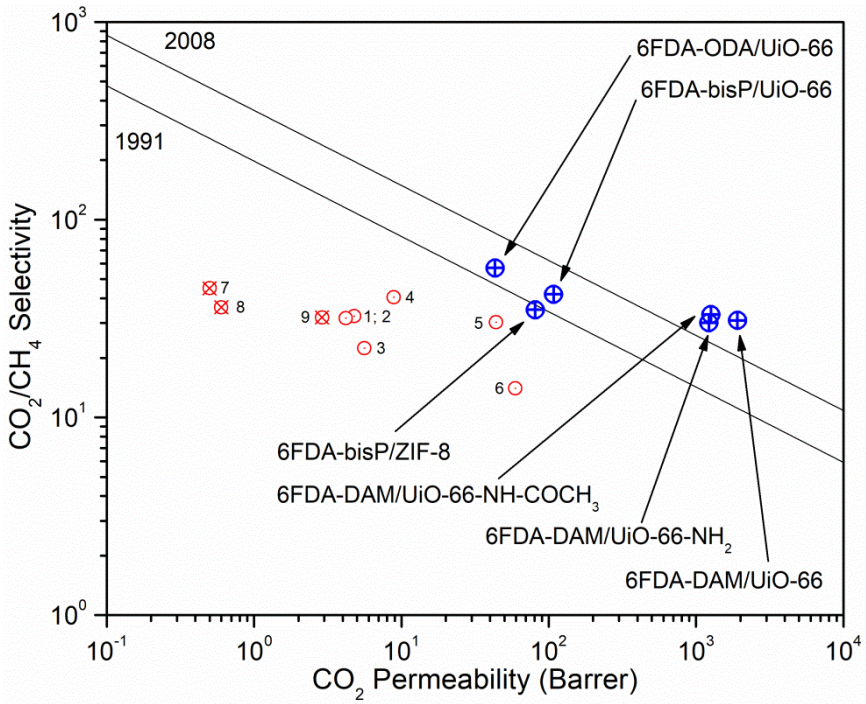

Fig. A-1: Rendimientos de las MMMs basadas en 6FDA-copolIimidas desarrolladas en esta tesis frente a las membranas poliméricas usadas industrialmente (tetra-bromo-policarbonato, TBPC (1), acetato de celulosa, CA (2), polisulfona, PSF (3), Matrimid® (4), poliimida, PI, poli (2,6-dimetil-1,4-fenileno) óxido, PPO) [41] y varios de los polímeros ampliamente estudiados en la última década (Torlon® poliamida-imida, PAI (7), polieterimida, PEI (8), polietersulfona, PES (9)). Los resultados se comparan también con los límites de Robeson en 1991 y 2008 [20,21].

7.1. Conclusiones

Esta investigación se estableció para investigar una nueva copoliimida basada en 6FDA y su uso para la fabricación de membranas de matriz mixta con MOFs nanométricos para la separación de CO_2/CH_4. En base a los objetivos establecidos y los estudios realizados dentro de esta tesis, se han obtenido las siguientes conclusiones:

1. Se logró la síntesis de una nueva membrana de copoliimida 6FDA, nombrada 6FDA-bisP con alto volumen libre (FFV = 0.196 - 0.214), para la separación de CO_2 / CH_4. La membrana se preparó mejor con una etapa adicional de disolución después de que la poliimida fue imidizada completamente (P_{CO2} = 33.9 – 35.3 Barrer y $\alpha_{CO2\ /\ CH4}$ = 25.6 – 27.5), y no se obtuvo directamente de la imidación térmica de sus componentes poliácido ámico. La preparación fue reproducible y se llevó a cabo en dos diferentes universidades.
2. Se presentó la metodología para la preparación de membranas de matriz mixta basadas en 6FDA-bisP y otras copoliimidas de 6FDA- (6FDA-ODA, 6FDA-DAM), con MOFs de tamaño nanométrico (ZIF-8, <100 nm; UiO-66, < 50 nm). En las cargas óptimas, 6FDA-bisP presentó un rendimiento mejorado del 130% y 37% para la permeabilidad al CO_2 y la selectividad de CO_2/CH_4, respectivamente, para ZIF-8, mientras que se lograron mejoras del 52% y 217% con UiO-66. Por otro lado, 6FDA-ODA (resultados de membrana pura P_{CO2} = 25.9 ± 3.0 barrer, $\alpha_{CO2/CH4}$ = 20.6 ± 2.0) presentó mejoras de selectividad y permeabilidad al CO_2 del 67% y 177%, respectivamente, con UiO-66. En el caso de 6FDA-DAM (rendimientos de membrana pura $\alpha_{CO2/CH4}$ = 29.2 ± 3.1, P_{CO2} = 997 ± 48 Barrer), la permeabilidad al CO_2 también aumentó en un 92% mientras que la selectividad CO_2/CH_4 se mantuvo.
3. La investigación de una MMM con una interacción en la interfase optimizada para mejorar el rendimiento de separación condujo a la preparación de UiO-66 funcionalizado con grupos amino y acetamida (tamaño de partícula<50 nm). La funcionalización se realizó a través de una modificación posterior a la síntesis. Se demostró pequeñas pero significativas mejoras de la permeabilidad al CO_2 en 6FDA-DAM de 23% y 27% con UiO-66-NH_2 y UiO-66-NH-$COCH_3$, respectivamente, con una mejora en la selectividad para las MMMs de UiO-66-NH-$COCH_3$ del 13 %, con su carga óptima. La incorporación de UiO-66 funcionalizado ha superado la difícil tarea de mejorar la selectividad de una

membrana de polímero altamente permeable. La medición de mezclas de gases de CO_2 a alta presión y CO_2 / CH_4 mostró resultados muy prometedores, donde la plastificación inducida por CO_2 no se observó hasta 40 bar en todas las membranas. La mejora en el rendimiento de la membrana se reflejó en sus propiedades físicas; a través de la fracción de volumen hueco y temperaturas de transición vítrea lo que indicó una buena compatibilidad entre los Zr-MOF y 6FDA-DAM.

4. Se demostró la estabilidad de las MMM en la separación de CO_2/CH_4 a alta presión, con la variación de diversos parámetros incluyendo la presencia de sulfuro de hidrógeno (H_2S). Las membranas presentaron alta estabilidad en condiciones de separación relevantes (presión, contenido de CO_2, temperatura) para el procesamiento de gases reales. Los Zr-MOFs no solo mejoraron las propiedades de separación de gases 6FDA-DAM, sino que también demostraron que disuade la plastificación e hinchazón. Además, en presencia de un alto contenido de H_2S (50,000 ppm en la mezcla de alimentación) a alta presión, tanto la plastificación inducida por CO_2 como la H_2S se suprimieron y solo presentó un efecto de adsorción competitivo reversible.

7.2. Recomendaciones: Perspectivas futuras

La eficacia de las membranas de matriz mixta de 6FDA-copolimida estudiadas, especialmente con los MOF basados en Zr, muestra que las MMMs son candidatas prometedoras para su aplicación industrial. Sin embargo, hay otros aspectos que deben abordarse de antemano, ya que presentan efectos significativos sobre el rendimiento general de la membrana de matriz mixta.

1. Además de los gases más estudiados como CO_2 y H_2S, que se están considerando como la mayor fracción de contaminantes por concentración en el gas natural, la presencia de vapor de agua e hidrocarburos condensables (nC_3 y nC_7, especialmente benceno) debe investigarse a fondo. Estos componentes condensables pueden causar una reducción en el rendimiento de separación de gases en la membrana debido a la condensación en la capa límite de la membrana, el efecto de adsorción competitivo y la ocupación del volumen libre de la matriz polimérica. La investigación también debe abordar el comportamiento de transporte del vapor condensable, especialmente el vapor de agua polar en los

MOF hidrófilos (ZIF-8, UiO-66 y derivados del UiO-66) y en las interfases de polímero-MOF. Por lo tanto, la comprensión de sus efectos en el rendimiento global de la membrana, así como el mantenimiento de la integridad estructural del material y la estabilidad es crucial para el futuro desarrollo de las MMMs.

2. El mecanismo de difusión de gas en las MMMs basadas en MOF necesita ser determinado así como también distinguir el paso limitante de velocidad involucrado en el proceso de separación. A través de la comprensión del mecanismo se proporcionaría la guía de mejora en términos de modificación de MOF y / o membrana para mejorar la separación y el rendimiento.
3. Dado los estudios antes mencionados, se concluyó que se necesita el desarrollo de una membrana asimétrica para maximizar el potencial de separación del sistema MMM, ya sea en forma de una fibra hueca o una membrana de lámina plana. Una membrana asimétrica, con una capa selectiva de matriz mixta delgada aumentará el flujo de permeación ya que la resistencia a la difusión masiva en la membrana disminuirá significativamente. Por lo tanto, una membrana asimétrica reducirá la necesidad de un área superficial efectiva más grande en un módulo de membrana. Sin embargo, el desarrollo presentará un nuevo conjunto de desafíos, particularmente para producir una capa de membrana fina sin defectos y con morfología ideal MOF-polímero. La difusión no selectiva a través de la capa delgada y los defectos interfaciales deberían eliminarse.
4. Y por último pero no menos importante, la aplicación de las MMMs estudiadas, especialmente los sistemas hidrofílicos Zr-MOF MMM, pueden utilizarse en otras aplicaciones, especialmente en la pervaporación y eliminación de vapores orgánicos.